Persistent photoconductivity and the metal-insulator transition in Cd(_1-x)Mn(_x)Te:In

Leighton, Christopher

Persistent Photoconductivity and the Metal-Insulator Transition in $Cd_{1-x}Mn_xTe$:In.

Christopher Leighton

University of Durham 1997

A thesis submitted in partial fulfillment of the requirements for the degree of Doctor of Philosophy

Declaration.

I hereby declare that this thesis is original and that no part of it has been submitted previously for a degree at any other university. All work presented in this thesis is my own unless otherwise stated. This thesis is within the word limit set by the examining body.

Acknowledgements.

I welcome this opportunity to express my gratitude to the many people who have supported me during the course of my PhD. Firstly I am grateful to Professors D. Bloor and B.K. Tanner for provision of the facilities at the Physics Department. I would also like to thank a number of friends and colleagues with whom I have worked over the past three years: Dr. Salamat Ali, Gwyn Ashcroft, Dr. Paul Barker, Najib Cheggour, John Clarke, Stuart Dailey, Ian Daniel, James Eggleston, Brian Fulthorpe, Debbie Hales, Dr. Hamidi Hamid, Dr. Damian Hampshire, Tom Hase, Alton Horsfall, Simon Keys, Dr. Paul Laughlin, Dr. Chaorong Li, Andrea Li-Bassi, Dr. Jon Makar, Dr. Peter Moch, Dr. Ian Pape, Dr. Harry Ramsbottom, Dan Read, Dr. Toni Rogers, and Adrian Sneary. Special thanks should also go to "The Beer Brothers", Dr. Dirk Rose and Dr. Sergei Petrov, as well as a close friend, James Eggleston. In particular though, I would like to thank Dr. Caroline Moore for her continual friendship and support.

Above all, I am indebted to my supervisor, Dr. Ian Terry, whose guidance and enthusiasm have been a source of inspiration. I would like to thank him for his time and patience over the last three years. Thanks are also due to P. Becla for the provision of the samples used in this study. I would also like to acknowledge the help of Matt Hogan, Dr. Ken Durose, Norman Thompson and Dave Pattinson who patiently taught me to how to use the electron microscope.

I would like to thank Mr. John Dobson for his invaluable technical assistance. Special thanks are in order for the construction of a particularly fine box. Also, I would like to take this opportunity to apologise for the attempt I made on his life while leak-testing The Blue Dewar. On a similar note I would like to thank the staff of the student workshop (under the supervision of Mr P. Armstrong), the main workshop (under the supervision of Mr T. W. Hogg), the electronics workshop (under the supervision of Mr T. Jackson) and the audio visual department (Mr M. Lee, Miss V. Greener and Mrs P. A. Russell). The able assistance of the secretarial staff, Miss J. Bell, Mrs. C. Davies, Mrs

L.A. Wilkinson, Mrs S. Fairless, Miss P. Carse and Mrs N. Bingham is gratefully acknowledged.

Finally, I would like to thank my family and friends who have supported and encouraged me for the last three years.

Abstract.

The persistent photoconductivity (PPC) effect in the diluted magnetic semiconductor $Cd_{1-x}Mn_xTe$:In has been studied in detail. Electrical transport measurements have been made on a large number of samples to build up an understanding of the phototransport properties of this material. In particular, the compositional dependence of the phototransport parameters has been measured up to $x \approx 0.2$.

Several samples exhibit an elevated temperature PPC effect which has been interpreted in terms of the formation of multiple DX centres. These samples can have a quenching temperature of up to 190 K, suggesting that $Cd_{1-x}Mn_xTe$:In could be an interesting material in terms of applications of room temperature persistent photoconductors.

The low field magnetoresistance has been measured and analysed quantitatively in order to attempt to identify the origin of the magnetoresistive effects in insulating and metallic samples. The positive magnetoresistance has been found to be linked with the magnetization of the sample. An anomalous negative magnetoresistance has been observed under certain experimental conditions. This negative magnetoresistance has been interpreted in terms of the formation of bound magnetic polarons and their contribution to spin-disorder scattering.

The main body of this thesis is concerned with the study of the Metal-Insulator Transition (MIT). The PPC effect allows us to study the MIT in a continuous fashion by fine tuning the carrier density by illumination. In this way we have made the first zero magnetic field study of the MIT in a magnetic semiconductor. The critical behaviour has been found to be consistent with the scaling theory of electron localization, which predicts a critical form $\sigma = \sigma_0(n/n_c - 1)^{\nu}$. The critical conductivity exponent, ν was

determined to be close to one, while the critical carrier density, n_c, was found to be ~ 2 x 10^{17} cm^{-3}, for x = 0.08.

The temperature dependence of the conductivity has been quantitatively analysed in both the metallic and insulating phases. On the insulating side of the transition, variable range hopping (VRH) conduction has been observed at low temperatures (down to 300 mK). The temperature dependence is consistent with VRH conduction with electron-electron interaction effects taken into account. In the metallic phase the temperature dependence of the conductivity (up to ~ 1 K) is consistent with a model where the zero temperature value of the conductivity is corrected by electron-electron interaction effects, and the effects of weak localization. The magnitudes of these corrections are found to be in reasonable agreement with theoretical predictions.

The electrical transport has also been studied in the weakly localized regime in $Cd_{1-x}Mn_xTe$:In and $Cd_{1-x}Mn_xTe$:In, Al. A rapid decrease in the conductivity occurs at low temperatures (< 1.5 K). This is interpreted in terms of the effect of the s-d exchange interaction, which leads to the formation of bound magnetic polarons. It is suggested that this drop in conductivity can only be observed in the paramagnetic phase, and that spin-glass ordering has a significant effect on the temperature dependence of the conductivity at low temperatures.

1. Introduction.

For many years semiconducting materials have been the subject of intense research activity due to the existence of new and interesting physics, but most importantly because of the plethora of everyday applications of semiconductor devices. This research has provided us with a very detailed understanding of the physics of semiconductors, along with an extremely well developed technology for fabricating and processing high quality semiconducting material. This work is concerned with a family of semiconductors known as Diluted Magnetic Semiconductors or DMS, which were originally fabricated to allow the study of dilute magnetism in a material whose properties, such as electronic structure, are very well understood [1]. As we shall see, these semiconductors display a number of properties which make them interesting due to the new physics involved, as well as in terms of the potential applications [2].

This chapter is intended to give a brief and general introduction to the contents of this thesis. Section 1.1 outlines the motivation for the work, summarises the areas in which the work has been done and discusses some of the potential applications of the phenomena studied. Section 1.2 is concerned with the layout of the chapters. A brief description of the contents of each chapter is given, along with its relevance.

1.1. Introduction, Motivation and Applications.

This thesis is concerned with the study of an effect known as Persistent Photoconductivity (PPC) in the Diluted Magnetic Semiconductor $Cd_{1-x}Mn_xTe$:In [3]. As well as studying the PPC to gain insights into the underlying physics behind this phenomenon, we also wish to use the PPC to learn about the transport mechanisms in this compound, which is a member of a very interesting family of magnetic materials. The phototransport properties of this material have been investigated in a systematic fashion in order to obtain a clear picture of the physics involved. Although the physics of the DX

centre (the defect centre responsible for the PPC) has been studied rather intensively in this (and other) material, there remain many open problems about the fundamental nature of the DX centre [4].

Our main use of the PPC effect however, is to study the Metal-Insulator Transition (MIT) by continuously varying the persistent photocarrier concentration. The MIT is a long standing problem in condensed matter physics which continues to be the focus of a great deal of experimental and theoretical activity. Recent advances have been made with the theory of the behaviour of disordered electronic systems in the critical region near the MIT, and in the weakly localized regime (WLR) [5]. It is this theory which we intend to test by making an in-depth study of the MIT in this magnetic system. Central problems include the determination of the critical exponent in zero magnetic field, understanding the temperature dependence of the conductivity in the metallic phase and observing the effect of a magnetic field on the critical behaviour. These encompass some of the most poorly understood aspects of the MIT. In particular, it is far from clear which universality class a magnetic material such as this will be in, and whether the application of a strong magnetic field will be of any relevance. PPC provides control over the carrier concentration, allowing us to continuously 'fine tune' the transition by illumination at low temperatures [6]. This provides the opportunity to investigate the critical region in great detail, giving us a large advantage over the vast majority of other experiments on the MIT, where no such fine tuning is possible.

The PPC effect also has a number of potential applications which are discussed at a later stage. This includes the possibility of optical switching, enabling one to write erasable metallic patterns on a non-conductive background [7]. These possibilities are particularly exciting given that some of this thesis is concerned with measurements on samples which display PPC up to temperatures around 200 K. This leads us to the prospect of a room temperature DX centre persistent photoconductor, with a huge application potential.

1.2. Layout of Chapters.

The purpose of this section is to outline the way in which this thesis is organised and to briefly describe the content of each chapter.

Chapter 2 introduces some aspects of the physics of semiconductors and magnetism, which are relevant to the rest of the thesis. This is followed by an introduction to DMS. Special attention is paid to the transport properties of DMS such as CdMnTe, as this is the focus of the rest of the work. The important role played by the formation of Bound Magnetic Polarons (BMPs) is emphasised.

In chapter 3, an introduction to the MIT is given, with emphasis on the phase transition in doped semiconductors. This chapter includes sections on weak localization, and the nature of the hopping conduction as the MIT is approached from the insulating phase.

Chapter 4 presents quite a detailed review of PPC, including the origin of the effect and the phototransport properties of CdMnTe:In. The physics of the DX centre and multiple DX centre formation is discussed in some detail.

Chapter 5 details the experimental arrangements used during the project, as well as giving some information on the sample preparation techniques. The design and construction of the equipment used to perform the transport measurements is described, along with the details of the compositional analysis by Energy Dispersive Analysis of X-Rays (EDAX). The operation of the He^3 system used for the low temperature conductivity measurements is explained. The physical principles underpinning the various measurements (e.g. Hall effect, resistivity etc) are discussed in detail.

Chapter 6 presents the results of the electrical characterization measurements on two separate sets of samples. The EDAX data on these samples is also presented.

Resistivity, Hall effect, magnetoresistance and mobility are discussed in detail along with values of activation energies, carrier concentrations etc. The dependence of these phototransport parameters on the Mn fraction, x is studied. The high temperature PPC effect and the physics of multiple DX centre formation is discussed in the second half of the chapter. A section on an apparently anomalous form of magnetoresistance at high temperatures is included here. This work is connected with the discussions of BMP formation which are present throughout this thesis.

Chapter 7 presents the main body of experimental data on the MIT in CdMnTe. Results are shown for several samples close to the transition, two of which can be used to fine tune the MIT by illumination. The temperature dependence of the conductivity is analysed quantitatively in both the metallic and insulating phases. In the critical region the scaling theory of electron localization is applied, and the value of the critical exponent deduced. The temperature dependence of the conductivity in the WLR is investigated, where evidence is found for the formation of BMPs which dominate the transport mechanisms at low temperatures. This chapter also includes a section on CdMnTe doped with indium and aluminium.

In Chapter 8 conclusions are drawn on the various aspects of the work including the x dependence of the PPC, the origin of the high temperature PPC, and, most importantly, the nature of the MIT in CdMnTe. Suggestions for further work are described briefly.

Chapter 1 - References.

1. J.K. Furdyna. J. Appl. Phys. **64** R29 (1988).

2. C. Leighton, I. Terry and P. Becla. Phys. Rev. B. **56** 6689 (1997).

3. I. Terry, T. Penney, S. von Molnar, J.M. Rigotty and P. Becla. Solid State Commun. **84** 235 (1992).

4. P.M. Mooney. J. Appl. Phys. **67** 3 (1990).

5. P.A. Lee and T.V. Ramakrishnan. Rev. Mod. Phys. **57** 287 (1985).

6. C. Leighton, I. Terry and P. Becla. In preparation.

7. T. Thio, R.A. Linke, G.E. Devlin, J.W. Bennett, D.J. Chadi and M. Mizuta. Appl. Phys. Lett. **65** 1802 (1994).

2. Introduction to the Physics of Diluted Magnetic Semiconductors (DMS).

The aim of this chapter is to provide a very brief, and selective, introduction to the physics of DMS. As the DMS $Cd_{1-x}Mn_xTe$:In is the material on which this thesis is based, the introduction is intended to highlight the physics involved with this particular semiconductor. Sections 2.1 and 2.2 give a very brief introduction to the theory of semiconductors and magnetism. In each case the intention is to introduce only the concepts relevant to the rest of the thesis. For each section a number of textbooks are given as references. These will contain other relevant material, presented in a more comprehensive style. Section 2.3 deals with the DMS themselves. Firstly the crystal structure and growth is discussed, with CdMnTe being used as an example. Sections 2.3.2 and 2.3.3 deal with magnetic properties and Bound Magnetic Polarons (BMPs). These sections outline the magnetic interactions within the material, along with the resulting form of the magnetism in different temperature and concentration regimes. Next, section 2.3.4 deals with transport and magnetotransport and, in particular, the mechanisms which are thought to give rise to the large positive and negative magnetoresistances observed. Finally section 2.3.5 gives a very brief review of the magneto-optical effects which have been observed in DMS. These include giant Faraday rotation and photoinduced increases in magnetization.

2.1. Basic Semiconductor Theory.

This section will give a very brief introduction to semiconductor physics. Textbooks giving more detailed coverage are found in refs [1, 2, 3, 4]. The concepts introduced and defined here relate mostly to the electrical properties of semiconductors, as this thesis is concerned primarily with electrical transport measurements.

At $T = 0$ K semiconductors have a completely filled valence band, separated by an energy gap (E_g), from a completely empty conduction band. This energy gap is a

region where electronic states are forbidden to exist due to the periodicity of the lattice producing regions where electron wavefunctions destructively interfere. The schematic figure 2.1.1 shows this situation in an E - k diagram, where E represents the energy of electrons and $\underline{k} = \frac{\underline{p}}{\hbar}$ is the electron wavevector. Here, the conduction band (CB), valence bands (VB), and energy gap, E_g, are clearly labelled. This picture describes an intrinsic semiconductor, where at $T \neq 0$ conduction occurs by thermal activation of electrons from the VB to the CB, resulting in the formation of electrons in the CB and holes in the VB. This process leads to an intrinsic free carrier concentration, n_I as given by,

$$n_I = 2\left(\frac{m_e^* k_B T}{2\pi\hbar^2}\right)^{3/2} \exp\left(\frac{-(E_g - E_F)}{k_B T}\right) \qquad (2.1.1),$$

where m_e^* is the effective mass in the CB (defined later), and E_F is the Fermi level (the energetic position where the probability of finding an electron using Fermi-Dirac statistics is 1/2). Note that this expression is valid only in the non-degenerate case.

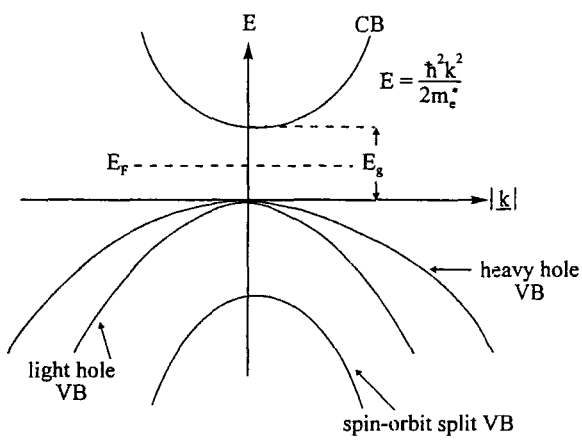

Figure 2.1.1. E - k diagram for a typical direct gap semiconductor.

The carrier concentration n_I is derived by calculating the density of allowed states in an incremental energy interval, and the probability distribution function for the electrons. The density of states (DOS) has a typical form for the conduction band of,

$$N_{CB} = \frac{1}{2\pi^2}\left(\frac{2m_e^*}{\hbar^2}\right)^{3/2}\left(E - E_g\right)^{1/2} \qquad (2.1.2).$$

while the probability distribution function used is the Fermi-Dirac function.

The effective mass m_e^* is used to describe the shape of the E - k curves. As can be seen from the diagram (2.1.1) the bands shown here are parabolic i.e.,

$$E = E_g + \frac{\hbar^2 k^2}{2m_e^*} \qquad (2.1.3).$$

So the free electron form for the relationship between E and k is modified by the inclusion of the effective mass which determines the degree of curvature of the parabolas in figure 2.1.1. This is known as the effective mass approximation and holds rather well for most real semiconductors in the limit of low k, where the bands are, to a good approximation, parabolic. This leads to the definition of the effective mass as,

$$m_e^* = \frac{\hbar^2}{\partial^2 E/\partial k^2} \qquad (2.1.4).$$

One of the most useful properties of semiconductors (which is in fact responsible for most of their applications) is that introduction of small amounts of impurity can drastically alter the electronic properties of the material. Basically impurities can be accommodated into the lattice in two situations : on a vacant lattice site (a substitutional impurity) or between host sites (an interstitial impurity). To a first approximation only the substitutional form is electrically active. These impurities introduce levels into the band gap of the semiconductor as shown in figure 2.1.2. These levels are classified as either deep or shallow levels. The deep levels are localized states which produce energy levels

well into the forbidden gap, whereas shallow levels form close to the CB or VB edge, depending on the bonding arrangement between the impurity and the host. For example, for the case of the semiconductor Si the bonding is tetrahedral so the introduction of a pentavalent impurity such as P would result in one excess electron which can then be donated to the CB leaving the shallow level just below the CB edge. For Si:B (silicon doped with boron) the situation is reversed ; one electron is accepted from the VB and the shallow acceptor level resides just above the VB edge.

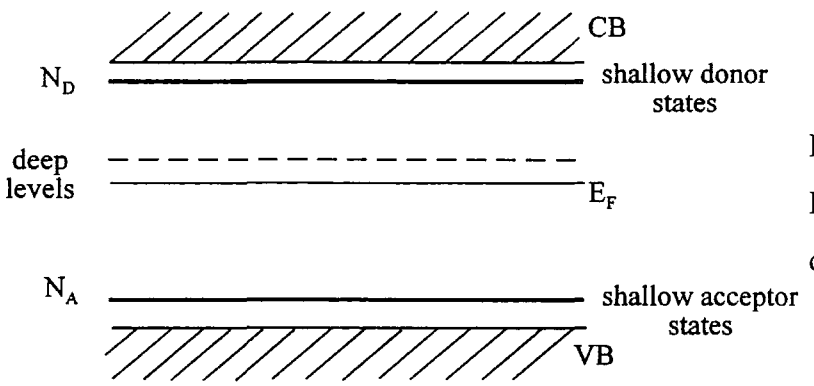

Figure 2.1.2.
Band Diagram for a typical doped semiconductor.

This process of introducing impurities into the material is called doping, and can be used to control the conductivity and free carrier concentration of the material. A material in which the majority carriers are electrons is termed n-type, whereas if the conduction proceeds by flow of holes the material is known as a p-type conductor. It should be noted that even a material deliberately doped n-type may contain a certain number of acceptor levels which act to 'cancel out' the effect of a number of the donor states. This process is known as compensation. A dimensionless compensation ratio can then be defined as $K = N_A / N_D$, where N_D is the concentration of donor levels and N_A is the concentration of acceptor levels.

Although the calculation of the binding energy of the deep levels is rather specific to the nature of the particular deep state involved (e.g. DX centres - see chapter 3), the energy of shallow levels can be calculated within the framework of the hydrogenic theory of shallow donors. Here the situation of an electron associated with a positively charged donor ion is modelled as for the hydrogen atom, but with the electron mass replaced by the effective mass, and the permittivity of free space replaced by the average permittivity of the material. This gives (for the ground state),

$$E_D = \frac{m_e^* / m_e}{\varepsilon^2}(13.6eV) \qquad (2.1.5),$$

and

$$a_B = \frac{\varepsilon}{m_e^* / m_e}\left(0.053nm\right) \qquad (2.1.6),$$

where a_B is known as the Bohr radius of the donor and m_e is the ordinary electron mass. These equations give quite reasonable estimates for many materials, for example the calculated and experimental values for lightly Si doped GaAs are 0.0054 eV and 0.0058 eV respectively. There are however, corrections to the theory, such as the chemical shift, which takes into account the specific chemical structure of the impurity.

This process of deliberately introducing shallow donor levels into the system can be used to control the conductivity as these states donate an electron into the CB, leading to an increase in the conductivity. For $k_BT < E_D$ the free carrier concentration in the CB, n, is given approximately by,

$$n = N_D e^{-E_D/k_BT} \qquad (2.1.7).$$

So the conduction is likely to occur via activation from the shallow level to the conduction band edge, particularly if the temperature is not high enough to allow VB to CB activation.

An important point to make in the context of this thesis is that these equations are not valid for the case of heavy doping. In this situation, as the concentration of impurity levels increases, the initially discrete energy levels merge to form bands. This leads to a rather different value for the energy level. This situation for the case of heavily Al, In doped CdMnTe will be discussed in more detail later.

The electrical transport measurements presented in this thesis are concerned with the measurement of conductivity ($\sigma = 1 / \rho$) and free carrier concentration, n. This carrier density is calculated from measurements of the Hall coefficient. Here a current flows in a magnetic field which is directed perpendicular to the direction of the current flow. An electric field is generated across the sample due to the electron path curvature in the applied magnetic field, which leads to accumulation of charge. It can be shown that [4],

$$R_H = \frac{V_H t}{BI} \qquad (2.1.8),$$

where R_H is the Hall coefficient, t is the sample thickness, B is the applied magnetic field and I is the current. Then we have, $R_H = 1 / (ne)$, allowing a determination of n. It is worth mentioning at this point that this analysis is restricted to the region of low magnetic fields, and indeed all of the Hall effect measurements presented in this thesis are performed in fields of 0.5 T or smaller. Also, 2.8 neglects the Hall scattering factor, r, which is of order unity. It is common practice to assume that this factor is unity in the analysis of Hall effect experiments [5]. Combined conductivity and Hall effect measurements allow a determination of the Hall mobility, μ through the relation $\sigma = ne\mu$. The mobility is defined as the magnitude of the drift velocity per unit applied electric

field, μ = v/E, and is of great interest, as it contains information on the scattering mechanisms taking place.

In a pure crystal at $T = 0$ the Bloch waves propagate through the perfectly periodic lattice without scattering. However at $T \neq 0$, or when imperfections are included, the electron waves are scattered by these imperfections, or by the oscillations at the atomic sites due to thermal vibration. Within the classical Drude theory the conductivity is given by $\sigma = ne^2\tau / m_e^*$, where τ, the inverse scattering rate, contains information regarding the scattering mechanisms. Quantum mechanical treatments of scattering mechanisms predict the value of τ, which is then used to calculate $\mu = e\tau / m_e^*$. This allows a comparison between theory and experiment.

Typical dominant scattering mechanisms in semiconductors are phonon scattering, neutral donor scattering, ionized impurity scattering, alloy scattering, piezoelectric scattering and dislocation scattering. Each of these leads to a certain temperature dependence of the mobility, making the mobility a useful method of determining the dominant scattering mechanisms present. In CdMnTe:In, phonon scattering and ionized impurity scattering are likely to be the most important. For this reason, a description of both of these mechanisms is given below (see refs [6, 7] for a fuller treatment).

In general both optical and acoustic phonons can play an important role in the scattering of electrons in semiconductors. However, for the specific case of a CdTe based compound such as CdMnTe, the analysis is simplified by the fact that in polar materials such as these, optical phonon scattering is the dominant scattering mechanism [7]. This leads to a form for the optical phonon scattering limited mobility, μ_0 of [8],

$$\mu_0 = \frac{2e}{3\pi^{3/2} \alpha m_e^* \nu}\left[f(z)\right] \qquad (2.1.9),$$

where $f(z)$ is given by,

$$f(z) = \chi(z)\frac{\left(e^{z}-1\right)}{z^{1/2}} \qquad (2.1.10).$$

Here, $z = h\nu / k_B T$, $\chi(z)$ is a weak function of z, and α is the so-called electron-phonon coupling constant [6]. Empirically this leads to a temperature dependence of the mobility which can be approximated by $T^{1/2}$ at high temperatures. So as one might expect, at higher temperatures the probability of scattering off a phonon increases, lowering the mobility. The form in equations 2.8 and 2.9 has been successfully applied to CdTe to model the observed temperature dependence of the mobility [7].

The most important scattering mechanism for CdMnTe:In is the ionized impurity scattering, which in particular, dominates at low temperatures, below 200 - 250 K. It should be noted that both in this study and previous ones [9,10], this is due to the heavy doping level. Several approaches to the problem of ionized impurity scattering have been made, most notably the Conwell-Weiskopf method and the Brooks-Herring model [11]. Here we are considering the problem of the scattering of an electron by the Coulomb field of the ionized impurity. In the Conwell-Weiskopf theory this is modelled by assuming that electrons are only scattered when they pass within a distance $d/2$ of the scattering center, where d is the average distance between centers. The Brooks-Herring approach reflects a slightly more realistic scenario, where the effects of electron screening are taken into account to modify the Coulomb potential. This leads to a form for the ionized impurity scattering limited mobility, μ_{II},

$$\mu_{II} = \frac{128\sqrt{2}\pi^{1/2}\varepsilon^{2}\left(k_B T\right)^{3/2}}{m_e^{*1/2} N_I Z^{2} e^{3}}\left[\ln\left(\frac{24 m_e^{*}\varepsilon\left(k_B T\right)^{2}}{n e^{2}\hbar^{2}}\right)\right]^{-1} \qquad (2.1.11),$$

where N_I is the density of ionized impurities. This formula shows a $T^{3/2}$ dependence of the mobility on temperature, and can be used to model the temperature dependence of the

mobility, along with the n dependence of the mobility at a fixed temperature during illumination.

2.2. Theory of Magnetism.

The aim of this section is to provide a very simple introduction to the various types of magnetism relevant to DMS, along with their origins. The exchange interaction is discussed after a short description of diamagnetism, paramagnetism, ferromagnetism and antiferromagnetism. The magnetic properties of any material arise due to the fact that an electron possesses angular momentum. This consists of a component due to its intrinsic spin and its orbital angular momentum. These two components are responsible for all the forms of magnetism listed above. Although there are other forms of magnetic behaviour these will not be discussed as they are not relevant to the DMS CdMnTe. The RKKY and Bloembergen-Rowland interactions are discussed in section 2.3.2 along with spin-glass formation. Refs [1, 2, 4, 12] all include a treatment of these phenomena in more detail.

Firstly we define the terms magnetic moment (m), Magnetization (M) and susceptibility (χ). If one considers a current loop of vector area $\underline{A}$, with a current I flowing then by definition, $\underline{m} = I\underline{A}$. The magnetization is then defined as the magnetic moment per unit volume, $\underline{M}$. In turn, the susceptibility can be defined by $\underline{M} = \chi\underline{H} = \chi\underline{B} / \mu_0$, where $\underline{H}$ is the applied field and $\underline{B}$ is the applied magnetic flux density. The susceptibility is the parameter which is usually used to characterize a material's magnetic response.

Diamagnetism is the type of magnetism which comes about if we examine the magnetic behaviour of an electron orbiting the nucleus with a certain angular momentum. In solids, diamagnetism is due to the 'closed shell' electrons which have no free spin. The diamagnetic susceptibility can be calculated using a semiclassical approach giving [1],

$$\chi_D = -\frac{\mu_0 NZe^2}{6m_e}\left\{r^2\right\} \qquad (2.2.1),$$

where N is the number of atoms per unit volume, Z is the atomic number, m is the mass of the electron and $\{r^2\}$ is the mean square radius of the electron orbit, which can be calculated from quantum mechanical theory. This susceptibility is negative and temperature independent. A plot of $\underline{M}$ against $\underline{H}$ will result in a straight line with negative slope. A typical size of the dimensionless volume susceptibility is 10^{-5}, with Ag and Au being examples of diamagnets.

Paramagnetism is due to the intrinsic spin of the electron, as well as its orbital angular momentum. The magnetic dipole moment associated with such a spin, s is given by $m_S = 2\mu_B [s(s + 1)]^{1/2}$, where μ_B is the Bohr magneton. For the case of paramagnetism, the intrinsic spin contribution is considered along with the orbital component to derive an expression for the susceptibility. The Boltzmann probability distribution is used to calculate the mean value of the moment, which leads to :

$$\chi_p = \frac{\mu_0 N g^2 \mu_B^2 J(J+1)}{3k_B T} \qquad (2.2.2)$$

where J is the total angular momentum quantum number calculated using Hund's rules from the spin and orbital angular momentum. This result is known as Curie's law. The susceptibility is a function of temperature but typical values are between 10^{-3} to 10^{-5} for materials such as Pt and Mn. A plot of $\underline{M}$ against $\underline{H}$ results in a straight line with positive gradient, until saturation occurs at high field, when all of the individual moments are aligned with the magnetic field vector (see equations 2.2.4 and 2.2.5).

The phenomena of ferromagnetism and antiferromagnetism are essentially different from diamagnetism and paramagnetism in that they have a spontaneous magnetic moment associated with them, due to the fact that the spins are arranged and

oriented in a regular manner. The temperature dependence of the susceptibility for the four types of magnetism considered here is shown in figure 2.2.1. For a ferromagnet, a spontaneous magnetic moment is observed below a certain temperature called the Curie temperature. This is the temperature below which magnetic order sets in. Above this temperature we have a paramagnetic phase of the ferromagnetism with,

$$\chi_F = \frac{C}{T - T_C} \qquad (2.2.3),$$

where T_C is the Curie temperature. This is known as the Curie-Weiss law. The mean field theory of ferromagnetism can explain the qualitative features of ferromagnetism quite well by assuming that an internal field produces the spontaneous magnetic moment. The origin of this internal field is actually the exchange interaction detailed later. Typical sizes of the dimensionless volume susceptibility for ferromagnetic materials like Fe and Ni are 50 to 10,000. The form of the $\underline{M}$ v $\underline{H}$ plot is given by the following equations in the paramagnetic phase [1,12],

$$M = NgJ\mu_B B_J(x) \qquad (2.2.4),$$

where $x = gJ\mu_B B / k_B T$ and $B_J(x)$ is the Brillouin function defined by,

$$B_J(x) = \frac{2J+1}{2J} ctnh\left(\frac{(2J+1)x}{2J}\right) - \frac{1}{2J} ctnh\left(\frac{x}{2J}\right) \qquad (2.2.5).$$

In antiferromagnetism the situation is similar other than that the magnetic moments are ordered antiparallel on two interconnecting sublattices below the Neel temperature T_N. A similar analysis leads to

$$\chi_{AF} = \frac{C'}{T+\theta} \qquad (2.2.6),$$

where θ is reasonably close to the actual Neel temperature, T_N. For a wide range of antiferromagnetic materials the value of θ / T_N is between 5.3 and 1.1.

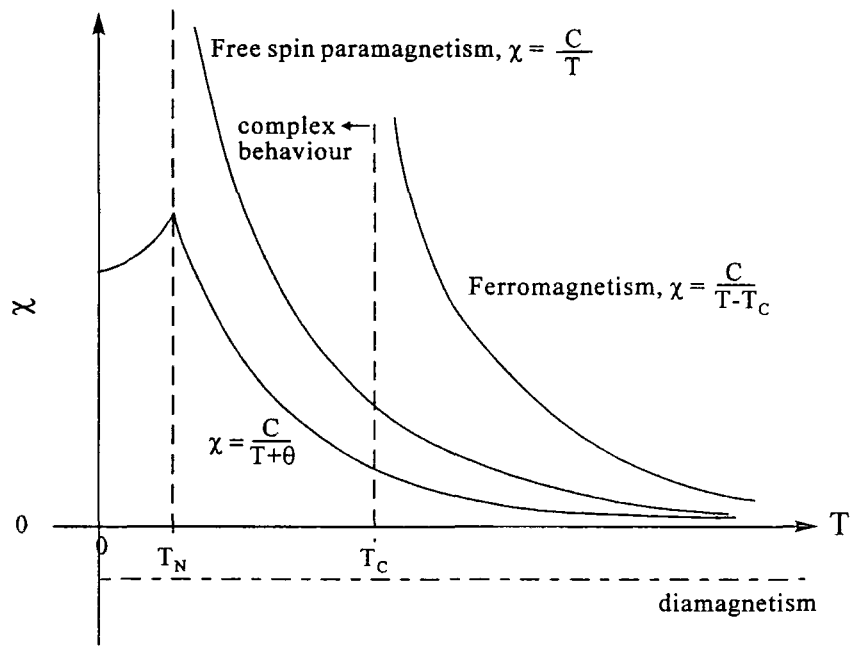

Figure 2.2.1. Temperature dependence of the susceptibility for diamagnetism, paramagnetism, ferromagnetism and antiferromagnetism.

As was mentioned briefly the source of the spontaneous magnetization is the quantum mechanical exchange interaction. This interaction between the spins of two electrons comes about due to the overlap of the electron wavefunctions i.e. the Coulomb interaction (along with the Pauli exclusion principle) is ultimately responsible. In a solid the exchange interaction Hamiltonian between two spins $\underline{S_i}$ and $\underline{S_j}$ can be written as

$$H_{ex} = -2\sum_{i,j}\left(\underline{S_i}.\underline{S_j}\right)J_{i,j} \qquad (2.2.7),$$

where $J_{i,j}$ is the nearest neighbour exchange integral and the sum is over all of the atoms in the solid. If $J_{i,j} < 0$ then the interaction is antiferromagnetic, whereas if $J_{i,j} > 0$ the interaction is ferromagnetic in nature. In practice, any one solid could have a number of varieties of exchange occurring. This situation is considered for CdMnTe in section 2.3.2. There are also varieties of exchange which are indirect. Some of these are relevant to the magnetic properties of CdMnTe and will also be discussed in section 2.3.2.

2.3. Diluted Magnetic Semiconductors.

Quite simply, Diluted Magnetic Semiconductors (DMS) are solid solutions of magnetic ions in a nonmagnetic host compound. These compounds are sometimes referred to as Semimagnetic Semiconductors (SMSC). DMS in various forms have been studied in great detail since the late 1970's [13] primarily as a result of some unique features which they display. These include : a large variety of magnetic phenomena in a host with a simple, well understood band structure, good control over carrier density, magnetic ion concentration etc, as well as some interesting magneto-optical properties. Several families of DMS exist along with several well studied forms of magnetic semiconductor such as $Gd_{3-x}v_xS_4$ [14] and EuS [15]. As well as the most popular $A^{II}_{1-x}Mn_xB^{VII}$ compounds, systems as varied as $CuFeS_2$ [16] and $(Cd_{1-x}Mn_x)_3As_2$ [17] have been studied. The material studied in this thesis is $Cd_{1-x}Mn_xTe$:In (although both ZnMnTe and HgMnTe are also studied in Durham), so this compound will be covered in most detail.

Solutions of Mn^{2+} ions in II-VI semiconductor lattices are extremely popular DMS, primarily due to the unique situation with regard to the electronic structure of Mn. The outer two electron shells consist of a half filled d shell, along with a full *s* shell. The 5 d electrons align parallel, giving $S = 5/2$, the maximum possible value. This configuration is energetically very stable as the addition of an extra electron would necessitate a spin being aligned in the opposite direction. The full *s* shell (2 electrons)

therefore acts like the outer electron shell making Mn behave like a group II element. Hence Mn is easily incorporated in a II-VI lattice. In addition to this, Mn is remarkable in that when it is added to a II-VI compound it acts as neither a donor nor as an acceptor, and hence does not perturb the density of states at the Fermi level. This is because the energy levels introduced by the Mn do not lie within the forbidden gap. These two facts have made $A^{II}_{1-x}Mn_xB^{VII}$ compounds the most intensively studied form of DMS.

2.3.1. Crystal Structure and Growth. CdMnTe.

Here we shall specifically discuss II-VI DMS based on Mn ions as a magnetic impurity. These compounds crystallize in the zinc-blende structure of the nonmagnetic host, up to considerable Mn concentrations. For the case of CdMnTe, the solubility limit, before the pure zinc-blende form is lost, is around 77% Mn [18]. This crystal structure is shown on figure 2.3.1, along with the lattice constant as a function of x for CdMnTe, HgMnTe and ZnMnTe. As can be seen from the figure, all of these materials obey Vegards law i.e. :

$$a = (1-x)a_{II-VI} + xa_{Mn-VI} \qquad (2.3.1),$$

where a is the lattice parameter of the ternary compound, a_{II-VI} is the lattice parameter of the II-VI compound (e.g. CdTe) and a_{Mn-VI} is the lattice parameter of the Mn-group VI compound (e.g. MnTe).

Figure 2.3.2. shows the band gap of $Cd_{1-x}Mn_xTe$:In as a function of the Mn concentration, x. The band gap opens from around 1.5 eV for CdTe, and extrapolates to about 3.1 eV for zinc-blende MnTe. An extrapolation beyond the solubility limit of similar curves for ZnMnTe and HgMnTe, result in the same value of 3.1 eV for the band gap of zinc-blende MnTe. However, MnTe actually crystallizes in the NiAs structure where it has a band gap of around 1.3 eV [19]. MnTe has been successfully grown in zinc-blende form though, by the non-equilibrium growth technique of Molecular Beam

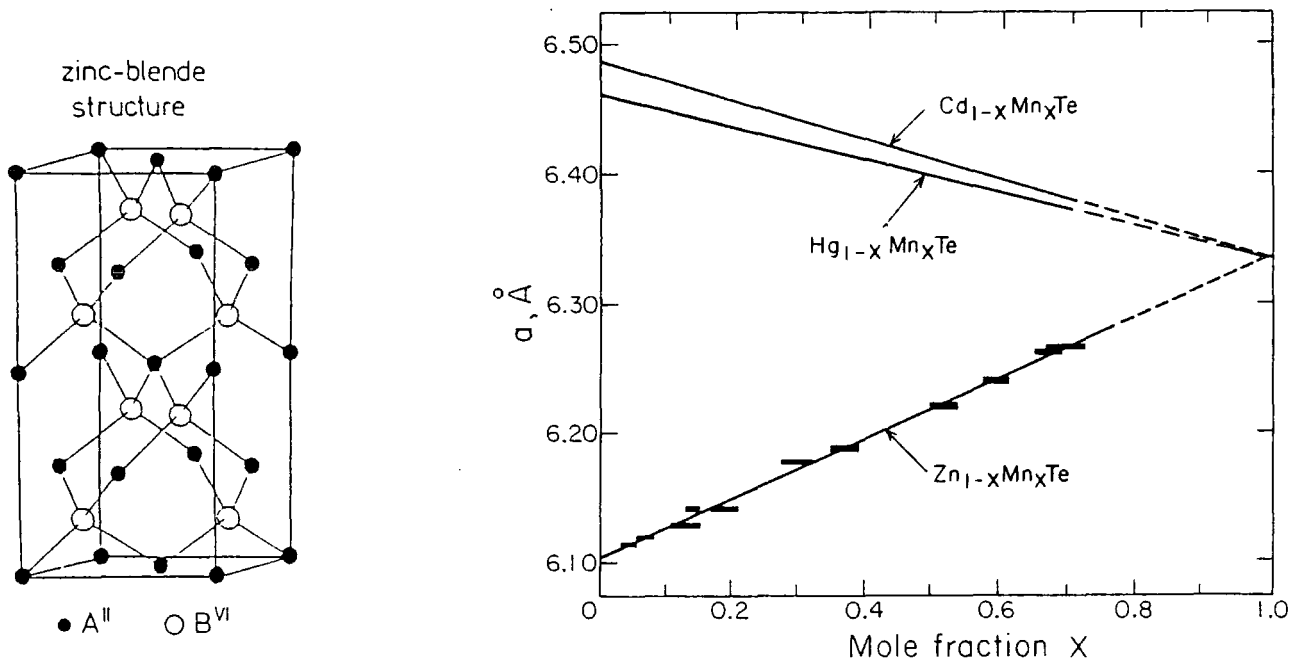

Figure 2.3.1. Crystal strucure of $A^{II}B^{VI}$ zinc-blende compounds. CdMnTe crystallizes in the same structure as CdTe up to77% Mn (see figure below). The variation of the lattice parameter with Mn composition for CdMnTe, ZnMnTe and HgMnTe is shown [20] .

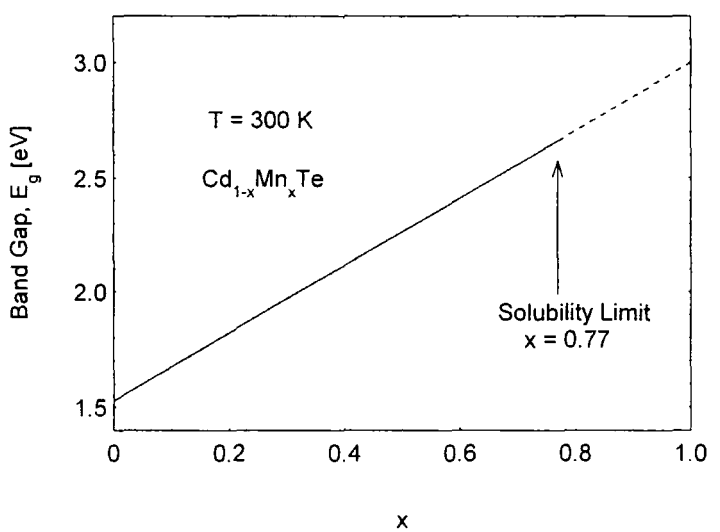

Figure 2.3.2. Band gap variation with Mn composition for $Cd_{1-x}Mn_xTe$ at room temperature. From [18].

Epitaxy (MBE)[19]. This growth did indeed produce a material with a band gap around 3.0 eV.

CdMnTe is grown in bulk form by the vertical Bridgman technique [16] as detailed by Furdyna [16]. As mentioned earlier, it can be grown in zinc-blende form up to x = 0.77, at which point mixed phases occur. The macroscopic quality of the CdMnTe crystals grown by this method is the best of any of the II-VI DMS. Like CdTe, CdMnTe bulk crystals often exhibit twinning and small Te inclusions. These points are mentioned in chapter 4 where it is made clear that samples in this study were examined for twinning under an infra-red microscope. It is also pointed out that Te inclusions were found using SEM / EDAX. As-grown crystals tend to be p-type, but as we point out in chapter 4 doping with In and annealing in Cd vapour produces n-type material.

2.3.2. Magnetic Properties.

A wide spectrum of magnetic behaviour is observed in the various families of DMS which have been studied thus far. Specifically for the case of CdMnTe, paramagnetism, spin glass formation and antiferromagnetism are seen in various concentration and temperature regions [20]. In addition to these magnetic phenomena, ferromagnetism has been observed in several DMS such as IV-VI Mn based compounds [21] and GaMnAs [22]. Compounds such as PbMnTe are particularly interesting as they show a large RKKY interaction [21]. Here the localized Mn moments interact indirectly via the sea of delocalized carriers in the material. The Mn spins polarize the surrounding electrons or holes, which can in turn align other Mn spins due to the delocalized nature of the current carriers. This form of magnetic interaction is obviously intimately linked with the conduction process. For the case of p - PbSnMnTe for example, the Curie-Weiss temperature can be seen to change sign to positive and increase rapidly with increasing hole concentration, above $2x10^{20}$ cm^{-3}. This indicates that for the case of coupling between d spins mediated by holes the interaction is ferromagnetic and a phase transition to a ferromagnetic state can be induced by increasing the hole concentration. No such

effect has been observed in n - CdMnTe down to 100 mK with carrier concentrations of up to $8x10^{17}$ cm^{-3} [23], suggesting that the RKKY interaction is not strong enough to induce a ferromagnetic phase in this system. This point will be commented on later in section 6.4.

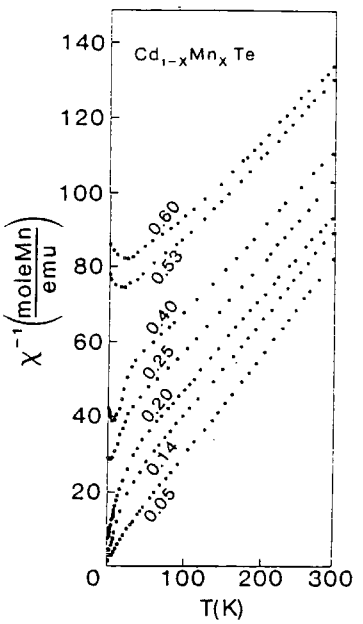

Figure 2.3.3. Temperature dependence of the inverse susceptibility for various values of x in $Cd_{1-x}Mn_xTe$. After [24].

An overview of the magnetic behaviour of CdMnTe will now be given. At high temperatures the susceptibility shows a paramagnetic Curie-Weiss behaviour with a negative Curie-Weiss temperature, indicative of the antiferromagnetic exchange interactions between $S = 5/2$ Mn spins. This behaviour is shown in figure 2.3.3 [24]. This Curie-Weiss temperature, θ, is given by,

$$\theta = \frac{2S(S+1)}{3k_B} x \sum_k z_k J_k \qquad (2.3.2),$$

where z is the co-ordination number, and J is the net value of the exchange integral. If we assume only nearest neighbour exchange interactions (experimentally, the nearest neighbour exchange integral has been found to be larger than the next nearest neighbour exchange integral by at least a factor of 10 [18]), with $z = 12$ and $S = 5/2$ then we obtain,

$$\theta = \frac{70xJ_{NN}}{k_B} \qquad (2.3.3),$$

where J_{NN} is the nearest neighbour exchange integral. Values of θ determined from direct susceptibility measurements in this way suggest $-J_{NN}/k_B \sim 6$ to 10 K [24].

In this paramagnetic regime the magnetization has been studied as a function of field and temperature [25]. Down to liquid helium temperatures, and in fields of up to 15 T the magnetization is well described by a Brillouin function with modified parameters. For example, the Mn concentration and spin are replaced by effective values which reproduce the experimental data. These 'effective values' are found to have a systematic dependence on composition and temperature. At higher fields more complicated behaviour is observed such as linear magnetization [25] and magnetization steps [26]. Both of these effects are thought to be related to the formation of clusters of Mn spins as explained below.

At lower temperatures (about 50 K for x = 0.1) deviations from this simple paramagnetic behaviour are seen, with the deviations occurring at higher temperature for higher x values. This effect is well understood and is due to the fact that the Mn spins begin to align and interact in clusters, an effect which is enhanced as the Mn concentration is increased. Quantitative agreement can be obtained between experiment, and theory based on the probability of formation of clusters of various numbers of Mn spins [27]. At temperatures below about 40 K, and at sufficiently large Mn fraction ($x >$ 0.17), a spin glass phase is observed [20]. Here, magnetic frustration due to competing exchange interactions leads to a situation where the most energetically favourable state is one in which the random alignments of the individual magnetic moments are frozen into place. This occurs below a certain temperature known as the spin glass freezing temperature, $T_f(x)$. The variation of T_f with x is shown in figure 2.3.4 for CdMnTe [24]. The susceptibilty shows a cusp at this temperature and values of the susceptibility below T_f depend on whether the sample is cooled in field or not, as shown in figure 2.3.5 [24].

In addition to this spin glass behaviour, an antiferromagnetic phase is observed for $x > 0.7$, as evinced by magnetization and specific heat capacity studies [28].

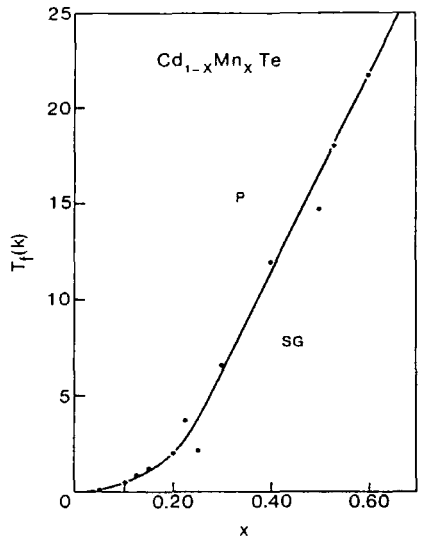

Figure 2.3.4. Variation of T_f with x for $Cd_{1-x}Mn_xTe$.

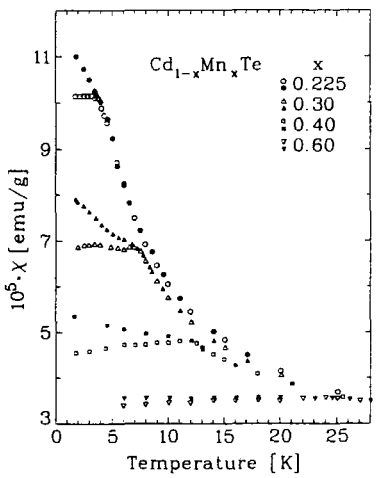

Figure 2.3.5. $\chi(T)$ near T_f in $Cd_{1-x}Mn_xTe$

In terms of the exchange interactions relevant to the behaviour of CdMnTe, we have seen that the d-d exchange between Mn spins is antiferromagnetic in nature with J_{NN} / k_B approximately 10 K. It should be noted that the dominant exchange mechanism here is that of antiferromagnetic anion superexchange. Here the interaction is indirect : a Mn $S = 5/2$ spin interacts with a Te ion which, in turn, interacts with another Mn spin, producing a net exchange interaction between the two Mn spins. Although mechanisms such as the RKKY interaction and the Bloembergen-Rowland interaction should also be taken into account, it is this superexchange which is dominant.

There also exists an s,p-d exchange interaction between conduction electrons or holes and the Mn d spins. The s-d exchange interaction has a positive exchange integral and is therefore ferromagnetic in nature. The p-d exchange is antiferromagnetic. The exchange interactions in CdMnTe are summarised in table 2.3.1, where α denotes the s-d exchange energy and β denotes the p-d exchange energy [29].

d - d	AF Superexchange	$-J_{NN} / k_B = 6$ - 10 K
s - d	Ferromagnetic	$\alpha = 0.22$ eV
p - d	Antiferromagnetic	$\beta = -0.88$ eV

Table 2.3.1. Values of the d-d and s,p-d exchange energies for CdMnTe.

The exchange interaction between conduction electrons or holes and localized Mn spins is the one which can have important effects on the electronic conduction process. One such effect is the formation of bound magnetic polarons as discussed in the next section.

2.3.3. The Bound Magnetic Polaron (BMP).

A bound magnetic polaron (BMP) is formed when a localized carrier orients a cluster of ionic spins within its localization radius. In other words the ionic spins in the local environment of the bound carrier respond to the s-d exchange interaction and lower the total energy of the localized state. For the case of CdMnTe:In, a donor bound magnetic polaron forms when the $S = 1/2$ electron polarizes the $S = 5/2$ Mn spins within its localization radius. This results in a ferromagnetically aligned cloud of Mn spins with a very large magnetic moment and susceptibility, which can have important effects on the transport (and magnetic) properties of the material.

If one considers the bound electron as being in a potential well of depth E, and width 2ξ, where ξ is the localization radius, then it is clear that formation of a BMP deepens the well to a depth $E + \delta E$, resulting in a reduction of the width to $2\xi - \delta\xi$. i.e. the state has become more localized. It is important to note that as the effective Bohr radius of acceptors is smaller than that of donors in compounds such as CdMnTe, the BMPs formed in p-type material will have a larger binding energy and hence will have a greater impact on the magnetic properties of the system.

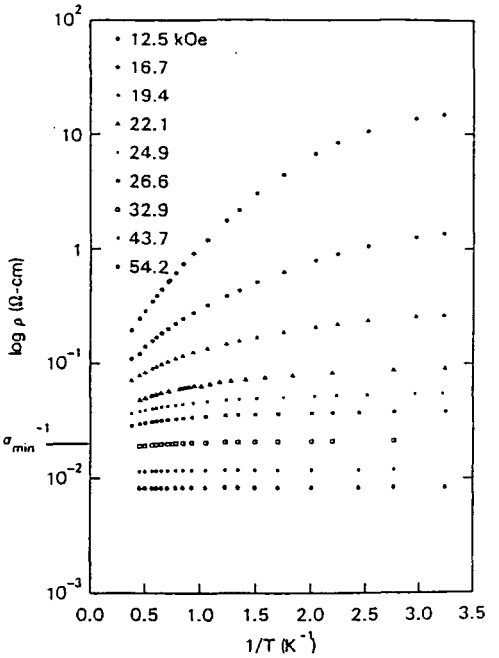

Figure 2.3.6. Temperature dependence of the resistivity of $Gd_{3-x}V_xS_4$ in various applied magnetic fields.

BMP's have been observed in a whole host of materials including magnetic and diluted magnetic semiconductors. For example, spin-flip Raman scattering experiments on n-CdMnSe [30] clearly revealed BMP formation, as did a luminescence study of p-CdMnTe [31]. Some of the most convincing evidence however, has come from transport, magnetotransport and magnetic measurements on systems such as $Gd_{3-x}V_xS_4$ by von Molnar *et al* [32]. Here a large negative magnetoresistance is observed at low temperatures as shown in figure 2.3.6. This is attributed to the destructive effect of the application of a magnetic field on the BMP. As the field is increased from zero the paramagnetic or antiferromagnetic response of the background aligns the moments which have not formed BMPs, until eventually the magnetization saturates and these moments have the same polarization as the polarons. At this point the binding energy of the polaron is zero and it ceases to exist. The microscopic mechanism for the negative MR depends on the conduction mechanism, but in all cases is due to the effect of the applied field on the BMPs. For instance, for the case of activated conduction, the spin-disorder scattering rate is reduced by the magnetic field (due to the reduction in the binding energy of the polarons). This clearly results in a negative MR. To summarise, when the applied field is

increased the binding energy of the polaron is reduced and the resistance of the sample decreases, as the background polarization slowly aligns with the oriented moments of the BMPs. This large negative contribution to the magnetoresistance is seen as a signature of the formation of BMPs.

BMPs effect the magnetotransport properties of DMS such as CdMnTe in a similar way as discussed in the next section, 2.3.4. The formation of BMPs and their effect on zero field transport at low temperatures is also discussed in detail in section 2.3.4. Finally, they are also of importance in the discussion of magneto-optical effects observed in DMS as discussed in section 2.3.5.

2.3.4. Transport and Magnetotransport Properties.

This section is intended to give a brief description of the salient features of the transport and magnetotransport in DMS, with particular emphasis on CdMnTe:In, and similar doped DMS such as CdMnSe. The electrical properties of relatively wide band gap DMS such as these are normally only studied in heavily doped samples, as the nominally undoped material is far too insulating. Obviously, narrow gap material such as HgMnTe is rather different. This compound displays semimetallic, semiconducting and insulating behaviour depending on the size of the band gap, which in turn is dependent on the Mn fraction.

CdMnTe:In displays persistent photoconductivity which is the subject of this thesis and is the method which we have used to study the MIT. The persistent photoconductivity of CdMnTe: In is discussed in section 4.3, while the MIT is discussed in detail in chapter 3. The remainder of this section is concerned with transport phenomena other than this PPC effect.

The transport properties of DMS such as CdMnTe:In are dominated by the distance from the MIT. As will be discussed in chapter 3, the MIT occurs at a critical

carrier concentration, n_c, which is dependent on the Mn concentration. Below this concentration the system is insulating, while above this concentration metallic conductivity is seen. In the insulating regime an activated form for the conductivity is expected, in accordance with equation 2.1.7. Analysis of Hall effect data allows the determination of the activation energy from the donor level to the conduction band. At lower temperatures the conduction is expected to proceed via a hopping mechanism. This involves electrons jumping from state to state in the direction of the applied electric field. The various possible hopping mechanisms and their temperature dependences are discussed in detail in section 2.4.5.

The magnetotransport properties of DMS such as CdMnTe are extremely interesting as they display large positive and negative magnetoresistances which are not present in the diamagnetic host material. Figures 2.3.7 and 2.3.8 illustrate this point. These figures show the magnetoresistance (MR) at $T \sim 2$ K for CdSe:In and $Cd_{0.95}Mn_{0.05}Se$:In, at various carrier concentrations [23]. The MR of CdSe is well understood. In the insulating phase the positive MR is due to the magnetic field shrinking the wavefunctions in the impurity band, causing a reduction in the wavefunction overlap and hence the hopping rate. In the metallic regime the MR is negative as is expected in a weakly localized system. This negative magnetoresistance and its origin is discussed in more detail in section 3.4 on weak localization. For the case of CdMnSe the situation is rather different : initially we see a positive MR, a peak in the resistance, followed by a negative MR as the field is further increased (small positive MR at the highest fields is due to the wave function shrinkage as seen in the nonmagnetic host). Qualitatively similar dependences have been observed in CdMnS [33], CdMnTe [32] and ZnMnSe [34]. It should be noted that the MR shows a very strong temperature dependence, with the positive component of the MR eventually vanishing at very low temperatures (below 0.2 K), leaving pure negative MR. Dietl *et al* [23] interpreted the positive MR in the WLR as being due to the enhanced spin-splitting, $h\upsilon_S$ as given by,

$$h\upsilon_s = g^*\mu_B H + \frac{\alpha}{g\mu_B} M_0(T,H) \qquad (2.3.4),$$

where g^* is the Lande g factor for the s electrons and $M_0(H,T)$ is the macroscopic magnetization of the d spins. Using data for $h\upsilon_S$ determined from magnetospectroscopic experiments they were able to quantitatively explain their positive MR data. The negative MR was interpreted in terms of two effects : the destruction of the magnetic polaron as discussed in the previous section with reference to $Gd_{3-x}V_xS_4$, and the redistribution of electrons between spin subbands. This second effect is again related to the large spin splitting.

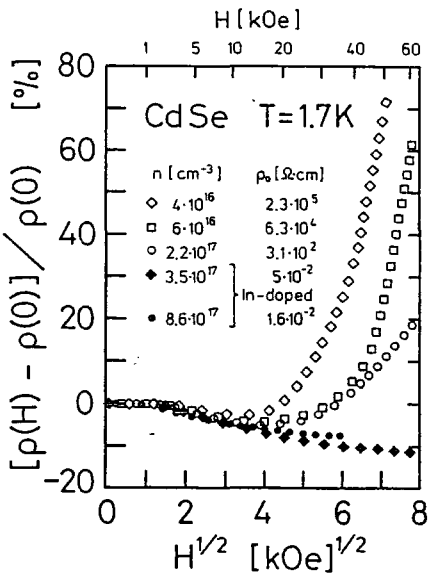

Figure 2.3.7. MR of CdSe at 1.7 K.

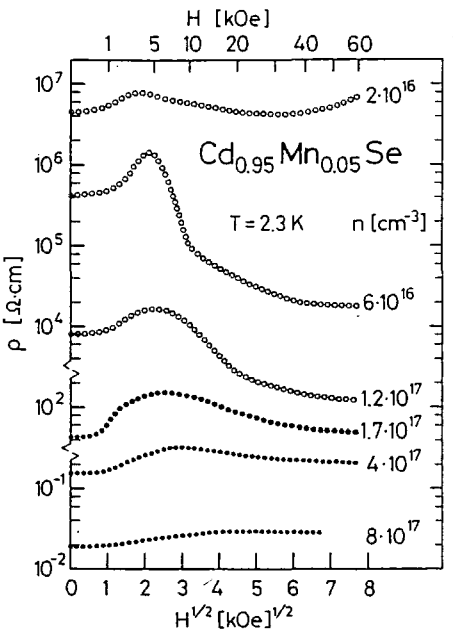

Figure 2.3.8. MR of CdMnSe at 2.3K. After [23].

Another model was developed by Terry *et al* to explain the form of the magnetoresistance in insulating CdMnTe:In [32, 35]. An example of this data is shown in figure 2.3.9, where the fractional MR is plotted as a function of the applied magnetic field at 1.38 K and 9.0 K for the persistent photocarrier concentration $4.3\text{x}10^{16}$ cm^{-3}. Terry *et al* commented that as well as a peak in the magnetoresistance at a certain temperature dependent field value, there is also a minimum in the static dielelectric constant at the same point. They suggested that the observed positive and negative MR could be

explained by the formation of BMPs. The basic idea is that the binding energy of the magnetic polaron increases with increasing field initially, reaches a maximum, and then decreases with increasing field, eventually reaching zero when the magnetization of the background and the polaron are equalized. This picture is slightly different to the one used to explain the pure negative MR in $Gd_{3-x}V_xS_4$ in that the binding energy of the polaron increases initially rather than decreasing to zero. This is simply due to the fact that the magnetic coupling between the bound s electron and the Mn d spins is weaker in DMS, meaning that in zero field the Mn spins are only partially aligned with the $S = 1/2$ spin. Therefore, when a field is applied the binding energy of the polaron increases initially due to the alignment of these spins.

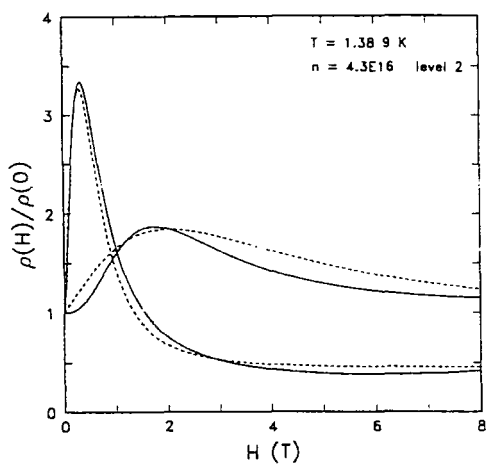

Figure 2.3.9. MR of CdMnTe, with x = 0.092 at 1.38 and 9 K. Solid line is a fit to the data with the model described here. After [35].

This effect was modelled by using a form for the polaron binding energy, E_H, of,

$$E_H(H) = E_H(0)\left[B(x_p) - B(x_0)\right] \qquad (2.3.5),$$

where $E_H(0)$ is the binding energy in zero field and $B(x_p)$ and $B(x_0)$ are the Brillouin functions describing the polaron and background respectively. This model results in the solid lines shown in figure 2.3.9. The agreement is rather good over the whole field range. It should be stressed that this model is only applicable to insulating material, while the model of Dietl *et al* is applicable in the WLR.

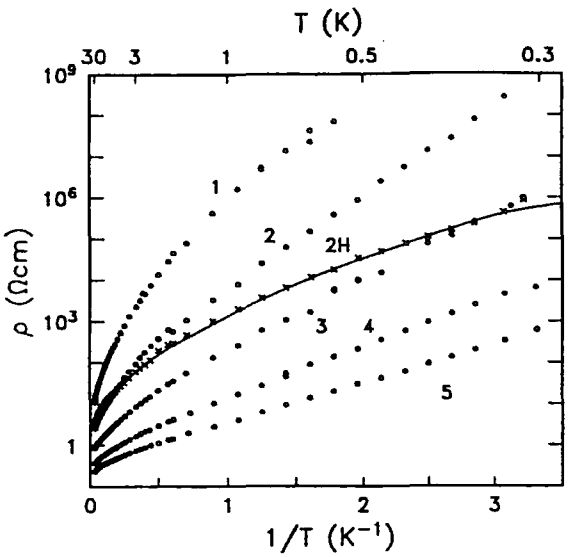

Figure 2.3.10. $\rho(T^{-1})$ for CdMnTe with x = 0.092, down to 300 mK. Five illumination levels are shown. After [36].

Bound magnetic polaron formation was also found to have an effect on the zero field transport in CdMnTe. Figure 2.3.10 shows the low temperature conductivity of CdMnTe : In at various photogenerated carrier concentrations [36]. The most insulating curve (n = 1.7x10^{16} cm^{-3}) shows Efros-Shklovskii $T^{1/2}$ hopping as discussed in detail in section 2.4.5, while the most conductive curve (n = 1.43x10^{17} cm^{-3}) shows an activated form. This activation energy was interpreted as being due to the formation of a magnetic hard gap in the density of states, caused by the formation of bound magnetic polarons. In this scenario hopping electrons can form BMPs at the final site of a hop, as the magnetic polaron relaxation time is far shorter than the time between electron hops. When a large magnetic field was applied the conductivity reverted to the $T^{1/2}$ hopping form, confirming that the hard gap is of magnetic origin. The intermediate carrier concentration curves, labelled 2, 3 and 4 in the figure were successfully fitted using a scaling relation of the form exp $[T_0/T + E_H^2/T^2]^{1/2}$, which allowed all of the data to be scaled onto a single curve.

Yet another influence of the s-d exchange interaction leading to the formation of BMPs was elucidated by Sawicki *et al* [23, 37]. They examined the temperature dependence of the conductivity of CdMnSe and found an unexpected and rapid decrease

in the conductivity below about 0.5 K, which did not exist in CdSe samples with comparable carrier concentrations. This effect is shown in figure 2.3.11 for the case of a metallic sample, although a similar effect was observed in the insulating phase. This data was interpreted in terms of the formation of BMPs at low temperatures which gives rise to an increased spin disorder scattering rate and hence results in a sharp decrease in conductivity below a certain temperature. This situation was modelled by the inclusion of an extra term in the spin disorder scattering rate to describe the efficient scattering of electrons by the BMPs i.e. the inverse spin disorder scattering rate in the expression $ne^2\tau_{sd}/m$, was replaced by $\tau_{sd}^{-1} + C\chi^2$, where C is a constant depending on a number of parameters relevant to the polaron binding energy and the polaron density, and $\chi(T)$ is the measured susceptibility. This produces the excellent fit given by the dotted line in figure 2.3.11.

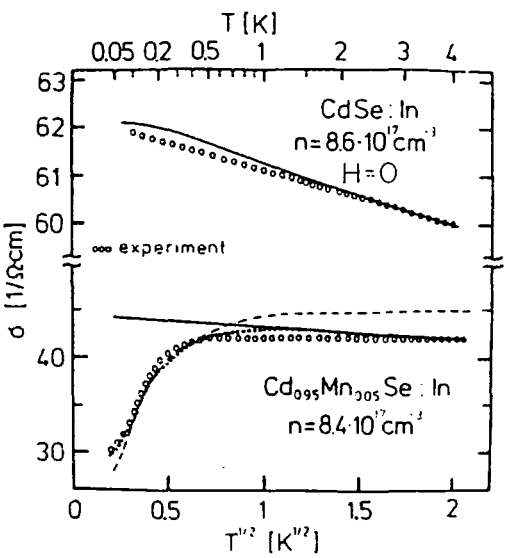

Figure 2.3.11. σ(T) down to 50 mK for CdMnSe and CdSe. The solid line is a fit to the data taking into account spin disorder scattering [37].

In conclusion it is clear that the formation of bound magnetic polarons has important consequences for the zero field transport properties of DMS, as well as the magnetoresistance observed in these systems.

2.3.5. Magneto-Optical Effects.

Optical experiments on DMS have proved to be important tools for studying the magnetism involved with the compounds in various different regimes. The large Zeeman splitting (due to the exchange enhanced *g* factor) mentioned in the previous section, has led to many experiments which probe the magnetic field dependence of energy levels in DMS. Compounds such as CdMnTe also exhibit a giant Faraday rotation, which has been utilised to study the dynamic magnetic susceptibility in the spin glass phase at low temperatures [38].

Some of the most interesting magneto-optical effects however, have been involved with photo-induced increases in the magnetization of DMS compounds. In $Cd_{1-x}Mn_xTe_{1-y}Se_y$:In a photomagnetization effect has been observed as shown in figure 2.3.12 [39]. Persistent changes in the magnetization are observed after illumination with infra red light, the total change in magnetization at saturation being around 0.4 %. This effect is obviously linked with the PPC effect detailed in chapter 4. As the sample is illuminated electrons are excited from deep DX^- levels to shallow donor levels where they form BMPs through the s-d exchange interaction. These BMPs are oriented by the small applied magnetic field of 100 Oe, due to their large susceptibility. This leads to the persistent change in the magnetization. Wojtowicz *et al* [39] obtained quantitative agreement between measurements of the low field magnetization and susceptibility, and existing theory of the BMP. It has been pointed out however, that the increase in the Pauli paramagnetism due to the changing free carrier concentration was ignored in this work [40], although it is likely to be rather small. Moreover, it is not at all clear whether the correlation between changes in carrier concentration and magnetization is as straightforward as suggested in the Wojtowicz work.

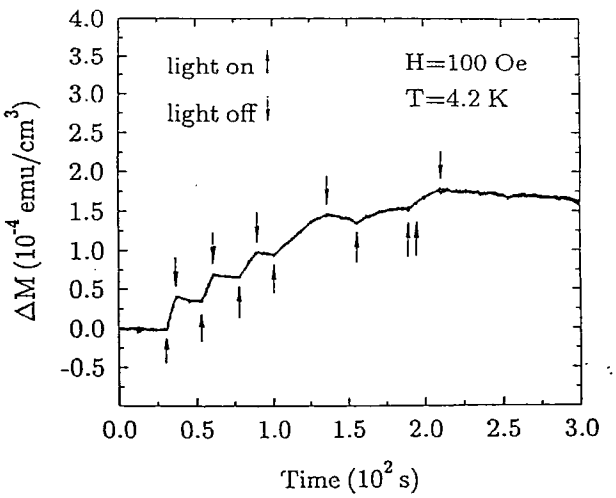

Figure 2.3.12. Photomgnetization effect observed by Wojtowicz *et al* [39].

Another (non-persistent) form of photomagnetization has been observed in DMS. This form involves the detection of minute changes in the magnetization of compounds such as HgMnTe and CdMnTe, when optically pumped with circularly polarized laser light. Krenn *et al* [41] observed an increase in magnetization on illumination, which peaked at 90° polarization, in narrow band-gap HgMnTe. Similar behaviour was seen in $Cd_{0.8}Mn_{0.2}Te$ by Awschalom *et al* [42] where the photo-induced change in magnetization was detected using an ultra high sensitivity integrated d.c. SQUID susceptometer. This photomagnetization signal was measured as a function of photon energy as shown in figure 2.3.13. At $E < E_g$ there is no photomagnetization as expected. As the energy is increased to reach the band-gap of the material, a large peak is observed around E_g, followed by a flat region up to 2.0 eV. The peak at E_g was interpreted in terms of the formation of bound magnetic polarons with a relatively large magnetization. At higher energies the photomagnetization is of the same form observed by Krenn, and is due to the fact that the circularly polarized light consists of photons with a non-zero angular momentum. This means that any excited electron will be given a preferential spin direction which is transmitted to the local Mn moments via the exchange interaction. This produces a tiny magnetization increase which is equivalent to that produced by a magnetic field of just 0.2 Oe.

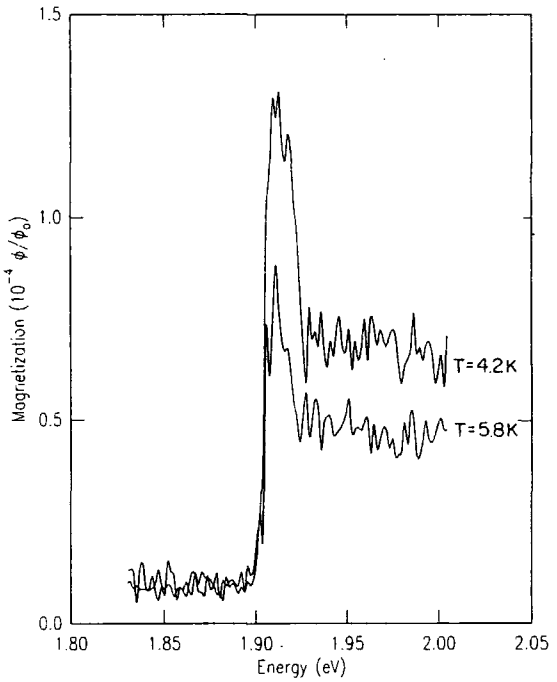

Figure 2.3.13. Photomagnetization as a function of photon energy [42].

Chapter 2 - References.

1. C. Kittel. *Introduction to Solid State Physics.* (Wiley, 1988).

2. N.W. Ashcroft and N.D. Mermin. *Solid State Physics.* (Saunders, 1976).

3. S. M. Sze. *Physics of Semiconductor Devices.* (Wiley, 1981).

4. H.M. Rosenberg. *The Solid State.* (Oxford, 1975).

5. G.E. Stillman, S.S. Bose, M.H. Kim, B. Lee ans T.S. Low. *Characterization and Properties of Semiconductors.* Handbook on Semiconductors. Ed. T.S. Moss. (Elsevier Science B.V.) (1994) p. 783.

6. B.K. Ridley. *Quantum Processes in Semiconductors* (Clarendon, Oxford 1988).

7. D.L. Rode in *Transport Properties of Semiconductors* eds R.K. Willardson and A.C. Beer (Academic Press)

8. R.L. Peritz and W.E. Scanlon. Phys. Rev. **97** 1620 (1955).

9. C. Leighton, I.Terry and P. Becla. Phys. Rev. B. **56** 6689 (1997).

10. I. Terry, T. Penney, S. von Molnar, J.M. Rigotty and P. Becla. Solid. State. Commun. **84** 235 (1992).

11. D. Chattopadhyay and H.J. Queisser. Rev. Mod. Phys. **53** 745 (1981).

12. A.H. Morrish. *The Physical Principles of Magnetism* (Wiley, London 1965).

13. R.R. Galazka. *Physics of Semiconductors.* Proc. 16th Int. Conf. on Semiconductors. (IOP). Ed B.L.H. Wilson. p133.

14. S. von Molnar and T. Penney in *Localization and Metal-Insulator Transitions* eds H. Fritzsche and D. Adler. (Plenum Publishing, 1985). p183.

15. S. Methfussel and D.C. Mattis. *Handbuch der Physik.* **18** (Springer, Berlin) (1968).

16. W. Giriat and J.K. Furdyna. *Diluted Magnetic Semiconductors.* Eds J.K. Furdyna and J. Kossut. *Semiconductors and Semimetals.* Vol **25** eds R.K. Willardson and A.C. Beer (Academic Press).

17. C.J.M. Denissen, S. Dalem, K. Kopinga, W.J.M. de Jonge, H. Nishihara, T.Sakakibara and T. Goto. Phys. Rev. B. **36** 5316 (1987).

18. J.K. Furdyna. J. Appl. Phys. **64** R29 (1988).

19. H. Anno, T. Koyanagi and K. Matsubura. J. Cryst. Growth. **117** 816 (1992).

20. T. Dietl. *Diluted Magnetic Semiconductors.* Handbook on Semiconductors. Ed T.S. Moss. (Elsevier Science B.V.) (1994) p. 1251.

21. T. Story, R.R. Galazka, P.J.T. Eggenkamp, H.J.M. Swagten and W.J.M. de Jonge in *Proceedings of the 8th International Conference on Vapour Growth Epitaxy.* Freiburg (1994).

22. H. Ohno, A. Shen, F. Matsukura, A. Oiwa, A. Endo, S. Katsumoto and Y. Iye. Appl. Phys. Lett. **69** 363 (1996).

23. T. Dietl, L. Swierkowski, J. Jaroszynski, M. Sawicki and T. Wojtowicz. Physica Scripta. **T14** 29 (1986).

24. S. Oseroff and P.H. Keesom. *Diluted Magnetic Semiconductors.* Eds J.K. Furdyna and J. Kossut. *Semiconductors and Semimetals.* Vol **25** eds R.K. Willardson and A.C. Beer (Academic Press).

25. See D. Heiman, E.D. Isaacs, P. Becla and S. Foner. Phys. Rev.B. **35** 3307 (1987), and the references therein.

26. E.D. Isaacs, D. Heiman, P. Becla, Y. Shapira, R. Kershaw, K. Dwight and A. Wold. Phys. Rev. B. **38** 8412 (1988).

27. S. Oseroff and P.H. Keesom. *Diluted Magnetic Semiconductors.* Eds J.K. Furdyna and J. Kossut. *Semiconductors and Semimetals.* Vol **25** eds R.K. Willardson and A.C. Beer (Academic Press). p. 75.

28. R.R. Galazka, S. Nugata and P.H. Keesom. Phys. Rev. B. **22** 3344 (1980).

29. J.A. Gaj, R. Planel and G. Fishman. Solid State Commun. **29** 435 (1979).

30. M. Nawrocki, R. Planel, G. Fishman and R.R. Galazka.
Phys. Rev. Lett. **55** 1875 (1981).

31. A. Golnik, J.A. Gaj, M. Nawrocki, R. Planel and C. Benoit a la Guillame. Proc. 15th Int. Conf. Phys. Semicond. Kyoto 1980. (Phys. Soc. Jpn., Tokyo) p. 819.

32. S. von Molnar, I. Terry, T. Penney and P. Becla. Physica B. **197** 151 (1994).

33. D. Heiman, Y. Shapira and S. Foner. Solid State Commun. **45** 899 (1983).

34. M. von Ortenberg, W. Erhardt, A. Twardowski and M. Demianiuk. Proc. Int. Conf. *Application of High Magnetic Fields in Semiconductor Physics.* Wurzburg 1986. (Springer - Verlag, Berlin).

35. I. Terry, T. Penney, S. von Molnar and P. Becla. J. Cryst. Growth. **159** 1070 (1996).

36. I. Terry, T. Penney, S. von Molnar and P. Becla. Phys. Rev. Lett. **69** 1800 (1992).

37. M. Sawicki, T. Dietl, J. Kossut, J. Igalson, T. Wojtowicz and W. Pleisewicz. Phys. Rev. Lett. **56** 508 (1986).

38. H. Kett, W. Gerbhardt, U. Kreg and J.K. Furdyna. J. Magn. & Magn. Mater. **25** 215 (1981).

39. T. Wojtowicz, S. Kolesnik, I. Miotkowski and J.K. Furdyna. Phys. Rev. Lett. **70** 2317 (1993).

40. I. Terry and A.B. Horsfall. Private Communication (1997).

41. H. Krenn, K. Kaltenegger, T. Dietl, J. Spalek and G. Bauer. Phys. Rev. B. **39** 10918 (1989).

42. D.D. Awschalom, J. Warnock and S. von Molnar. Phys. Rev. Lett. **58** 812 (1987).

3. The Metal-Insulator Transition.

The study of the Metal-Insulator Transition (MIT) began around 1949 [1] when Mott began to consider the simple problem of a crystalline array of hydrogen atoms with a lattice constant, a_H. Mott postulated that as a_H is reduced, then metallic conduction will occur when the overlap of neighbouring wavefunctions becomes suitably large. It became clear that there exists some critical value of a_H separating the insulating and metallic regimes. This value is discussed in more detail in section 2.4.1. This kind of transition, which is clearly due to electron-electron interaction effects, became known as a Mott transition.

Another huge conceptual development was made in 1958 [2] when Anderson proved that a transition from metallic to insulating conduction can occur due to increasing disorder. He discussed a situation such as the impurity band of a heavily doped semiconductor, and showed that if randomness is included by allowing the potential well depth at any particular lattice point to fall within a range of values, then, under certain conditions, diffusion is absent. i.e. the electron wavefunctions are spatially localized at that point. This situation is known as an Anderson transition. As will become clear in this section, real metal-insulator transitions (as marked by the vanishing of the d.c. conductivity at the absolute zero of temperature) are invariably Anderson-Mott transitions in the respect that they include a significant degree of disorder, as well as electron-electron interaction.

Sections 3.1 and 3.2 of this chapter discuss the Mott and Anderson transitions in more detail. Section 3.3 goes on to introduce the celebrated scaling theory of electron localization, which is based on the Anderson model, although electron-electron interaction effects can be included. The development of the scaling theory was a breakthrough in the understanding of the MIT, as it predicts a continuous and critical behaviour for experimentally observable quantities such as the conductivity. This puts the

MIT, which is a quantum phase transition occurring at absolute zero, on a similar footing to other phase transitions. The scaling theory is easily the most widely accepted theory of the MIT, and is the one we have used in our analysis of the conductivity near the transition in CdMnTe. In section 3.4 we discuss the values of the conductivity critical exponent as determined from various forms of the scaling theory along with the experimental determinations that have been possible. Section 3.5. discusses the situation in the weakly localized regime, just on the metallic side of the MIT. This is a very interesting region, where the effects of weak localization and electron-electron interaction can have a large influence on the transport properties of the system. It is an attractive regime in which to work because the transport theory is well developed due to the fact that the disorder can be treated perturbatively. This is obviously not true closer to the MIT, or in the insulating phase. Finally, section 3.6 is concerned with hopping conduction, particularly in the vicinity of the MIT. A discussion of phonon assisted nearest neighbour hopping is followed by an introduction to variable range hopping. The effects of electron-electron correlations (i.e. the formation of a Coulomb gap) on the variable range hopping is discussed.

3.1. Mott Transition.

As mentioned above, Mott considered the MIT which occurs when the lattice parameter of an array of hydrogen atoms is varied. This transition is purely driven by the size of the overlap between electron wavefunctions, i.e. it is due to the effects of electron-electron interaction. More explicitly, Mott considered the value of the Hubbard correlation energy, U [3]. This parameter takes into the account the repulsive energy between electrons if there is any tendency for them to favour the same site - exactly what will happen if the electron density is increased. This situation is depicted schematically in figure 3.1.1 where the electron energy is plotted as a function of n, the electron density. Initially the electrons at any site can occupy one of two levels : the 1s state at E = -1Ry, or the state in which an extra electron is added with E = -0.055Ry. As n is increased these levels broaden into two bands which are known as the upper and lower Hubbard bands.

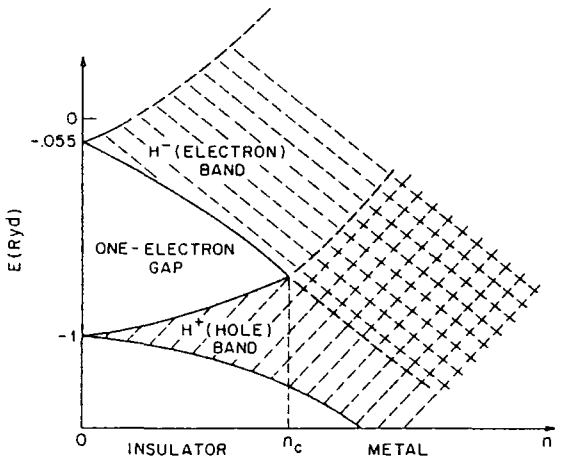

Figure 3.1.1. Carrier density dependence of the electron energy in the Hubbard bands.

The critical carrier concentration for the MIT, is the point at which these two bands cross as shown in the diagram. Mott was able to derive a simple formula (which became known as the Mott criterion) relating n_c and the Bohr radius, a_H,

$$n_c^{1/3} a_H \approx 0.26 \qquad (3.1.1).$$

Figure 3.1.2 [4] shows the huge variety of systems for which this equation appears to be valid. Even in doped semiconductors, where the relevant Bohr radius is that of the donor atom, and these donors occupy random lattice positions rather than a regular arrangement, this criterion still appears to be valid. This is a remarkable point which it seems cannot be said of the other prediction for the nature of the MIT in this model, the minimum metallic conductivity, σ_{min}. Mott suggested that at $T = 0$ one cannot have a non-zero value of conductivity less than,

$$\sigma_{\min} = \frac{Ce^2}{\hbar a} \qquad (3.1.2),$$

where $C \approx 0.026$ [5]. So the conductivity should show a discontinuous jump at the MIT critical point. Although several systems have shown a very sharp transition, there has been no experimental verification of this prediction at all. In fact a continuous transition is usually observed as shown in figure 3.1.3, where the zero temperature extrapolation of the conductivity is shown as a function of carrier concentration in Si:P [6]. This point will be discussed in detail in section 3.3. It should be noted that several points in figure 3.1.3 have a conductivity well below σ_{min}.

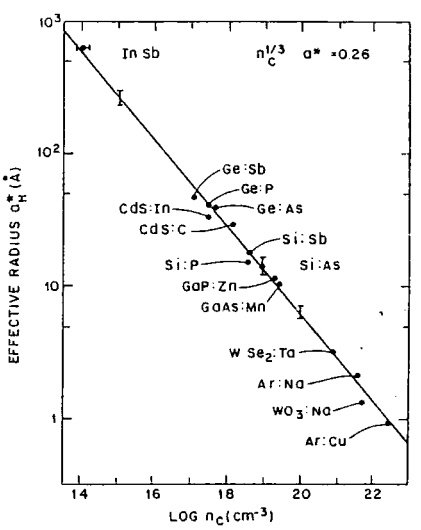

Figure 3.1.2. Effective Bohr radius against $\log_{10}(n_c)$, verifying the Mott criterion [5].

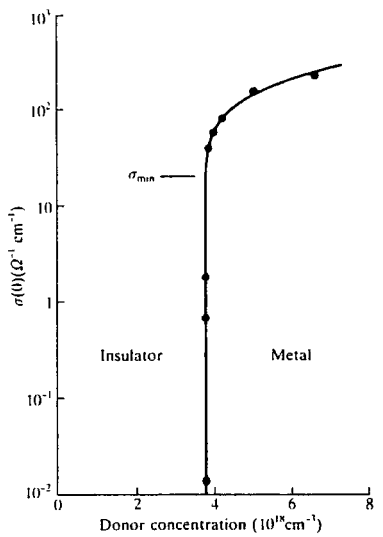

Figure 3.1.3. n dependence of the zero temperature conductivity in Si:P [6].

Although there has been no direct experimental evidence for the existence of a minimum metallic conductivity, it is worth noting that it could have some significance in terms of a pre-exponential factor for activated conduction, and that it does provide a rough estimate for the conductivity at which the MIT is likely to occur [7]. Evaluating σ_{min} and n_c for CdTe from the Mott formulae gives 5 $(\Omega\text{cm})^{-1}$ and $1.1\text{x}10^{17}$ cm^{-3} respectively.

3.2. Anderson Localization.

Anderson [2] considered the model shown in figure 3.2.1. A crystalline array of potential wells is modified by the inclusion of a random potential at each well, the depths lying in the range V_0. This V_0 is shown in figure 3.4 along with the width of the band without disorder, B. Anderson found that B/V_0 is a very important dimensionless parameter. In fact he showed that there existed a critical value of V_0/B : if $V_0/B > (V_0/B)_{crit}$ then the electron wavefunctions become localized in character, but if $V_0/B < (V_0/B)_{crit}$ then the wave functions are extended in space. This is the essence of the Anderson transition. In the strongly disordered case, the wavefunctions are said to be exponentially localized i.e. :

$$|\psi(\underline{r})| \propto \exp\left[-\frac{|\underline{r}-\underline{r}_0|}{\xi}\right] \qquad (3.2.1),$$

where ξ is the localization length. ξ is supposed to be infinite at the critical point, but as the disorder increases, its value is smoothly decreased.

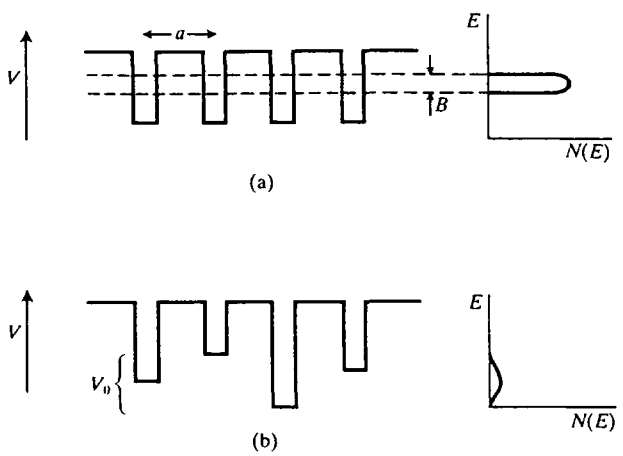

Figure 3.2.1. Potential wells and DOS for the situations with no disorder (a), and the Anderson model (b), where random disorder is included over a range V_0 [7].

Mott went on to realise that there was an extra subtlety involved in that, at moderate levels of disorder (V_0/B), it was possible that states in the band tails would be localized, whereas states with slightly higher energy would have spatially extended wavefunctions [7]. This situation is shown in figure 3.2.2. Mott showed that a critical energy called the mobility edge marks the transition between these two possibilities. So the mobility edge, E_c is the point at which the MIT occurs : if $E_F < E_c$ then the conductivity at absolute zero is zero, whereas if $E_F > E_c$ then the conductivity is finite. For the situation where $E_F < E_c$ then the conductivity proceeds either by activation to the mobility edge or via some hopping mechanism as detailed in section 3.6, whereas if $E_F > E_c$ then the conductivity is metallic in nature.

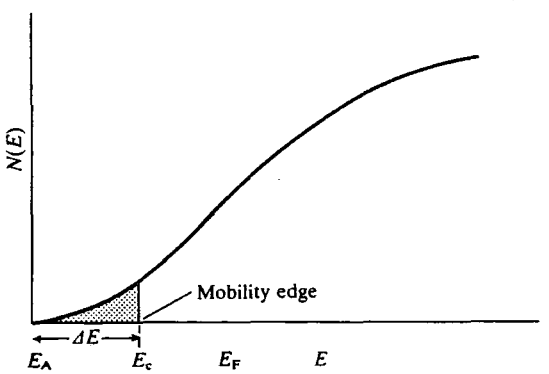

Figure 3.2.2. Schematic of a typical band tail, showing the mobility edge, E_c. Localized states are shaded [7].

Mott went on to show that the Anderson model was also consistent with his previously derived concept of a minimum metallic conductivity. He suggested that at absolute zero there can exist no non-zero conductivity less than,

$$\sigma_{\min} = \frac{\pi e^2}{4z\hbar a}\left[\left(\frac{B}{V_0}\right)_{crit}\right]^2 \qquad (3.2.2),$$

where z is the co-ordination number of the lattice. Although the critical value of V_0/B is difficult to determine exactly due to the fact that the Anderson model does not have an exact solution, it has been estimated to be about 2 [8]. Thus,

$$\sigma_{min} = 0.026 e^2/\hbar a \qquad (3.2.3),$$

and we arrive at the same value for the minimum metallic conductivity as earlier. As we shall see in the next section, the scaling theory of electron localization, which was born from the Anderson localization concept, predicts that a continuous transition should occur rather than Mott's discontinuity. This is shown in figure 3.2.3.

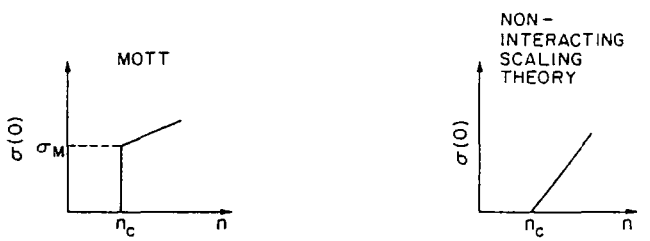

Figure 3.2.3. n dependence of the zero temperature conductivity for the case where σ_{min} exists, and for the case where the scaling theory applies.

3.3. The Scaling Theory of Electron Localization.

In the 1970's Thouless *et al* began to formulate a scaling theory based on the Anderson model described above [9]. This work eventually led to a fully developed scaling theory from Abrahams *et al* [10]. Thouless formulated a theory by imagining *microscopic* samples of material of side L in d dimensions, e.g. cubes of volume L^3 in $3d$, squares of area L^2 in $2d$ etc. He then showed, that given the eigenstates of the sample of side L, then one can deduce the eigenstates of a sample of side $2L$, constructed from two samples of side L, with no further information. Hence, because the conductivity of the

system is derived from the quantum mechanics of the situation (i.e. the eigenstates), then if we know the conductance, $\Sigma(L)$, of the sample of side L then one can determine the conductance of the sample of side $2L$, from L and $\Sigma(L)$. Thouless further noticed that one can calculate the ratio V_0/B in the Anderson model, by using his 'block building' scenario. The quantity V_0 is by definition the energy difference between two random sites, whereas the quantity B can be identified with the energy shift due to the changed wavefunction boundary conditions when two samples of size L are merged to form one of side $2L$. Thouless also appreciated that the conductance $\Sigma(L)$ of his sample could be expressed in fundamental units of $e^2/2\hbar$, a fact which he used to define a dimensionless conductance, $G(L)$,

$$G = \Sigma/\left(e^2/2\hbar\right) = \Sigma\frac{2\hbar}{e^2} \qquad (3.3.1).$$

So then in d dimensions one can write,

$$\Sigma = L^{d-2}\sigma \qquad (3.3.2).$$

We can now proceed to estimate a value for the quantity V_0/B. We first calculate B by expressing the time an electron takes to travel a distance L, in terms of the diffusion coefficient, D :

$$\tau = L^2/D \qquad (3.3.3).$$

Now, we know that in general the wavefunction of an electron will include a factor $\exp\left(iEt/\hbar\right)$, and that when we construct a sample of side $2L$ from samples of side L then the phase is forced to shift by an amount of order unity, so,

$$B\tau/\hbar \approx 1 \qquad (3.3.4),$$

hence,

$$B = \hbar D/L^2 \qquad (3.3.5).$$

We can now calculate the value of V_0 and find a value for V_0/B. In the Anderson model the energy probability distribution, $P(E)$, is defined as $P(E) = 1/V_0$, within the allowed energy range of width V_0. Therefore $V_0 = 1/P(E) = 1/n(E)L^3$ in $3d$, where $n(E)$ is the density of states. Generally, in d dimensions,

$$V_0 = \left[n(E)L^d\right]^{-1} \qquad (3.3.6).$$

So taking the ratio B/V_0 we obtain,

$$\frac{B}{V_0} = \frac{\hbar D}{L^2} n(E)L^d = \hbar D n(E)L^{d-2} \qquad (3.3.7).$$

If we then employ a form of the Einstein relation, $\sigma = De^2n(E)$ we arrive at,

$$\frac{B}{V_0} = \frac{\hbar\sigma}{e^2} L^{d-2} \qquad (3.3.8).$$

Recalling that $G(L) = \Sigma(L)(\ 2\hbar/e^2\ )$ and that $\Sigma(L) = L^{d-2}\sigma$ we have that $G(L) = \left(L^{d-2}\right)(\ 2\hbar\sigma/e^2\ )$. Comparing with equation 3.3.8 gives,

$$G(L) \sim B/V_0 \qquad (3.3.9),$$

so we can identify the parameter B/V_0 from the Anderson model with the dimensionless conductance G. Hence the fact that there exists a critical value of B/V_0, implies that there is a critical value of the dimensionless conductance at the MIT, rather than a critical value of the conductivity as suggested by Mott.

The point now is that if we continue our edge doubling procedure, building larger and larger samples from samples of side L then we can investigate the limit $L \to \infty$, and determine the scaling theory prediction for G in the macroscopic limit. The simplest way to do this mathematically is to express the fact that we can deduce $G(2L)$ from $G(L)$ and L using a differential equation :

$$\frac{d\ln G}{d\ln L} = \beta(G) \qquad (3.3.10),$$

where $\beta(G)$ is an unknown function independent of L. The origin of this equation can be understood as follows.

$$\frac{d\ln G}{d\ln L} = \frac{L}{G}\frac{dG}{dL} = \beta(G) \qquad (3.3.11),$$

so that,

$$\frac{dG}{dL} = \frac{G\beta(G)}{L} \qquad (3.3.12),$$

or,

$$dG = \beta(G)G\frac{dL}{L} \qquad (3.3.13).$$

Now for our edge doubling procedure $dL=L$ so that,

$$\Delta G = \beta(G) \times G(L) \qquad (3.3.14),$$

eventually giving,

$$G(2L) = G(L) + \beta(G) \times G(L) \qquad (3.3.15),$$

which is just a statement of the fact that *G(2L)* can be determined from *G(L)* simply by multiplication by the factor $\beta(G)$. We need therefore to calculate this β function to calculate the macroscopic prediction for the conductance.

Simple physical arguments give values for β when $G >> 1$ and $G << 1$:

(i) $G >> 1$.

This is where B/V_0 is large i.e. the metallic regime. Ordinary classical transport theory holds so that,

$$G(L) = \frac{2L^{d-2}\sigma\hbar}{e^2} \qquad (3.3.16).$$

Hence

$$\frac{d \ln G}{d \ln L} = d - 2 \qquad (3.3.17),$$

meaning that,

$$\lim_{G \to \infty} \beta(G) = d - 2 \qquad (3.3.18).$$

(ii) $G << 1$.

This is where B/V_0 is small i.e. the insulating regime. Here the wavefunctions are exponentially localized and the only way the conductivity can proceed is via tunnelling from one state to the next. Hence we can assume that,

$$G = G_0 \exp(-L/\xi) \tag{3.3.19},$$

where ξ is the localization radius. We obtain,

$$\frac{d \ln G}{d \ln L} = -\frac{L}{a} = \ln\left(\frac{G}{G_0}\right) \tag{3.3.20},$$

so that,

$$\lim_{G \to 0} \beta(G) = \ln\left(\frac{G}{G_0}\right) \tag{3.3.21}.$$

We can now plot these two asymptotes on a plot of $\beta(G)$ against G. The form of the entire curve shown in figure 3.3.1 was explicitly calculated by Abrahams *et al* [10] although it is natural to assume that our two asymptotic values are joined by smooth curves. There are number of important conclusions to be drawn from this figure :

(i) for $d = 1$, $\beta < 0$ always, meaning that $d\ln G/d\ln L < 0$. Hence if we perform our edge doubling procedure and let $L \to \infty$ then G tends to zero and the system is always insulating. *Metallic conduction can not take place in 1 dimension.*

(ii) for $d = 2$ an interesting and marginal situation occurs because although $d\ln G/d\ln L$ is always negative, it is small as $G \to \infty$. Still though it seems that the conduction must always be insulating [11].

(iii) In the d = 3 situation, which is of greatest interest to us, $d\ln G/d\ln L$ can be both positive and negative - $\beta(G)$ crosses the G axis. Clearly there exists a critical value of the dimensionless conductance, G_c which separates the insulating and metallic regimes. For $G > G_c$, β is positive, G increases as $L \to \infty$, and the system is metallic. For $G < G_c$, β is negative, G reduces to zero as $L \to \infty$, and the material is an insulator. So whether the system is insulating or metallic is determined by the size of the conductance of the microscopic disordered system at a cut-off length scale, L^*, in comparison to the critical conductance G_c. Hence critical disorder is attained when $G = G_c$, at a length scale L^*. This is an unstable fixed point in that small deviations from it result in a qualitatively different situation as $L \to \infty$.

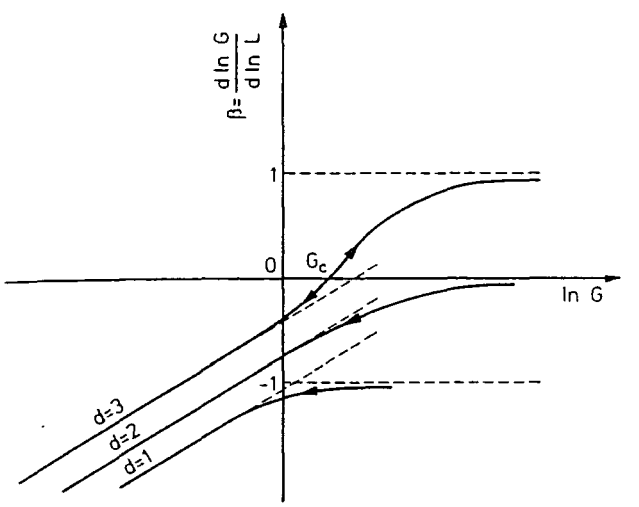

Figure 3.3.1. Plot of $\beta(G)$ against $\ln G$, after [10]. Curves are shown for d = 1, 2 and 3.

It is clear that the scaling theory of electron localization is unlike any previously developed transport theory in that it can treat insulators and metals on an equal level. The final success of the theory though is that it can predict the form of the conductivity in the critical region. Consider the fixed point $\beta(G)$ = 0 and suppose that β has a slope $1/\nu$ at this point. This can be written,

$$\beta(G) = \delta G / \nu \qquad (3.3.22),$$

where δG ($<<1$) is the difference in conductance between our starting point and G_c. Integrating this equation from our conductance starting point at length L^*, out to $\beta \approx 1$ at large L, it can be shown that,

$$\sigma = \left(\frac{AG_c}{l}\right)(\delta G)^{\nu} \qquad (3.3.23),$$

where A is constant of order unity, and l is the microscopic length scale at our starting point. Hence there is no minimum metallic conductivity, the conductivity obeys the critical form shown here, with a critical conductivity exponent, ν. Furthermore, Abrahams *et al* were able to prove that in 3 dimensions the value of ν for this non-interacting theory is unity. Also, if we write the conductivity as $\sigma \propto G_c/\xi$ then it is clear that the correlation length has a similar scaling behaviour,

$$\xi = \left(\frac{l}{A}\right)(\delta G)^{-\nu} \qquad (3.3.24),$$

with the same exponent, ν.

In terms of the conductivity of a doped semiconductor with a carrier concentration, n, these equations can be rewritten in the form,

$$\sigma = \sigma_0\left(\frac{n}{n_c} - 1\right)^{\nu} \qquad \& \qquad \xi = \xi_0\left(\frac{n_c}{n_c - n}\right)^{\nu} \qquad (3.3.25),$$

where n_c is the critical carrier concentration. This can be done for any parameter that can induce a transition ; magnetic field, composition etc. It is this result of the scaling theory which we can apply to our experimental data on the MIT.

It should be made clear at this point that if one includes different effects in the scaling theory, electron-electron interactions for example, then different critical exponents can be predicted. The various exponents predicted by theory, and the experimentally determined ones are considered in the next section.

3.4. The Critical Conductivity Exponent.

So we have seen that a simple formulation of the scaling theory of electron localization has predicted a critical conductivity exponent, ν, and a localization length exponent, s, which are equal. It can also be shown [12] that the dielectric constant has a scaling form with a critical exponent $\nu' = 2\nu$. Various scaling treatments of the Anderson problem have led to a spectrum of values for the critical exponents. To be more explicit several authors have worked on scaling theory with interactions included and derived a critical exponent $\nu = 1$ [13,14], whereas theories without interactions often predict 1/2 for the exponent [15,16]. In another study a value of $\nu = 1.35$ has been suggested [17].

One thing which has become clear due to these theoretical investigations is that the concept of a universality class is a useful one in the study of the MIT. The basic idea is that there are separate classes of materials with the same critical behaviour at the transition. These materials are not necessarily similar. From a theoretical viewpoint the systems are classed according to symmetry considerations. Examples evinced by theory are the large spin-orbit splitting and high magnetic field universality classes. From an experimental viewpoint there is some evidence that random solids such as Si:P should be in one universality class if they are uncompensated, but should be in another if the compensation is high [18]. It is worth mentioning that even if it is not clear exactly which

universality class a material is a member of, there are certain indications as to whether electron-electron interactions are important. For example, Efros-Shklovskii variable range hopping is indicative of the formation of a Coulomb gap due to electron-electron correlation effects, so if a material displays this phenomenon close to the MIT then it may be reasonable to assume that these effects are important in the critical region.

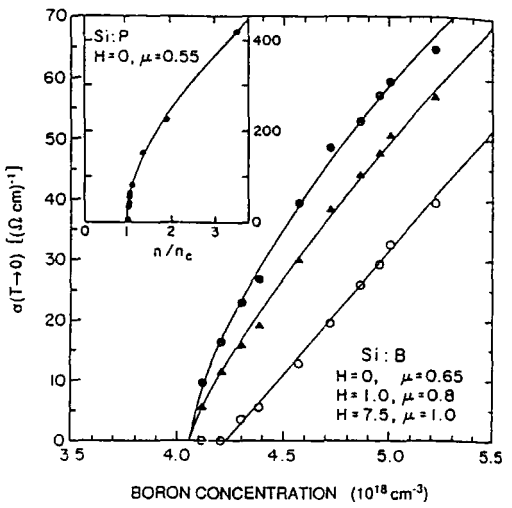

Figure 3.4.1. *n* dependence of $\sigma(0)$ for Si:B in various fields [21]. Data for Si:P is shown in the inset.

Several experimental groups have set out to study the MIT in doped semiconductors, as well as various other materials such as alloys, metal-ammonia solutions, amorphous conductors etc [7]. Doped semiconductors are a good choice because systematically varying the dopant level allows one to study the temperature dependence of the conductivity as the distance from the MIT is varied. This process has been performed in materials such as Si:P [6], Si:As [19], Ge:As [20] etc. The Si:P data is displayed in figure 3.1.3 as an example. An exponent close to 0.5 was found from this very low temperature data. Most of these studies seemed to indicate that in compensated systems the exponent is 1.0, whereas in uncompensated systems the exponents are scattered over the range 0.5 to 0.8. The reason for this is unexplained, as is the exponent of 0.5 in Si:P, where theoretically one might expect $\nu = 1.0$. A very interesting set of experiments has been carried out on Si:B [21] where Dai *et al* measured the critical behaviour in zero field and in a field of 7.5 T. They found that the critical exponent

shifted from a value close to 0.5 up to 1.0 in the strong field limit. The data is shown in figure 3.4.1. This is the first clear indication of a material in which the conductivity exponent changes with field. They noted that in zero field the anomalous exponent is probably of the same origin as the exponent of 0.5 in Si:P, but that the result in high field is exactly as expected for Si:B.

It is worth noting at this point that amorphous materials such as Nb_xSi_{1-x}, Ge - Au alloys, and many others [18] usually exhibit a conductivity critical exponent close to 1.0, in agreement with scaling theory including interactions.

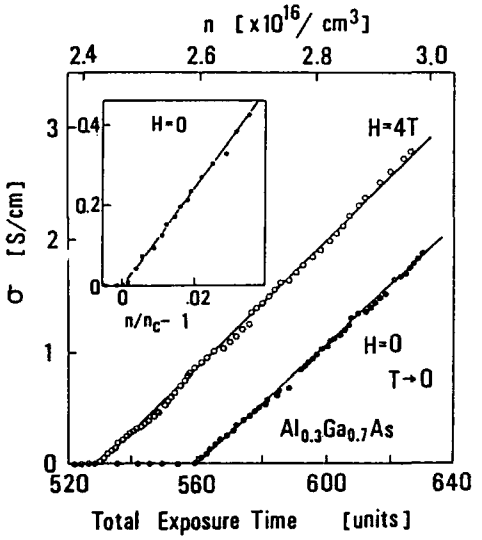

Figure 3.4.2. *n* dependence of $\sigma(0)$ for AlGaAs:Si as probed by PPC [24]. Results are shown for 0 and 4 T.

Techniques which allow the variation of one controllable parameter to 'fine tune' the MIT have an enormous advantage over studies involving discrete samples. Methods used so far include application of stress to Si:P [22], application of magnetic field [23] and the use of PPC in AlGaAs [24]. The stress tuning experiments in Si:P were used to probe the critical region very close to the MIT but produced the same exponent as the previous study - the anomalous exponent in Si:P remains unexplained. An excellent study of the MIT in AlGaAs:Si was done by Katsumoto [24] who used the PPC effect to fine tune the persistent photocarrier concentration, and hence the MIT. Figure 3.4.2 shows the

results of this experiment. An exponent of 1.0 was found in both zero field and a field of 4 T. This experiment is one of the most revealing ever performed on the MIT, because the ease with which the carrier concentration can be varied allows a very rigorous test of the scaling theory, in the region very close to the transition.

Finally, some experiments have been done on magnetic semiconductors. von Molnar *et al* acquired the data shown in figure 3.4.3, where the transition is tuned via the application of magnetic field in $Gd_{3-x}V_xS_4$ [25]. The large negative magnetoresistance used to induce a transition is due to the formation of BMPs as discussed in detail earlier. Again, an exponent of 1.0 is obtained. This work was extended to include a study of the temperature dependence of the conductivity, and will be commented on later. Other work on CdMnSe and HgMnTe by Dietl *et al* [26] produced critical conductivity exponents close to one, although in all cases magnetic field had to be used to tune the transition. Our work is the first magnetic semiconductor study which has been done without the use of a magnetic field. It is worth noting at this point that Dietl *et al* suggested that DMS such as CdMnSe actually belong to a separate universality class known as the spin polarized universality class.

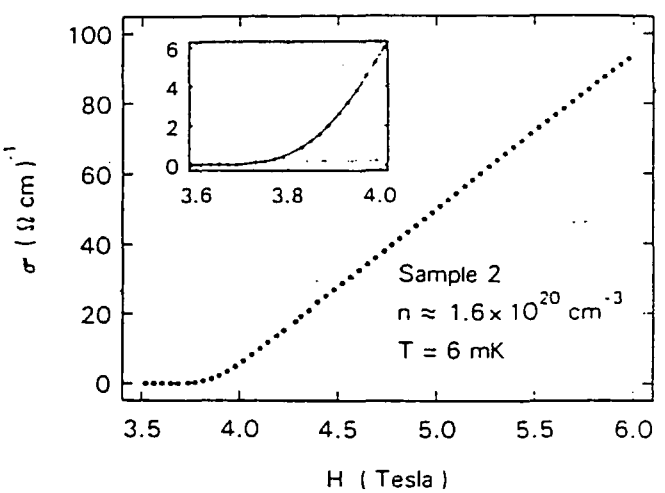

Figure 3.4.3. Magnetic field dependence of the conductivity at 6 mK for $Gd_{3-x}V_xS_4$ [25].

3.5. Dirty Metals - The Weakly Localized Regime.

The Weakly Localized Regime (WLR) exists just beyond the insulator-metal transition where, in doped semiconductors, n is just larger than n_c. In this region the effects of electron-electron interaction and correlation are very influential, as are the effects of weak localization. By weak localization we mean an effective localization of the electrons which comes about due to the interference of electronic wavefunctions. In the region where the Boltzmann equation for conductivity is valid, and the wavelength of the electron is much less than the mean free path, interference effects can be neglected. However, when the mean free path is reduced and becomes comparable to the wavelength then these effects cannot be overlooked. This region is the WLR. It turns out that one consequence of taking these effects into account is that electronic wavefunctions can (under certain conditions) destructively interfere, resulting in a decreased probability of electron diffusion along certain paths. In other words the conductivity is being decreased by a tendency for the wavefunction to become more localized [27].

These electron-electron and weak localization effects have a very direct influence on the conductivity. They both introduce a quantum correction to the low temperature conductivity and have a profound effect on the magnetoresistance. The electron-electron correlation effect introduces a $T^{1/2}$ term in to the conductivity, where the sign of the contribution can be positive or negative depending on the value of n/n_c. This $T^{1/2}$ term has been observed in an enormous variety of metals [28]. The weak localization effect introduces a term which is proportional to $T^{p/2}$, with the coefficient and the value of p being dependent on the details of the material being considered [27]. Both of these effects will be considered in detail here. The weak localization effects the magnetoresistance, as the application of a magnetic field affects the phase of the wavefunction, destroying the phase coherence necessary for the localization to occur. Hence a negative magnetoresistance is expected - the increasing field reduces the interference, therefore increasing the conductivity. It can be shown that this leads to a $H^{1/2}$ dependence in the magnetoresistance. This is an effect which has been widely observed [28] and studied in

great detail by Bergmann in thin metallic films [29], who found excellent agreement between experiment and detailed theory.

We return now to the quantum corrections to the conductivity mentioned earlier. They result in a low temperature conductivity in the WLR which can be described by,

$$\sigma(n,T) = \sigma(n, T = 0) + m(n)T^{1/2} + B(n)T^{p/2} \qquad (3.5.1),$$

where the first term represents the zero temperature conductivity, the second term arises from the e^--e^- effects and the third is due to the weak localization. Comprehensive analyses of experimental data based on this equation have been performed by Dai *et al* [21] and Thomas *et al* [30]. Data from [30] is shown in figure 3.5.1 where the localization and e^--e^- terms are shown clearly. A suitable theoretical review is given by ref [10].

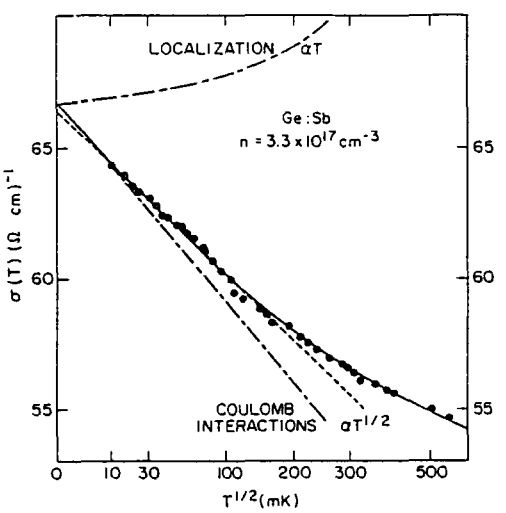

Figure 3.5.1. σ(T) for Ge:Sb showing the localization and e^--e^- contributions [30].

For the case of a doped semiconductor, all three terms are *n* dependent. Dealing with the e^--e^- term first, *m(n)* is given by,

$$m(n) = \alpha\left[\frac{4}{3} - \left(\frac{3}{2}\gamma F_\sigma\right)\right] \qquad (3.5.2),$$

where,

$$\alpha(n) = \frac{e^2}{\hbar}\left(\frac{1.3}{4\pi^2}\right)\left(\frac{k_B}{2\hbar D}\right)^{1/2} \qquad (3.5.3).$$

Here the factor γF_σ is the Coulomb interaction parameter, where γ is a constant which can be calculated from the band structure, and F_σ is related to the Fermi liquid parameter F by,

$$F_\sigma = \left(-\tfrac{32}{3}\right)\left[1 - \tfrac{3F}{4} - \left(1 - \tfrac{F}{2}\right)^{3/2}\right]F^{-1} \qquad (3.5.4),$$

where $F = (1/x)\ln(1+x)$, and $x = (2k_F / K)^2$, with k_F the Fermi wavenumber and K the Thomas-Fermi screening wavevector. Dai *et al* used temperature dependent conductivity data on the metallic side of the MIT to determine m as a function of n, which then allowed a determination of the n dependence of the interaction parameter. Alternatively, Thomas *et al* succeeded in calculating the parameters F and γ and predicted the form of $m(n)$ which they found to be in agreement with their data. In chapter 7 a quantitative analysis of this form is given for CdMnTe.

Turning to the weak localization term, $B(n)T^{p/2}$ we have that,

$$\tau_\phi^{-1} \propto T^p \qquad (3.5.5),$$

where τ_ϕ is the relaxation time of the dominant dephasing mechanism. Theory predicts that electron-electron scattering will result in $p = 2$ and 3/2 for the clean and dirty limit respectively, while electron-phonon scattering will make $p = 3$. As we will see in chapter

7, our data suggests that $p = 2$, making the weak localization term linear in T. This is in agreement with the work of Thomas *et al.* The prefactor $B(n)$ is given by,

$$B(n) = \frac{e^2}{\hbar\pi^2}\left[\frac{S_0\eta}{2}\left(\frac{c}{D}\right)^{1/2}\right] \qquad (3.5.6),$$

where η is the valley degeneracy and S_0 is a constant which can be calculated from the effective mass anisotropy and η. For the case of CdTe the situation is simplified by the fact that $S_0\eta = 1$. So this analysis is actually simpler for the case of a CdTe based compound, than it is for Si and Ge where it has been previously applied. The equation for B can be used to compare experiment with theory if B is extracted from experimental data on temperature dependent conductivity. This is done in chapter 7 for CdMnTe.

It is interesting to note that in most of the systems studied and analysed in this fashion the values of m and B are remarkably similar [10, 24, 30, 31], although in some systems the n dependence is weak [24], whereas in others such as Si, the sign of $d\sigma/dT$ changes and m and B are more rapid functions of n (or H). This will be discussed with reference to our results in chapter 7.

3.6. Hopping Conduction Near The MIT.

In section 2.3.4. when the transport properties of DMS were discussed, impurity conduction was mentioned briefly. It was shown that doping semiconductors leads to the formation of energy levels within the forbidden gap, which can lead to activated conduction processes. These processes are referred to continually in chapter 6, and the interesting problems associated with very heavy doping are discussed. In this section we outline the hopping conduction phenomenon which occurs at low temperatures in doped semiconductors, as well as systems such as amorphous conductors [7]. The basic idea is that in a system where the Fermi level lies below the mobility edge then the conduction

can proceed either by activation to the Fermi level or by electrons tunnelling, or hopping, from one state to the next in the direction of the applied electric field. An essential ingredient here is the existence of some degree of compensation to produce empty states to hop to.

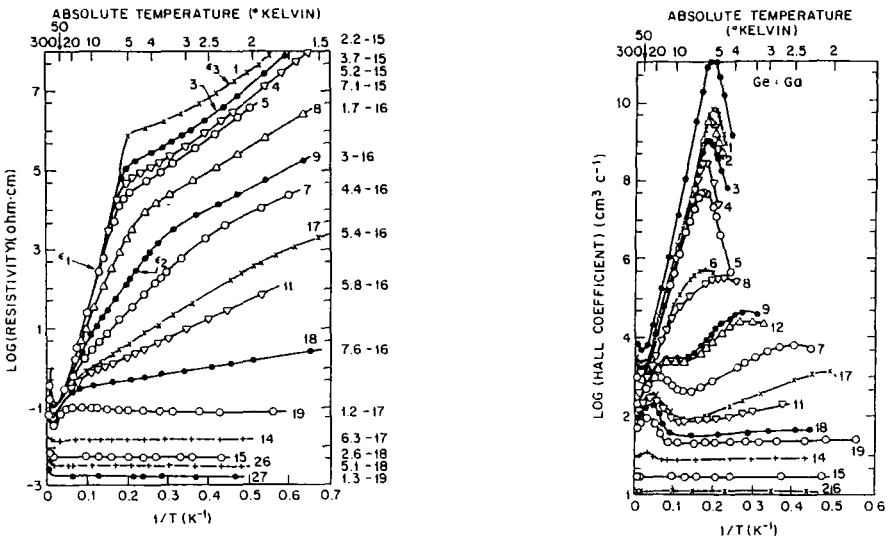

Figure 3.6.1. Temperature dependence of the resistivity and Hall coefficient in Ge:Ga, for various carrier densities [33, 34]. At low temperatures the nearest neighbour hopping is observed, hence the linear variation in the resistivity plot and the turnover in the Hall coefficient.

The simplest form of hopping conduction is the Miller and Abrahams phonon assisted nearest neighbour hopping [32]. Here the electron simply accepts energy from a phonon to make it resonant with a neighbouring empty site, at which point the tunnelling event occurs. The temperature dependence of the resistivity is expected to take the form,

$$\rho = \rho_3 \exp(E_3/k_B T) \qquad (3.6.1),$$

where the energy E_3 is used, as E_1 and E_2 correspond to activation to the conduction band, and to the equivalent of the upper Hubbard band, respectively. Conduction of this type

was observed by Fritzsche [33,34] in Ge:Ga as shown in figure 3.6.1 where the resistivity and Hall coefficient are shown. At low temperatures the E_3 behaviour is observed in the resistivity, while the Hall coefficient peaks and then falls off. This behaviour of the Hall coefficient is typical for a system crossing over to hopping conduction as the temperature is lowered. It is associated with the fact that the conventional theory of the Hall effect breaks down when the transport is no longer ballistic. There are other points which are signatures of this form of conduction. For example, ρ_3 is expected to vary hugely as the donor concentration is changed whereas ρ_2 is changed by a relatively small amount. The variation of the three activation energies in n-type Ge is shown in figure 3.13, where a is the separation between donor centres. This characteristic peak in E_3 as n is varied is a signature of nearest neighbour hopping [35]. This effect occurs because at low values of n, when the separation (a) is high, the states are all at effectively the same level, but when the density is increased the scatter in the energies of these levels begins to widen, meaning that the average energy difference between neighbours (E_3) increases. At high values of n the metallic regime is approached, $E_F \rightarrow E_c$ and the E_3 value decreases again.

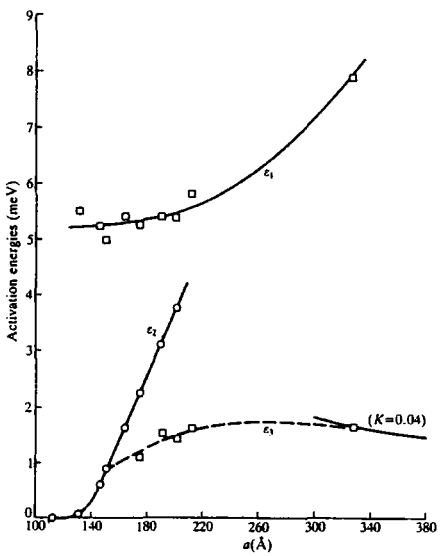

Figure 3.6.2. Variation of the activation energies of n-Ge with the distance between centres, a.

At lower temperatures Mott [36] was the first to point out that the dominant hopping mechanism was most likely not to the nearest neighbour. He suggested that as k_BT is small the electron would have to hop over longer distances in order to find a site within k_BT of its own initial energy. This is known as variable range hopping. Assuming that the density of states at the Fermi level is constant over a small range, then the density of states per unit energy near E_F is given by $(4\pi/3)R^3N(E_F)$, where R is the distance from a given site. For an electron to hop a distance R the activation energy ΔE will be,

$$\Delta E = 1/\left(4\pi/3\right)R^3 N\left(E_F\right) \qquad (3.6.2).$$

There is the added effect that hopping over a distance R will involve tunnelling through that distance, so the probability for a hop will be modified by the factor $\exp(-2\alpha R)$, where α is the inverse localization length of the wavefunction (= $1/\xi$). So to find the optimum hopping range R_0 we need to maximise the expression,

$$\exp\left(-2\alpha R\right)\exp\left(-\Delta E/k_B T\right) \qquad (3.6.3).$$

This will occur when,

$$2\alpha R + 1/\left[\left(4\pi/3\right)R^3 N\left(E_F\right)k_B T\right] \qquad (3.6.4),$$

has its minimum value. This is found to be $R_0 = [1 / 8\pi N(E)\alpha k_BT]^{1/4}$. Putting this value of R in equation 3.6.4 gives :

$$\sigma = \sigma_0 \exp\left[-\left(\frac{T_0}{T}\right)^{1/4}\right] \qquad (3.6.5),$$

where $T_0 = B/N(E_F)\xi^3$. This form for the hopping conduction has been observed in a number of materials such as amorphous $Si_{1-x}Cr_x$ [37], GaAs and InP [38, 39]. From a very early stage though it became clear that this was not the full story of variable range hopping as an exponent of 1/2 rather 1/4 was often found experimentally. Efros and Shklovskii [40] were the first to show that electron-electron correlation effects could be used to explain this phenomenon.

Efros and Shklovskii suggested that the long range Coulomb interaction between localized states meant that states energetically close to the Fermi level should be spatially well separated. This in turn leads to a reduction in the density of states close to the Fermi level. In fact this results in a parabolic dependence of the DOS, $N(E) \propto |E-E_F|^2$, around the Fermi energy. This is a soft gap, in that the DOS is only zero at one point rather than being zero over a finite energy interval. This form for the DOS leads to a new form for the hopping conductivity,

$$\sigma = \sigma_0 \exp\left[-\left(\frac{T_0}{T}\right)^{1/2}\right] \qquad (3.6.6),$$

where $T_0' = 2.8e^2 / \kappa\xi$, where κ is the static dielectric constant which enters the theory through the Coulomb interaction. The data of figure 3.6.3 shows this dependence in neutron transmutation doped Ge:Ga, with increasing carrier concentration [41]. This data brings about the interesting question of the n dependence of the T_0 in the Efros-Shklovskii hopping expression. In the vicinity of the MIT the dielectric constant, and the localization length will diverge, each having a separate critical exponent, ν' and ν respectively. This means that T_0 should scale with a critical exponent $\lambda = \nu' + \nu$. Scaling behaviour is often found for $T_0(n)$, but the results are confusing in that if ν is determined from the conductivity and λ is determined from T_0, it is often found that $\nu' \neq 2\nu$, as predicted by Wegner. In order to examine this problem several studies of the scaling behaviour of the dielectric constant have been made via capacitance measurements [e.g.

24, 42]. Conflicting results are obtained : sometimes $\nu' = 2\nu$, and λ has a consistent value while in other cases the dielectric constant and the conductivity appear to have the same exponent. The situation is no doubt clouded by the fact that such studies of the dielectric constant are limited due to the difficulty of the measurements. It should also be noted that it has been suggested that there are scenarios where the localization length and the conductivity have different exponents which will add another degree of complexity.

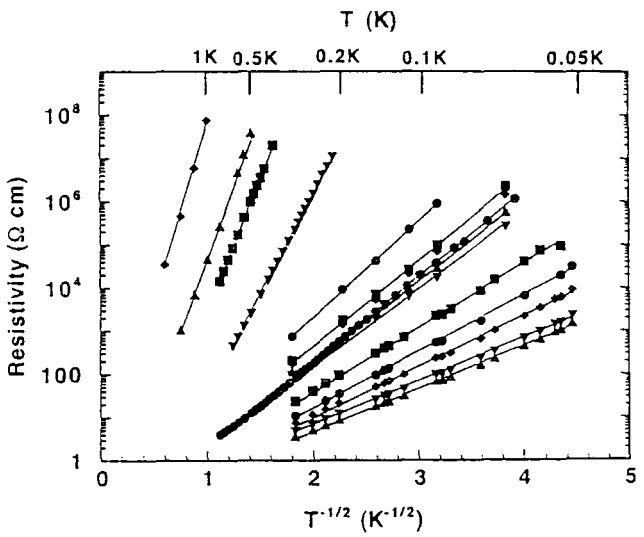

Figure 3.6.3. VRH in Ge:Ga for various doping levels, from $0.16n_c$ to $0.99n_c$ [41].

Finally, the magnetoresistance in the variable range hopping regime is worthy of some discussion. A positive magnetoresistance is observed due to the diamagnetic shrinking of the wavefunctions in an applied magnetic field. This effect reduces wavefunction overlap leading to positive MR. Efros and Shklovskii [40] showed that,

$$\ln\left(\frac{\rho(H)}{\rho(0)}\right) = t\left(\frac{a}{\lambda}\right)^4\left(\frac{T_0}{T}\right)^y \qquad (3.6.7),$$

where for the $T^{1/2}$ law, $y = 3/2$ and $t = 0.0015$. Here, λ is the magnetic length defined as $(c\hbar/eH)^{1/2}$. So ln $[\rho(H) / \rho(0)]$ is expected to be linear in B^2, as is found experimentally in many cases [43]. This expression will be used in later chapters in an attempt to identify the origin of the positive MR found in CdMnTe. It should also be noted that a relatively weak negative magnetoresistance can occurr in the VRH regime [44]. This effect is due to interference associated with the fact that a long range hop encompasses many other electronic states. In certain cases these states can destructively interfere, reducing the probability of a hop from one state to another, therefore increasing the resistance of the sample. When a weak magnetic field is applied the destructive interference is suppressed because the field results in an added phase change in the electronic wavefunctions. Hence the probability of the hop will increase from its original value, and a negative magnetoresistance is observed. This effect is found to lead to a $\ln(\sigma/\sigma_0) \propto H^2$ dependence at weak fields, followed by $\ln(\sigma/\sigma_0) \propto H$ at higher fields, until eventually saturation occurs.

Chapter 3 - References.

1. N.F. Mott. Proc. Phys. Soc. A. **62** 416 (1949).

2. P.W. Anderson. Phys. Rev. **109** 1492 (1958).

3. J. Hubbard. Proc. R. Soc. London Ser. A **277** 237 (1964).

4. P.P. Edwards and M.J. Sienko. Phys. Rev. B. **17** 2575 (1978).

5. N.F. Mott. *Metal-Insulator Transitions.* (Taylor and Francis, 1974). p31.

6. T.F. Rosenbaum, K. Andres, G.A. Thomas and R.N. Bhatt. Phys. Rev. Lett. **43** 1723 (1980).

7. N.F. Mott. *Conduction in Non-Crystalline materials.* (Oxford Science, 1987). p32.

8. J.T. Edwards and D.J. Thouless. J. Phys. C. **5** 807 (1972).

9. For a review see D.J. Thouless. Phys. Rep. **13** 93 (1974).

10. E. Abrahams, P.W. Anderson, D.C. Licciardello and T.V. Ramakrishnan. Phys. Rev. Lett. **42** 673 (1979). A review of the scaling theory thus developed is given by P.A. Lee and T.V. Ramakrishnan Rev. Mod. Phys. **57** 287 (1985).

11. It seems that d = 2 may be a special case because the conductivity and conductance are identical in 2 dimensions. Despite the fact that metallic conduction is disallowed by the theory, insulating to conductive transitions have been observed experimentally in 2d. e.g. T. Wang, K.P. Clark, G.F. Spencer, A.M. Mack and W.P. Kirk. Phys. Rev. Lett. **72** 709 (1994).

12. C. Wegner. Z. Phys. **B25** 327 (1976) ; **B35** 207 (1976).

13. A.M. Finkelstein. Sov. Phys. -JETP **57** 97 (1983).

14. C. Castellani, C. Di Castro, P.A. Lee and M. Ma. Phys. Rev. B. **30** 527 (1984) ; Phys. Rev. B. **34** 5935 (1986).

15. A. Kawabata. Solid State Electron. **28** 131 (1985).

16. K.B. Efetov. Adv. Phys. **32** 53 (1988).

17. A. MacKinnon and B. Kramer. Phys. Rev. Lett. **47** 1546 (1981).

18. W. Sasaki in *Anderson Localization.* Eds T. Ando and H. Fukuyama (Springer-Verlag, Berlin 1987) p.10.

19. W.N. Shafarman, D.W. Koon and T.G. Castner. Phys. Rev. B. **40** 1216 (1989).

20. A.N. Ionov, M.J. Lea and R. Rentzsch. JETP Lett. **54** 473 (1991).

21. P. Dai, Y. Zhang and M.P. Sarachik. Phys. Rev. B. **45** 3984 (1982).

22. M.A. Paalanen, T.F. Rosenbaum, G.A. Thomas and R.N. Bhatt. Phys. Rev. Lett. **48** 1284 (1982).

23. R.M. Westervelt, M.J. Burns, P.F. Hopkins, A.J. Rimberg and G.A. Thomas in *Anderson Localization.* Eds T. Ando and H. Fukuyama (Springer-Verlag, Berlin 1987) p.33.

24. S. Katsumoto in *Anderson Localization.* Eds T. Ando and H. Fukuyama (Springer-Verlag, Berlin 1987) p.45.

25. S. von Molnar, A. Briggs, J. Flouquet and G. Remenyi. Phys. Rev. Lett. **51** 706 (1983).

26. T. Dietl, M. Sawicki, T. Wojtowicz, J. Jaroszynski, W. Pleisewicz, L. Swierkowski and J. Kossut in *Anderson Localization.* Eds T. Ando and H. Fukuyama (Springer-Verlag, Berlin 1987) p.58.

27. B.L. Altshuler and A.G. Aranov. *Electron-Electron Interaction in Disordered Conductors* in *Electron-Electron Interactions in Disordered Systems* (Elsevier, 1985). p. 1.

28. H. Fukuyama. *Interaction Effects in the Weakly Loclized Regime of Two and Three Dimensional Systems* in *Electron-Electron Interactions in Disordered Systems* (Elsevier, 1985). p. 155.

29. G. Bergmann. Phys. Rep. **107** 1 (1984).

30. G.A. Thomas, A. Kawabata, Y. Ootuka, S. Katsumoto, S. Kobayashi and W. Sasaki. Phys. Rev. B. **26** 2113 (1982).

31. S. von Molnar, J. Flouquet, F. Holtzenberg and G. Remenyi. Solid State Electron. **28** 127 (1985).

32. A. Miller and S. Abrahams. Phys. Rev. **120** 745 (1960).

33. H. Fritzsche. Phys. Rev. **99** 406 (1955).

34. H. Fritzsche. *The Metal-Nonmetal Transition in Disordered Systems* eds L.R. Friedman and D.P. Tunstall (SUSSP, Edinburgh 1978). p193.

35. E.A. Davis and W.D. Compton. Phys. Rev. **A140** 2183 (1965).

36. N.F. Mott. J. Non-cryst. Solids **1** 1 (1968).

37. A. Mobius. J. Phys. C. **18** 4639 (1985).

38. M. Benzaquen and D. Walsh. Phys. Rev. B. **30** 7287 (1984).

39. M. Benzaquen, K. Mazuruk and D. Walsh. J. Phys. C. **18** 1107 (1985).

40. B.I. Shklovskii and A.L. Efros. *Electronic Properties of Doped Semiconductors.* (Springer-Verlag, Berlin, 1984) p.212.

41. K.M. Itoh *et al* Phys. Rev. Lett. 77 4058 (1996).

42. I. Terry, T. Penney, S. von Molnar and P. Becla. Phys. Rev. Lett. **69** 1800 (1992).

43. A.N. Ionov and I.S. Shlimak. *Hopping Conduction in Heavily Doped Semiconductors* in *Hopping Transport in Solids* eds M. Pollak and B. Shklovskii (Elsevier, 1991). p397.

44. B.I. Shklovskii and B.Z. Spivak. *Scattering and Interference Effects in Variable Range Hopping Conduction* in *Hopping Transport in Solids* eds M. Pollak and B. Shklovskii (Elsevier, 1991).p 271.

4. Review of Persistent Photoconductivity.

The aim of this chapter is to give a relatively in-depth review of the physics behind the effect of Persistent Photoconductivity (PPC). The motivation for this is simple; CdMnTe:In is a persistent photoconductor and the main section of this thesis is involved with studying this effect, and using it to study the MIT.

Section 4.1 will outline the PPC effect and its discovery, as well as giving an indication of which materials are known to show PPC. Section 4.2 describes the large lattice relaxation negative U model, which is the leading model used to explain the DX centre PPC seen in materials such as CdMnTe. Section 4.3 then deals with the PPC seen in CdMnTe : In, and gives an outline of the work performed so far. Section 4.4 reviews the work done on PPC (or at least long lived photoconductivity) in systems where the mechanism behind the effect is *not* based on DX centres. A rather in-depth review of studies of multiple DX centres is given in section 4.5 along with the prevailing theories. This section is included as a large part of chapter 6 is based on measurements on samples of CdMnTe:In which appear to show multiple DX centre formation. Finally, section 4.6 explains how PPC presents us with a wonderful opportunity to study the metal-insulator transition in a controllable fashion - the main aim of this thesis.

4.1. Discovery In $Al_xGa_{1-x}As$.

PPC is an effect displayed by certain materials where the exposure of the material to light of some wavelength, below a certain temperature, results in an increase in the conductivity which persists after the illumination is ceased. There is a rather diverse range of materials which display PPC under certain conditions ; II - VI semiconductors (CdTe under hydrostatic pressure[1], CdZnTe [2, 3] and of course CdMnTe:In or Ga [4, 5]), III -

V semiconductors (GaAs [6], GaSb [7, 8], InSb [9], AlGaAs [10] etc) as well as more exotic systems such as thin films of the superconductor YBCO [11] and some CMR (Colossal Magnetoresistance) perovskites [12]. The mechanisms producing the PPC in these materials can be very different. Here I will concentrate on PPC in semiconducting materials before moving on to CdMnTe:In in detail (section 4.3).

PPC was discovered in $Al_xGa_{1-x}As$:Te, and then $Al_xGa_{1-x}As$:Si, after a considerable amount of research on deep donor levels and the related doping problems in such compounds as GaAs and GaAsP [10]. After the realisation that deep defect centres were at the root of the so-called doping problem [13], the major breakthrough in the search for an explanation of the effect was given by Lang and Logan [14]. They suggested that the PPC was linked with a deep state with a large Stokes shift (i.e. the optical depth much larger than the thermal depth), and a small capture cross-section at low temperatures, leading to a PPC effect. They concluded that in order that the defect have a large Stokes shift, the electron capture to the deep state must be accompanied by a large lattice relaxation. In other words, the lattice is distorted around the defect centre. This defect became known as a DX centre, because at the time it was thought to be a complex of a deep state (D) and an unknown defect (X). It is now known that the DX centre actually originates from isolated donors rather than some donor complex. These ideas were successfully combined and used to construct the large lattice relaxation negative U model, which is described in the next section.

This PPC effect is shown in figure 4.1.1., where the carrier concentration of a sample AlGaAs is plotted as a function of the inverse temperature. A large difference between the dark and illuminated concentration is seen below a certain temperature, known as the quenching temperature T_Q. This increase in concentration is accompanied by a corresponding increase in the electrical conductivity. The behaviour shown here is rather typical of a DX centre PPC material.

Figure 4.1.1. Plot of carrier concentration against inverse temperature for AlGaAs. From [15].

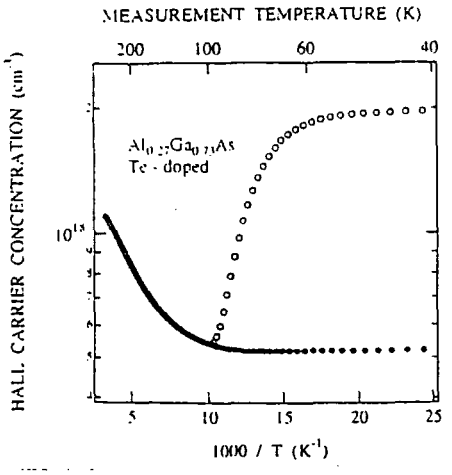

4.2. Large Lattice Relaxation Negative 'U' Model.

After the experiments of Lang *et al* [14] which suggested that the DX centre involved a large lattice relaxation, a complete model of the DX centre was forwarded by Chadi and Chang in the late 1980's [16,17]. They suggested that the experimental work on AlGaAs pointed to the fact that the PPC was due to the formation of two types of donor states : a regular shallow effective mass level residing just below the conduction band edge, and a localised deep DX level with a large degree of lattice relaxation. (The two activation energies associated with these levels had been extracted from the transport data on AlGaAs as shown in figure 4.2.1.). A qualitative description of the structure and formation of the defect was given, followed by a theoretical analysis which showed how the experimental findings of a large stokes shift and the observed pressure and composition dependencies (figure 4.2.1.) could be reproduced by the model. This theory was based on an *ab initio* pseudopotential approach from which the binding energy of the centre was calculated.

Figure 4.2.1. x dependence of the DX level in AlGaAs. From [18].

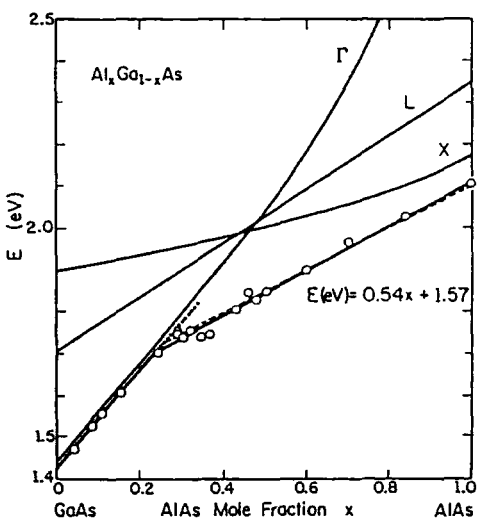

The DX centre was proposed to be the result of the following set of reactions,

$$d^0 \rightarrow d^+ + e^- \qquad (4.2.1),$$

$$d^0 + e^- \rightarrow DX^- \qquad (4.2.2),$$

adding to give,

$$2d^0 \rightarrow d^+ + DX^- \qquad (4.2.3).$$

Here d represents the shallow effective mass donor, e an electron, and DX the DX level deep state. So, the DX^- state is formed after capture of an electron and is therefore negatively charged, the whole defect centre capturing two electrons. These two electrons obviously repel each other via the Coulomb interaction. This is why the large lattice relaxation is important - the Coulomb repulsion is overcome by a lattice distortion around the DX deep level making the whole centre energetically stable. This model is referred to as a negative U model as two trapped electrons lead to a negative Hubbard correlation energy, U.

The precise form of the lattice distortion was elucidated by the pseudopotential calculations, which showed that the Ga - Si bond in the defect is ruptured and the interatomic distance altered, as shown in figure 4.2.2. It is easily seen how this situation leads to PPC if the configuration co-ordinate diagram in figure 4.2.3. is examined. Here the two states (the deep level and the shallow level) are shown, and the relevant energies labelled. When the sample is cooled in the dark the electrons freeze into the deep level and the system shows insulating behaviour. On illumination at low temperatures the electrons are excited to the shallow state, and the conductivity (and free carrier concentration) increases. The following reaction is occurring,

$$d^+ + DX^- \rightarrow (h\nu) \rightarrow 2d^+ + 2e^- \qquad (4.2.4).$$

As can be clearly seen from the configuration co-ordination diagram, at sufficiently low temperatures, the photoconductivity will be persistent as the electrons are unable to

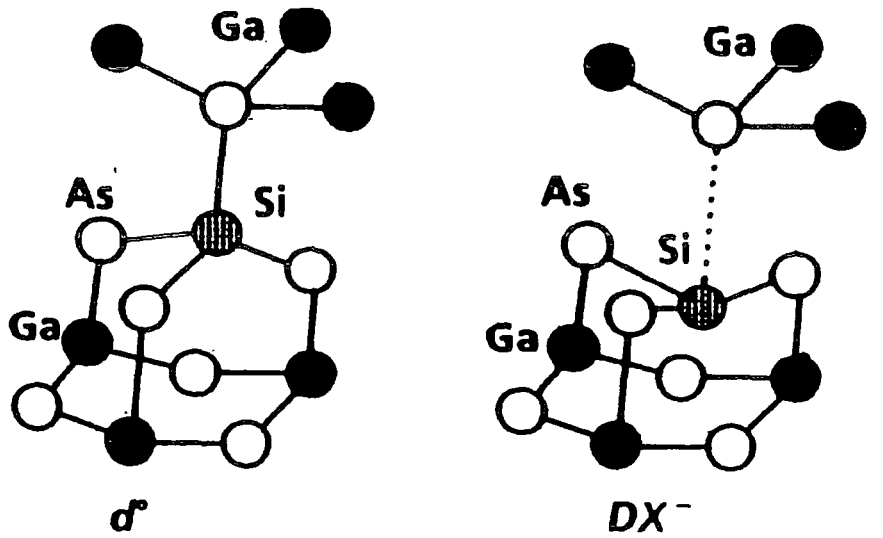

Figure 4.2.2. Atomic configuration of the shallow donor (d^0) and the DX^- deep level in AlGaAs:Si [16, 17].

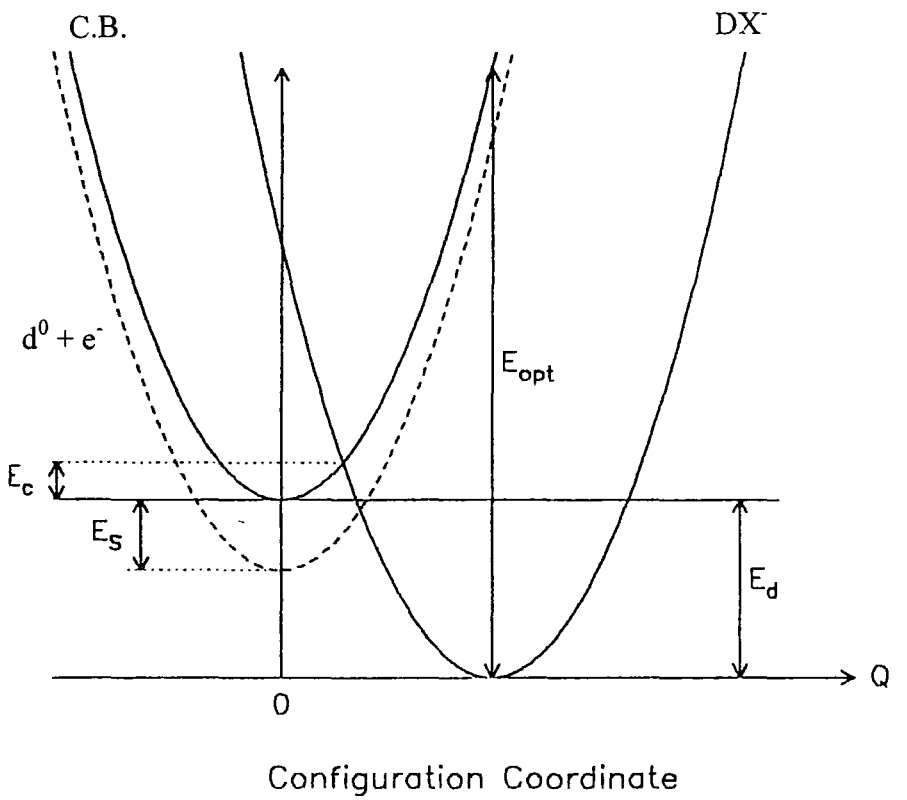

Figure 4.2.3. Configuration co-ordinate diagram for the negative U model of the DX centre [16, 17].

surmount the barrier to recapture to the deep state. This leads to PPC below a temperature T_Q, where $k_B T_Q$ is the size of the barrier to recapture.

This model leads to a temperature dependence of the resistivity, in a DX centre persistent photoconductor, as shown in the schematic in figure 4.2.4. As the sample is cooled in the dark the activation energy of the deep level is observed until $k_B T < E_D$. Below this temperature the activation energy of the shallow level (E_S) is observed. On illumination the conductivity increases and remains high after the illumination is ceased. When the sample is warmed, the conductivity remains higher than the dark level up to the quenching temperature, T_Q, where the two curves meet.

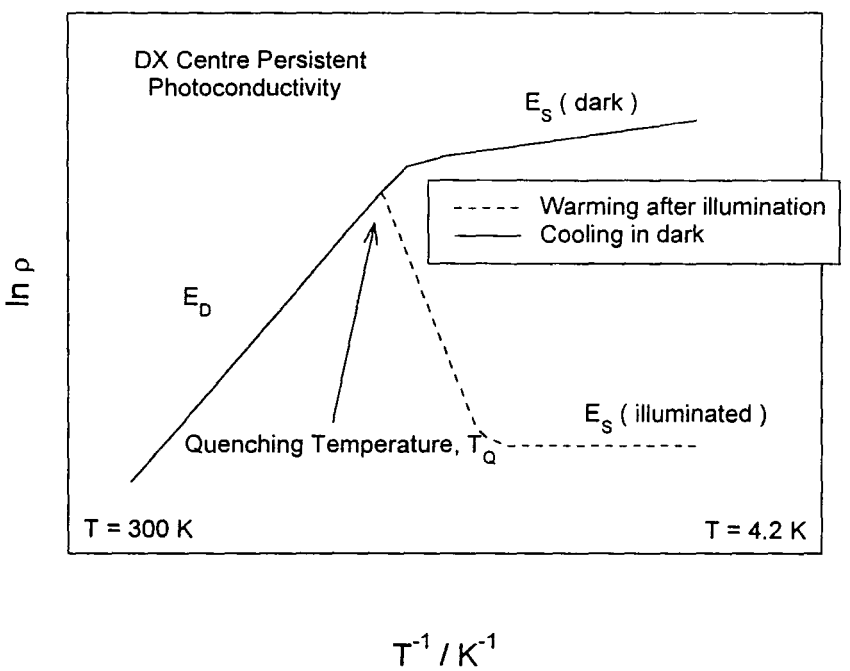

Figure 4.2.4. Schematic of the temperature dependence of the resistivity in a DX centre PPC material.

As mentioned earlier this model is rather successful as it explains the x dependence of the DX deep level energy in $Al_xGa_{1-x}As$, the pressure dependence of the deep level, as well as the large Stokes shift observed. As there are two electrons captured in the ground state of the DX^- level the model also predicts that the ground state should be diamagnetic, with the electrons having opposite spin directions. This was apparently confirmed by the absence of an EPR (Electron Paramagnetic Resonance) signal in AlGaAs [19], an effect which was observed in a number of studies. Although the negative U model is now widely accepted there is a certain amount of controversy surrounding it, after an experiment performed by Khachaturyan *et al* [20] appeared to show that the ground state of the DX centre was paramagnetic. A similar experiment (to measure the magnetic moment of the centre) was performed by Katsumoto *et al* [21] with rather different results. It is clear that there are some problems involved with the interpretations of these measurements, despite the fact that measuring the magnetic susceptibility would appear to be the most direct method of determining the spin of the ground state. The negative U model remains the most popular model for the explanation of the PPC effect in compounds such as these.

4.3. PPC in CdMnTe.

As was mentioned earlier, PPC was discovered in CdMnTe:In [4] and CdMnTe:Ga [5] after work on the effect in CdTe under hydrostatic pressure [1] and CdZnTe:Cl [2, 3]. The PPC observed in this material is completely analogous to that seen in AlGaAs i.e. it is due to the formation of both shallow and deep DX^- levels when doped with In or Ga. So figures 4.2.2 and 4.2.3 both hold, but with In taking the place of Si, Ga replacing (Cd / Mn), and Te replacing As.

The work done on CdMnTe:Ga was concerned with transport properties linked with the PPC effect. In particular the resistivity, carrier concentration and mobility were all shown to have a typical form for a DX centre persistent photoconductor, the quenching temperature being of the order of 100 K. In addition to these measurements,

Semaltianos *et al* [5] also measured the photoionization transients as a function of temperature and magnetic field. One of the most interesting results they obtained was that magnetic fields of up to 6 T produced no observable effect on these transients. This suggests that the deep DX^- level is insensitive to local Mn spins, and hence that the centre should be diamagnetic in nature - further evidence for the negative U model. One might expect that the shallow levels associated with the PPC would be Zeeman split, producing an effect on the photoconductivity transients. The reason why no such effects are observed is unclear, although it is worth noting that if both deep and shallow levels are split to the same extent then this would have little effect on the PPC.

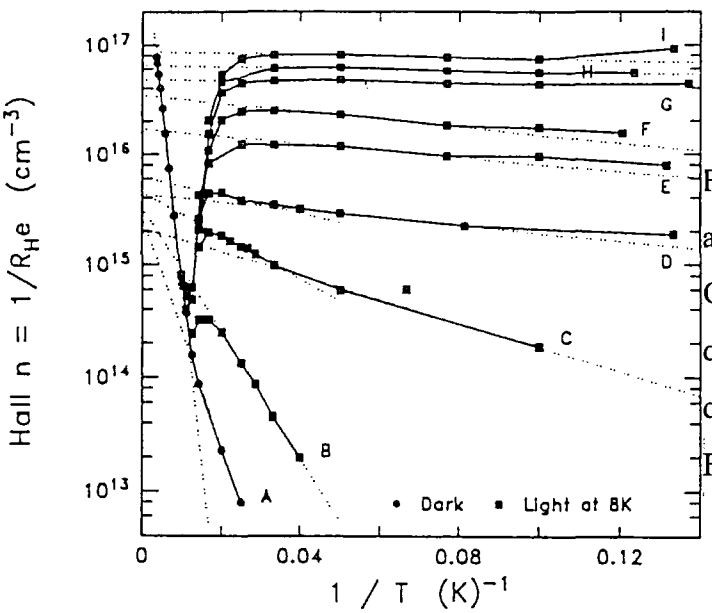

Figure 4.3.1. Hall carrier density against inverse temperature for $Cd_{0.9}Mn_{0.1}Te$: In. A is the dark data. Curves B to I represent a different illumination level. From [4].

Experiments on CdMnTe:In showed again that the phototransport properties were typical of a DX centre persistent photoconductor. Figure 4.3.1. shows the Hall carrier concentration of $Cd_{0.9}Mn_{0.1}Te$:In plotted as a function of the inverse temperature. Each of these curves corresponds to illumination to a different level at 8 K. The PPC effect is clearly seen with a quenching temperature of around 100 K. Samples with several compositions were studied, and deep level activation energies were found to be in the range 2.42 to 151.8 meV with a rather strong dependence on x. This x dependence of

phototransport properties (such as E_D) will be discussed in detail later in this thesis (section 6.1.3) and appears in [22]. Interestingly, the shallow level activation energy, E_S was found to vary as $1/ (n_S^3)$ for the sample shown in figure 4.3.1, and some analysis allowed a determination of the density of states as a function of the activation energy. This produced an approximation to the exponential form usually associated with a band tail in the density of states. This paper [4] was the first to make clear the motivation for this work : to study the metal-insulator transition in a magnetic semiconductor by control of the illumination level. Unfortunately all of the samples used in [4] were found to be insulating after illumination. Measurements of the low temperature transport properties, hopping conduction [23] and dielectric constant [24] were all made in the insulating phase as the transition was approached. These are commented on in more detail in the sections of this thesis devoted to the MIT.

The PPC effect in $Cd_{1-x}Mn_xTe$:In was also utilised to study the carrier concentration dependent magnetoresistance [25, 26], highlighting the applicability of the technique to study any carrier concentration dependent phenomenon. This work is discussed in more detail in section 2.3.3. where the magnetotransport properties of diluted magnetic semiconductors (and in particular $Cd_{1-x}Mn_xTe$:In) are reviewed.

4.4. PPC Unrelated to DX Centres.

As previously mentioned in section 4.1. there exists a wide variety of materials which show a PPC effect of some form. Not all of these display DX centre PPC. In fact materials are often labelled persistent photoconductors when the induced photoconductivity is a long lived phenomenon but not truly persistent. One of the clearest examples of a system which shows such a long lived or persistent photoconductivity is that of a semiconductor interface. For example, samples of n-GaAs on an insulating GaAs:Cr substrate show a very long lived PPC up to $T > 140$ K [27, 28]. A similar effect is seen in MBE grown samples of ZnSe:Ga on an insulating GaAs substrate [29]. These effects are explained in terms of photoexcited electrons, being hindered in their attempts

to recombine with holes, by macroscopic potential barriers at the interface. This explanation differs fundamentally with the DX centre materials where the potential barriers involved in the PPC are *microscopic.*

For the case of n - GaAs on GaAs substrates [27, 28] the photons absorbed by the material generate electron hole pairs; the holes diffusing into the insulating substrate, while the electrons remain in the n - GaAs layer producing an excess conductivity. This photoconductivity is persistent as the electron hole pairs are now spatially separated by the interface potential barrier, plus the fact that the holes in the substrate will be trapped in localized states. The interesting point here is that the form of the relaxation of the photoconductivity can be explained by a model based on spatial separation of the carriers. An initial fast relaxation is due to the recombination of carriers separated spatially by small amounts. After this, slow relaxation at long times is due to the gradual recombination of carriers separated by a large distance. A simple modelling of this process leads to the following form for the conductivity :

$$\sigma(t) = \sigma(t = 0) - 0.5AaN \ln(t / \tau_0) \qquad (4.4.1)$$

where a is the Bohr radius of the electron, N is the density of the traps in the substrate, and A is a constant depending on the mobility and width of the conducting layer. This equation seems to explain the data rather well [27].

The explanation of the PPC effect in the ZnSe epilayers is of a similar nature. Here a large band offset between the GaAs substrate and the layer produces a potential barrier at the heterojunction. So again the photocarriers are spatially separated, with the recombination being limited by tunnelling processes. In these samples this actually leads to a quenching temperature of 350 K. The technological significance of a quenching temperature above room temperature is commented on in section 4.5. It should also be noted that other layers of ZnSe on GaAs show pure DX centre behaviour, if the samples are grown such that the large band offset does not occur.

Similar ideas have been used to explain the long lived photoconductivity observed in nominally undoped ZnCdSe bulk samples [30, 31]. Jiang and Lin proposed that compositional fluctuations produce variations in the conduction band minima, which in turn result in random local potential fluctuations. Firstly, it is important to realise that the 'persistent' photoconductivity seen here is easily discernible from DX centre PPC as the relaxation, and the temperature dependence of the relaxation, is rather different. In fact the work on CdZnSe showed relaxations of up to 80 % of the photoconductivity in 1500 s, compared to typical values of 5 % in 100 s, followed by no further measurable relaxation up to 1500 s in CdMnTe:In [22] (see chapter 6). The problem with the proposed random potential fluctuation model is that the theoretical work of Shik and his co-workers [32, 33], on PPC in inhomogenous semiconductors, concludes that such a mechanism on its own will not lead to PPC. They assert that the addition of a high level of compensation would lead to PPC however, as these compensating centres can lead to the band edge modulation required for long lived photoconductivity and 'residual conductivity'.

4.5 Multiple DX Centres.

A fairly complete review of PPC and the negative U model (with reference to CdMnTe:In in particular) has been given, along with a description of some forms of long lived photoconductivity which are unconnected with DX centres. In this section the concept of multiple DX centres is outlined. Here, the idea is that it is perfectly plausible that any particular material may be able to support more than one type of DX centre. Each DX centre would have a different binding energy, and therefore, a different quenching temperature. Two forms of multiple DX centres will be discussed ; those due to different atomic configurations, and those due to the effects of the local atomic environment on the binding energy of the centre. These two models have received a good deal of attention in

the recent literature on CdZnTe:Cl and AlGaAs, respectively. It will be seen in chapter 5 that these models could well be applicable to CdMnTe:In also.

4.5.1. DX Centre Configurations.

DX centre persistent photoconductivity was examined in CdZnTe:Cl by Thio *et al* [34, 35] with the surprising result that certain samples showed PPC existing up to approximately 200 K, rather than the typical value for CdZnTe:Cl of 150 K [36]. This behaviour is shown in figure 4.5.1, where the conductivity and carrier density of $Cd_{0.72}Zn_{0.28}Te$:Cl is shown as a function of temperature, both before and after illumination. Clearly, the illuminated conductivity shows a second peak around 165 K, where it would normally be decreasing to intersect with the dark curve. This increase in the conductivity is accompanied by a corresponding increase in the carrier concentration. It is this behaviour which leads to a high quenching temperature of ~200 K.

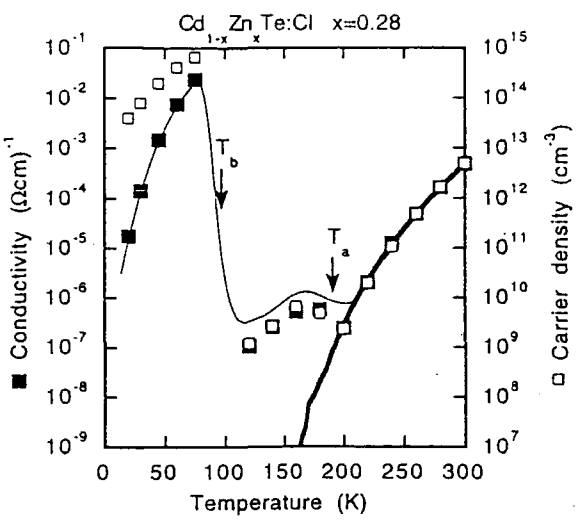

Figure 4.5.1. : Temperature dependence of the conductivity and carrier density before and after illumination in $Cd_{0.72}Zn_{0.28}Te$:Cl. From ref [36].

This behaviour was interpreted by the authors in terms of a second metastable DX state. This interpretation was aided by the theoretical calculations of Park and Chadi [37] which showed that for the case of CdZnTe:Cl, three distinct types of DX-like structures are stable. Each of these states has a slightly different atomic configuration around the Cl donor, giving a different binding energy, and hence T_Q. So the data of Thio *et al* (shown in figure 4.5.1) was interpreted in terms of the existence of two centres giving rise to the

two different T_Q values of 150 K and 190 K. Detailed first principles pseudopotential calculations predict that these different configurations are characterized by either bond rupture (as in the original DX state) or bond compression, each centre having different Cd-Cl bond lengths and angles. These calculations were also able to predict the binding energies of each of the centres.

Detailed calculations were also performed for the case of CdTe [38] doped with group VII (e.g. Cl) and group III (e.g. In) impurities. As for CdZnTe:Cl, three types of DX centre were found to be stable for CdTe:VII. Interestingly, the work of Park and Chadi predicts that the situation for group III donors, such as In, is rather different. In this case the calculations find that there is only one stable state and that multiple DX centre formation is *not* possible. Unsurprisingly, this state was found to be almost identical to the DX centre formed by Si in AlGaAs. CdTe and CdTe-based compounds would therefore seem to be something of a special case in terms of DX centre formation, when doped with group VII elements.

4.5.2. The Effect of the Local Atomic Environment.

Several authors have commented, in work on AlGaAs, that the deep DX^- level is likely to have a binding energy which is dependent on the local atomic environment of the donor atom (e.g. Si, Te etc) [39, 40, 41, 42]. They observed that group IV donors in AlGaAs display a splitting of their ground state in the DX centre configuration, due to different possible numbers of Al neighbours. Reference to figure 4.2.2 shows that there are four possible options : i = 0, 1, 2 or 3 Al atoms in the DX configuration, with binding energies E^i_{DX}. It is clear that a situation such as this can lead to the appearance of more than one quenching temperature. Contreras *et al* [40] obtained electrical transport data on Si doped AlGaAs and AlAs / GaAs superlattices which supports the conclusion that a number of DX states are apparent due to this 'alloy splitting'. A similar conclusion was reached by Mooney *et al* from DLTS (Deep Level Transient Spectroscopy) experiments on Si doped samples of GaAs and AlGaAs [42]. In this work a single DLTS peak is found

in GaAs:Si, whereas in AlGaAs:Si they found three distinct peaks. This would appear to be a very convincing result indeed. It should be noted that it is not only the Si DX centre which shows sensitivity to the local atomic environment. Sallese *et al* [41] have observed that the Te related DX centre also shows this alloy effect.

Although these experimental investigations seem to give extremely convincing evidence for the hypothesis that the DX centre binding energy is sensitive to the local atomic environment, the question of why it is only observed in some samples remains to be resolved. One of the few publications which addressed this problem [43], made the comment that multiple peaks in the DLTS spectra were only observable in low quality or highly doped samples grown by molecular beam epitaxy. They also suggest that such structure would only be observable in transport measurements if the samples were heavily doped, or of low quality. It seems clear that gaining information on the quality of the crystals is important when attempting to understand the origin of a multiple DX centre effect.

The final point to make in the discussion of multiple DX centre formation (whether it is due to different configurations, or to the effects of the local atomic environment), is that it could lead to PPC with a rather high quenching temperature. This begs the obvious question of whether it is possible to produce a material which displays DX centre PPC at room temperature, and, if so, what are the potential applications? This is a question which has been the subject of recent research by Thio *et al* [44, 45]. They have suggested that one immediate application of such a material would be to write erasable conductive patterns on an insulating background. This process could be utilised in optical switching, holography, and even high density data storage. It has already been demonstrated [44] that writing conductive patterns in an insulating background is possible in AlGaAs. Moreover, it has been possible to write a 'conductivity grating' in this material and then observe optical diffraction from this optically generated structure, formed from patterns of illuminated regions [45]. It is worth noting that the optical diffraction intensity increases with the square of the thickness of such samples, meaning

that bulk systems will be preferred over epitaxial layers. One final relevant point to be made is that if such applications can be realised, then it may not be necessary to warm the material to its quenching temperature to erase the patterns. It has been shown that far infra-red illumination can induce the capture of electrons by DX centres, leading to quenching of the PPC [46].

4.6. Photodoping Through The MIT.

As has already been mentioned the main aim of this thesis is to discuss the MIT in CdMnTe:In, studied using the PPC effect. Quite simply, we are using illumination to control very accurately the carrier concentration and conductivity in an attempt to induce an insulator-metal transition. This process has been carried out before for the case of AlGaAs:Si, by Katsumoto *et al* [47]. The results of this experiment were discussed in detail in section 3.4, where some of the data is also displayed. The principle of our experiment is identical, although we are able to study the MIT in a magnetic system, allowing a zero magnetic field transition to be induced. This point, along with the details of the experiment will be discussed in detail in section 7.2. At this point though, it may be helpful to clarify the situation with regards to past work on PPC in CdMnTe:In. As mentioned in section 4.3 the PPC has been used to study the conductivity and dielectric constant on the approach to the MIT. This was done because of the difficulty in finding a sample which is suitable to study the transition. First of all, the vast majority of the samples grown for this project were far too insulating, due to the high concentration of Cd vacancies, leading to a large compensation ratio. The second problem is that as n increases towards n_C, the change in conductivity and carrier concentration on illumination decreases. This means that it is rather difficult to obtain samples which are conductive enough to be near the transition on the insulating side, but also have a large enough change in conductivity on illumination to reach the metallic phase. Details of two samples which do just this, as well as several other samples which are metallic before illumination is given in chapter 7.

Chapter 4 - References.

1. G.W. Iseler, J.A. Kafalas, A.J. Strauss, H.F. MacMillan and R.H. Bube. Solid. State. Commun. **10** 619 (1972).

2. B.C. Burkey, R.P. Khosla, J.R. Fischer and D.L. Losee. J. Appl. Phys. **147** 1095 (1976).

3. K. Khachaturyan, M. Kaminska, E.R. Weber, P. Becla and R.A. Street. Phys. Rev. B. **40** 6304 (1989).

4. I. Terry, T. Penney, S. von Molnar, J.M. Rigotty and P. Becla. Solid. State. Commun. **84** 235 (1992).

5. N. G. Semaltianos, G. Karczewski, T. Wojtowicz and J.K. Furdyna. Phys. Rev. B. **47** 12540 (1993).

6. *Physics of DX Centers in GaAs and Alloys.* ed J.C. Bourgoin. *Solid State Phenomena.* **Vol 10.** (Sci-Tech Publications, Vaduz) 1990.

7. B.B. Kosicki, W. Paul, A.J. Strauss and G.W. Iseler. Phys. Rev. Lett. **23** 1175 (1966).

8. B.B. Kosicki, A. Jayaraman and W. Paul. Phys. Rev. B. **172** 764 (1968).

9. S. Porowski, M. Konczykowski and J. Chroboczek. Phys. Stat. Sol. **A 63** 291 (1974).

10. For a review see P.M. Mooney.J. Appl. Phys. **67** 3 (1990).

11. V.I. Kudinov, I.L. Chaplygin, A.I. Kirilyuk, N.M. Kreines, R. Laiho, E. Lahderanta and C. Ayache. Phys. Rev. B. **47** 9017 (1993).

12. V. Kiryukhin, D. Casa, J.P. Hill, B. Keimer, A. Vigliante, Y. Tomioka and Y. Tokura. Nature **386** 813 (1997).

13. P.M. Mooney and T.N. Theis. Comments. Cond. Mat. Phys. **16** 167 (1992).

14. D.V. Lang and R.A. Logan. Phys. Rev. Lett. **39** 635 (1977).

15. T. Laine, J. Makinen, K. Saarinen, P. Hautojarvi, C. Corbel, M.L. Fille and P. Gibart. Phys. Rev. B. **53** 11025 (1996).

16. D.J. Chadi and K.J. Chang. Phys. Rev. Lett. **61** 873 (1988).

17. D.J. Chadi and K.J. Chang. Phys. Rev. B. **39** 10063 (1989).

18. N. Chand, T. Henderson, J. Klem, W.E. Masselink, R. Fischer, Y.C. Chang and H. Morkoc. Phys. Rev. B. **30** 4481 (1984).

19. P.M. Mooney, W. Wilkening, U. Kaufmann and T.I. Kuech. Phys. Rev. B. **39** 5554 (1989).

20. K.A. Khachaturyan, D.D. Awschalom, J.R. Rozen and E.R. Weber. Phys. Rev. Lett. **63** 1311 (1989).

21. S. Katsumoto, N. Matsunaga, N. Yoshida, Y. Sugiyama ans S. Kobayashi. Jpn. J. Appl . Phys. **29** L1572 (1990).

22. C. Leighton, I.Terry and P. Becla. Phys. Rev. B. **56** 6689 (1997).

23. I. Terry, T. Penney, S. von Molnar and P. Becla. Phys. Rev. Lett. **69** 1806 (1992).

24. I. Terry, S. von Molnar, A.M. Torressen and P. Becla. Phil. Mag. B. **65** 1245 (1992).

25. I. Terry, T. Penney, S. von Molnar and P. Becla. J. Cryst. Growth. **159** 1070 (1996).

26. S. von Molnar, I. Terry, T. Penney and P. Becla. Physica B. **197** 151 (1994).

27. H.J. Quiesser. Phys. Rev. Lett. **54** 234 (1985).

28. H.J. Quiesser and D.E. Theodorou. Phys. Rev. B. **33** 4027 (1986).

29. T. Thio, J.W. Bennett, D.J. Chadi, R.A. Linke and M.C. Tamargo. J. Electron. Mater. **25** 229 (1996).

30. J.Y. Lin and H.X. Jiang. Phys. Rev. B. **41** 5178 (1990).

31. H.X. Jiang and J.Y. Lin. Phys. Rev. Lett. **64** 2547 (1990).

32. A.Ya. Shik. Sov. Phys. -JETP. **41** 932 (1976).

33. M.K. Sheinkman and A.Ya. Shik. Sov. Phys. Semicond. **10** 128 (1976).

34. T. Thio, J.W. Bennett, D.J. Chadi, R.A. Linke and P. Becla. J. Cryst. Growth. **159** 345 (1996).

35. T. Thio, J.W. Bennett and P. Becla. Phys. Rev. B. **54** 1754 (1996).

36. J.W. Bennett, T. Thio, S.E. Kabakoff, D.J. Chadi, R.A. Linke and P. Becla. J. Appl. Phys. **78** 5827 (1995).

37. C.H. Park and D.J. Chadi. Phys. Rev. B. **52** 11884 (1995).

38. C.H. Park and D.J. Chadi. Appl. Phys. Lett. **66** 3167 (1995).

39. E. Calleja, F. Garcia, A. Gomez, E. Munoz, P.M. Mooney, T.N. Morgan and S.L. Wright. Appl. Phys. Lett. **56** 934 (1990).

40. S. Contreras, V. Mosser, R. Piotrzkowski, P. Lorenzin, J. Sicart, P. Jeanjean, J.L. Robert and W. Zawadzki. Semicond. Sci. Technol. **6** B58 (1991).

41. J.M. Sallese, D.K. Maude, M.L. Fille, U. Willke, P. Gibart and J.C. Portal. Semicond. Sci. Technol. 7 1245 (1992).

42. P.M. Mooney, T.N. Theis and E. Calleja. J. Electron. Mater. **20** 23 (1991).

43. L. Dobaczewski, P. Kaczor, M. Missous, A.R. Peaker and Z.R. Zytkiewicz. J. Appl. Phys. **78** 2468 (1995).

44. T. Thio, R.A. Linke, G.E. Devlin, J.W. Bennett, D.J. Chadi and M. Mizuta. Appl. Phys. Lett. **65** 1802 (1994).

45. R.A. Linke, T. Thio, D.J. Chadi and G.E. Devlin. Appl. Phys. Lett. **65** 16 (1994).

46. J.J. Plombon, W.W. Bewley, C.L. Felix, M.S. Sherwin, P. Hopkins, M. Sundaram and A.C. Gossard. Appl. Phys. Lett. **60** 1972 (1992).

47. S. Katsumoto. *Anderson Localization,* edited by T. Ando and H. Fukuyama. (Springer-Verlag, Berlin. 1987) p. 45.

5.1 Sample Preparation And Compositional Analysis.

This section deals with the preparation and compositional analysis of the $Cd_{1-x}Mn_xTe$:In samples.

5.1.1 Preparation of Samples For Electrical Measurement.

Bulk crystals of the diluted magnetic semiconductor $Cd_{1-x}Mn_xTe$ were grown using the vertical Bridgman technique, by P. Becla [1]. The samples were deliberately doped to a relatively high level of approximately 10^{18} - 10^{19} dopant atoms cm^{-3} with indium. All samples grown in this fashion were found to be n-type. The In doping was done to allow the study of persistent photoconductivity arising due to the fact that In forms a DX centre when doped in $Cd_{1-x}Mn_xTe$. This atomic concentration of In was determined for some of the samples, either from atomic absorption spectroscopy, or by mass spectroscopy. The as-grown material was annealed in Cd vapour at temperatures in the range 600 to 800 °C immediately after the growth. This was done to reduce the number of Cd vacancies arising within the material. These Cd vacancies act as acceptors, drastically reducing the room temperature free carrier concentration of the material. In fact, annealing in Cd vapour increased the room temperature carrier concentration by up to two orders of magnitude.

Individual samples were prepared by cutting cross sectional wafers, typically about 1mm thick, from the crystal then mechanically polishing them. In order to perform electrical measurements, the samples were then etched to remove any oxide layer from the surface, hence ensuring that electrical contact is made to the actual material rather than a layer of impurity. Contacts were always deposited immediately after the etch process to prevent re-formation of an oxide layer. The chemical etchant used in the process is a 2.5 % (by volume) solution of bromine in methanol. The polished sample is immersed in the CH_3OH / Br solution for a period of about one minute. The sample is then thoroughly washed in pure CH_3OH and left to dry at room temperature.

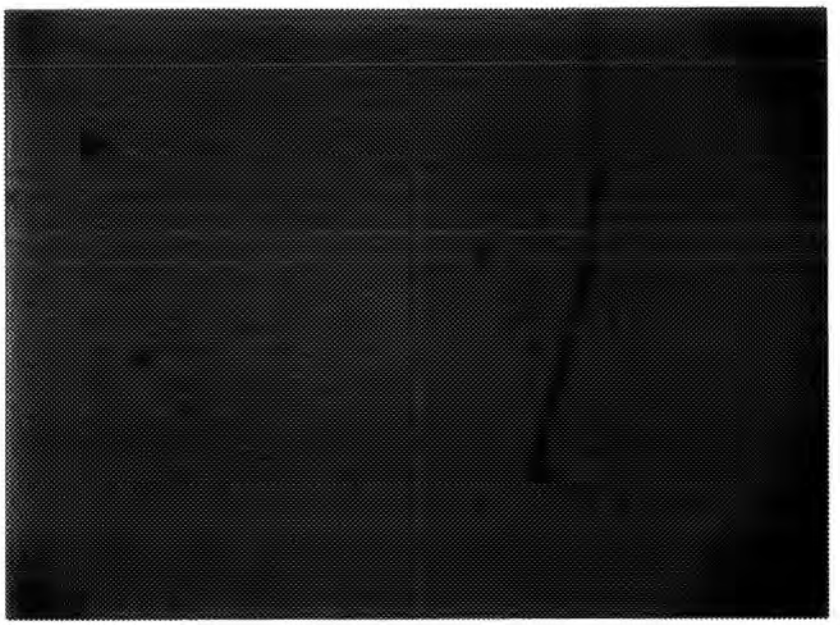

Figure 5.1.1. Infrared microscope image of a fairly uniform sample (A2).

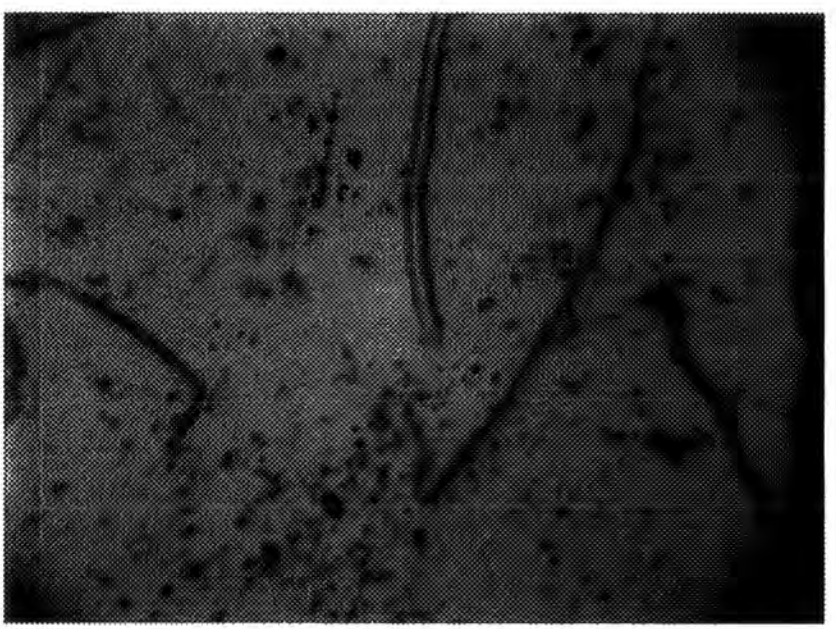

Figure 5.1.2. Infrared microscope image of a heavily pitted and scratched sample.

Scale : ←→
10 μm

At this point the homogeneity of the crystals can be examined using infra-red microscopy. This is done using an optical microscope operating in transmission mode, with an infra-red edge filter inserted on the optical path between the light source and the sample. In this case an 850 nm filter was used. The image is detected using an ordinary camcorder as the CCD in such devices can detect light in the infra-red region up to about 1μm. A typical image obtained in this way is shown in figure 5.1.1. The uniformity of these samples is rather good. The visible features consist mostly of light surface scratches and etch pits. Figure 5.1.2 shows an image of the surface of a crystal which is heavily pitted and shows surface scratches, which are almost invisible on inspection of the sample with the naked eye. Such samples are clearly unsuitable for performing electrical transport measurements. Only uniform looking samples are contacted and experimented on.

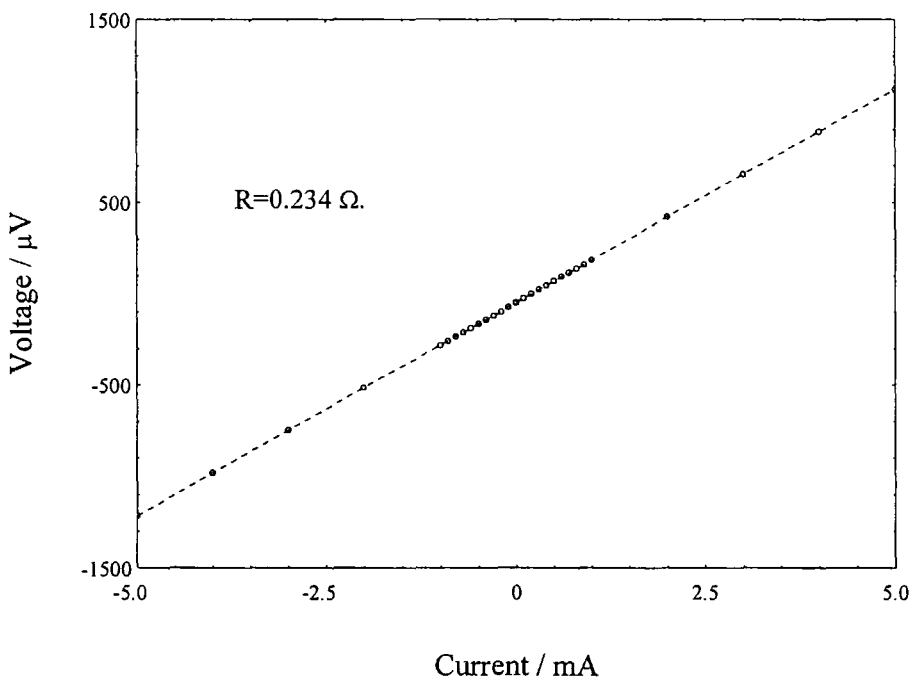

Figure 5.1.3. A typical V - I curve for In contacts on CdMnTe. Ohmic behaviour is observed.

Ohmic contacts are produced by indium soldering gold wires to the surface of the sample. 99.9999% pure indium is cleaned and the oxide layer scraped off the surface before use. The contacts are deposited in the Van der Pauw configuration as described in section 5.2. The Ohmic nature of the contacts is always checked by varying the sensing current and measuring the V-I relationship for the sample. A typical characteristic is shown in figure 5.1.3., where a very linear appearance is observed. Contact resistances vary depending on the conductivity of the sample. For samples with relatively low resistivity in the 0.05 to 0.5 Ωcm range the contact resistances are usually of the order of (or less than) 1 Ω. Very insulating samples, such as those with Mn concentrations of ~ 15 % or greater, are more difficult to contact to, as the contacts tend to be non-Ohmic. This, along with the problems involved with measuring very large resistances make transport measurements very difficult in this regime.

5.1.2. Compositional Analysis.

The manganese concentration of many of the samples of $Cd_{1-x}Mn_xTe$:In was determined from EDAX (Energy Dispersive Analysis Of X-Rays) measurements, otherwise known as electron microprobe analysis. These measurements were done in a Cambridge Stereoscan S 600 scanning electron microscope with an EG&G EDAX head fitted. The EDAX data was collected and analysed using an AN 2001 analyser. The technique relies on the fact that when a material is bombarded with a beam of electrons, X-rays are emitted with an energy characteristic of the atom from which they were emitted. The emitted X-rays are then spectrally analysed to allow determination of the elements present in the sample.

A typical EDAX spectrum of $Cd_{1-x}Mn_xTe$:In is shown in figure 5.1.4. The characteristic emission lines of Cd, Mn, and Te are labelled. Quantitative analysis is most often carried out by comparing the peak intensity of characteristic X-ray lines from

Figure 5.1.4. Typical EDAX spectrum from CdMnTe:In

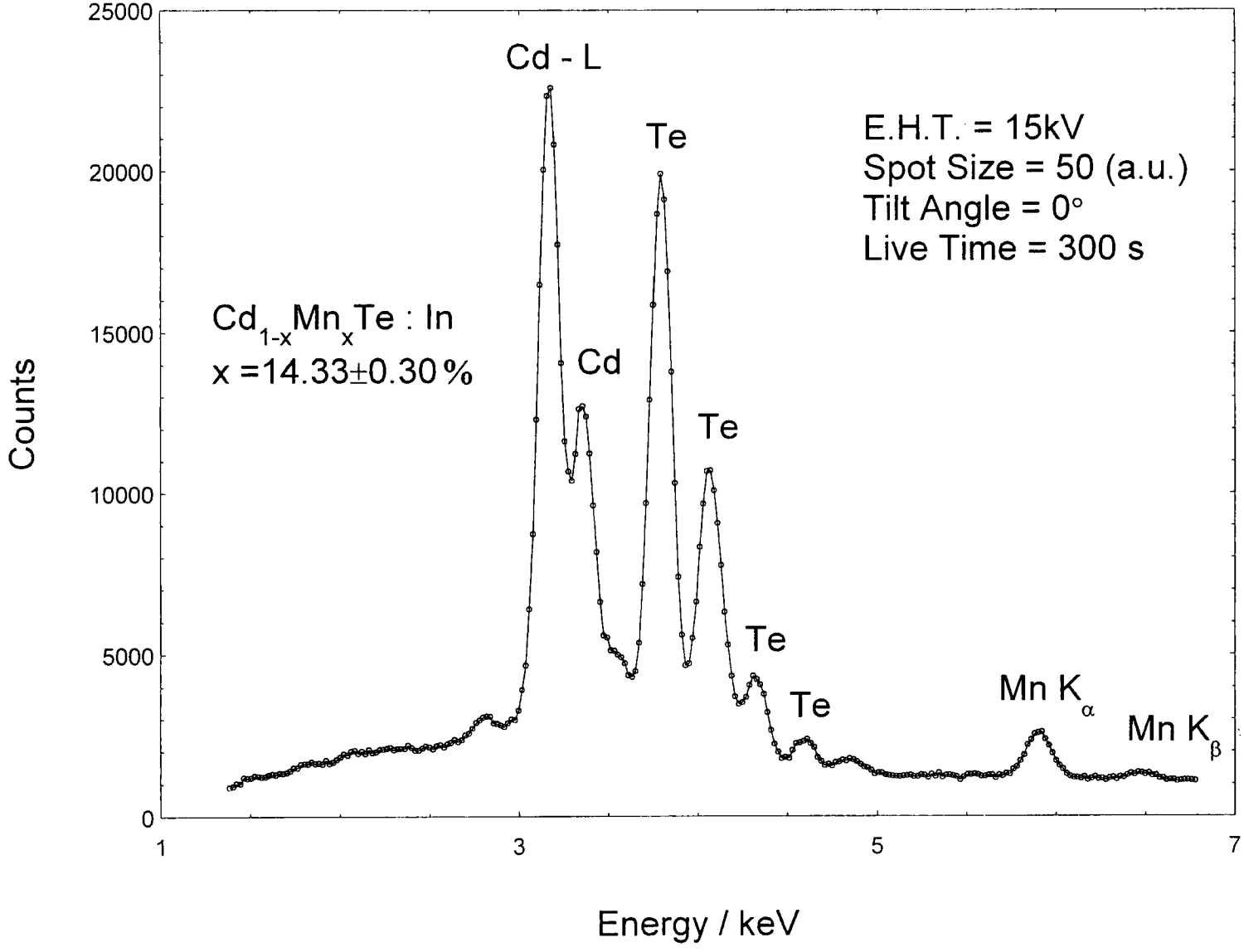

the sample with those of the pure element as a reference standard. Provided that all of the conditions are then maintained, then the concentration of that particular element in the sample can be determined. In practice this is an over simplified picture, with many corrections needing to be taken into account. For example, X-ray absorption and fluorescence are important, as an X-ray generated at a certain point within the material can interact with the atoms in the material and be absorbed for instance. Some of these corrections can be taken into account using the ZAF method [2] which corrects for effects due to the Z number of the sample, X-ray absorption and X-ray flourescence. For the case of CdMnTe the situation is simplified by the availability of six samples of known concentration. These samples' composition had been determined by either mass spectrometry or electron microprobe analysis as described above using the relevant corrections and reference standards.

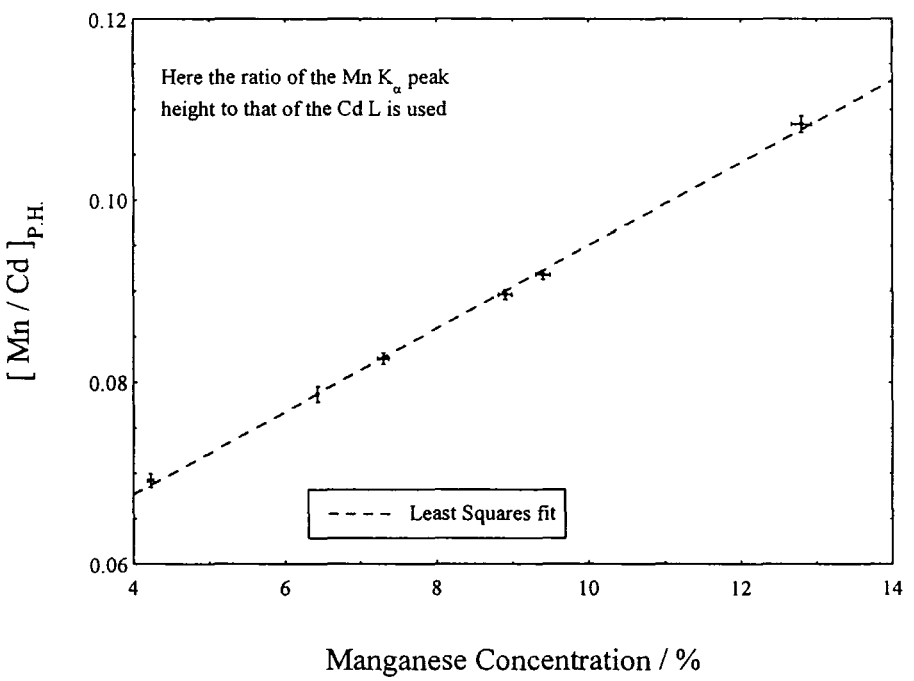

Figure 5.1.5. The calibration curve used to determine the Mn composition of many of the samples of $Cd_{1-x}Mn_xTe$:In.

A calibration curve was produced by taking EDAX spectra of these samples and plotting the ratio of the heights of the Mn to Cd peaks against known Mn concentration, x. Throughout this series of measurements the same conditions were maintained i.e. the accelerating E.H.T. voltage, the electron beam spot size, angle of tilt etc were kept constant. This calibration curve is shown in figure 5.1.5. This shows excellent linearity over the whole concentration range investigated. Using a least squares fit to this data enables the Mn concentration of any sample of $Cd_{1-x}Mn_xTe$:In to be determined (provided that it has a concentration in the range $4.22\% \leq x \leq 12.8\%$.) from the expression,

$$x(\%) = \frac{\left(\frac{I_{Mn}}{I_{Cd}}\right) - 0.0494}{0.00456} \qquad (5.1.1),$$

where I_{Mn} and I_{Cd} are the heights of the Mn K-α and the Cd-L peaks respectively. Using this method the error on x is usually about 0.3% Mn. This arises due to random counting errors in the EDAX spectra, but can be minimised by using long counting times.

5.2. Electrical Characterisation and PPC Equipment.

In order to perform electrical characterisation and persistent photoconductivity measurements a piece of equipment was constructed to investigate transport and magnetotransport properties in a variable temperature environment. The experimental arrangement is shown in figure 5.2.1. The equipment is capable of measuring resistivity, Hall effect and magnetoresistance at temperatures from 400 K down to 3.6 K, in magnetic fields of up to 0.75 T, as a function of illumination level.

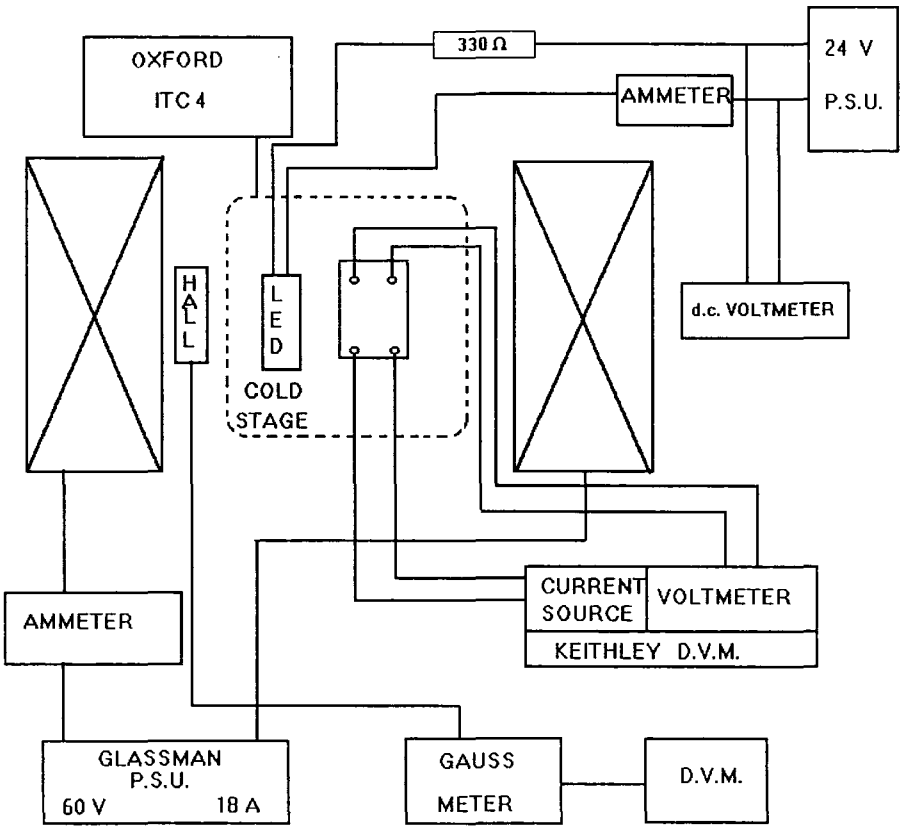

Figure 5.2.1. The system used for electrical characterisation and PPC measurements.

The variable temperature environment is provided by an Oxford Instruments CF1200 continuous flow cryostat as shown in figure 5.2.2. The principle of operation of the system is as follows. The cryostat is continuously connected to a transport dewar of liquid helium via a gas shielded transfer siphon which is evacuated to $< 1x10^{-6}$ torr. A helium diaphragm pump is used to induce a flow of liquid from the dewar, through the siphon and into the cryostat. The sample space of the cryostat is thermally shielded from the ambient environment with a high vacuum space and a polished copper radiation shield. The liquid flows down tubes within the cryostat to a copper heat exchanger which cools the sample space. This flow of liquid can be controlled by needle valves on the transfer tube and flow meter. A heater and a AuFe(0.03%) - chromel thermocouple are mounted on the heat exchanger block to control its temperature. The AuFe - chromel

thermocouple type is chosen due to its small magnetic field dependent errors. For example the error due to a field of 2.5T at 4.2 K is only $\Delta T / T = 3\%$ and falls to 0.1 % at 100 K [3]. The sample is mounted on a probe as shown in figure 5.2.3. The probe makes

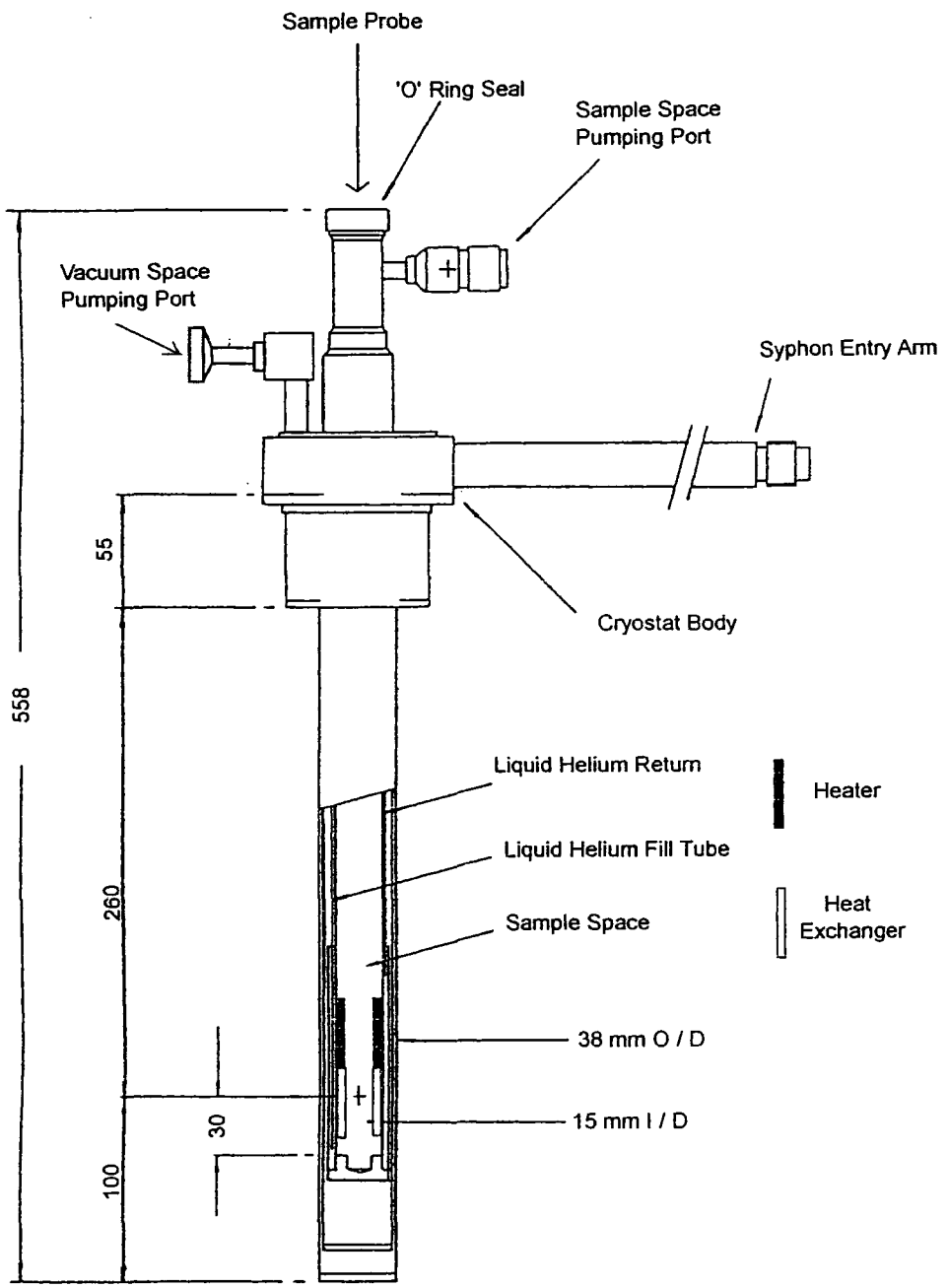

Figure 5.2.2. The Oxford Instruments CF 1200 continuous flow cryostat which provides a variable temperature environment from 3.6 K up to 360 K.

good thermal contact with the heat exchanger via a copper collar which fits flush inside a steel tube with a copper rim, as shown in the figure. The sample space is evacuated and then filled with dry helium exchange gas to further promote heat transfer between the sample and the heat exchanger. The actual sample temperature is measured with a RhFe resistance sensor housed within the copper sample holder on the bottom of the probe. Having the sensor inside the same block of copper as the sample is mounted on, eliminates errors of measurement due to the fact that the sample and temperature sensor could be at slightly different temperatures. In addition to this, the RhFe type of resistance thermometer is far more accurate and reproducible than the thermocouple. The temperature of the heat exchanger, and hence the sample, can be reduced below 4.22 K by pumping on the liquid collected in the heat exchanger with the diaphragm pump, while the needle valve to the transport dewar is closed. In this way a base temperature of 3.6 K can be achieved quite easily.

An Oxford Instruments ITC 4 intelligent temperature controller is used to control the temperature of the heat exchanger using the 40 Ω heater and AuFe - chromel thermocouple which are supplied ready calibrated with the instrument. This method of control, combined with the regulation of the flow rate via the transfer tube and flow meter needle valves, allows the temperature of the heat exchanger to be stabilised to within 100mK over the whole temperature range. The ITC is also used to monitor the temperature of the sample with the RhFe resistance sensor. A sensing current of 1mA is used with this thermometer which results in no visible heating effects even at the base temperature. This sensor was calibrated in liquid helium at atmospheric pressure, and at room temperature. This method of calibration results in an error on the sample temperature measurement of 0.5 K at 77.4 K, which was considered suitable for this application. However, at low temperatures the error on the temperature measurement made by the RhFe sensor is far smaller than this, as it has been calibrated at 4.22 K. In fact at 4.22 K the accuracy of the thermometry, even with drifts in stability taken into account, is ± 20 mK, in zero magnetic field. The magnetic field dependent errors for

RhFe result in a temperature error ΔT / T of 11% at 2.5 T at 4.2 K [3]. The fields produced by the magnet in this experimental arrangement are $\leq$ 0.75 T, and in fact no field dependent error was observed to 100 mK resolution.

The probe which is inserted into the cryostat (as shown in figure 5.2.3.) is constructed from thin walled stainless steel tubing in order to reduce thermal conduction to the cold end. The copper sample holder is connected via a section of nylon rod used to isolate the sample holder from the rest of the probe to encourage fast equilibration of the copper holder. Three copper baffles are attached along the probe to shield the cold end from room temperature radiation incident from the top of the probe. The wires required for the electrical measurements (i.e. the temperature sensor resistance, sample resistance and LED connections) are insulated constantan, again to reduce the heat leak to the cold region, with the exception of those used to measure the sample resistance. Here copper was chosen as the relatively high resistivity of the constantan wires (44 $\mu\Omega$ cm compared to 1.7 $\mu\Omega$ cm for copper [4]) can lead to errors in the measurement of the resistance of the sample if all four wires are not of exactly the same resistance. This is particularly important if the sample resistance is small - as for some of the samples in this study (some are ~ 1Ω at 4.2 K). All of the wires were twisted into pairs to reduce the level of electrical noise. The wires were wound around the stainless steel tube and heat sunk with high thermal conductivity varnish at regular intervals. They were heat sunk again at the copper block with the exception of the two wires used to power the LED. These were left in poor thermal contact with the sample holder to avoid heating the sample when the relatively large currents (up to 10 mA) are flowing in the diode circuit when the sample is being illuminated. Electrical connections are made at the top of the probe via a vacuum sealed connector. External to the cryostat the electrical cable is shielded and earthed to the same point to minimise the noise level.

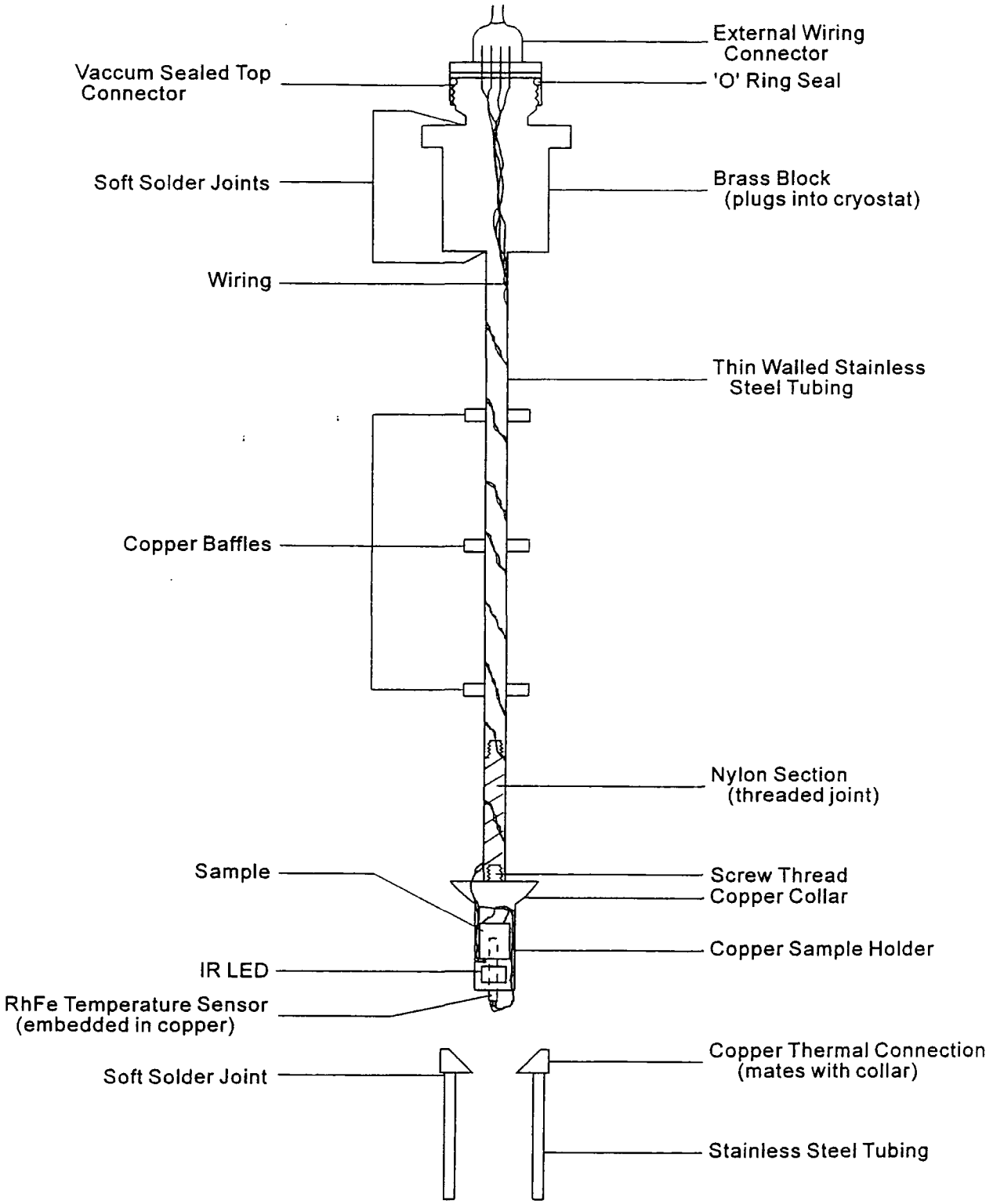

Figure 5.2.3. Continuous flow cryostat probe for electrical transport measurements.

The sample resistance and Hall voltage are then measured using the four probe method with a Keithley digital voltmeter. This enables resistances in the range from 1mΩ to 300 MΩ to be measured. Regular checks are made to ensure that no sample self heating occurs due to the sensing current being too large.

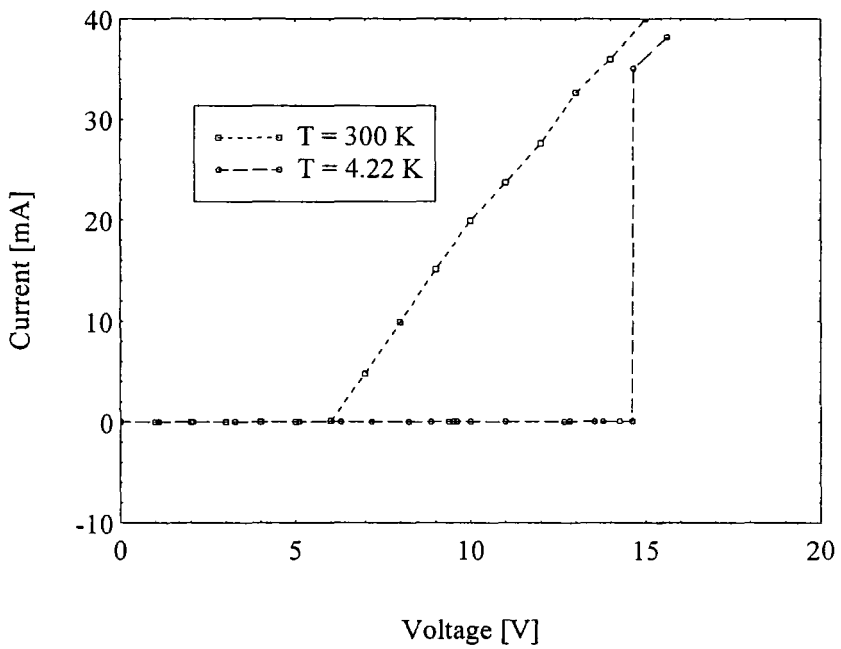

Figure 5.2.4. The V-I characteristics of the Kodenshi LEDs at 300 K and 4.2 K.

The infra-red LED is energised using the circuit shown in figure 5.2.1. A 330 Ω resistor is wired in series with the LED so that the current flowing in the LED can be controlled easily by varying the voltage across the diode. Without the resistor, fine control of the LED current was found to be impossible. A Farnell 24 V d.c. power supply is used as the voltage source, with the LED current being measured by a Keithley ammeter. Kodenshi GaAs LEDs [4] were found to be capable of operation at temperatures of 4.2 K, albeit with a rather different V - I characteristic. This V - I characteristic is shown in figure 5.2.4. The emission spectrum is shown in figure 5.2.5., where it can be seen that the emission peaks at a wavelength of 933 nm.

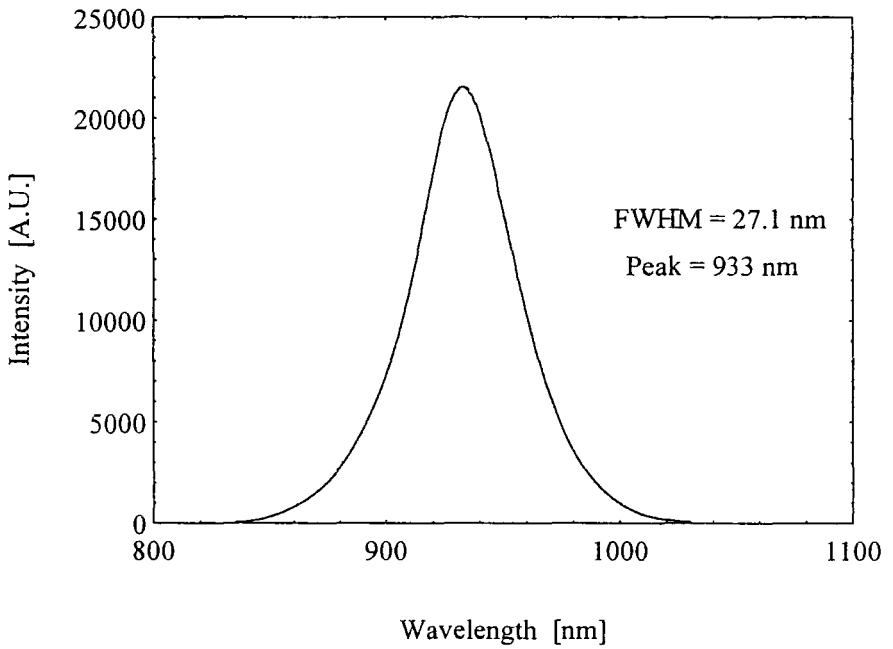

Figure 5.2.5. The emission spectrum for the infra-red LED used at 300 K.

The cryostat is mounted between the pole pieces of a Newport electromagnet, such that the sample is in the centre of the field and is in a homogeneous field region. The magnet is powered with a Glassman supply rated at 60 V, 18 A. The magnetic field measurement is made using an F.W. Bell Hall effect gaussmeter and probe. The probe is mounted in close proximity to the sample with the homogeneity of the field ensuring that the sample and probe experience the same size field. The gaussmeter is connected to a digital voltmeter to read the Hall voltage.

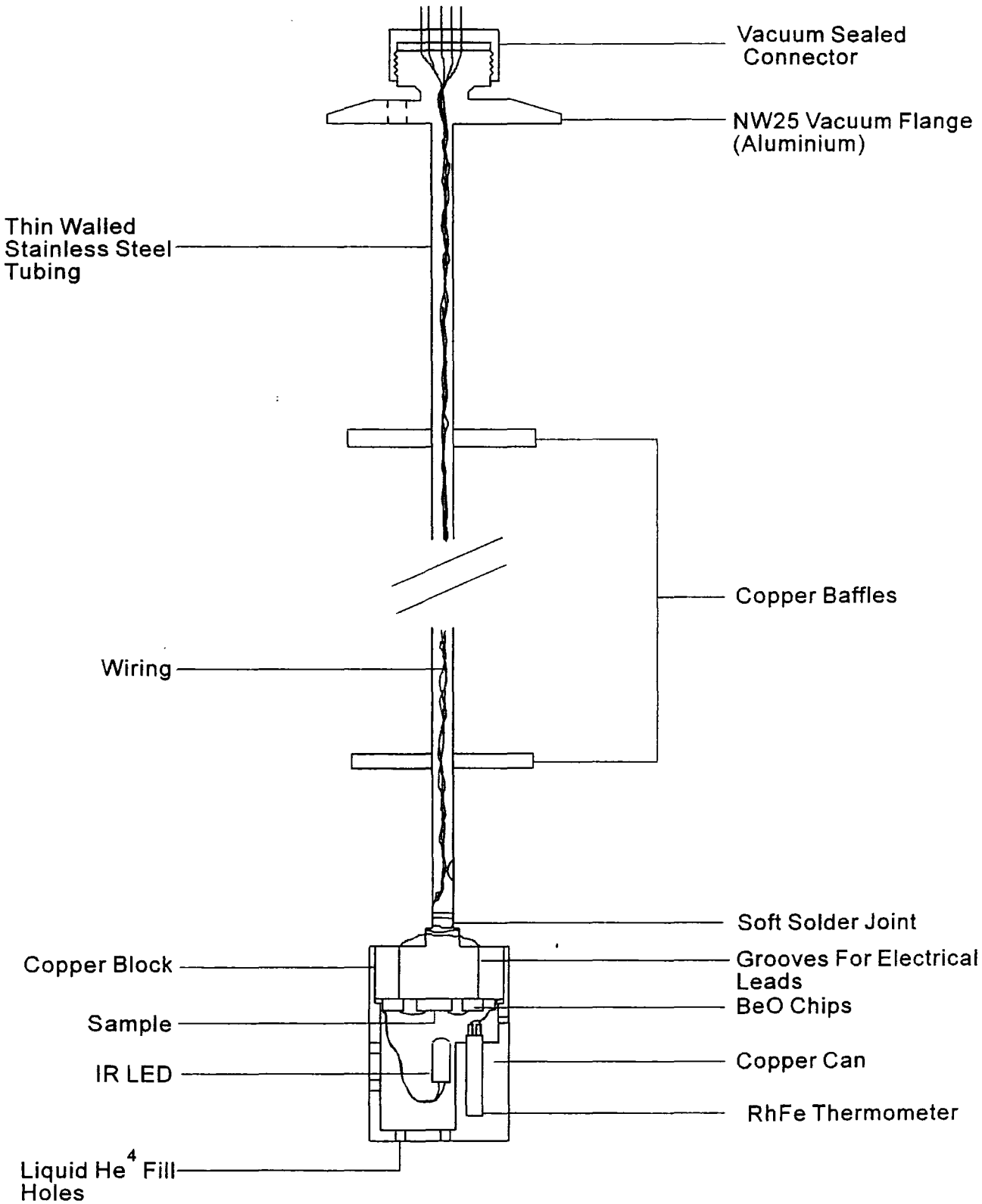

Figure 5.2.6. Direct immersion probe for transport measurements to 4.2 K.

In addition to the system described in the previous section another probe was constructed to measure photoconductivity. This probe was designed to be immersed in a 120 litre transport dewar of liquid helium. This allows measurements to be made extremely quickly and with relative ease. The system is shown in figure 5.2.6. The construction is rather simple : an NW 16 vacuum flange is welded to a thin walled stainless steel tube which has five copper baffles attached to it at regular intervals down the probe. The bottom consists of a copper block upon which the sample and LED are mounted. A copper can, which is perforated with helium fill holes, is placed over the sample block and held tight with a grub screw. A RhFe temperature sensor slides flush inside a hole drilled in the can, ensuring a good thermal contact between the sample and temperature sensor. The wires are run down the inside of the stainless steel tube from a vacuum sealed connector at the top, and are thermally anchored to the copper at the bottom of the probe, using high thermal conductivity varnish. The four wires for the sample resistance measurement are heat sunk to the sample block using beryllium oxide chips affixed with Stycast 2850 FT epoxy.

The conductivity measurements are made as a function of temperature by slowly raising the probe above the liquid helium level at regular intervals, and allowing the whole sample block to warm up rather slowly at around 1K / min. This type of dynamic technique is less accurate than using a cryostat as described in the section above, but far quicker, hence making it ideal for selecting the best samples to investigate in more detail.

For all of the electrical measurements the Van der Pauw [5] technique was employed. A schematic diagram of the arrangement is shown in figure 5.2.7. This is a four contact technique whereby the current is injected via two of the contacts, and the voltage developed is measured between two opposite contacts. For this technique to be applicable the sample must be singly connected and of uniform thickness, with the contacts placed on the perimeter of the sample. The resistivity is then given by,

$$\rho = \frac{\pi t}{\ln 2} \frac{(R_{AB,CD} + R_{AC,BD})}{2} f\left(\frac{R_{AB,CD}}{R_{AC,BD}}\right) \tag{5.2.1}$$

where $R_{AB,CD}$ and $R_{AC,BD}$ are the resistances measured by injecting current through contacts A and B and measuring the voltage across C and D, and injecting current through A and C and measuring the voltage across B and D, respectively. The function f is equal to 1 when $R_{AB,CD} / R_{AC,BD} = 1$, and falls to 0.9 when $R_{AB,CD} / R_{AC,BD} = 3$ [5]. All of the samples in this study have values of $R_{AB,CD} / R_{AC,BD}$ close to 1.0, so the factor f is neglected. The Hall effect is measured by injecting a current through contacts A and D and measuring the voltage developed across B and C. The current is then injected through B and C and the voltage measured across A and D. In addition to this, the direction of the current is reversed also. This current reversal process is always carried out to ensure that spurious thermal voltages are accounted for [6]. These can occur if the sample has a small thermal gradient across it, but reversing the current direction and averaging the two values compensates for this. The average of these four values is taken to be the Hall voltage, V_H. The apparent Hall carrier concentration, n, can then be calculated from,

$$V_H = \frac{BI}{net} \tag{5.2.2}$$

where B is the magnetic field applied perpendicular to the sample, I is the sensing current, e is the electronic charge and t is the thickness of the sample [6]. An actual measurement of n is made by sweeping the applied field B, through both negative and positive values, and measuring all four voltage configurations for each field point. In general, at zero field the Hall voltage is actually finite due to slight contact misalignment which means that there is a potential drop between the two contacts due to the resistance of the sample. This can cause problems with measuring the Hall voltage at low temperatures, where this offset can be rather large due to the increasing sample resistance. This adds a further complication as the magnetoresistance of the samples can be rather large (50 % at 4.2 K is not unusual). In fact, these problems place a lower limit on the temperature at which

the Hall carrier concentration can be measured, this limit being lower for more conductive samples, where the offset voltage is much smaller.

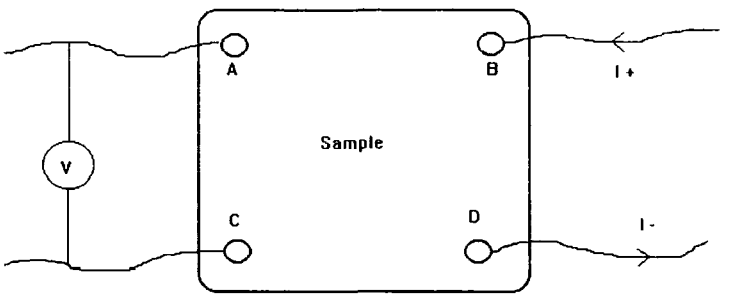

Figure 5.2.7. The Van der Pauw technique. The configuration $R_{AC,BD}$ is shown as an example of the notation used here.

5.3. Low Temperature Transport Measurements.

The aim of this thesis is to discuss the electronic transport properties of $Cd_{1-x}Mn_xTe$:In as probed by PPC. The central theme however, is the use of this PPC effect to fine tune the MIT, as discussed in earlier sections. This work requires that we perform our transport measurements at very low temperatures in order that we are able to observe the behavior of the conductivity in the zero temperature limit. For this reason a sorption pumped ^{3}He refrigeration system has been used to perform transport measurements down to 300 mK. This section outlines the experimental arrangements used to perform these measurements.

Section 5.3.1 describes the operation of the ^{3}He refrigerator used for these very low temperature measurements. Section 5.3.2 gives a very brief description of the helium dewar (which houses a 13 T superconducting solenoid) in which some of the experiments were performed. Finally, section 5.3.3 describes the measurement details.

5.3.1. Heliox ^{3}He Probe.

This system is an Oxford Instruments sorption pumped ^{3}He probe. The principle of operation is simple : a charcoal sorption pump is used to reduce the pressure above a bath of liquid ^{3}He, hence lowering the temperature to approximately 300mK. The probe is shown in figure 5.3.1. The design of the probe will not be discussed in detail as it is a commercial system.

The system consists of a sealed charge of ^{3}He gas attached via a central tube to the ^{3}He pot at the bottom of the probe. A 1K pot is attached via a large diameter tube to a vacuum flange at the top of the probe. ^{4}He is supplied to the 1K pot from the main bath through a vacuum insulated pick up tube and needle valve. The 1K pot is filled and pumped on with a large capacity (40 m^3h^{-1}) rotary pump. The sorption pump is placed in the line connecting the charge of ^{3}He with the ^{3}He pot. In order to control the pumping rate of the sorption pump, its temperature is controlled with a heat exchanger connected to the main bath via another vacuum insulated pickup tube and needle valve. Temperature control is obtained by varying the heater power supplied to the heat exchanger, along with control of the ^{4}He flow rate using the needle valve. A helium diaphragm pump is used to flow the ^{4}He around the sorb heat exchanger. A brass can is placed over the lower end of the probe forming a greased cone vacuum seal. This forms the inner vacuum can (IVC).

Before cooling the probe, the sample is mounted on the base of the ^{3}He pot and the IVC is filled with recovery grade ^{4}He. The insert is then cooled in a bath of ^{4}He. In our case the probe is placed inside a superconducting solenoid, or inside a liquid helium transport dewar. Once the 1K pot has been cooled to below 10K, the needle valve to the main bath is opened and the pot pumped on. The temperature of the 1K pot can be reduced to about 1.5 K in this way. At this point the needle valve is then closed and the volume of ^{4}He left in the pot is pumped to 1.2 K. At this stage the ^{3}He will be condensing into the ^{3}He pot (^{3}He boils at 3.19 K at atmospheric pressure [7]). The temperature of the sorb is then lowered to 4.5 K by flowing liquid from the main bath through the heat

exchanger. This maximizes the pumping rate of the sorb and the temperature of the ^{3}He pot falls to the base temperature of 285 mK, the hold time being greater than 30 hours. Obviously added heat load will result in a higher base temperature, in fact a heat load of 250 μW raises the base temperature to 384 mK.

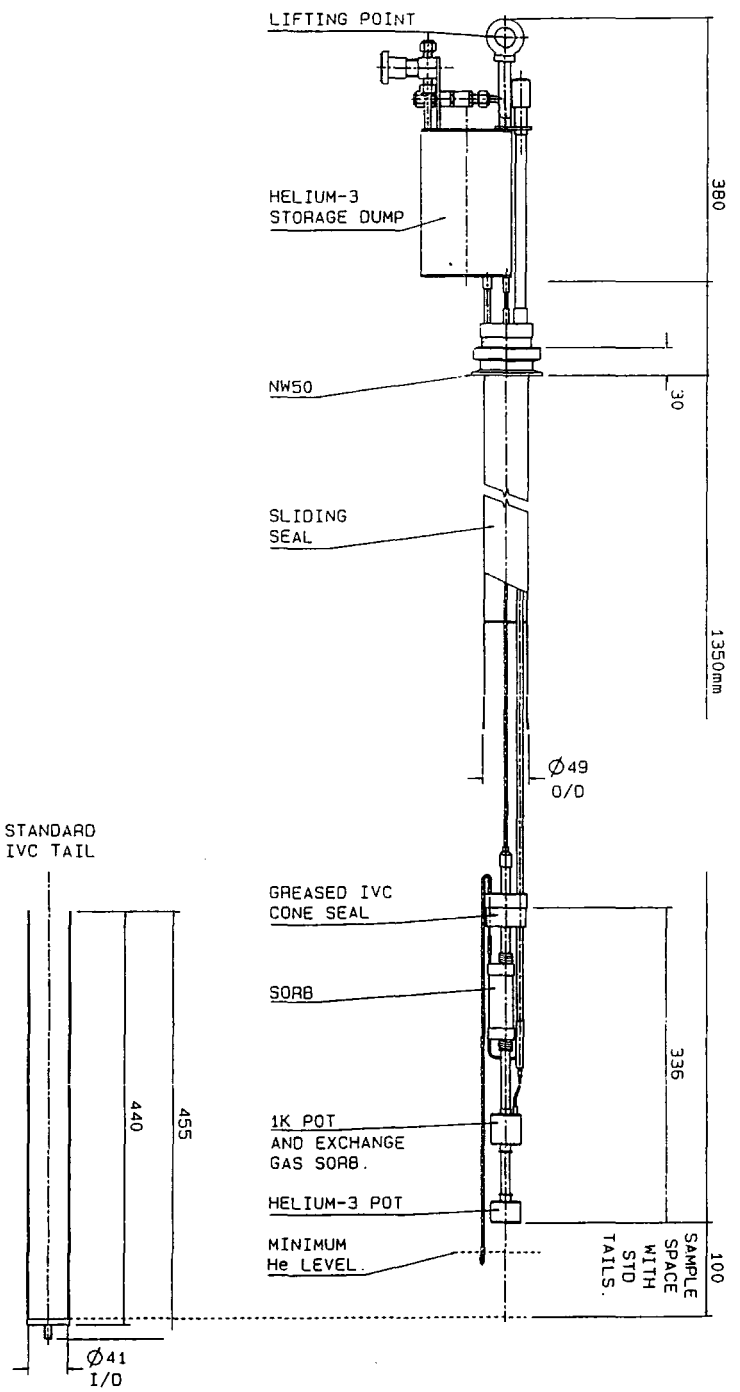

Figure 5.3.1. Schematic of the Oxford Instruments sorption pumped ^{3}He insert.

Below 1.2 K the temperature is controlled by varying the temperature of the sorb, and hence its pumping power. This method of control provides a temperature stability of better than 1 mK. Figure 5.3.2 shows a typical dependence of the ^{3}He pot temperature on the sorb heat exchanger temperature. As can be seen from the figure, below about 10 K the sorb pumps at a maximum rate and the temperature of the ^{3}He pot is independent of the sorb temperature. Above 10K a rather rapid dependence is seen until the ^{3}He pot reaches the temperature of the 1K pot. Above 1.2 K (the temperature of the 1 K pot) temperature control is achieved by direct heating of the ^{3}He pot with a 200 Ω wire wound heater, while the sorb temperature is coarsely controlled at about 45 K. As an example, the temperature can be controlled to better than 100 mK at 10 K using this method.

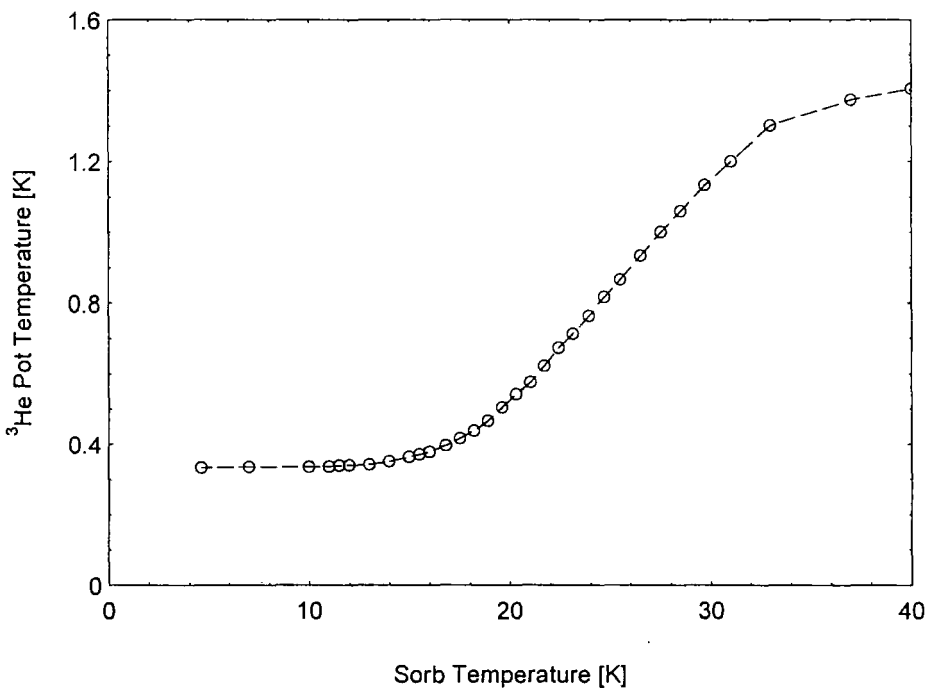

Figure 5.3.2. The dependence of the ^{3}He pot temperature on the sorb temperature for the Heliox ^{3}He insert.

The thermometry used on the insert will now be described. All of the thermometers are shown in table 5.3.1. along with their location, accuracy and usable temperature range. For higher temperature use the insert is equipped with a pre-calibrated RhFe resistance sensor, with a usable range from 1.4K up to 300K. At 1.4 K the sensor is accurate to ± 16 mK, which increases to ± 18 mK at 10 K. At lower temperatures the temperature of the ^{3}He pot is monitored using a "470Ω" Speer resistance sensor. This sensor is used from 10 K down to base temperature with an estimated accuracy of 2 mK at 335 mK. An identical Speer resistor is fitted to the 1K pot to allow the temperature of the pot to be monitored during cool down. The temperature of the sorb heat exchanger is measured using a '270 Ω' Allen-Bradley resistor. This sensor is not intended to be highly accurate - it is simply used to monitor and control the temperature of the sorb rather coarsely. The temperature of the ^{3}He pot and sample is then measured accurately. All of these thermometers are used in conjunction with an Oxford Instruments ITC 503 intelligent temperature controller, to read, and where appropriate, control the temperature. For each of the thermometers the sensing current is adjusted so that no errors due to self heating are encountered.

Sensor Type	Position	Usable Range	Accuracy
Allen - Bradley	Sorb heat exchanger	250 K → 4.2 K	~ ± 2 K at 200 K ~ ± 0.5 K at 10 K
Speer A	1 K pot	10 K → 1.2 K	~ ± 100mK at 1.2K
Speer B	^{3}He pot	10 K → 250 mK	± 2 mK at 335 mK
RhFe	^{3}He pot	300 K → 1.4 K	± 16 mK at 1.4 K ± 18 mK at 10 K

Table 5.3.1. The thermometry on the ^{3}He insert : position, range and accuracy.

The ^{3}He insert is usually used in the temperature range from 0.3K up to 10K. The insert can be used at temperatures well above this, but in our case it is far more economical to use another system at higher temperatures (see section 5.2).

5.3.2. Superconducting Magnet System.

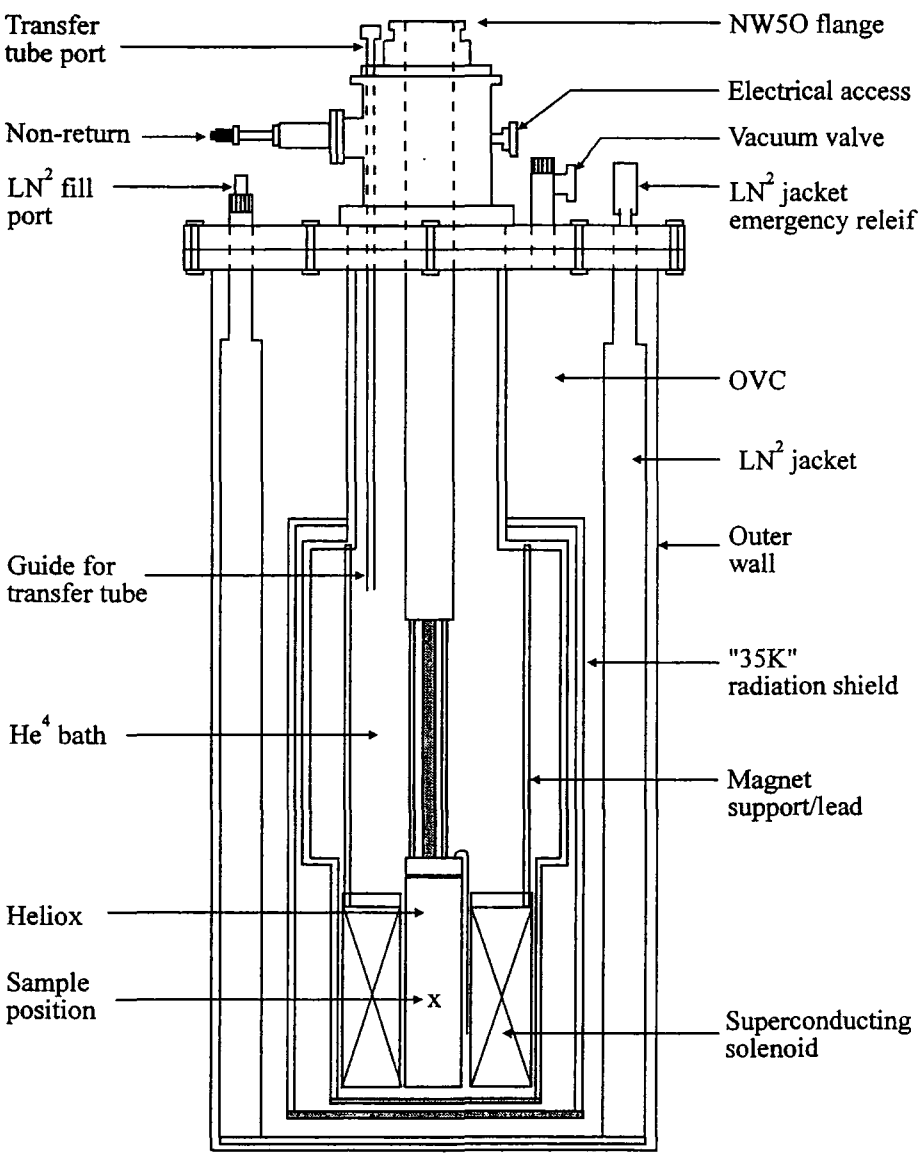

Figure 5.3.3. Schematic of the superconducting magnet and dewar system.

The magnet system comprises of a superconducting solenoid housed within a low loss liquid helium dewar. The magnet system is a commercial Thor Cryogenics 13 T solenoid. A schematic of the dewar and magnet is shown in figure 5.3.3. As can be seen from the figure the magnet is suspended within the liquid helium reservoir which is surrounded by both a gas cooled 35 K radiation shield and a liquid nitrogen reservoir. Superinsulation is used to further shield the helium space from incident radiation. The solenoid is constructed from NbTi multifilamentary wire, with the inner high field windings being Nb_3Sn. All of these windings are encapsulated in epoxy resin to prevent wire movement and premature quenching. A series of high power resistors are used as protection in the event of a quench.

This system was used as a helium reservoir for measurements with the ^3He sorption pumped insert as well as the direct immersion probe detailed in section 5.2.

5.3.3 Experimental Arrangement.

The previous two sections have described briefly the He^3 insert and the superconducting magnet and dewar used in these experiments. This section will deal with the measurement system used, the sample thermometry, sample mounting etc.

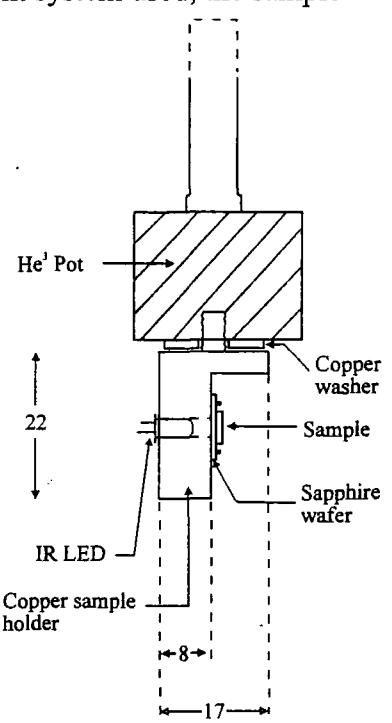

Figure 5.3.4. Typical sample holder. This arrangement screws directly into the ^3He pot.

Samples are first mounted on a 10 mm x 10 mm sapphire wafer of thickness 0.5 mm with GE varnish. Sapphire is used because of its excellent thermal conductivity at low temperatures, along with its very large electrical resistivity. 50 μm gold wires are used to connect the sample contacts with 4 pads of indium mounted next to the sample on the sapphire wafers. The system wiring is then simply soldered onto these indium pads, making the changing of samples very simple. The sapphire wafer is mounted on a copper sample holder, again with a small amount of GE varnish. A typical sample holder is shown in figure 5.3.4. The electrical connections to the sample holder are made via a 'plug-in' connector just below the 1 K pot, allowing one to change sample holders with ease. The arrangement shown in figure 5.3.4 was used for zero magnetic field measurements and was screwed directly into the He^3 pot to ensure good thermal contact. In this arrangement the Speer resistor mounted on the ^3He pot itself was used to measure the sample temperature. Excitation voltages as low as 100 μV are used to ensure that errors due to self heating of the resistance sensor are negligible.

The actual sample resistance is measured using a variable d.c. current source and voltmeter. The current is variable from 100 nA up to 1 mA with the uncertainty on these currents being 800 ppm and 400 ppm respectively. The voltage is then measured using a Racal Dana model 5900 voltmeter with a sensitivity of 1 μV. As an example, for a sample with a resistance of 1Ω at 300 mK, the resistance can be measured to 10 mΩ resolution with a power dissipation of 10^{-10} W. In order to reduce the noise level on the measurement to a minimum, all of the wiring internal to the cryostat is in the form of twisted pairs, whereas external to the cryostat the signal is carried by earth shielded coaxial cable. This results in a noise level which is typically below 100 nV. At the base temperature, the V-I characteristic is checked for non-ohmic effects which could be due to sample self heating. In the event of any non-linearity being observed the excitation current is reduced accordingly.

When the sample resistance is being measured the direction of the current flow is always reversed and both voltages recorded to ensure that spurious thermal voltages do not affect the measured value. This is in addition to the usual checks for inherent anisotropy in the sample resistance which are carried out periodically when measuring the sample resistance as a function of temperature. Also, adequate time is allowed for temperature equilibration of the sample both after the initial cool down to base temperature and after every temperature set point is reached.

It should be noted that in all cases great care is taken with the wiring in the region of the ^{3}He pot to ensure that wires are thermally anchored to prevent a source of heat leak to the sample. The wires are wrapped around the ^{3}He pot itself and GE varnished in place to ensure good thermal contact. This process is repeated at the sample holder before the leads are eventually connected to the pads on the sapphire wafer. The wiring is also heat sunk at the 1 K pot before the wires are run down the insert to prevent a large heat load on the pot.

The LED's used in these experiments are of the same type mentioned in section 5.2. These were found to operate satisfactorily at 300 mK, although the V-I characteristic is such that voltages of up to 20 V need to be applied to sustain a suitable current flow. When illumination is performed at the base temperature a pulse technique is used to avoid warming the entire sample holder and ^{3}He pot. A simple circuit based on a 555 timer chip was used to produce a device which applies a suitable variable pulsed voltage to the LED with a variable mark to space ratio.

Chapter 5 - References.

1. P. Becla. Deptartment of Materials Science and Engineering, Massachusetts Institute of Technology, Cambridge, MA 02139.

2. V.D. Scott, G. Love and S.J.B. Reed. *Quantitative Electron Probe Microanalysis* (Ellis Horwood, 1995). p40.

3. H.H. sample and L.G. Rubin. Cryogenics. Nov. 1997. 597.

4. *CRC Handbook of Chemistry and Physics, 73rd edition.* ed. D.R. Lide.(CRC Press, 1992-93). p. 12-147.

5. L.J. van der Pauw. Philips Res. Reports. **13** 334 (1958).

6. G.E. Stillman, S.S. Bose, M.H. Kim, B. Lee and T.S. Low. *Characterization and Properties of Semiconductors* in *Handbook on Semiconductors* ed T.S. Moss (Elsevier, 1994). p790.

7. O.V. Lounasama. *Experimental Principles and Methods Below 1 K.* (Academic Press, 1974).

6. Electrical Characterization and PPC.

This chapter presents the results of extensive electrical measurements on two sets of samples of $Cd_{1-x}Mn_xTe$:In. All of the samples studied in this thesis were grown by P. Becla [1]. Set A is a large set of samples which have been used to determine the effect of composition on the PPC in these materials. Several samples in this set were identified as being suitable for studying the MIT and the WLR. These are discussed in full in chapter 7. The second set of samples have been studied in detail due to the fact that they exhibit several interesting phenomena. In particular, several samples display high temperature PPC, which we believe is due to the presence of multiple DX centres. In addition to this, some samples show an anomalous magnetoresistance at around 100 K, which we believe is linked with the formation of BMPs under certain conditions.

6.1. Sample Set A.

The samples discussed in this section are detailed in table 6.1.1, where the nominal composition from the growth data, the composition determined by EDAX and the annealing temperatures are shown.

Sample	Nominal Composition	EDAX Composition	Annealing Temperature / °C
A1	5 %	4.7 ± 0.2 %	800
A2	5 %	6.1 ± 0.2 %	800
A3	7.5 %	6.28 ± 0.10 %	600
A4	7.5 %	6.43 ± 0.01 %*	600
A5	10 %	8.1 ± 0.2 %	800
A6	15 %	14.8 ± 0.3 %	600
A7	20 %	16.6 ± 0.3 %	800

Table 6.1.1. Details of sample set A. * denotes determination by mass spectroscopy.

The measurements made on these samples include : resistivity from 360 K down to 3.6 K, Hall effect/Hall mobility from 360 K down to approximately 10 K, magnetoresistance from 30 K down to 3.6 K, along with the resistivity and mobility as a function of carrier concentration at fixed temperatures. This data is summarised in table 6.1.2.

6.1.1. Resistivity and Hall Effect Measurements.

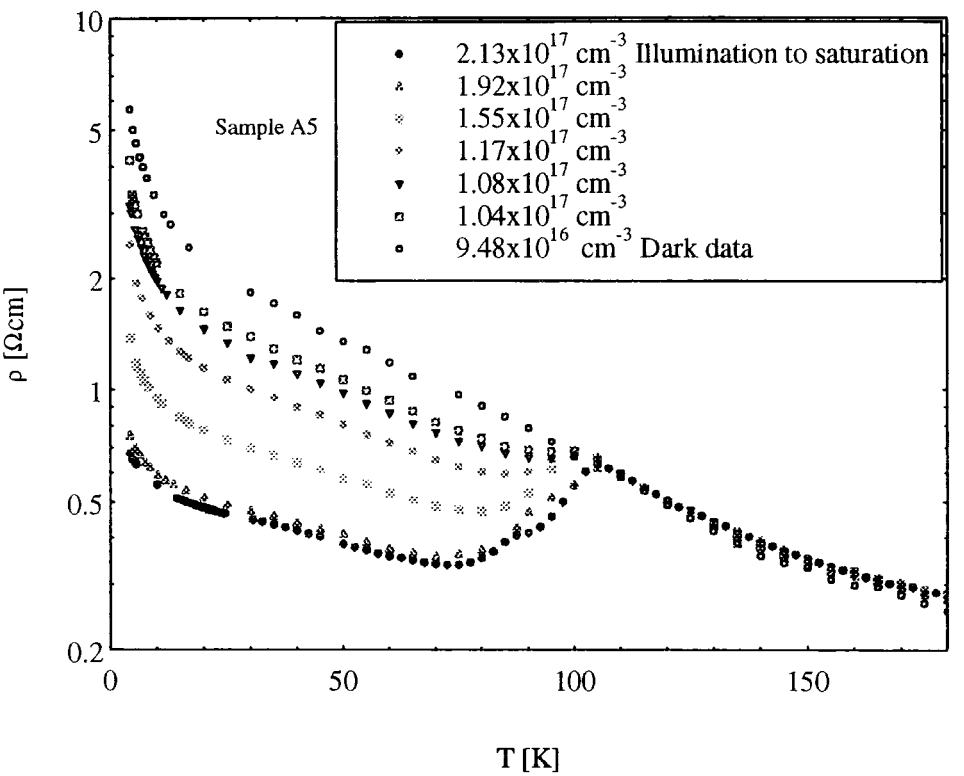

Figure 6.1.1. Temperature dependence of the resistivity of sample A5.

The PPC effect is clearly visible in all of these samples, and a consistent pattern of behaviour emerges. The temperature dependence of the resistivity of sample A5 is shown in figure 6.1.1 as an example. This is a sample which can be photodoped through the MIT and will be discussed in detail in the next chapter, along with measurements on samples A1

and A2, which are metallic before illumination. The dark level is shown here, along with five photogenerated carrier concentrations. Initially the sample is cooled in the dark from room temperature to 4.2 K. The dark data is taken on warming the sample from 4.2 K. The other curves are obtained by cooling the sample in the dark to 4.2 K then illuminating for a certain period of time, followed by warming the sample slowly and measuring $\rho(T)$. Eventually saturation is reached, at which point further illumination produces no persistent conductivity increase. It is important to note that immediately after illumination there is some relaxation of the conductivity. At low temperatures the relaxation is small and rapid, but as the temperature increases towards the quenching temperature, the relaxation becomes more significant. This will be discussed in greater detail in section 6.1.4. Suffice to say that at low temperatures the photoinduced increase in the conductivity is persistent for many months [2] ! At a certain temperature known as the quenching temperature, T_Q, the curves meet, and the light and dark conductivity has the same value. Above this point no PPC is observed. This is the point at which k_BT is as large as the barrier to recombination discussed in chapter 4.

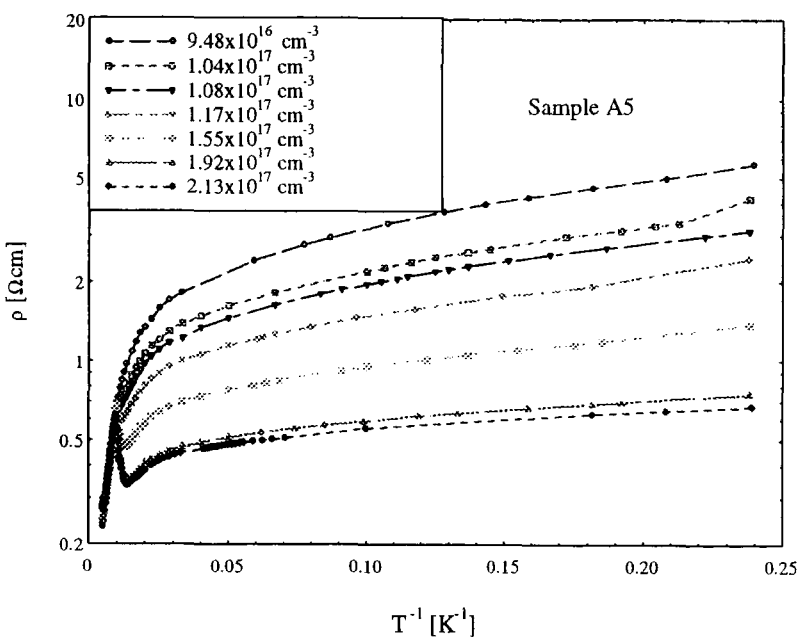

Figure 6.1.2. Temperature dependence of the resistivity of A5 - logρ against T^{-1}.

Figure 6.1.2 shows the same data plotted as log (ρ) v. T^{-1} to elucidate the conduction mechanisms taking place. In the dark at high temperatures the conduction occurs via activation from the DX centre deep level to the conduction band edge. At lower temperatures, k_BT is too small for this process to occur, so activation from the shallow level to the band edge is the dominant mechanism. Hence, the straight line section on this plot allows a determination of the deep level activation energy. The curves in figures 6.1.1 and 6.1.2 are labelled with the photogenerated carrier concentration determined from Hall measurements at a fixed temperature of 10.0 K. Figure 6.1.3 shows a plot of the resistivity as a function of the persistent photocarrier concentration. Here the sample is illuminated in stages at a fixed temperature, and the resistivity is measured at each illumination level. As expected, the resistivity falls rapidly with increasing carrier concentration. This plot can be used as a calibration curve, to label any measurement of $\rho(T)$ with the relevant carrier concentration.

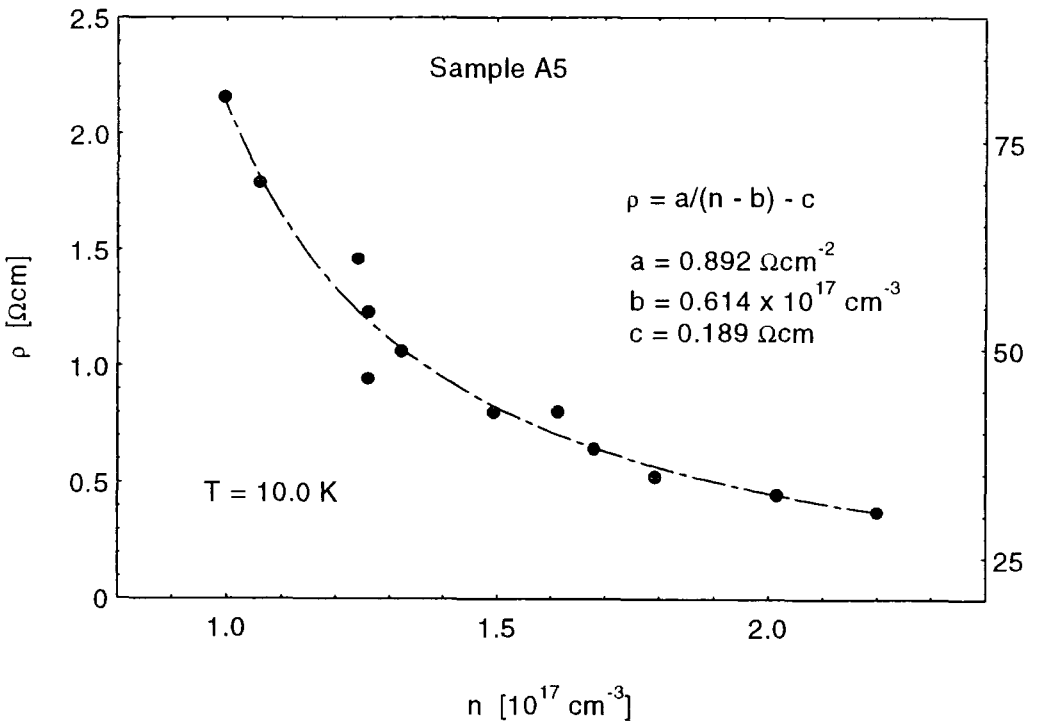

Figure 6.1.3. n dependence of the resistivity in sample A5.

The temperature dependence of the carrier concentration is shown in figure 6.1.4. As expected the carrier concentration shows an activated form, allowing the determination of the deep level activation energy. It is this value which is displayed in table 6.1.2, as Hall measurements produce a more reliable value of the activation energy than the resistivity. This is because the resistivity also includes the temperature dependence of the mobility, which although weak, can have an effect.

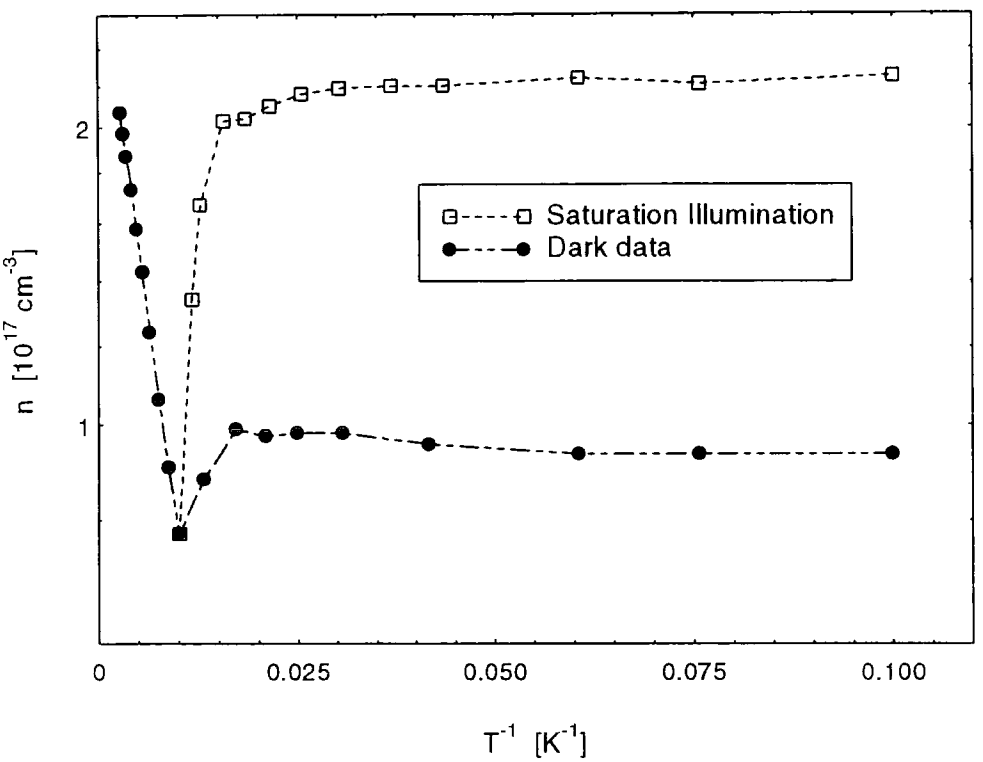

Figure 6.1.4. Temperature dependence of the Hall carrier density for sample A5.

Clearly, at low temperatures the carrier concentration is practically temperature independent, due to the fact that these samples are rather close to, or beyond, the IMT. The fact that the carrier density is constant over this temperature range means that a determination of *n* from a calibration curve such as figure 6.1.3. is a very reasonable procedure.

Sample Number	Mn Fraction	ρ(300K) Ωcm	ρ(4.2K) Ωcm	R	E_D meV	E_S meV	T_Q K	$\Delta\rho / \rho_{ill}$ (4.2K) %	n(300K) $10^{17}cm^{-3}$	μ(300K) $cm^2V^{-1}s^{-1}$
A1	4.7 %	0.046	0.103	2.24	4.44	0.02	93.0	16.9	3.0	453
A2	6.1 %	0.052	0.126	2.42	5.44	0.03	91.1	23.8	2.3	508
A3	6.28 %	0.126	9.657	9.78	12.85	0.67	98.2	80.2	1.4	340
A4	6.43 %	0.150	2.844	18.96	14.84	0.18	96.6	67.1	1.1	373
A5	8.1 %	0.155	5.339	34.44	18.64	0.12	104.4	87.5	2.0	202
A6	14.8 %	11.65	-	-	~160	~ 22	121.0	-	0.26	208
A7	16.6 %	2.942	-	-	175.2	25.35	123.0	-	0.11	191

Table 6.1.2. Summary of the transport data for the seven samples in set A. The parameters shown are the composition (see table 6.1.1 for details), resitivity at 300 K, resistivity at 4.2 K, the ratio of the resistivities at 4.2 and 300 K, deep level activation energy, shallow level activation energy, quenching temperature, % change in resisitivity on illumination at 4.2 K, 300 K carrier concentration and 300 K Hall mobility. These samples are used in the analysis of the compositional dependence in section 6.1.4, along with samples from [2].

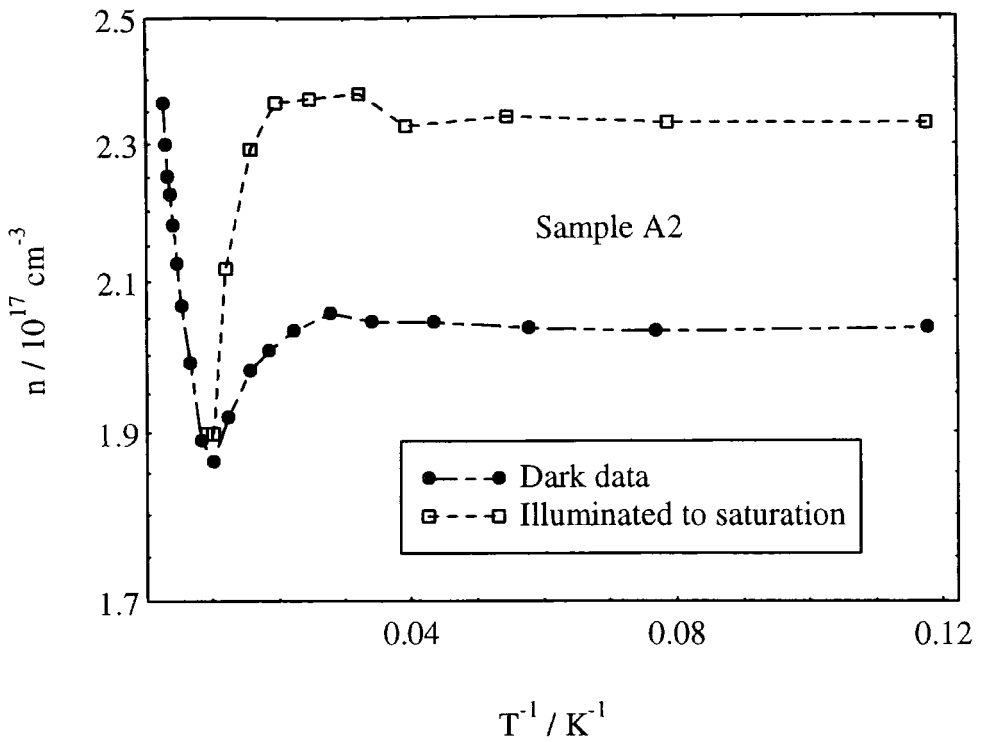

Figure 6.1.5. Temperature dependence of the Hall carrier density in sample A2.

It is interesting to examine the temperature dependence of the carrier density around 100 K where the conduction is presumably exhibiting a crossover from activation from the deep level, to activation from the shallow level. A small dip in n is seen in this region in all of the more conductive samples. Figure 6.1.5. shows similar data for the more conductive sample A2, where the effect is even more pronounced. A further interesting point emerges in that the Hall effect is slightly non-linear in this region, whereas above and below this temperature region the Hall effect is linear. This effect is shown in figure 6.1.6, where the Hall voltage is plotted as a function of the magnetic field up to 0.75 T. The voltage is seen to deviate from linear above about 0.3 T. This effect has also been seen in heavily doped $Cd_{0.99}Mn_{0.01}Te$:In [3]. It seems clear that this irregularity in the Hall data is due to the crossover in the conduction mechanisms. A non-linear Hall effect might be expected in such a situation [4]. It should also be noted that this effect only occurs in the more conductive samples.

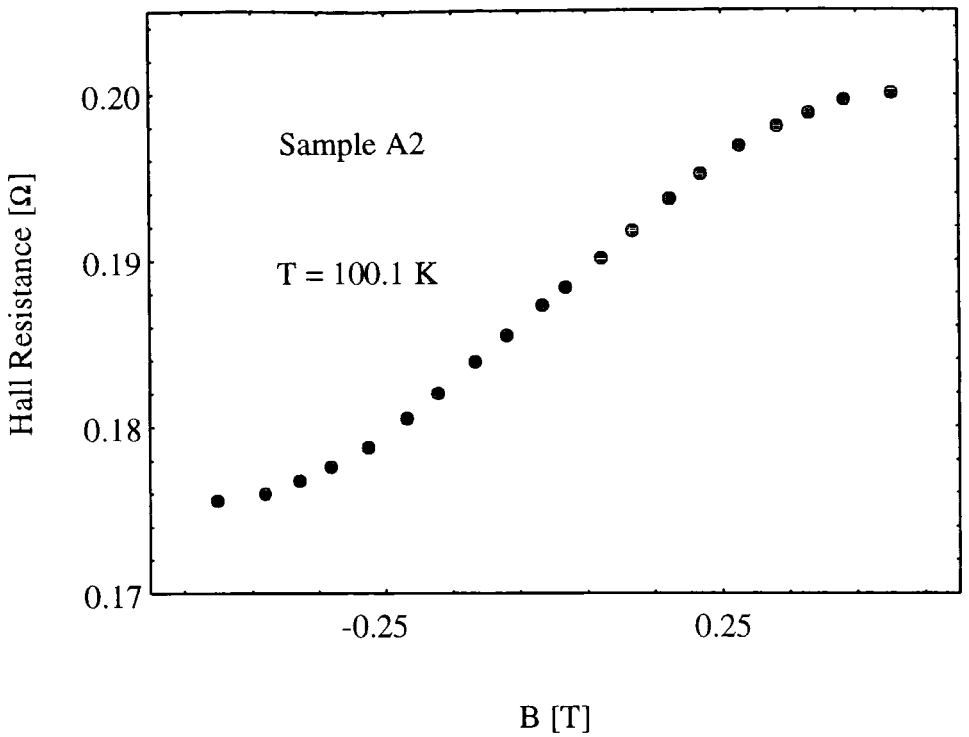

Figure 6.1.6. Field dependence of the Hall resistance at 100.1 K in sample A2.

We propose that this irregularity in the Hall effect is due to the fact that the conduction mechanism crosses over from activation to the conduction band edge, to impurity band conduction at lower temperatures. For the case of sample A2 (which will be shown to be metallic even before illumination in chapter 7) the impurity band conduction will be metallic in nature. This explains why the anomaly in the temperature dependence of the Hall coefficient is observed in metallic samples, but not in insulators : in the insulating case the conduction mechanism simply crosses over from activation from the deep level to activation from the shallow level, whereas in the metallic samples the conduction mechanism changes from activation to metallic conduction in an impurity band.

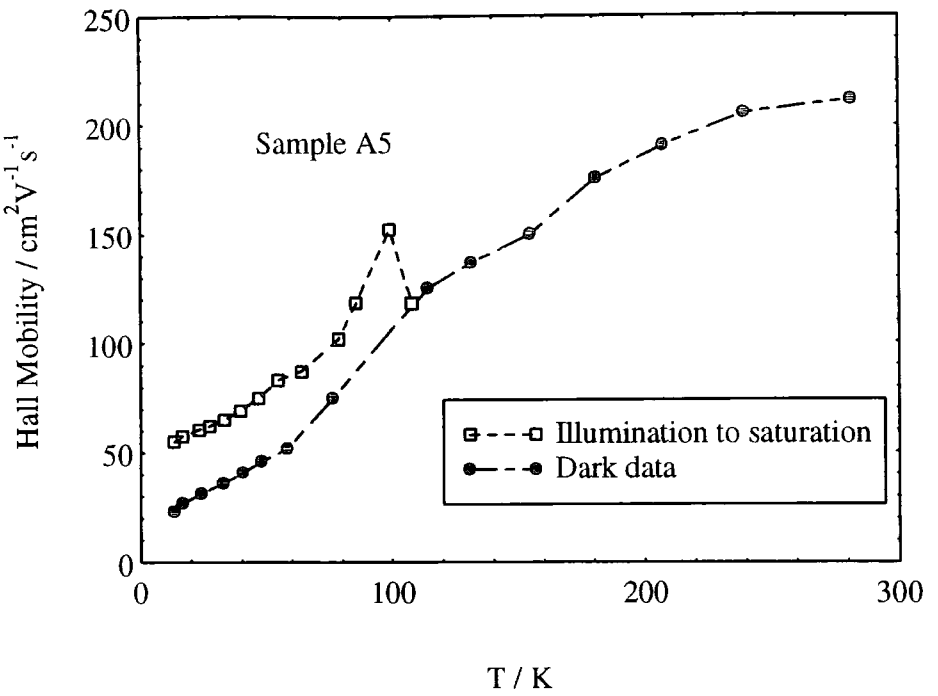

Figure 6.1.7. Temperature dependence of the Hall mobility for sample A5.

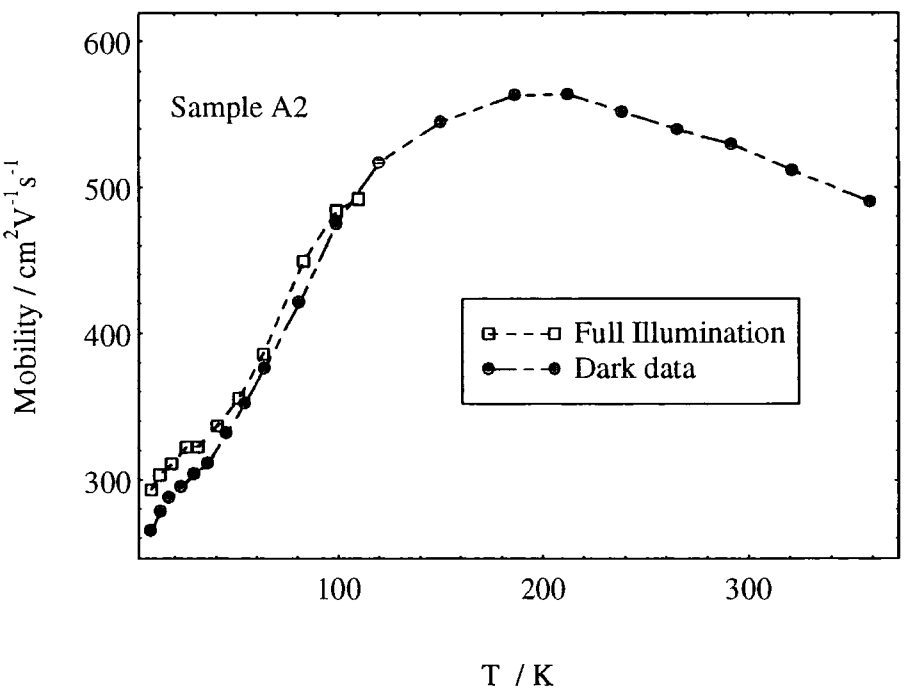

Figure 6.1.8. Temperature dependence of the Hall mobility in sample A2

Figures 6.1.7 and 6.1.8 show the Hall mobility of samples A5 and A2 as a function of temperature. In the dark all samples show a qualitatively similar behaviour : at low temperatures the mobility is dominated by ionized impurity scattering with a $\sim T^{3/2}$ temperature dependence, whereas at higher temperatures the mobility is dominated by phonon scattering with a $\sim T^{1/2}$ dependence [5]. This leads to a turnover in the $\mu(T)$ dependence as shown in figure 6.1.8. Mobilities for the A5 sample are in the range 20 to 200 $cm^2V^{-1}s^{-1}$, while for sample A2 they reach values as high as 570 $cm^2V^{-1}s^{-1}$. This is as expected, as sample A5 is insulating before illumination (and spans the critical region), whereas A2 is a metallic sample. It can also be seen that the mobility increases with illumination. This effect is shown more clearly in figure 6.1.9, where the mobility is plotted as a function of the carrier concentration at a fixed temperature of 10.0 K. Just as for figure 6.1.3, the sample is illuminated in stages and measurements made at each illumination level. This data is in qualitative agreement with the data of Terry *et al* [2].

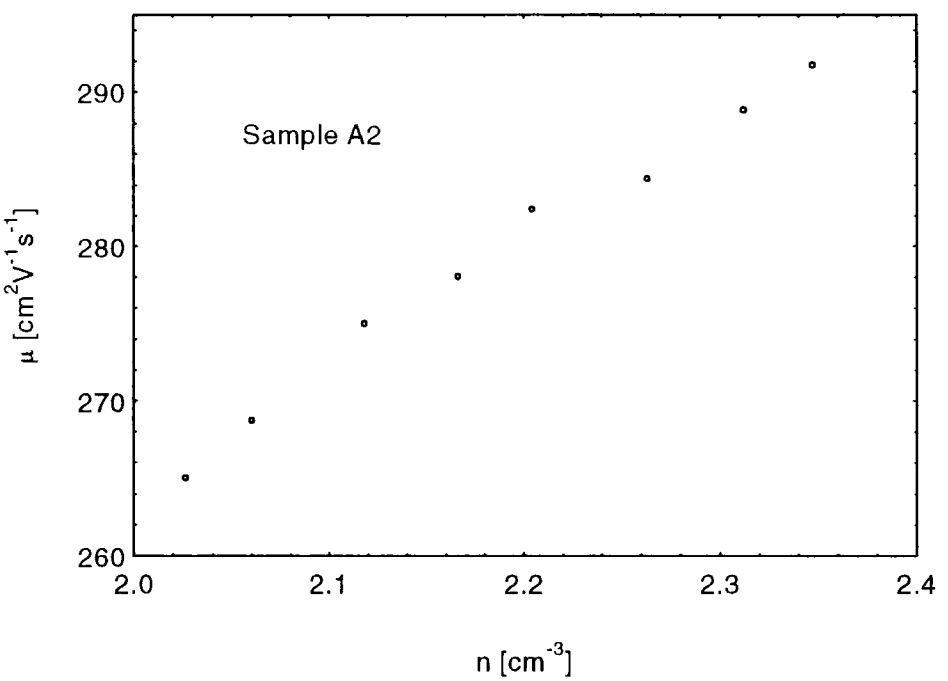

Figure 6.1.9. *n* dependence of the Hall mobility for sample A2. T = 10.0 K.

where a similar, roughly linear, increase is observed. In fact all measurements on CdMnTe thus far have resulted in an increase in the mobility on illumination [2,6], while measurements on AlGaAs have yielded both increases and decreases [7]. The n dependence of the mobility measured by Terry et al was successfully modelled using the Brooks-Herring theory of ionized impurity scattering, taking the number of ionized impurities to have a constant value. This is in complete agreement with the Chadi and Chang negative *U* model as discussed in some detail in chapter 4. Here the number of scattering centres is constant during illumination, as the indium donors behave as charged impurities in the deep state as well as in the shallow state. Figure 6.1.10 shows similar data for sample A5, where the dependence is qualitatively different : the mobility shows a tendency to saturate at high values of *n*. This curvature is also evident at 12.0 K, 16.5 K, 23.4 K and 35.0 K. This sample is unique in displaying this feature. Other samples, regardless of whether they are insulating or metallic show a more linear dependence. The anomalous behaviour of sample A5 may be related to the fact that it is extremely close to the MIT critical region, and can in fact be illuminated from the insulating to the metallic phase. This point will be discussed in more detail in section 6.1.5.

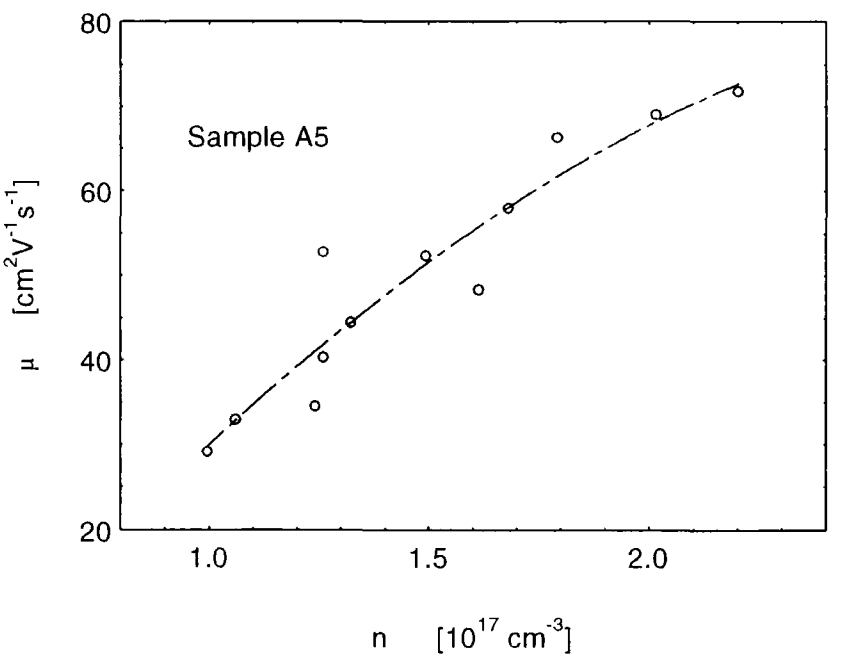

Figure 6.1.10. *n* dependence of the Hall mobility in sample A5. T = 10.0 K.

Although the PPC effect shows a compositional dependence as discussed in section 6.1.4, by far the most important factor in determining the phototransport properties of any particular sample, is the distance from the MIT. The two samples discussed thus far have been metallic, either in the dark or after illumination, meaning that they have a relatively high conductivity which is weakly temperature dependent. Several other samples show more insulating behaviour. Figure 6.1.11 shows the temperature dependence of the resistivity of sample A3 as an example of a sample which is just on the insulating side of the transition after illumination. The slightly stronger temperature dependence is seen clearly, the resistivity at 4.2 K being around 10 Ωcm with a carrier density at room temperature of 1.4×10^{17} cm^{-3}. The temperature dependence of sample A6 is shown in figure 6.1.12 as an example of a very insulating sample. The room temperature carrier density of this sample is only 2.6×10^{15} cm^{-3}, with a resistivity of 11.65 Ωcm. As can be seen from this figure, the resistivity is strongly temperature dependent. In fact the deep level activation energy is as high as 162.5 meV. The resistivity becomes unmeasurably large (>300 MΩ in this case) at about 80 K in the dark. If one examines the illuminated curve, it is interesting to note that the quenching process occurs over a much wider temperature interval than in more metallic samples. Sample A2 exhibits a very sharp quenching, with the temperature at which the illuminated resistivity starts to increase, occurring within 10 K of the point at which the two curves meet. For this sample the 'transition' occurs over a temperature range from 60 K up to 120 K. This is a feature which is common to all samples which are rather insulating in nature, and is due to a large relaxation as discussed more fully in section 6.2, where the relaxation is measured as a function of temperature for several samples.

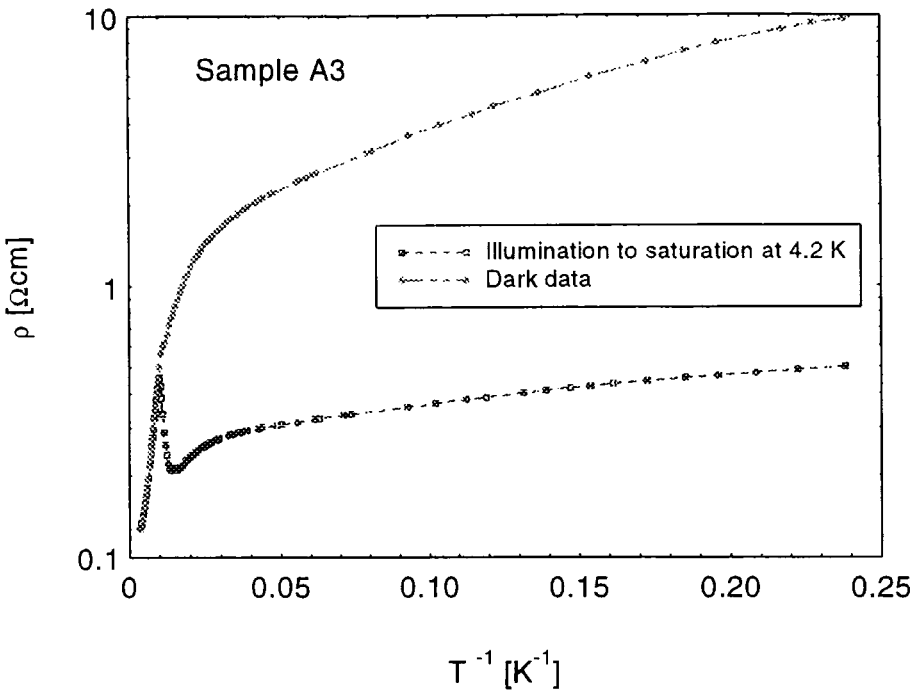

Figure 6.1.11. Temperature dependence of the resistivity for sample A3.

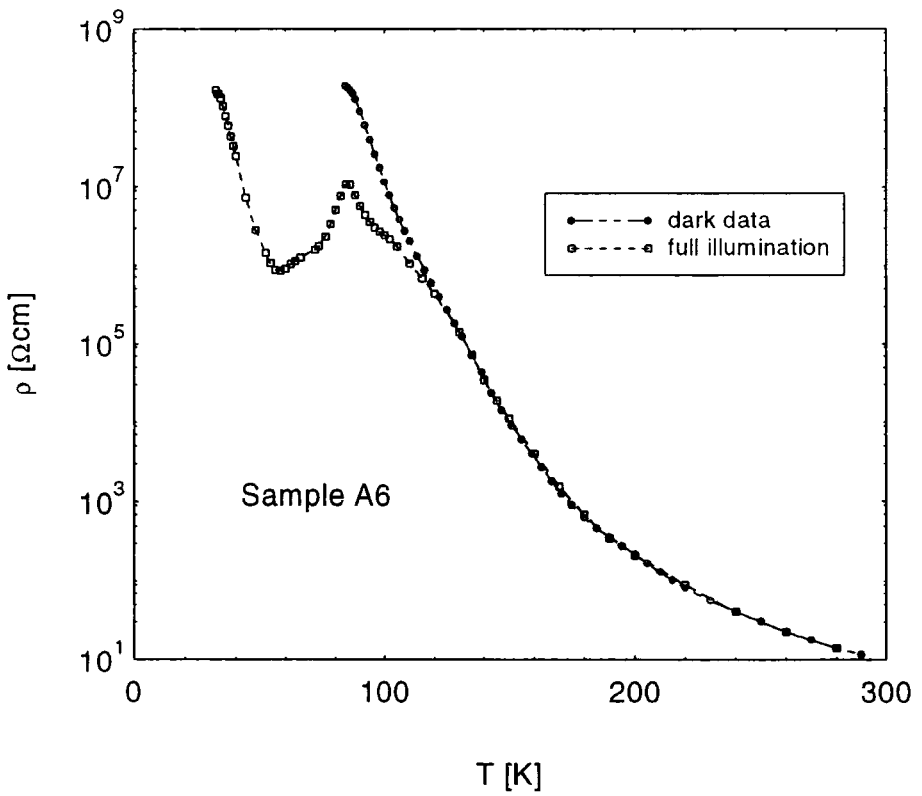

Figure 6.1.12. Temperature dependence of the resistivity of sample A6.

6.1.2. Proximity To The MIT.

In chapter 3 the Mott criterion was discussed, along with the minimum metallic conductivity, which should give a rough estimate for the conductivity expected in the critical region. The minimum metallic conductivity, σ_{min} and the MIT critical carrier concentration, n_c were determined to be 5 $(\Omega cm)^{-1}$ and $1.1x10^{17}cm^{-3}$ respectively, for CdTe. It was also mentioned that for $Cd_{1-x}Mn_xTe$, the value of n_c would increase due to the behaviour of the Bohr radius on going from $x = 0$ to $x = 1$. The effective mass and dielectric constant are unknown for MnTe, meaning that it is impossible to predict the exact relationship between the Bohr radius and x. Shapira *et al* performed an experimental investigation of the magnetoresistance near the MIT and suggested that $n_c = 1.7$ to $2.1x10^{17}$ cm^{-3} for a sample with $x = 0.05$ [8], although it should be noted that this is an estimate as these measurements were done at relatively high temperatures.

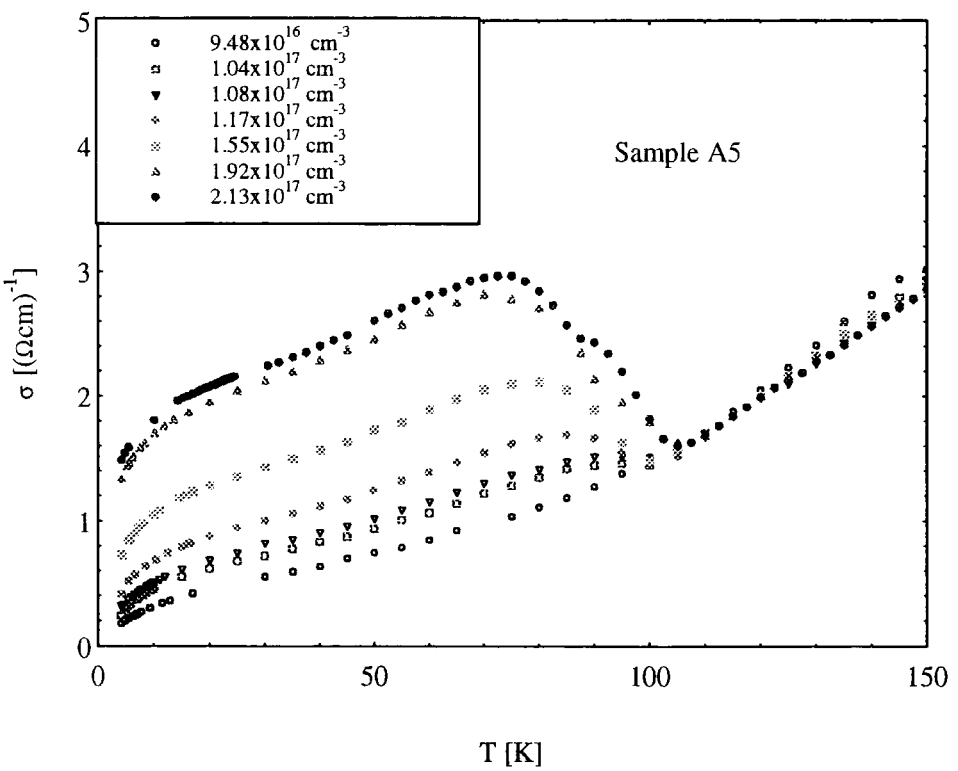

Figure 6.1.13. Temperature dependence of the conductivity of sample A5.

Several of the samples in set A have low temperature carrier concentrations and conductivities close to these values. In particular, samples A1, A2 and A3 are near the MIT. In fact lower temperature measurements presented in the next chapter show conclusively that Samples A1 and A2 are metallic even before illumination, while sample A5 can be illuminated from the insulating to metallic phase. Figure 6.1.13 shows the resistivity data for sample A5 plotted as conductivity against temperature to illustrate this. As can be seen from the figure, the dark curve appears to be an insulator with $\sigma(T = 0) = 0$, whereas the full illumination curves appear to have a finite value of $\sigma(T = 0)$. Clearly measurements need to be made at much lower temperatures to really draw conclusions about the nature of this transition. These will be presented in the next chapter. Chapter 7 also includes a section on a series of samples doped with both indium and aluminium, which are all in the critical or metallic regions.

6.1.3. Low-Field Magnetoresistance.

As discussed in section 2.3.4, DMS such as $Cd_{1-x}Mn_xTe$:In display magnetoresistance effects which are not present in the diamagnetic host material [9]. Previous work has shown that the MR is initially positive, and is followed by a negative MR at higher fields. This section presents data taken on samples in set A at low field < 1T, which, as we shall see is an interesting region. An in depth study of the MR in high fields has been done in the insulating regime [10,11], which has resulted in a very plausible theory for the origin of the MR based on BMP formation as discussed in section 2.3.4.

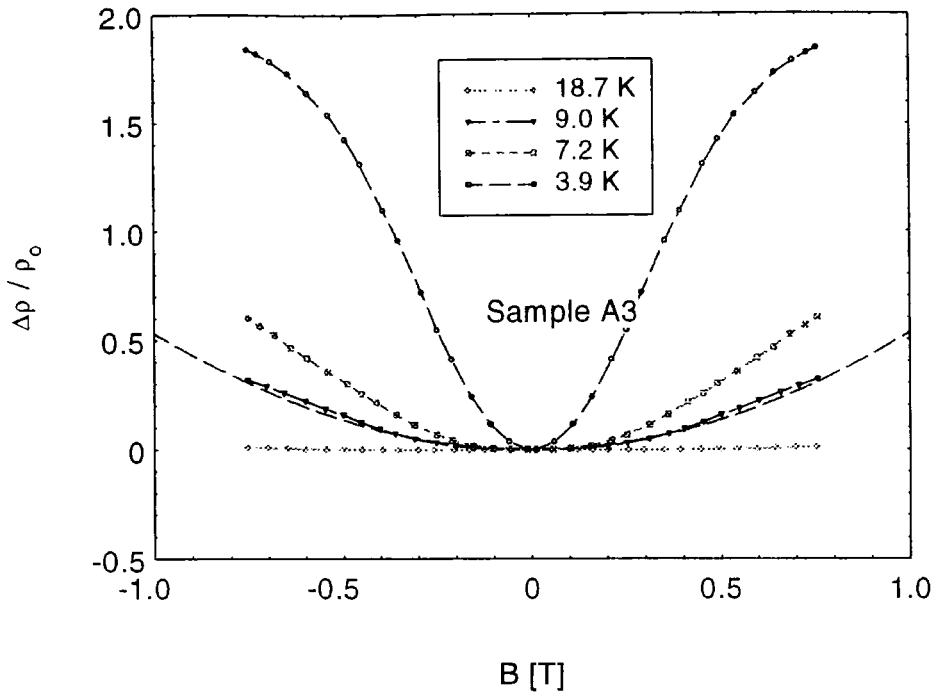

Figure 6.1.14. Magnetoresistance of sample A3. Data taken in the dark. The dashed line is the result of a calculation based on equation 3.6.7.

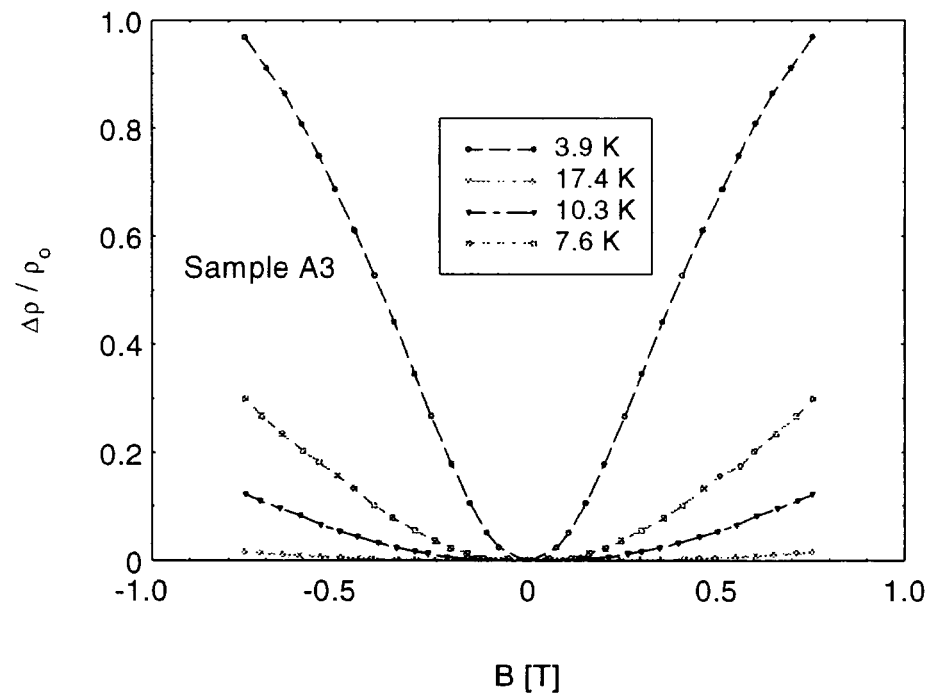

Figure 6.1.15. Magnetoresistance of sample A3. Data taken at full illumination.

Figures 6.1.14 and 6.1.15 show the MR of sample A3 as a function of temperature, in the dark and at full illumination respectively. The plane of the sample is perpendicular to the magnetic field. This sample is chosen as it is on the insulating side of the transition and shows behaviour typical of semiconducting CdMnTe:In. The low field MR is indeed positive as observed in other samples. At higher fields the resistivity begins to turn over, and presumably at the highest fields the negative MR would take over. As can be seen from the figure, the MR is almost non-existent down to about 20 K, at which point it increases rapidly with decreasing temperature.

There are several observations which show quite convincingly that the MR is intimately linked with the dilute magnetism of the system. First of all the PMR is far too large to be due to conventional PMR due to the Lorentz force. One very realistic possibility however is that it is associated with the hopping conduction which could well be taking place in an insulating sample at these temperatures. If this were the case then one would expect an $\exp(aB^2)$ dependence on field (equation 3.6.7). This is actually rather well obeyed at very low fields, but obviously at high fields where the MR is turning over, this is not the case.

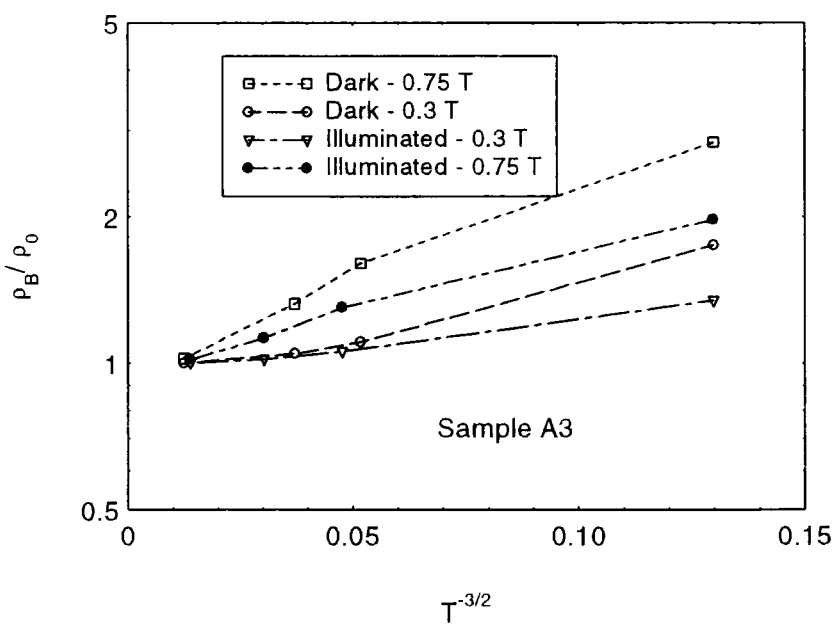

Figure 6.1.16. Temperature dependence of the magnetoresistance in sample A3.

The temperature dependence would be expected to be of the form in equation 3.6.7 with y = 3/2. Hence a plot of $\ln(\rho_B/\rho_0)$ against $T^{3/2}$ would be expected to be linear. The dark data is plotted in this fashion in figure 6.1.16. Clearly this temperature dependence is not an accurate description of this data. If the MR is measured at 0.3 T then the temperature dependence is faster than linear at low temperatures, whereas if the MR is measured at 0.75 T it is slower than linear due to the turnover in $\rho(B)$. This temperature dependence is not obeyed by samples A2 or A5 either. Moreover, if conventional hopping PMR due to wavefunction shrinkage is the cause of this effect, then there should be a considerable orientation dependence of the MR [12], due to the fact that this is an orbital effect. Figure 6.1.17, where the MR is shown with the field both parallel and perpendicular to the plane of the sample, shows that this is not true. In fact there does not appear to be any orientation dependence at all.

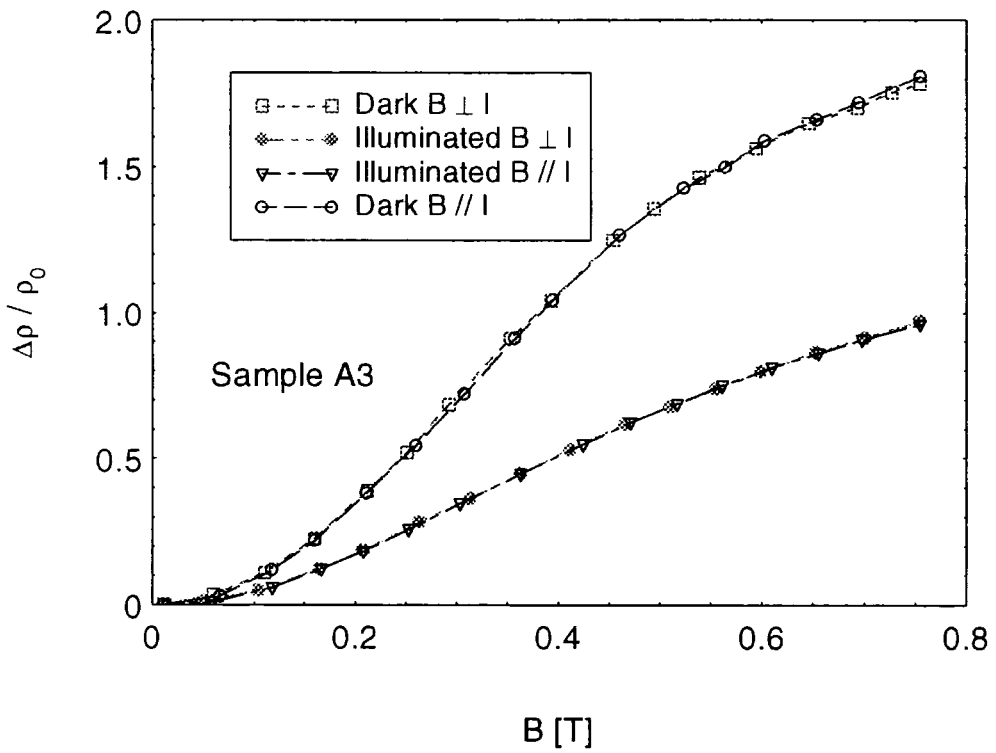

Figure 6.1.17. Orientational dependence of the magnetoresistance in sample A3, at 3.9K.

As a final piece of evidence against interpreting the positive MR in terms of conventional hopping MR it should be noted that the absolute size of the effect is much larger than theoretical predictions from equation 3.6.7. Evaluating this expression for the case of the dark data for sample A3 at 3.9 K, results in the dashed line shown in figure 6.1.14. Clearly the observed effect is far larger than theory predicts.

It seems clear therefore that this positive MR must be due to the magnetism of the sample. In fact it has been noted [10] that it is possible to collapse all of the data on to a

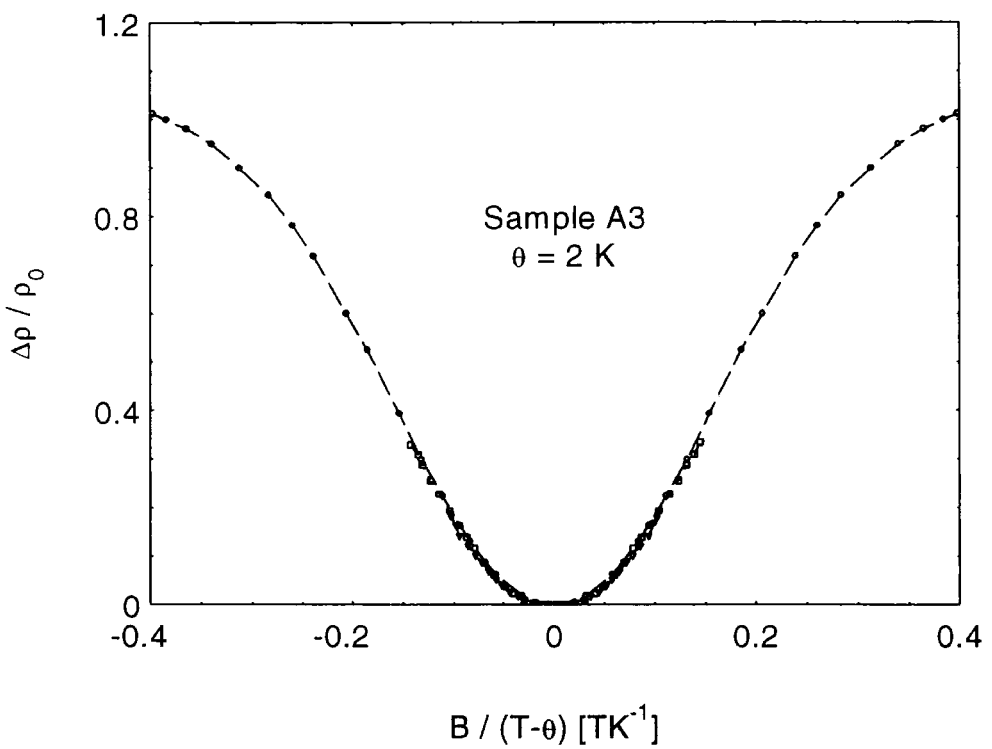

Figure 6.1.18. All of the data of figure 6.1.15 plotted as MR against $B/T-\theta$.

single curve by replotting the field axis as $B / (T - \theta)$, suggesting that the magnetization of the sample dominates the MR. Figure 6.1.18 shows that this is true for this sample, with θ = 2K. The same data for sample A5 is shown in figure 6.1.19 as a further example. This θ is determined by incrementing the value of θ in steps of 0.2 K and measuring the deviation

of the points from identical behaviour. The appropriate value of θ is the one which minimises this deviation. The interesting point is that this sample and all of the others investigated (A1, A2 and A5) suggest $\theta = 2$K in the dark and after illumination, whereas one might expect a negative value because the d-d interactions in this material are antiferromagnetic. One tentative explanation for this effect is that the effects of the (ferromagnetic) RKKY interaction between Mn d spins is becoming important, as is the case in PbMnTe (see section 2.3.2). Although no such behaviour has ever been reported from measurements of the magnetic properties of this system, it should be pointed out that these samples are all near the MIT or metallic, so the carrier densities are likely to be far higher than in previous studies of the magnetism where the samples used are often undoped. Another interesting point is that the MR obviously samples the magnetism of the material on a short length scale of the order of the mean free path (or mean hopping length if the sample is in the hopping regime), rather than in the bulk of the material as with a magnetization measurement. In summary, we can conclude that the origin of the low field PMR is certainly linked with the magnetization of the system, although the value of θ is puzzling.

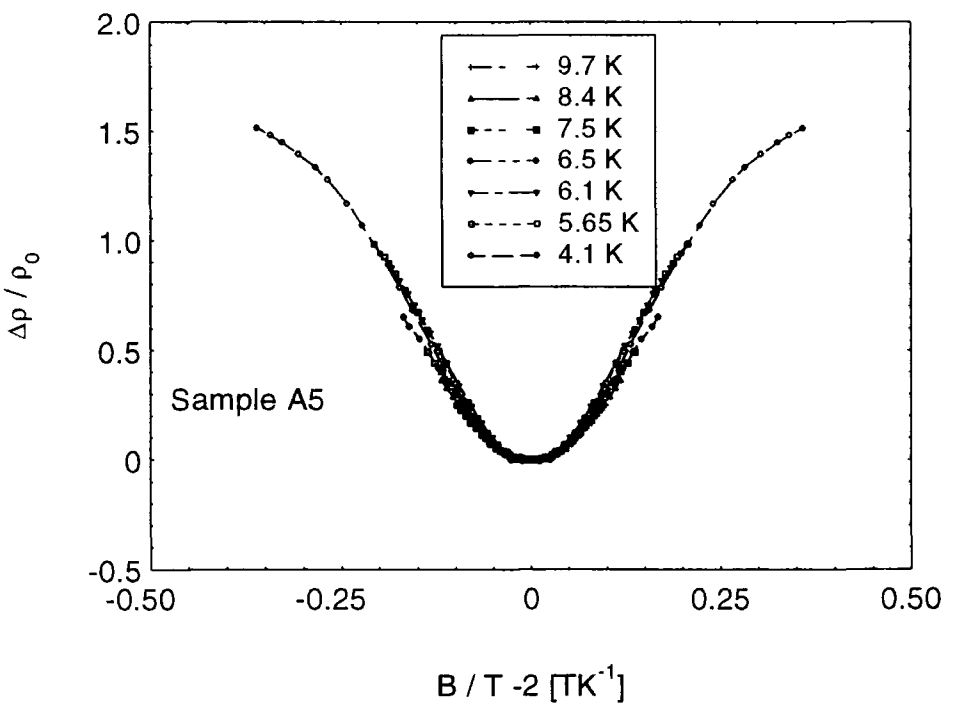

Figure 6.1.19. MR plotted against B/T-2K for sample A5.

The magnetoresistance in samples A1 and A2, which both have carrier concentrations in excess of the anticipated n_c, and have been shown to be metallic from low temperature measurements (see chapter 7), show similar behaviour to the insulating samples. Figure 6.1.20 shows the MR data as a function of illumination at 3.9 K. The interesting point here is that the change in carrier density on illumination, albeit a rather small one, has a negligible effect on the MR. This is the case for all metallic samples. θ = 2K is found from the temperature and field dependence of the MR, both before and after illumination, just as for the insulating samples. Obviously if measurements of the magnetoresistance were made at very low temperatures then significant differences between the insulating and metallic phases would be expected.

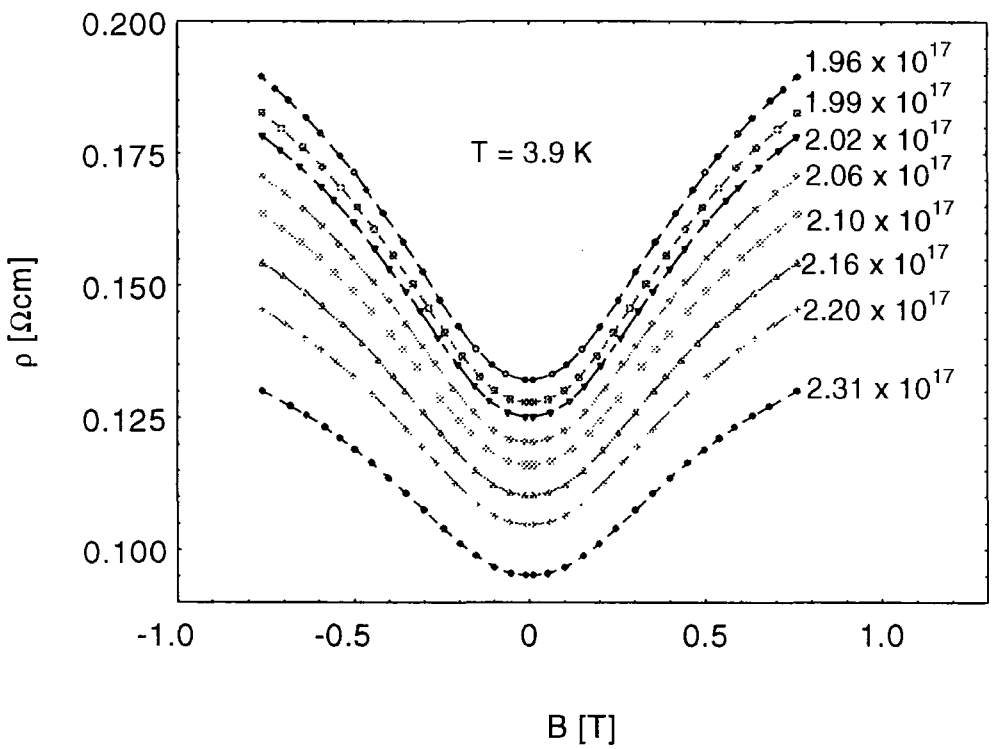

Figure 6.1.20. Magnetoresistance of sample A2 at T = 3.9 K for various carrier densities.

6.1.4. Compositional Dependence Of The PPC Parameters.

Several general trends can be identified from the behaviour documented above. First of all, at room temperature the resistivity tends to increase with x, whereas the mobility and carrier density tend to decrease. This can be partially accounted for by the increase in the alloy scattering rate which is bound to occur as x increases. The most important factor however is that the deep level activation energy, E_D shows a dramatic increase with x, making the high x samples very insulating. It should be noted that the carrier density extrapolated to infinite temperature shows no systematic variation with x. This is in contrast to the situation in $Cd_{1-x}Zn_xTe$:Cl [13] where $n(T = \infty)$ decreases with x due to the increasing difficulty in obtaining n-type doping.

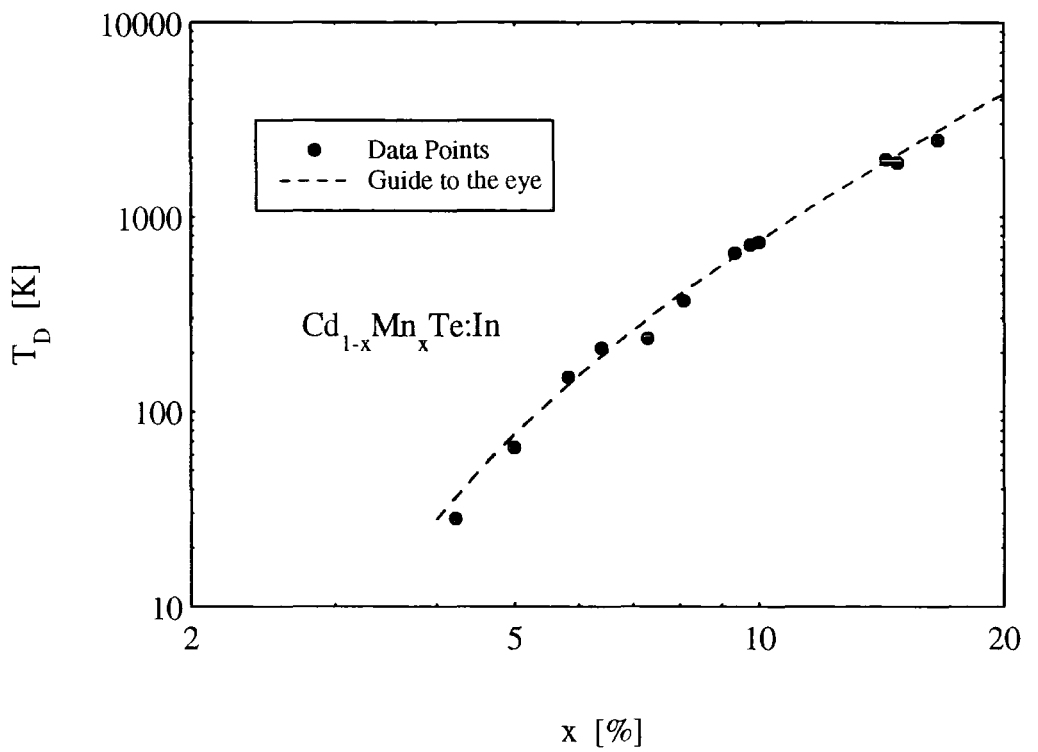

Figure 6.1.21. x dependence of the DX^- deep level activation energy.

The x dependence of the deep level activation energy is shown in figure 6.1.21, for the seven samples studied here along with several from a previous study [2]. A rapid

increase of the activation energy is observed on increasing the Mn fraction, so clearly the DX^- deep level is deepening with increasing x. The shallow level however, has a dependence on x, as shown in figure 6.1.22. Again an increase with x is observed. The shallow level activation energy, E_S, can be estimated for CdTe from the hydrogenic theory of shallow donors (eqn 2.5), using a static dielectric constant of 9.7 and an effective mass $0.096m_e$. One obtains 13.8 meV. However, for the case of $Cd_{1-x}Mn_xTe$:In, in order to calculate $E_S(x)$, the x dependences of m^* and ε_r are required. As the value of these constants is unknown for MnTe, this is not possible. This value though, is certainly in rough agreement with the activation energies of the higher x samples (~20meV).

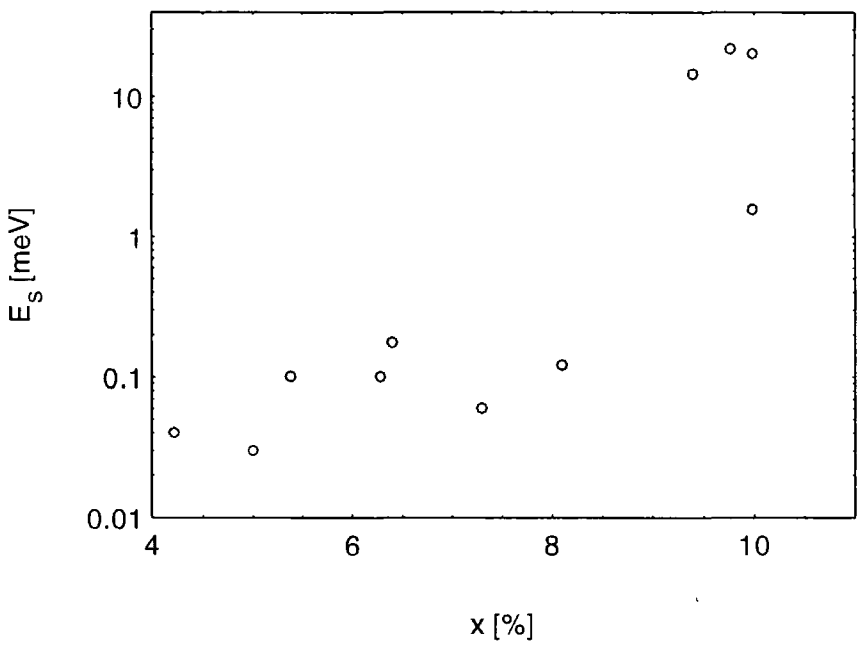

Figure 6.1.22. x dependence of the shallow level activation energy.

The interesting feature of figure 6.1.22 however, is that at low x the activation energies are invariably far smaller than the hydrogenic estimate. This is because the samples with low x are often rather conductive because of the small values of E_D and n_c - in fact some of them are metallic. In the case of the metallic samples a very small apparent activation energy is measured as the temperature dependence of the conductivity is so weak. The temperature dependence is obviously not actually of an activated form - the

values of the activation energy quoted here are from 'force fits' to the data. Another interesting point, which shall be returned to later during the discussion of the indium and aluminium doped samples in chapter 7, is that as the IMT is approached the shallow level activation energy will reduce due to the effects of banding. As the electron density in the impurity band is increased, the width of the impurity band, $B = 2zI$, is increased, where z is the co-ordination number and I is the transfer integral, leading to a decrease in the energy separation between the top of the impurity band and the bottom of the conduction band. In fact it is possible to imagine the situation where these bands actually merge, producing a strangely shaped band tail at the bottom of the conduction band. This would lead to unusual effects in the transport properties of very heavily doped samples near the MIT. This point is returned to in chapter 7.

The x dependences of the DX^- deep level and hydrogenic shallow level energies are shown in figure 6.1.23, along with the x dependence of the energy gap. The top of the valence band is taken as zero in this diagram. The relatively weak x dependence of the shallow level and the very strong dependence of the DX^- deep level is shown very clearly here. One final parameter which displays an interesting systematic variation with the Mn fraction is the quenching temperature, T_Q. Figure 6.1.24 shows the x dependence of T_Q. It is important to note that we define the quenching temperature as the temperature at which the dark and maximum illumination curves intersect. It has already been pointed out that the point at which the illuminated resistivity curve begins to increase with temperature to join the dark curve, can be significantly different from T_Q.

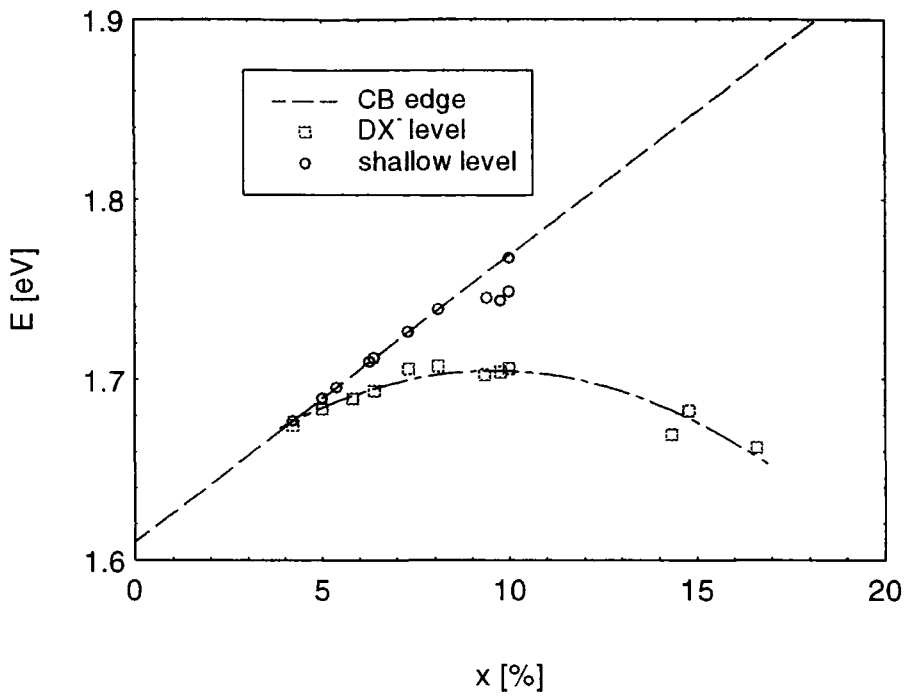

Figure 6.1.23. CB edge, DX^- level, and shallow level as a function of x.

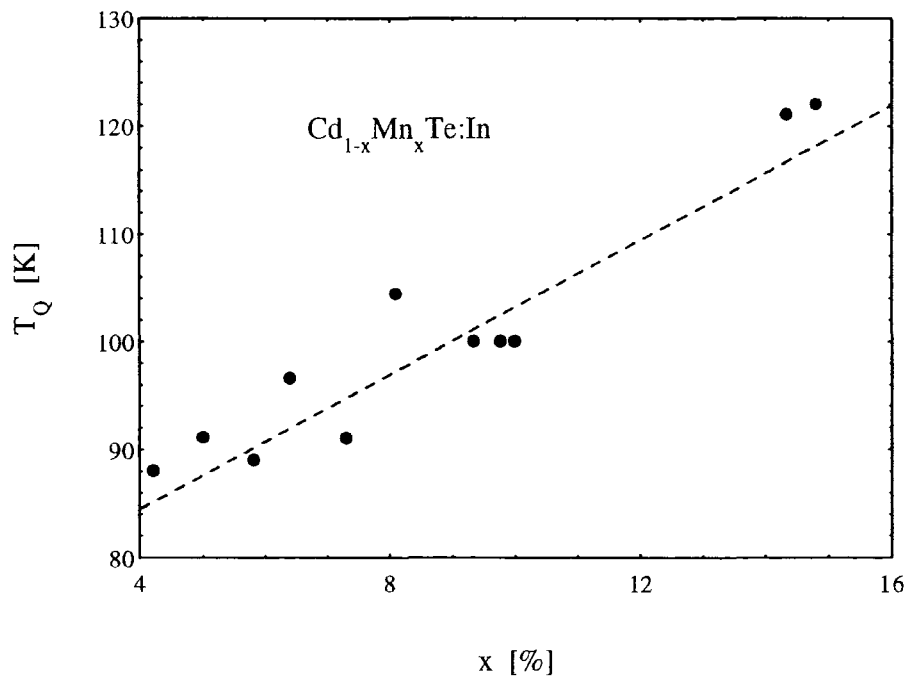

Figure 6.1.24. x dependence of the quenching temperature, T_Q.

As can be seen from the figure, T_Q increases roughly linearly with x in the region studied. T_Q represents a measure of the barrier to recapture of electrons to the deep state, so this behaviour implies that as well as the DX^- level deepening with x, the energy barrier separating the shallow and deep levels is increasing as the Mn fraction is increased. As mentioned briefly earlier, at low temperatures the conductivity relaxation is small but as $T \rightarrow T_Q$ this relaxation becomes increasingly significant. This means that the conductivity at T close to T_Q is time dependent : if the sample is warmed very slowly through T_Q then a lot of relaxation takes place as electrons are recaptured by the deep level. In fact if the sample was kept at a certain temperature just below T_Q then eventually the conductivity would relax fully. Hence the value of T_Q measured is dependent on the rate at which the sample is warmed. Slow warming leads to a smaller measured value of T_Q than if the sample is warmed very quickly through the transition. This effect is shown in figure 6.1.25 where T_Q is plotted as a function of the average warming rate, R_{av}, for sample B5, which is discussed in the next section.

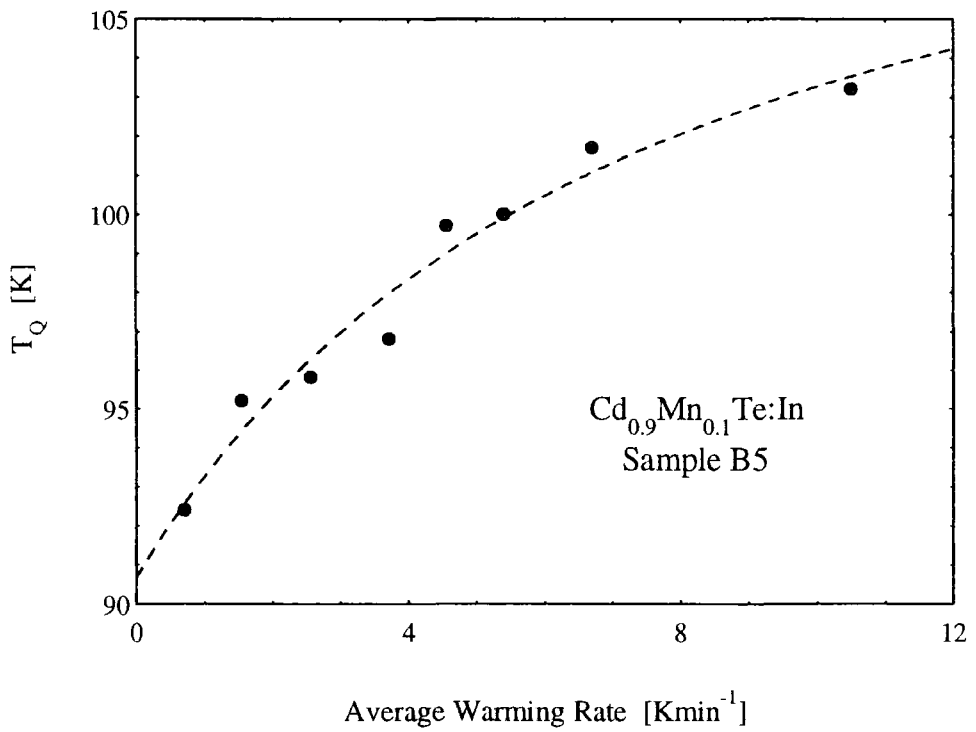

Figure 6.1.25. Measured T_Q against the average warming rate.

One final point on the compositional dependence of the PPC parameters is that it is possible to estimate composition from the x dependence of quantities such as E_D and T_Q. This procedure is carried out for the samples in set B, where a comparison to the values determined by EDAX is made. Good agreement is obtained.

6.1.5. Hopping Conduction - Sample A7.

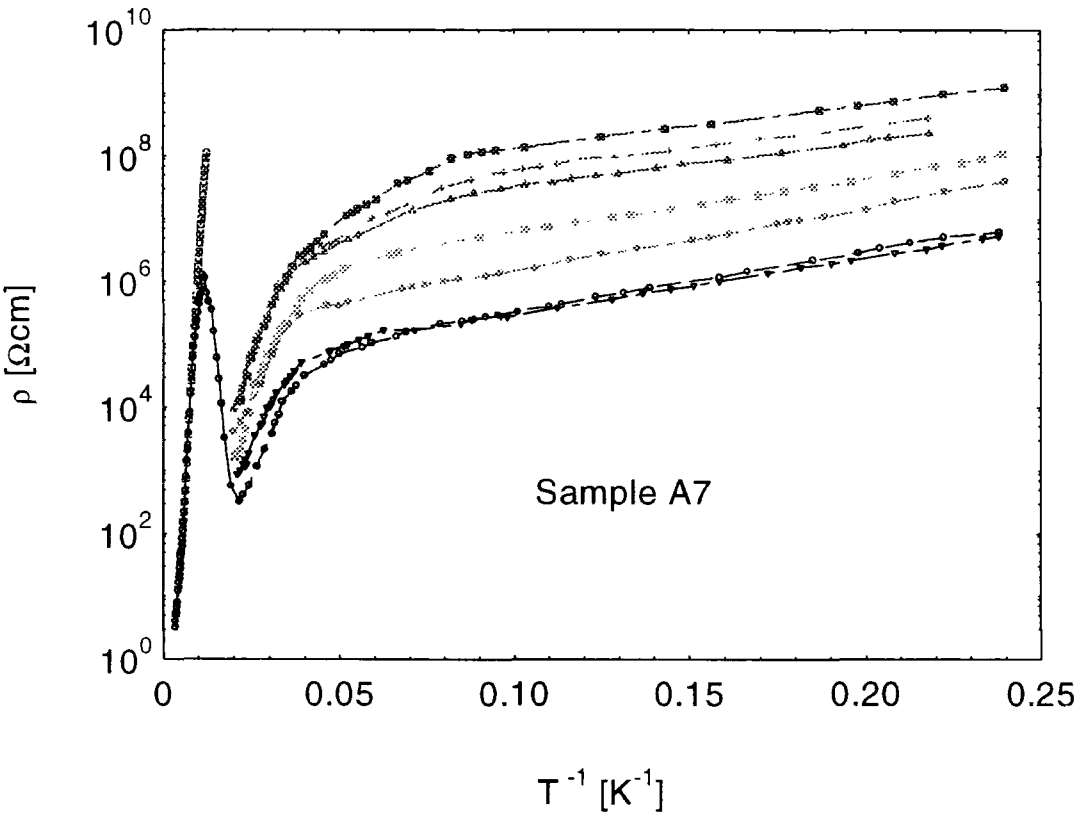

Figure 6.1.26. Temperature dependence of the resistivity for sample A7.

Sample A7, which can be seen from table 6.1.2 to be rather insulating, shows some interesting effects in the low temperature transport properties which are not observed in other samples. Figure 6.1.26 shows the temperature dependence of the resistivity plotted

as $\ln\rho$ against T^{-1} for the dark level and six photogenerated carrier concentrations. At first sight this would appear to be rather typical behaviour for this system, with the conduction crossing over from activation from the deep level, to activation from the shallow level at lower temperatures. Closer analysis shows that this interpretation is in fact flawed. First of all this figure shows that there is another linear region (in a plot of $\ln\rho$ v T^{-1}) between about 50 and 25 K. Secondly the extracted activation energies from the low temperature linear region are of the order of 1 to 2 meV, compared to the values of about 20 meV expected for such a sample. In addition to this, the activation energies in the region between 50 and 25K are around 20 meV which is consistent with this region being due to activation from the shallow level. It is possible that we are observing a crossover from activation from the shallow level to some other form of conduction below about 25 K. Given that this other form of conduction shows an $\exp(E/T)$ dependence on the conductivity it is tempting to interpret this data in terms of nearest neighbour hopping conduction. We shall now show that there are several other pieces of evidence to support this hypothesis.

n [cm^{-3}]	E_s [meV]	E_3 [meV]	ρ_3 [Ωcm]
2.1×10^{14}	46.40	1.389	2.67×10^{7}
2.3×10^{14}	43.90	1.397	1.20×10^{7}
3.7×10^{14}	38.12	1.458	5.96×10^{6}
1.1×10^{15}	34.93	1.768	7.29×10^{5}
5.1×10^{15}	31.74	1.993	1.33×10^{5}
7.5×10^{15}	25.36	1.940	3.63×10^{4}
1.0×10^{16}	25.01	1.803	3.63×10^{4}

Table 6.1.3. Transport data for sample A7. The carrier density, shallow level activation energy, E_3 and ρ_3 are shown.

Table 6.1.3 shows the transport parameters extracted from this data assuming that we are indeed observing conduction of the form $\rho_3\exp(E_3/k_BT)$ at low temperatures. The

carrier densities are measured at an arbitrary temperature of 35 K. There are several points to note about the values listed in this table : (i) E_s, the shallow level activation energy, decreases with n as expected (presumably due to increased banding), (ii) E_3 shows a peak as the carrier concentration is increased from 2.1 x 10^{14} cm^{-3} up to 1.0 x 10^{16} cm^{-3}, and (iii) ρ_3 decreases rapidly with increasing carrier concentration.

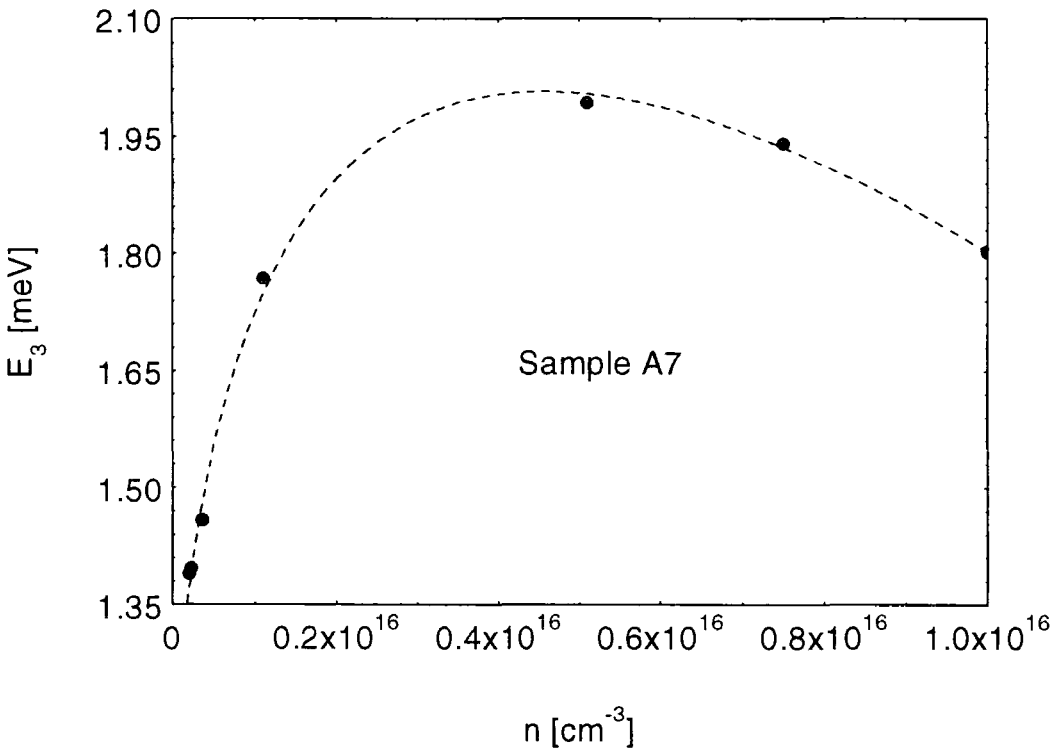

Figure 6.1.27. n dependence of the nearest neighbour hopping energy, E_3.

Figure 6.1.27 shows the dependence of E_3 on the carrier density, where the peak in E_3 can be seen very clearly. This is exactly the expected behaviour for nearest neighbour hopping conduction as discussed in section 3.6. It should also be noted that if we are observing nearest neighbour hopping then one would expect the hopping probability to include a term like $\exp(-2\alpha R)$ [14], where R is the mean distance between centres i.e. $R = (3/4\pi n)^{1/3}$. This gives the hopping probability proportional to $\exp-(1.241/a_B n^{1/3})$, where a_B is the Bohr radius of the donor. Hence a plot of $\ln\rho_3$ against $n^{-1/3}$ should result in a straight

line with gradient $1.241/a_B$. This plot is shown in figure 6.1.28, where a reasonable linear dependence is observed with an extracted Bohr radius of ~19 nm. Although this value is a little high (a typical donor Bohr radius for CdTe is about 5 nm) this is certainly another piece of evidence for the hypothesis that we are indeed observing nearest neighbour hopping conduction.

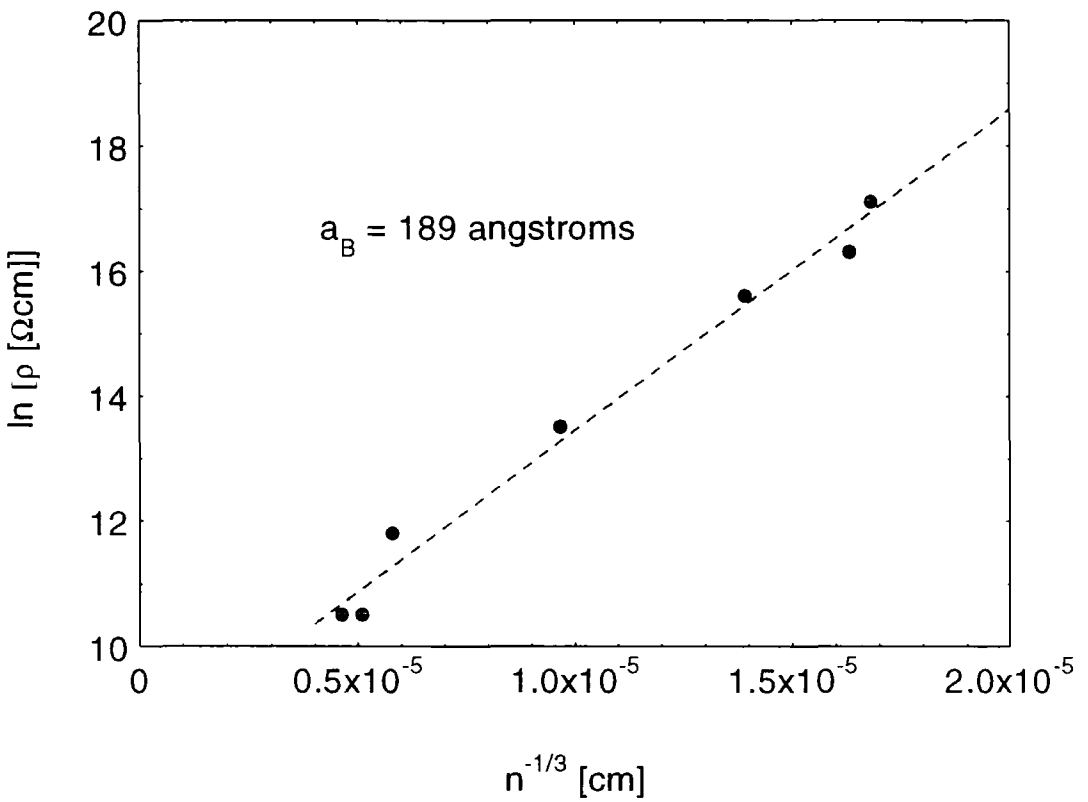

Figure 6.1.28. ln ρ plotted against $n^{-1/3}$ for the data of figure 6.1.26.

These data on sample A7 are of particular significance as the nearest neighbour hopping regime is rarely accessible in such heavily doped systems, whereas the variable range hopping conduction has been observed in many diverse materials [14]. We shall return to the low temperature impurity conduction in this sample in chapter 8 where suggestions for further work are discussed.

6.1.6. Discussion Of Results.

It has been shown that CdMnTe:In shows behaviour typical of a DX centre persistent photoconductor. Activated conduction due to the deep DX^- level and shallow hydrogenic donor is observed. Typical quenching temperatures are about 100 K. Several samples have been identified as possible candidates for a study of the MIT critical regime and the weakly localized regime. The transport properties such as the temperature dependence of the resistivity, carrier density and Hall mobility seem to be rather well understood. The magnetoresistance has been shown conclusively to arise from the dilute magnetism of the sample. It is intimately linked with the magnetization of the sample. The value of θ determined from this analysis is puzzling as it is a positive value suggesting that the relevant interactions are of a ferromagnetic nature. A tentative explanation in terms of the increased influence of the RKKY interaction has been given.

The temperature dependence of the Hall carrier concentration has been shown to exhibit an anomaly in near-metallic and metallic samples, which has been interpreted in terms of a crossover in the conduction mechanism taking place. At high temperatures activation from the deep level to the conduction band edge dominates. At lower temperatures we propose that the dominant conduction mechanism switches to metallic conduction in an impurity band. It is in the region where these two mechanisms are in competition that we see the anomalous behaviour of the Hall coefficient.

An unexplained phenomenon is that of the saturating mobility depicted in figure 6.1.10, for sample A5. As was mentioned at the time it is rather suspicious that this effect is only observed in the sample in the MIT critical region. In fact it is interesting to compare this figure with the data of Yamanouchi *et al* [15] on Si:P. They measured the Hall mobility at 4.2 K as a function of the net donor concentration, $n = N_D - N_A$, from the insulating to metallic phase. Initially small increases in n result in large increases in the mobility, but at n_c saturation begins to occur, until eventually the mobility is decreasing with n. They argued that the mobility saturates and eventually begins to decrease at the

carrier density which drives the Fermi level into the conduction band. It is quite possible that a similar situation occurs here in CdMnTe. We have already discussed the possibility that the density of states could be a strange shape due to the merging of the impurity band and the conduction band tail in the limit of heavy doping. If this were the case then mobility would certainly be strongly dependent on the position of the Fermi level, which is being shifted by the photodoping.

The compositional dependence of the phototransport data reveal a consistent picture for the x dependence of the energy levels in the forbidden gap. Such data has also been obtained for AlGaAs [16]. In that system the situation is complicated by the fact that the conduction band edge has a peculiar dependence on x due to the Γ - X crossover which occurs around 40 % Al. However Chadi and Chang [17] were able to predict the x dependence of the DX^- deep level in agreement with the experimental data. Unfortunately this process is at present impossible for the case of $Cd_{1-x}Mn_xTe$, as vital parameters are unknown for MnTe.

Section 6.1.5 presented data on sample A7 which seems to indicate that we have a rather strong case for suggesting that we are observing nearest neighbour hopping conduction at low temperatures in this sample. This provides us with an opportunity to study nearest neighbour hopping in a persistent photoconductor, where we can fine tune the resistivity of the sample with illumination. Measurements as a function of photogenerated carrier density have clearly shown a peak in E_3, and have allowed a determination of the Bohr radius.

In summary the PPC effect in $Cd_{1-x}Mn_xTe$:In has been studied in a detailed and systematic fashion and has revealed a consistent and fairly well understood set of phenomena.

6.2. Sample Set B.

This section presents the results of electrical transport measurements on sample set B. This set contains 5 samples of indium doped $Cd_{1-x}Mn_xTe$, with various compositions as listed in table 6.2.1. The composition estimated from the growth, and the composition determined by EDAX are both listed. The annealing temperature for this set of samples was 800 °C. As we shall see, this set of samples would appear to be rather heavily compensated, suggesting that the annealing process was not particularly efficient in this case.

Sample Number	Nominal x from growth	EDAX x
B4	10 %	10.0 ± 0.6
B5	10 %	10.0 ± 0.4
B6	10 %	12.9 ± 0.3
B7	10 %	9.07 ± 0.3
B8	10 %	14.2 ± 0.3

Table 6.2.1. Composition details for sample set B.

The measurements made on these samples include resistivity from 360 K to 3.9 K, Hall effect / Hall mobility from 360 K to 10 K, magnetoresistance from 140 K to 3.9 K, photoconductivity relaxation from 200 K to 3.9 K, and EDAX measurements on compositional homogeneity.

6.2.1. Resistivity and Hall Effect - Multiple DX Centres.

Samples B5, B7 and B8 exhibit perfectly normal PPC behaviour, similar to that observed in the previous section. However, they are far more resistive than samples of similar composition in set A, leading to the obvious conclusion that they are less heavily

doped or more heavily compensated. The growth data indicates that both sample sets are doped to approximately the same level, suggesting that the density of post-annealing compensating centres is larger for set B than set A.

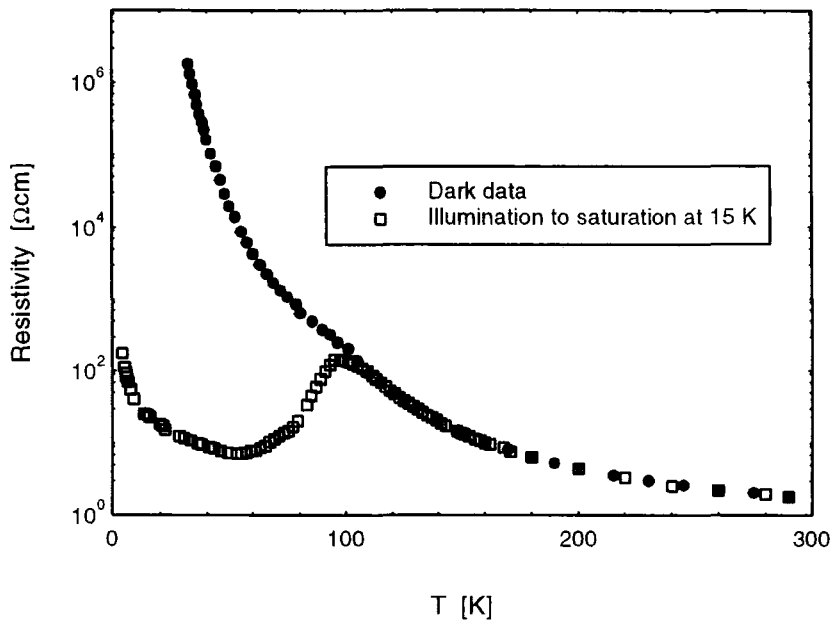

Figure 6.2.1. Temperature dependence of the resistivity for sample B5.

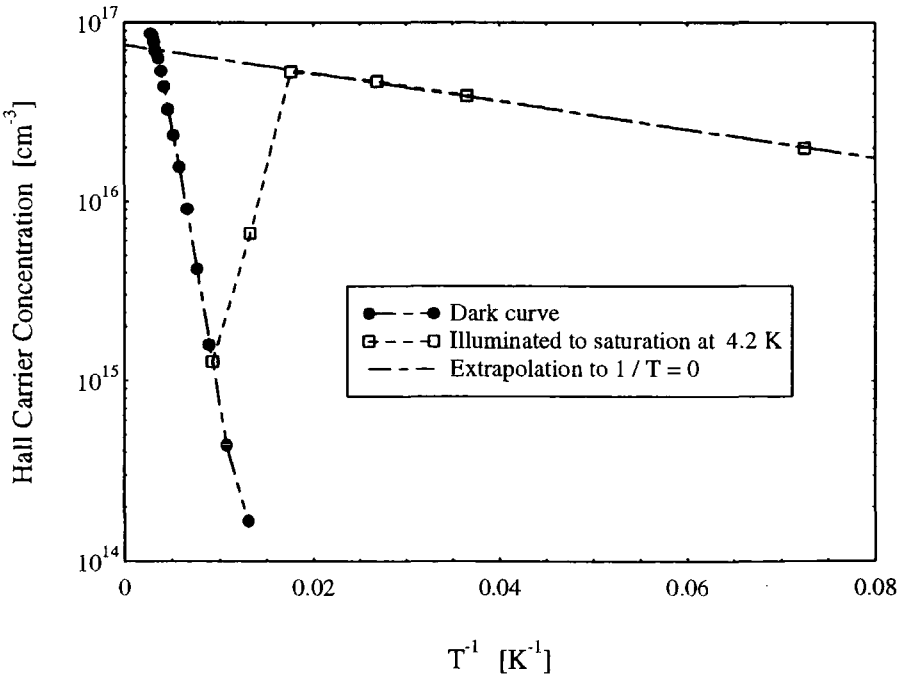

Figure 6.2.2. Temperature dependence of the Hall carrier density in sample B5.

Data for sample B5 is presented as an example of the behaviour observed. Figures 6.2.1, 6.2.2 and 6.2.3 show the temperature dependence of the resistivity, carrier concentration and Hall mobility for this sample, in the range 360 K down to 4.2 K. Clearly this sample is an insulator - the resistivity and carrier concentration show typical activated forms, while the mobility is of the same form as samples discussed previously. The PPC parameters such as resistivity, mobility, activation energies, quenching temperatures etc are shown in table 6.2.2 for all of set B. The most important point to note is that the quenching temperature of this sample along with samples B7 and B8 is around the 100 K region as expected. This is not the case for samples B4 and B6. Another point to make before we discuss these two samples in more detail, is that as mentioned in the last section very reasonable estimates of the Mn composition can be made from the determined values of the quenching temperature and the deep level activation energy. These values are listed in table 6.2.2. Reasonable agreement is found between these estimates and the EDAX values. This is reassuring as EDAX is a surface sensitive technique, whereas the transport parameters are bulk values.

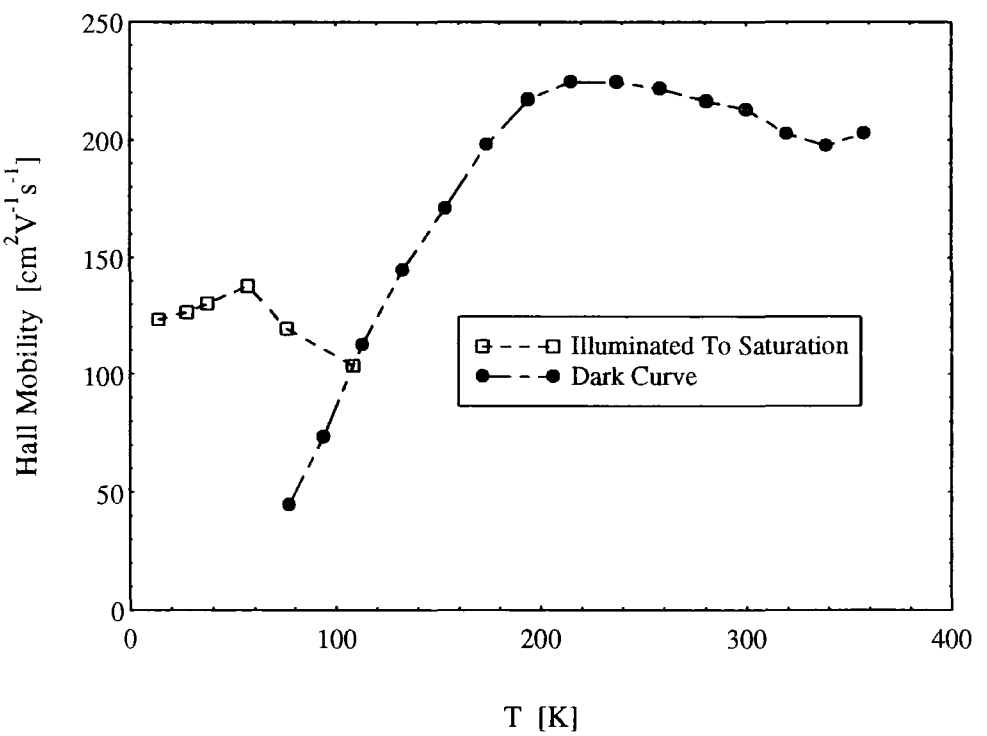

Figure 6.2.3. Temperature dependence of the Hall mobility in sample B5.

Sample Number	EDAX x	ρ (300 K) Ωcm	n (300 K) cm^{-3}	μ (300 K) $cm^2V^{-1}s^{-1}$	E_D meV	T_Q K	x from T_Q	x from E_D
B4	9.99 %	4.03	6.4×10^{15}	242	28.0	-	-	8.46 %
B5	9.97 %	0.41	6.7×10^{16}	227	36.4	109	11.86 %	9.19 %
B6	12.92 %	1.34	1.6×10^{16}	299	162.6	-	-	14.73 %
B7	9.07 %	2.19	3.7×10^{16}	78	50.5	108	11.54 %	10.19 %
B8	14.23 %	4.85	6.4×10^{15}	203	172.4	115	13.79 %	15.00 %

Table 6.2.2. Summary of transport data for sample set B. The quantities shown are the Mn fraction determined by EDAX, the resistivity at 300 K, the carrier concentration at 300 K, the mobility at 300 K, the deep level activation energy, the quenching temperature, the Mn fraction determined from the quenching temperature, and the Mn fraction determined from the deep level activation energy.

Sample B4 is typical of a small number of samples which show a very different behaviour to that presented previously. Figure 6.2.4 shows the temperature dependence of the resistivity and carrier concentration for this sample, in the dark and at full illumination, from 360 K down to 4.2 K. On cooling in the dark perfectly normal behaviour is observed with the resistivity becoming unmeasurably large at ~ 20 K. The sample was then illuminated at liquid helium temperature and warmed slowly. Normal behaviour is seen up to about 100 K, at which point the resistivity begins to fall again rather than increasing to join the dark curve. The resistivity eventually rises and joins the dark curve at 190 K. As can be seen from this figure, the increase in conductivity above 100 K is accompanied by a corresponding increase in the free carrier concentration as determined by Hall effect measurements.

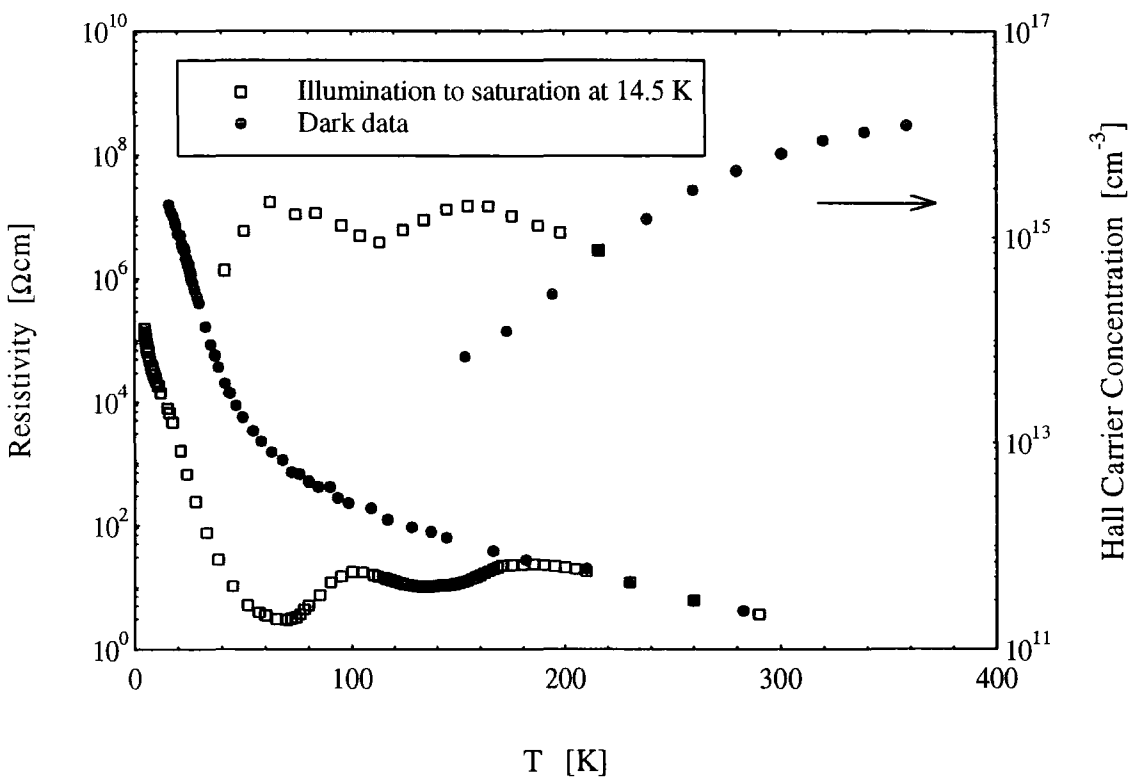

Figure 6.2.4. Temperature dependence of the resistivity and carrier density for sample B4.

So this sample would appear to be a persistent photoconductor with a quenching temperature of almost 200 K. This data is in fact very reminiscent of the data of Thio *et al* [18] on CdZnTe:Cl, where the behaviour was interpreted in terms of the formation of multiple DX centres as discussed in some detail in chapter 4. To ensure that this effect is truly high temperature PPC we need to measure the relaxation transients after illumination, as a function of temperature. This data is presented in the next section for samples B5 and B4, to allow a comparison between this new situation and a typical persistent photoconductor.

It should be noted that the resistivity curve in 6.2.4 was measured at a number of different rates of warming, to ensure that the 'second bump' in the data was not an experimental artefact due to, for instance, a thermally stimulated current [19]. The data of the next section show conclusively that the effect we are seeing is a genuine increase in the PPC quenching temperature.

6.2.2. Conductivity Transients - PPC Relaxation.

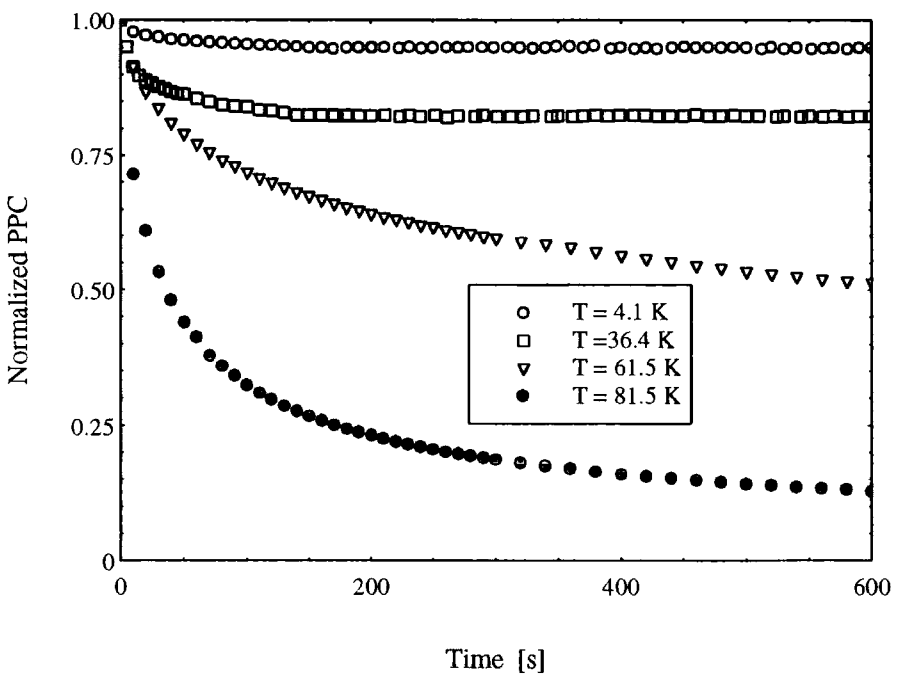

Figure 6.2.5. Photoconductivity relaxation for sample B5.

Figure 6.2.5 displays the relaxation curves for sample B5 at a number of temperatures. Here the sample is cooled in the dark to the specified temperature, illuminated to saturation, then the illumination is removed. The conductivity is then measured as a function of time. As can be seen from this figure the relaxation is a small effect at low temperatures - the photoconductivity is truly persistent. As the temperature is increased the relaxation becomes increasingly important, until the situation is reached where the photoconductivity is long lived rather than persistent. This behaviour is typical of all of the CdMnTe samples in set A.

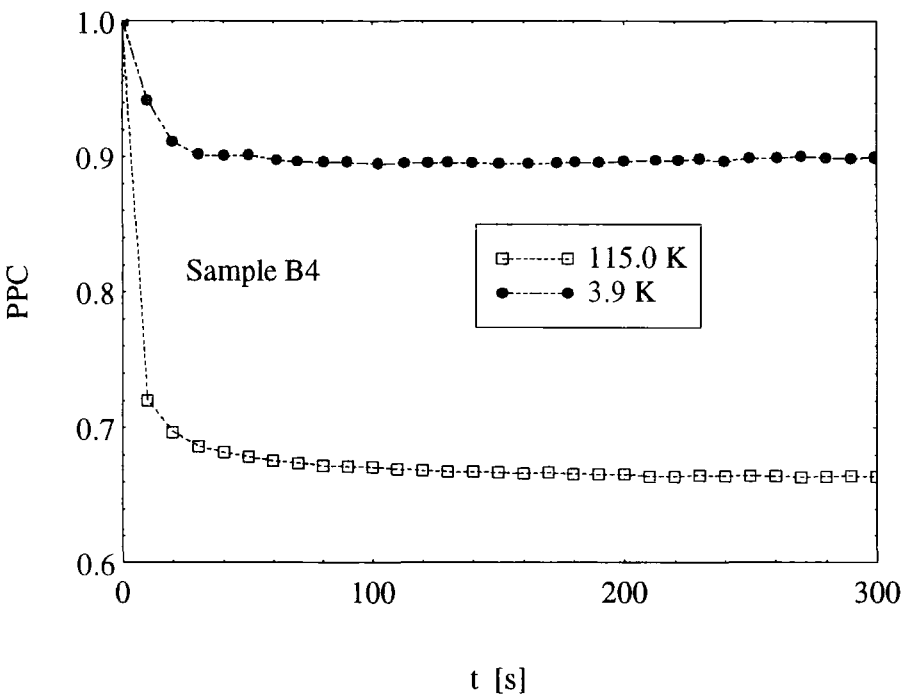

Figure 6.2.6. Relaxation curves at 3.9 K and 115.0 K for sample B4.

The situation is rather different for sample B4. Figure 6.2.6 shows the relaxation curves for this sample at 3.9 K and 115.0 K as an example. At 3.9 K the relaxation is small and rapid as expected, but at a high temperature of 115.0 K the photoconductivity is still persistent, albeit with a larger initial drop in conductivity. Relaxation curves were obtained

at a total of 13 temperatures between 3.9 K and 180 K. This data is summarised in figure 6.2.7 where a quantity termed ΔG is plotted as a function of temperature. This quantity is the conductance drop which occurs between 100 and 200 seconds on the relaxation curve. So if the photoconductivity is persistent then this quantity will be zero, but if long term relaxation is occurring then ΔG will have a finite value. Figure 6.2.7 shows convincingly that we are really observing high temperature PPC. As the temperature is increased the relaxation becomes increasingly large until ~ 120 K where ΔG drops to zero. As the temperature is increased further relaxation appears once more until eventually the PPC is quenched at a temperature of approximately 190 K. This constitutes the first observation of elevated temperature PPC in this system [20]. Similar high temperature PPC effects have been observed in other samples, including B6.

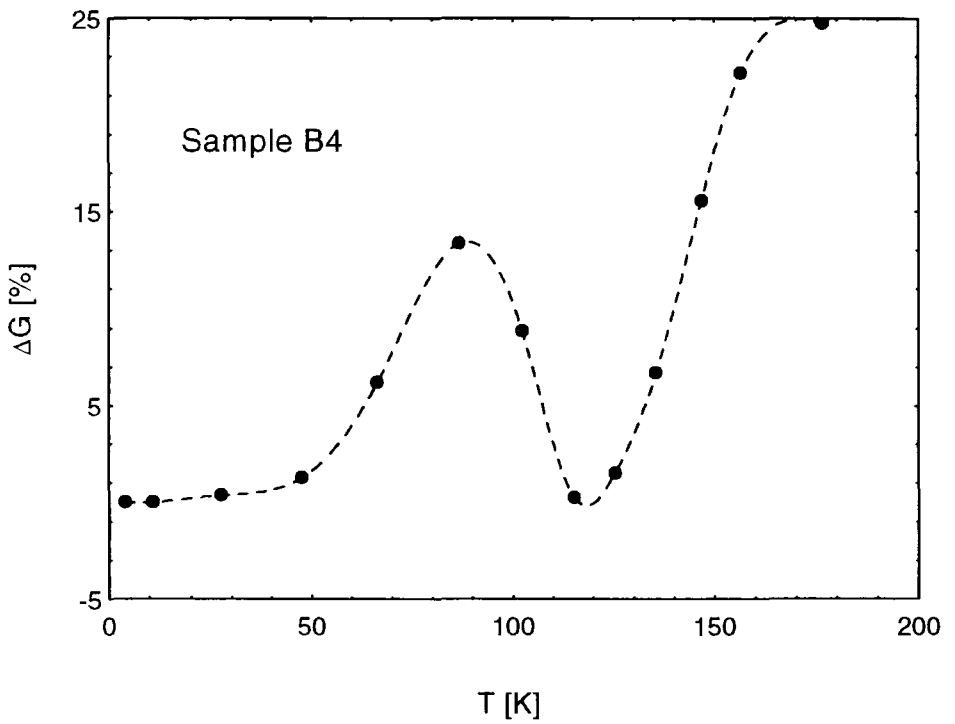

Figure 6.2.7. Temperature dependence of the quantity ΔG as defined in the text.

As mentioned earlier, this data is reminiscent of the kind of behaviour one observes when dealing with multiple DX centre formation [18]. The situation with regard to this

phenomenon was discussed in detail in chapter 4, where the effects of the local atomic environment and the formation of DX centres with slightly different atomic configuration was outlined. Clearly this data could be explained by the formation of more than one DX centre, regardless of the detailed mechanism involved. There are, however, some other plausible explanations. It was shown in section 6.1.4 that the PPC quenching temperature increases with x, meaning that if this sample contains a macroscopic inhomogeneous region with a very large Mn fraction then it is possible that it could support PPC up to 190 K. Although $T_Q(x)$ was only measured up to 20 % Mn, an extrapolation of this data suggests that a region with a Mn composition of 38 % would be required to produce a T_Q of 190 K. This has to be considered extremely unlikely in a 10 % sample, particularly in the light of the EDAX measurements presented in the next section. In addition to this situation, it is also possible that we are observing PPC which is not due to the formation of DX centres at all. Compositional or compensational fluctuations can lead to long lived photoconductivity as detailed in chapter 4. There are several arguments against this viewpoint. Firstly, the relaxation measurements suggest that the photoconductivity we observe is truly persistent, rather than simply long lived as would be expected from the fluctuation model. Secondly, in all of these experiments we are illuminating with a 940 nm (1.3 eV) LED i.e. we are using sub band gap radiation to deliberately excite the DX centre PPC. Hence, band to band transitions which could lead to long relaxation times in the presence of fluctuations, should be negligible. Even in the presence of fluctuations in the position of the conduction band edge, the minimum band gap which can occur at any point is that of CdTe i.e. 1.5 eV. In spite of the fact that these two explanations based on inhomogeneity appear rather unlikely, we have attempted to measured the extent of the compositional fluctuations in the next section.

6.2.3. EDAX Measurements.

The EDAX technique described in section 5.1 can be used to measure the Mn fraction as a function of position while scanning the electron beam across the surface of the sample. Obviously this is a surface sensitive technique, but it should be noted that

individual samples are simply sliced from the original as-grown crystal, meaning that the surface of any particular sample is in no way special in terms of the composition. A PC based Monte Carlo simulation program [21] was used to calculate the penetration depth of the electron beam, along with the width of the generation volume, which provides an effective spatial resolution of the technique. Simulations for CdTe suggest that at a beam voltage of 15 kV the mean and maximum penetration depths are 0.45 and 1.35 μm respectively. The spatial resolution at this voltage is predicted to be 2.0 μm. In all of the measurements made on these samples, no beam voltage dependence of the measured Mn fraction was observed in the range 10 kV up to 25 kV, suggesting that, at least in the surface region, the Mn fraction is independent of depth.

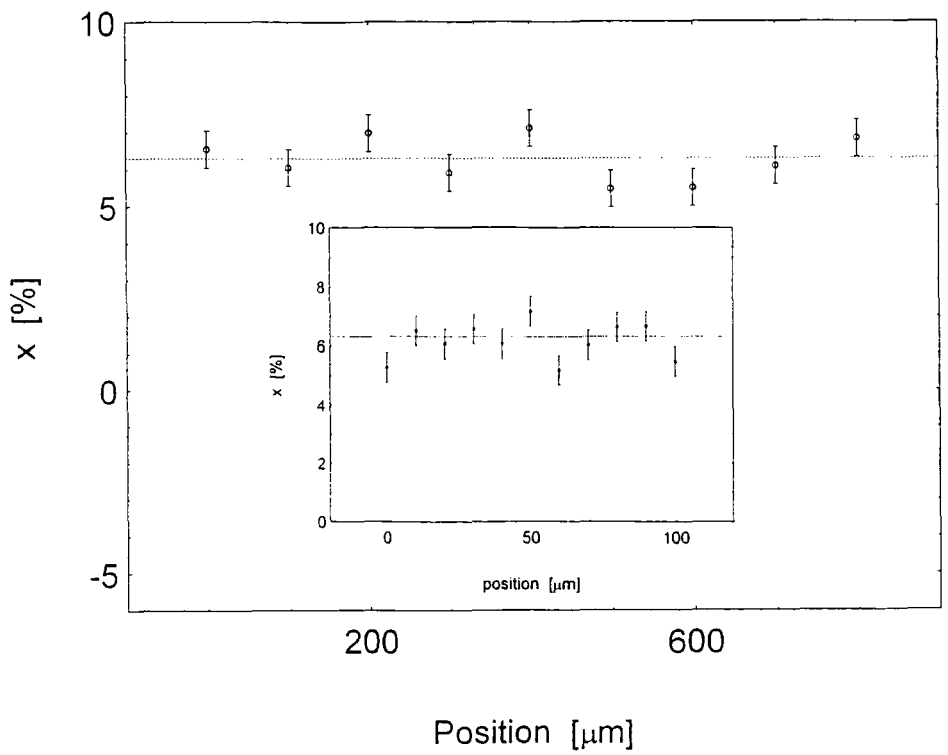

Figure 6.2.8. EDAX data for sample A2 - compositional homogeneity.

Figure 6.2.8 shows EDAX data for sample A2, as an example of a crystal which shows no elevated temperature PPC. The main figure shows measurements over a range of 800 μm, while the inset shows measurements over 100 μm at 10 μm intervals. Good

compositional homogeneity is observed. In the main figure the standard deviation of the points is only 0.62 % Mn, while in the inset the standard deviation is 0.83 % Mn. Scans were also done over 100μm x 100μm areas at random positions on the crystal surface. These produced a mean value of x of 6.3 ± 0.3 % in agreement with x = 6.14 ± 0.22 % determined from a scan of the whole surface. All in all it appears that the compositional homogeneity of this sample is rather good. This data is typical of all of the samples studied.

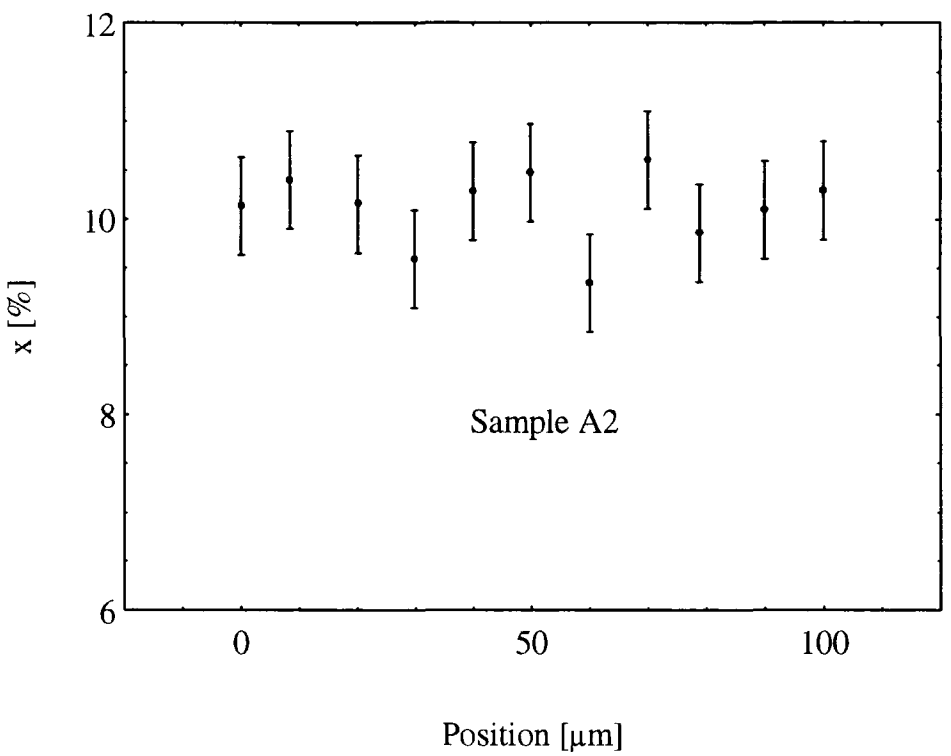

Figure 6.2.9. EDAX data for sample B4 - compositional homogeneity.

Similar data for sample B4 is shown in figure 6.2.9. The standard deviation of these points is only 0.61 % Mn, while the mean is in agreement with the value of 10.0 ± 0.6 %, as determined by a scan of the whole surface. Six scans over an area 100μm x 100μm at random positions produced x values of 10.7 %, 9.7%, 9.5%, 10.0.%, 9.0 % and 9.0 %. It should be noted that this sample, as with all of the others, was also checked for

macroscopic compositional homogeneity under an infrared microscope. No inhomogeneity was observed.

It seems therefore that sample B4, as well as others displaying elevated temperature PPC, show no evidence of large scale compositional fluctuations or macroscopic regions of very large Mn fraction. Indeed, the level of fluctuations evident in these samples is very similar to that observed in other samples which do not display this phenomenon. We can therefore conclude that the origin of the elevated temperature PPC effect we see here is due to some form of multiple DX centre formation. It is very tempting to describe the data in terms of the Park and Chadi [22] model of multiple DX centre formation, where several states are possible, each having a slightly different atomic configuration. The main problem with this interpretation is that their calculations specifically predict that this situation is not possible in CdTe based compounds doped with group III elements such as In. They claim that multiple DX centre formation should only be seen for the case of group VII donors such as Cl in CdZnTe. Thus, either the high temperature PPC effect seen here has some other origin unconnected with this form of multiple DX centre, or there may be a limit to the applicability of the Park-Chadi theory. The situation is complicated by the fact that multiple DX centres with slightly different binding energies can arise because of the sensitivity of the impurity centre to its local atomic environment, as discussed in chapter 4.

A problem with interpreting the data in terms of the effects of the local atomic environment is that one might expect to observe DX centres with a spectrum of binding energies corresponding to i = 0,1,2 or 3 Mn atoms in the defect configuration. In our case it appears that we only observe two DX centres, although it should be noted that very careful examination of figure 6.2.4 reveals some structure in the resistivity curve around 140 K. Moreover, this anomaly is repeatable. It is possible to calculate the probability of formation of DX centres with i = 0,1,2 or 3 Mn atoms as a function of the Mn fraction. The results of an extremely simple calculation to determine the probability of finding i Mn atoms around any particular In atom is shown in figure 6.2.10 (see appendix A for details

of the calculation). Clearly, for a 10 % Mn sample the probability of finding states with i = 2 or 3 is extremely small. It is also interesting to note that in a crystal with a certain density of In atoms, a number N_{DX} DX centres will form. Hence there are $4N_{DX}$ atoms of Cd or Mn in the DX centre configurations. For a crystal with a Mn fraction x, then there are $4xN_{DX}$ Mn atoms in the DX configurations. Therefore the average number of Mn atoms in a particular defect centre is simply $4x$. So for a 10 % sample we get an average number of Mn atoms in the DX configuration of only 0.4.

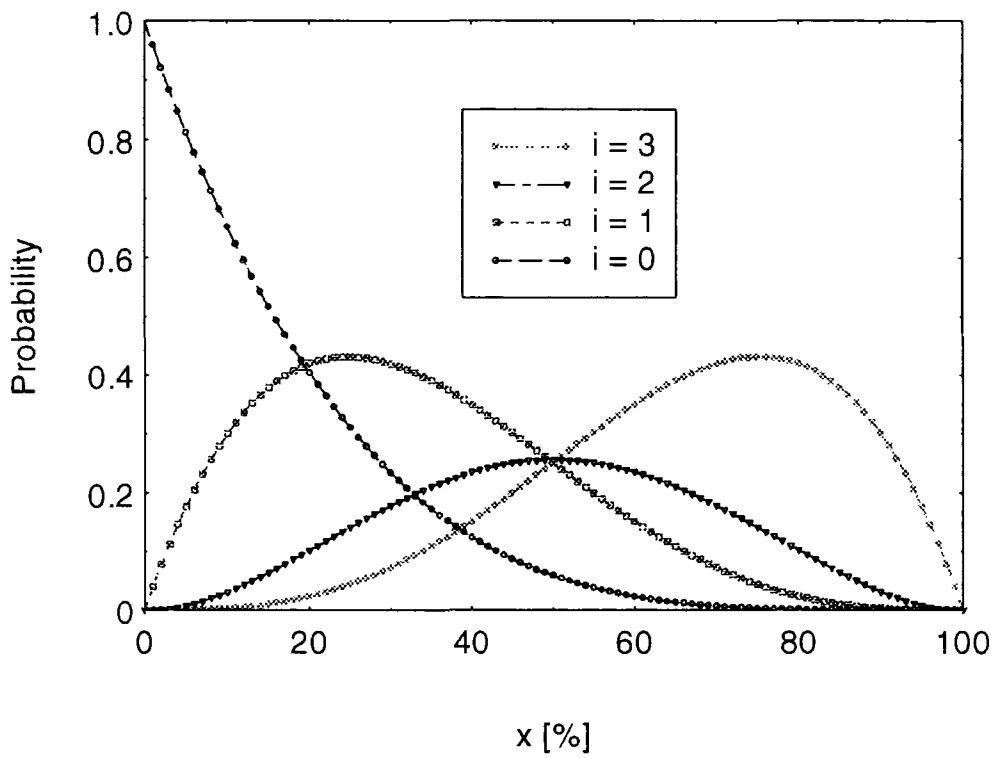

Figure 6.2.10. Probability of finding DX centres with i Mn atoms, as a function of x.

This fact along with the results shown in figure 6.2.10 could well explain why we only seem to be observing only two DX centres - the probability of forming DX centres with anything other than 0 or 1 Mn atoms is very small. It should also be noted that most of the measurements on AlGaAs, in which the effects of the local atomic environment are

seen, are involved with samples with Al fractions greater than 22 % [see section 4.5.2]. Hence it is far more likely that 4 centres are observed.

6.2.4. Negative Magnetoresistance.

As we have seen in section 6.1.3 one usually observes positive low field MR at low temperatures in CdMnTe:In. This behaviour is carrier concentration dependent, with the more insulating samples showing a larger MR effect. This is indeed true of the samples studied in set B, where a relatively large positive MR effect is observed at temperatures below approximately 20 K. As an example, sample B5 has a value of $\Delta\rho/\rho_0$ of 0.8 in a 0.3T magnetic field at 4.2 K. All of the samples show a positive MR at low temperatures which has the same qualitative features as the samples in set A.

An interesting feature observed in sample B5 is the existence of a negative MR at high temperatures under certain experimental conditions. If the sample is continuously illuminated at temperatures around 100 K, a very sharp negative MR is observed at low fields, followed by the usual positive MR at slightly higher fields. The magnetoresistance in this region is usually unmeasurably small. Figure 6.2.11 shows the magnetoresistance of this sample in the low field region at 106.7 K, for various illumination levels. The dark data is shown along with three other curves where the sample is *continuously illuminated* with the LED current shown. Obviously the greater the LED current the greater the photon flux at the sample, as the LED is kept at a constant temperature throughout the measurement. This figure shows clearly that in the dark no MR is observed, but as the photon flux is increased the negative MR becomes increasingly large. The size of the negative MR increases with the photon flux up to the largest LED currents possible. The negative MR itself is rather sharp, and occurs up to fields of about 0.05 T before the positive MR takes over. It should be noted that the anisotropy in the MR observed here is due to the additional contribution of the Hall effect superimposed on the resistance. This is normally subtracted from the MR data, but the unusual shape of the MR in this case prohibits this.

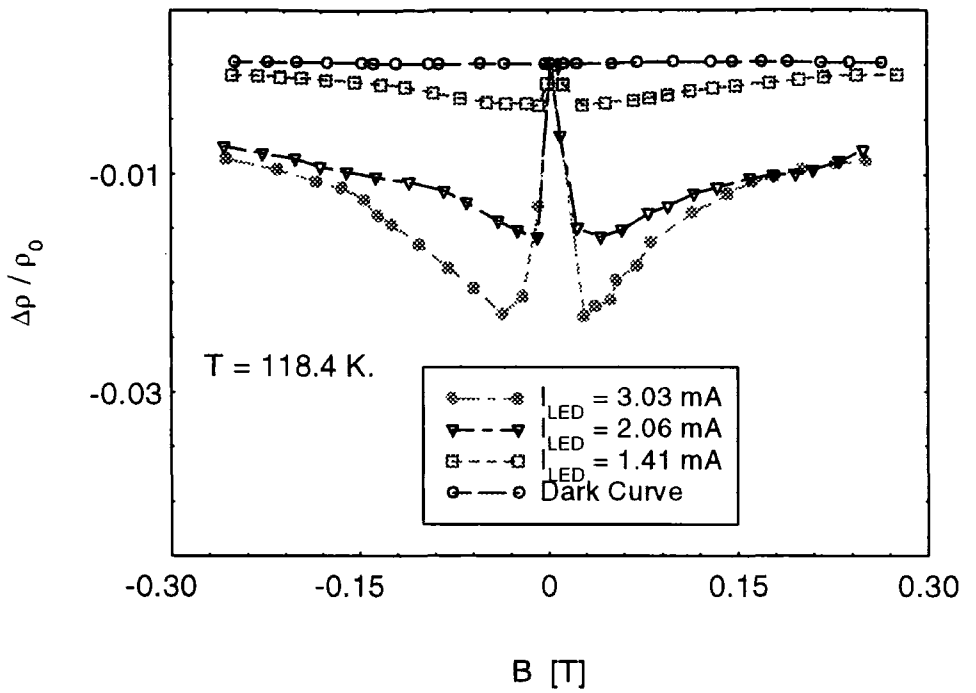

Figure 6.2.11. Negative MR in sample B5 at 118.4 K, as a function of illumination level.

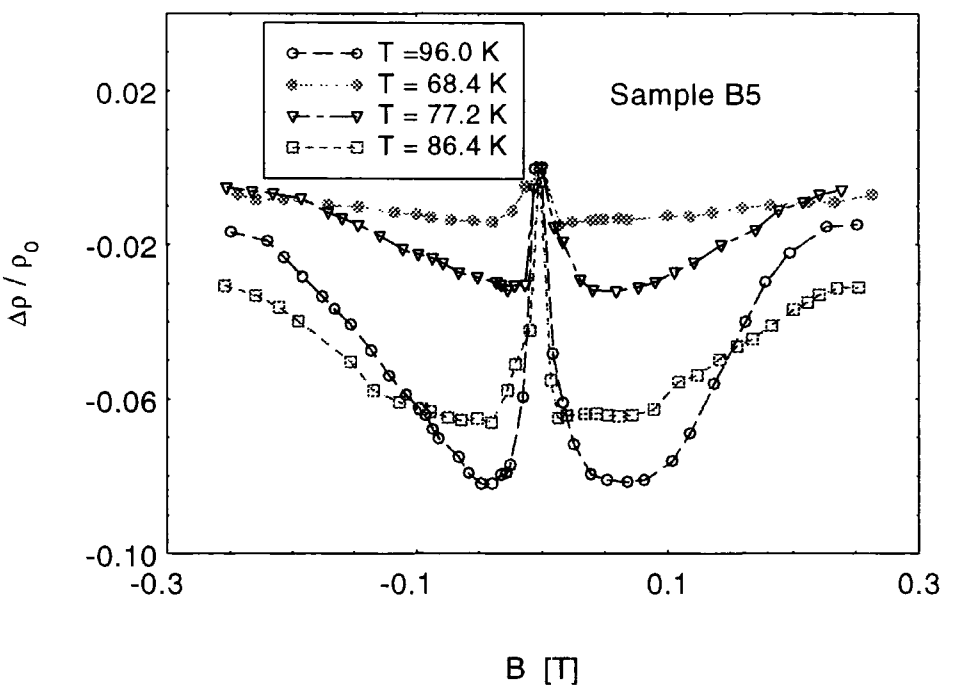

Figure 6.2.12. Negative MR as a function of temperature in sample B5.

This negative MR is also a strong function of temperature. Figure 6.2.12 shows the MR up to 0.3 T at a number of temperatures in the range 68.4 K up to 96.0 K, at a fixed LED current of 3.0 mA. The negative MR shows a monotonic increase with increasing temperature. The curves are all of qualitatively similar shape although it is clear that at low temperatures where the effect is smaller, the negative MR is less sharp. The full temperature dependence of this effect is shown in figure 6.2.13, where the value of $\Delta\rho/\rho_0$ at 0.05 T is plotted as a function of temperature from 60 K up to 150 K. This figure gives the first indication as to the origin of this phenomenon. Clearly the negative MR effect peaks at a temperature of ~ 95.8 K. The quenching temperature of this sample as determined by the PPC measurements is 97.8 ± 4.4 K, where the relatively large uncertainty is due to the fact that the T_Q value is dependent on the warming rate, which cannot be controlled perfectly.

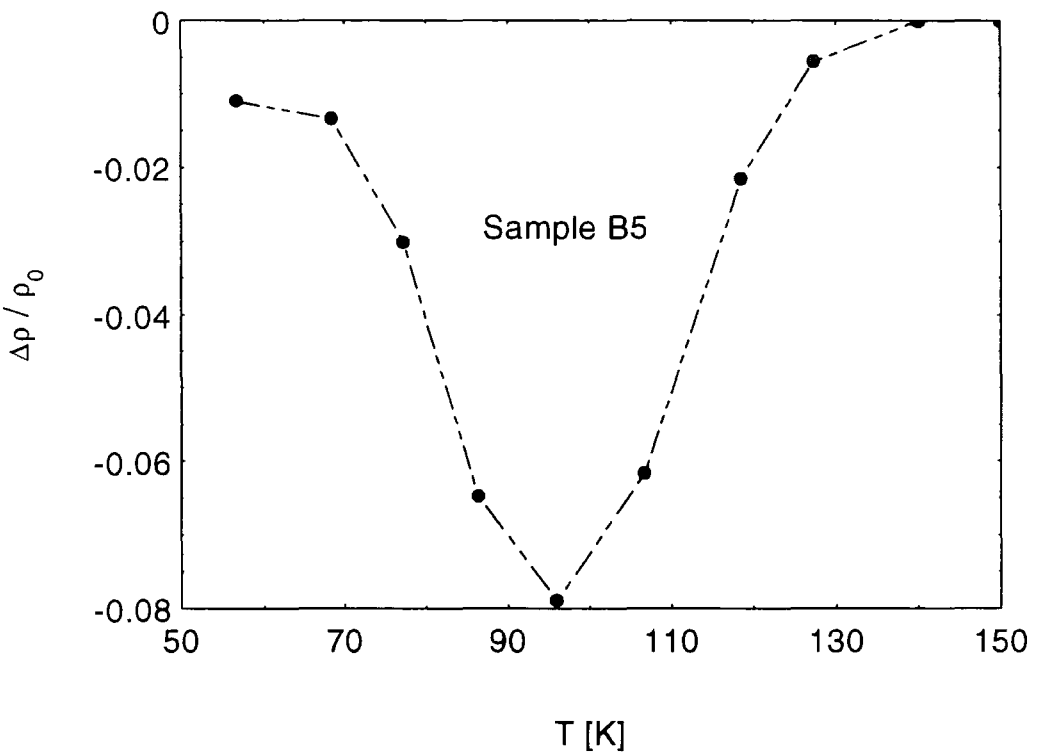

Figure 6.2.13. Temperature dependence of the fractional MR at 0.05 T in sample B5.

It seems that there are two essential ingredients for the negative MR to occur : temperatures close to T_Q, and continuous illumination. Consider the case of a negative U DX model, where T is just less than T_Q and the sample is being constantly illuminated with photons of a suitable wavelength to excite the DX centres. As T is close to T_Q considerable relaxation will be occurring after illumination i.e. electrons are being thermally excited over the barrier to recapture, and in to the DX^- deep states. If however, the sample is being constantly illuminated in this situation, then a quasi-equilibrium is eventually reached, where the relaxation and photoconductivity effects are balanced and the sample resistance is constant. This is the condition in which these measurements have been made. The essential point here is that normally the deep level contains two electrons which are supposed to have opposite spin producing a diamagnetic defect centre. However, in our quasi-equilibrium situation there will be a significant number of *single* electrons in these deep states, the other electron having been promoted to the shallow level after absorption of a photon. It is feasible then, that this deeply bound single electron can interact with the Mn atoms in its vicinity to form a BMP. This BMP formation would naturally lead to a sharp negative MR as discussed in some detail in section 2.3.4. As the field is increased from zero the individual magnetic polarons align with each other to minimize the spin-disorder scattering rate leading to negative MR. The negative MR only persists up to small fields as the polarons align very quickly due to their large susceptibility. This is what we observe in our experiments, where the MR persists up to about 0.05 T. It must be stressed that the only reason that we can observe such behaviour at temperature around 100 K, is that we are not dealing with a BMP formed in the shallow impurity levels. We are dealing with electrons in deep states, with small localization radii. In fact, in a DX deep level the size of the polarons is presumably comparable to the lattice constant i.e. about 0.6 nm. This suggests that any polaron formed will have only one or two Mn atoms within its localization radius.

It should be noted that small magnetic polarons such as these have been suggested as a possible mechanism for the negative colossal MR observed in the magnetoresistive

perovskites [23]. These effects are in fact observed in a similar (or even higher) temperature region to our own measurements.

If our explanation of the origin of this effect were correct then one obvious prediction is that it should be possible to observe some form of photomagnetization in this temperature region at low fields. This is because illumination will lead to the formation of BMPs which will have a very large low field susceptibility leading to an increase in the magnetization on illumination. Figure 6.2.14 shows this photoinduced increase in the magnetization, ΔM, as a function of temperature [24]. Although the data set is limited, this plot certainly suggests that ΔM reaches a maximum (positive) value in the region where the MR peaks i.e. the quenching temperature. So the MR and photomagnetization data seem consistent with each other and with our simple model.

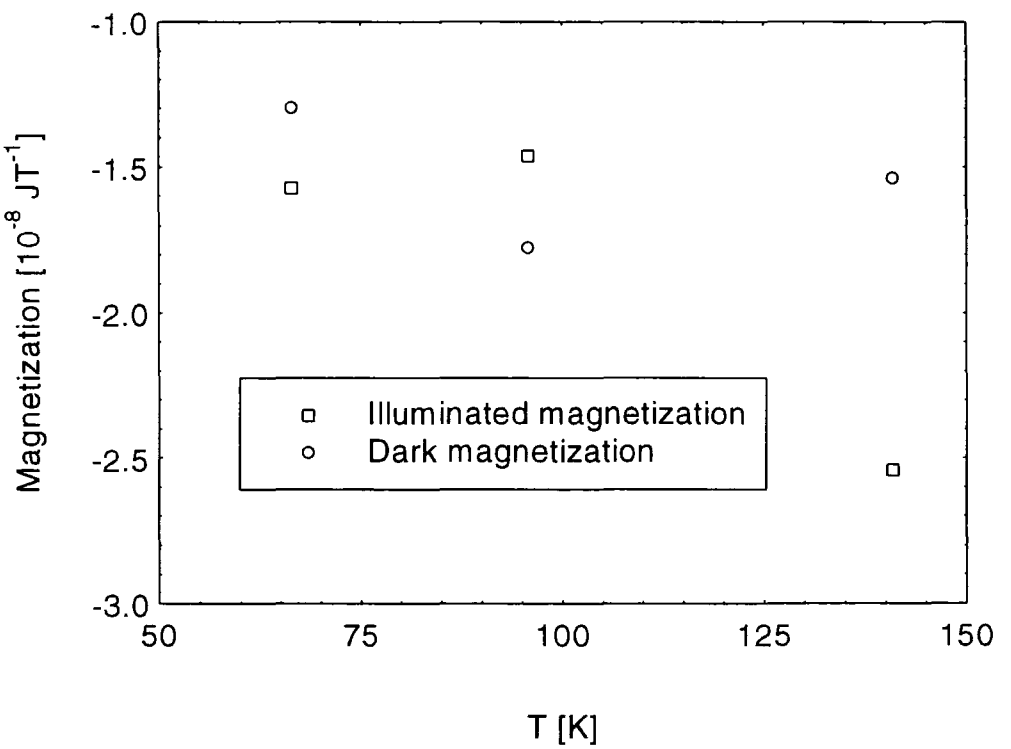

Figure 6.2.14. Photomagnetization against temperature in the region where the negative MR effect is observed.

The final point to be addressed here is why do we observe this negative MR effect in some samples but not in others. We believe that the answer to this question may lie in the temperature dependence of the mobility. It seems clear that for this effect to be visible, the spin-disorder scattering (which is responsible for the MR) must be a significant effect. In many insulating samples the ionized impurity scattering is so large in the 100 K region that it could well swamp any contribution for a spin-disorder scattering effect. For example, samples such as B6 and B8 have low mobility around 100 K and show a very rapid decrease in the mobility below about 150 K due to the effects of ionized impurity scattering. Samples such as B5 (see figure 6.2.3) have a higher mobility in this region, and show a weaker temperature dependence of the mobility. In summary, we suggest that samples with high mobilities in the region around 100 K (along with a weak temperature dependence of the mobility) are likely to display the negative MR effect.

6.2.5. Discussion Of Results.

We have seen that the transport properties of sample set B are in general similar to that observed in most samples, with the obvious exception that they are all insulating. Sample B4 is representative of a small number of samples which show elevated temperature PPC. We have analysed the experimental and theoretical situation in depth and have been led to the conclusion that this behaviour is due to the formation of some form of multiple DX centre. We are left with the possibility that these centres form due to the effects of the local atomic environment or because several centres with slightly different configurations are possible. It is rather difficult to distinguish between the two, although it should be noted that other systems which show multiple DX behaviour due to the effects of the local atomic environment often need measurements such as DLTS or TSCAP to clarify the subtle behaviour, whereas we see this effect very clearly in the resistivity. On the other hand, the theory of Park and Chadi suggests that multiple DX centres with different atomic configurations are not possible for CdMnTe:In. Although the

situation cannot be clarified completely at this stage it is clear that the behaviour we observe is due to some form of multiple DX centre formation.

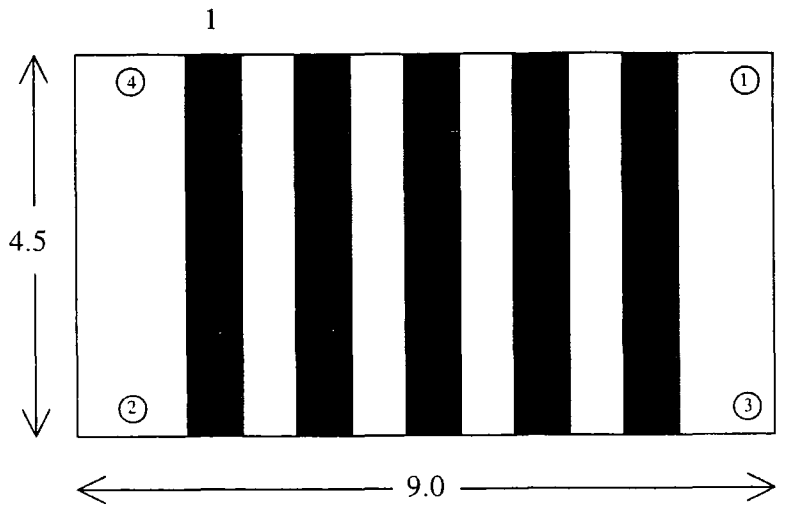

Figure 6.2.15. Diagram of the sample used for the photoinduced anisotropy measurements.

The huge application potential of a room temperature persistent photoconductor is something which has already been mentioned. This potential has been highlighted by the experiments on AlGaAs [25, 26] which have shown that it is indeed possible to write conductive patterns on an insulating background using this technique. A very simple experiment has been performed on CdMnTe:In with the same conclusion. A piece of sample B7 of dimension 9.00 mm x 4.50 mm x 1.34 mm was covered with 1 mm wide stripes of tape which is opaque to infra red radiation. The sample is shown in figure 6.2.15. Due to the rectangular shape of the sample, some anisotropy in the resistivity is measured. This anisotropy, $\kappa = R_{41,23} / R_{42,13} = 0.916$ at 300 K. The sample was then cooled to 77.4 K in the dark and the resistivity measured again. The measured resistances were of course much larger, but the anisotropy is unchanged as expected. On illumination for 5 minutes at 940 nm the anisotropy was seen to change to $\kappa = 2.332$, meaning that we have photoinduced a change in the anisotropy by a factor of 2.545. The natural explanation of this effect is that we have been able to write conductive stripes on the material, which account for the observed anisotropy. In light of this experiment and the

observation of 200 K PPC in this material, it seems clear that CdMnTe is an interesting material in terms of room temperature applications of PPC.

Finally, we have discussed an interesting negative MR effect observed in sample B5 when continuously illuminated with infra-red. A simple theory based on the formation of BMPs around single electrons in deep levels has been put forward to explain our data. Photomagnetization experiments performed by A.B. Horsfall *et al* [24] support this hypothesis, and are consistent with the MR data. If this is indeed the correct interpretation of our data, then this is an exciting piece of physics as BMPs are rarely observed at such temperatures, particularly in DMS.

Note : The sample numbering scheme used throughout this chapter is inconsistent with that used in ref [20]. In that paper samples A1, A2, A3 and A4 correspond to samples A2, A4, A5 and A6 in this chapter.

Chapter 6 - References.

1. P. Becla. Department of Materials Science and Engineering, Massachusetts Institute of Technology, Cambridge, MA 02139.

2. I. Terry, T. Penney, S. von Molnar, J.M. Rigotty and P. Becla. Solid State Commun. **84** 235 (1992).

3. J. Stankiewicz and F. Palacio. Phys. Rev. B. **56** 1 (1997).

4. A.C. Beer in *Solid State Physics* eds F. Seitz and D. Turnbull (Academic Press, NY, 1963). p.150.

5. B.K. Ridley. Quantum Processes in Semiconductors. (Oxford Clarendon Press, 1988).

6. N.G. Semaltianos, G. Karczewski, T. Wojtowicz and J.K. Furdyna. Phys. Rev. B. **47** 12540 (1993).

7. K.J. Malloy and K. Khatchaturyan in *Semiconductors and Semimetals* vol 28 eds R.K. Willardson and A.C. Beer. (Academic Press, Ny, 1993). p.235.

8. Y. Shapira, N.F. Oliveira Jr, P. Becla and T.Q. Vu. Phys. Rev. B. **41** 5931 (1990).

9. T. Dietl, M. Sawicki, T. Wojtowicz, J. Jaroszynski, W. Plesiewicz, L. Swierkowski and J. Kossut. *Anderson Localization.* Eds. T. Ando and H. Fukuyama. (Springer Verlag, 1987).p 58.

10. I. Terry, T. Penney, S. von Molnar and P. Becla. J. Cryst. Growth. **159** 1070 (1996).

11. S. von Molnar, I. Terry, T. Penney and P. Becla. Physica B. **197** 151 (1994).

12. A.L. Efros and B.I. Shklovskii. *Electronic Properties of Doped Semiconductors.* (Springer Verlag, 1984) p.168.

13. T. Thio, J.W. Bennett and P. Becla. Phys. Rev. B. **54** 1754 (1996).

14. N.F. Mott. *Conduction in Non-Crystalline Materials.* (Clarendon Press, 1987).

15. C. Yamanouchi, K. Mizuguchi and W. Sasaki. J. Phys. Soc. Jpn. **22** 859 (1967).

16. N. Chand, T. Henderson, J. Klem, W.E. Masselink, R. Fischer, Y.C. Chang and H. Morkoc. Phys. Rev. B. **30** 4481 (1984).

17. D.J. Chadi and K.J. Chang. Phys. Rev. B. **39** 10063 (1989).

18. T. Thio, J.W. Bennett and P. Becla. Phys. Rev. B. **54** 1754 (1996).

19. R.H. Bube. *Photoconductivity Of Solids* (Wiley, 1960). p. 275.

20. C. Leighton, I. Terry and P. Becla. Phys. Rev. B. In press.

21. E. Napchan. *Monte Carlo Simulations* Ver.5A29 (1992).

22. C.H. Park and D.J. Chadi. Phys. Rev. B. **52** 11884 (1995).

23. J.M. De Terese, M.R. Ibarra, P.A. Algarabel, C. Ritter, C. Marquina, J. Blasco, J. Garcia, A. del Moral and Z. Arnold. Letters to Nature. **386** 256 (1997).

24. C. Leighton, A.B. Horsfall, I. Terry and P. Becla. In preparation.

25. T. Thio, R.A. Linke, G.E. Devlin, J.W. Bennett, D.J. Chadi and M. Mizuta. App. Phys. Lett. **65** 1802 (1994).

26. R.A. Linke, T. Thio, D.J. Chadi and G.E. Devlin. App. Phys. Lett. **65** 16 (1994).

7. The Metal-Insulator Transition in $Cd_{1-x}Mn_xTe$.

This chapter presents the results of the experiments on samples of CdMnTe, in the vicinity of the MIT. Transport measurements have been made on four samples of CdMnTe:In - A1, A2, A5 and C5 (a sister sample of A5). In addition to this, 3 samples of CdMnTe:In,Al and one sample of CdMnTe:Al, have been studied as they are either metallic or close to being critical. These samples are dealt with in section 7.4. All of the samples in both set A and B are shown in figure 7.1.1, where the resistivity is plotted against the free carrier density at 300 K. The resistivity shows a dramatic decrease with increasing carrier density, as expected. Although the exact value of the critical carrier density is different for each of these samples (because of their differing compositions), the critical carrier density of CdTe is shown, to give some indication of where the MIT occurs.

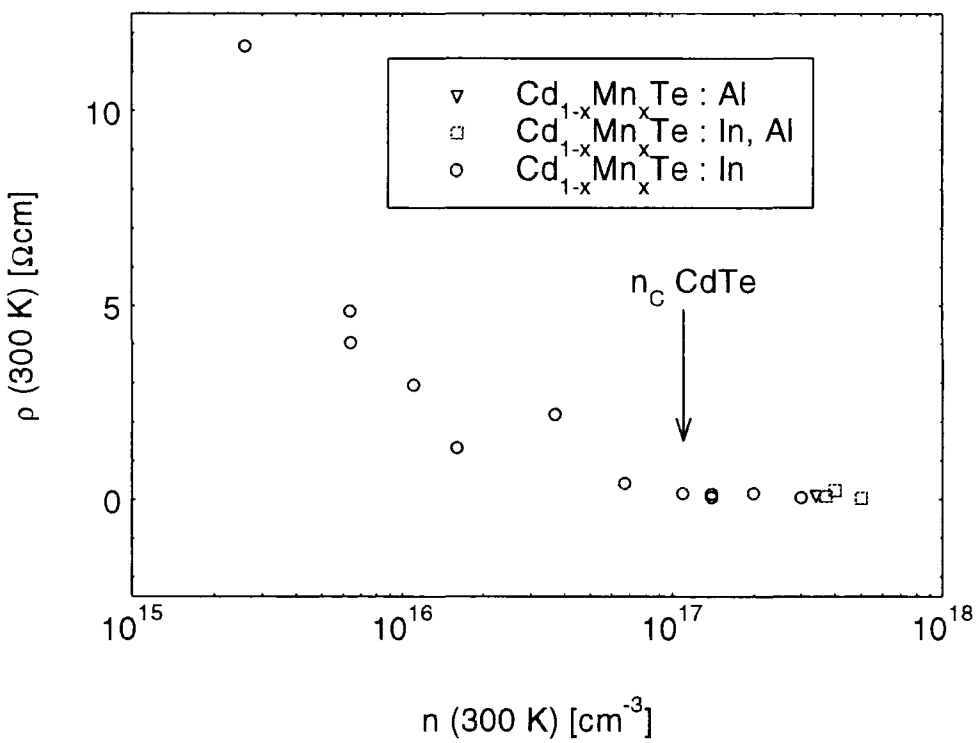

Figure 7.1.1. Resistivity against Hall carrier concentration at 300 K for all of the samples studied.

The chapter is organised as follows. Section 7.1 presents the resistivity and Hall effect measurements down to 4.2 K on the indium doped samples. Section 7.2 discusses the zero magnetic field MIT as probed by PPC experiments performed at temperatures down to 300 mK. The temperature dependence of the conductivity in the insulating and metallic phases is discussed quantitatively, and the scaling theory of localization is applied in the critical region. Finally, section 7.3 discusses the temperature dependence of the conductivity in the WLR.

7.1. Near Metallic and Metallic Samples.

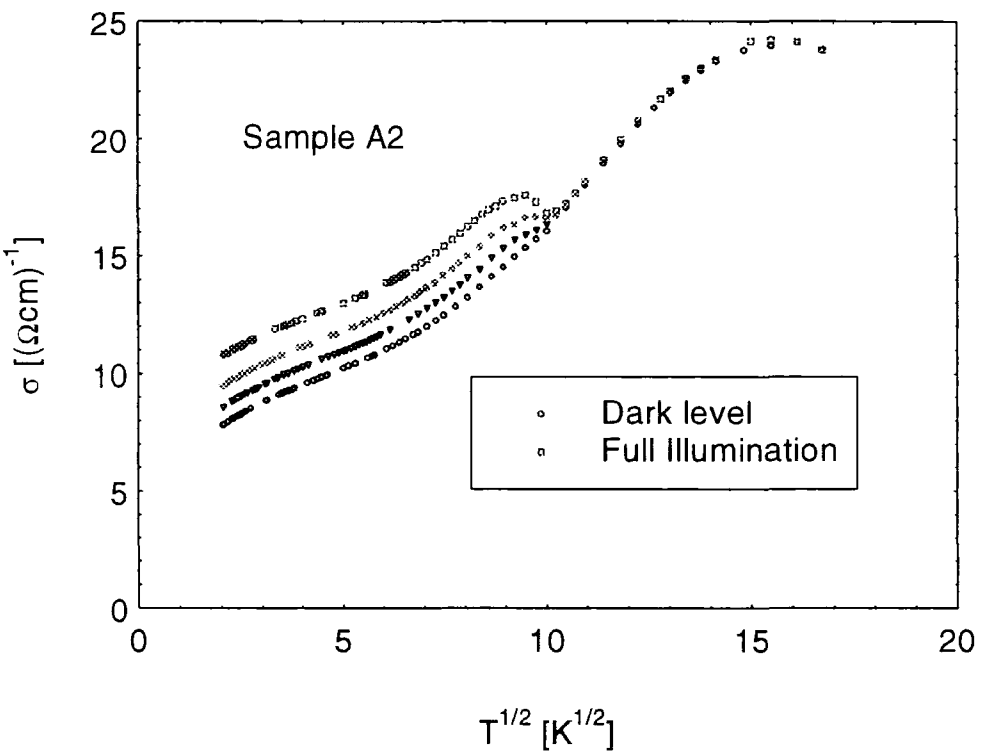

Figure 7.1.2. Temperature dependence of the conductivity of sample A2

Sample A5 has already been discussed in some detail in chapter 5, where it was mentioned that this sample can be driven through the MIT by illumination, as can its sister sample C5, which has almost identical transport properties above 4.2 K. The whole of

section 7.2 is devoted to these two samples. Samples A1 and A2 are also of interest, due to their proximity to the MIT. Figure 7.1.2 shows the temperature dependence of the conductivity for sample A2, where it can be seen that this sample would appear to be metallic even before illumination. Lower temperature transport measurements presented in section 7.3 confirm this.

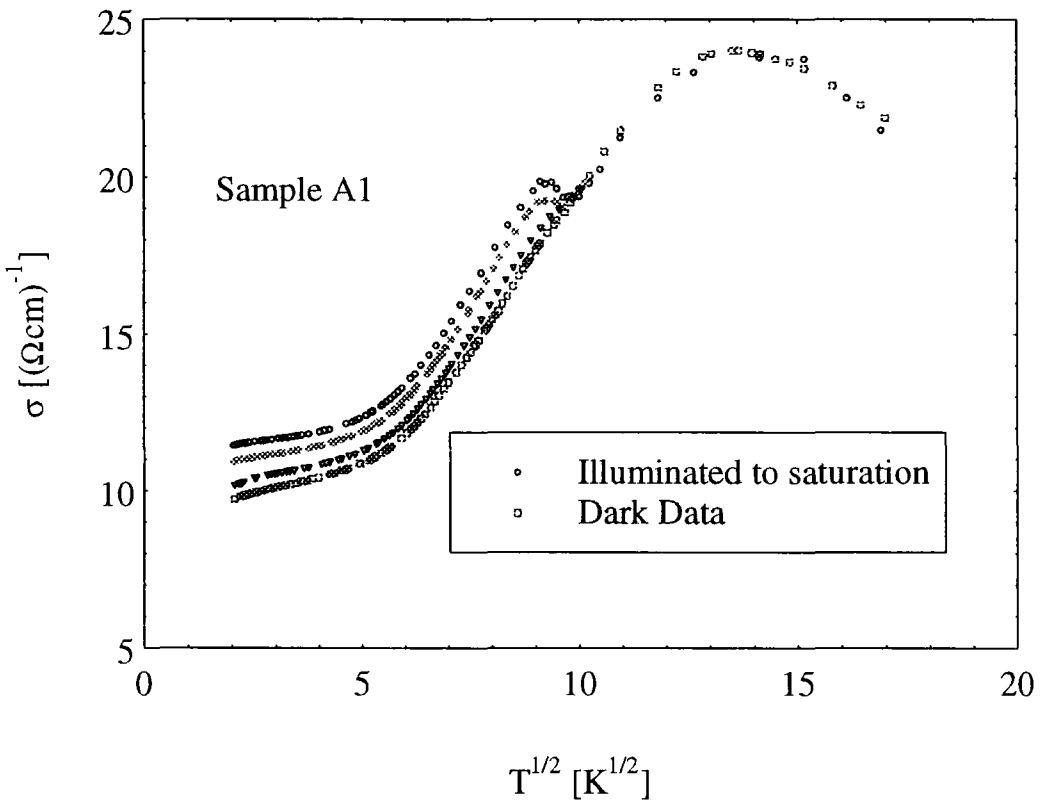

Figure 7.1.3. Temperature dependence of the conductivity of sample A1.

Figure 7.1.3 shows the temperature dependence of the conductivity for sample A1, in the dark and at 3 photogenerated carrier concentrations. This sample is rather interesting as the values of the conductivity and carrier concentration are the largest measured in a sample of CdMnTe:In in this study. A very weak temperature dependence of the conductivity is observed, while the extrapolated zero temperature conductivity would appear to be as high as ~ 11 $(\Omega cm)^{-1}$. If this data is plotted as $\ln\rho$ against T^{-1}, a

force-fit to an activated form at low temperatures leads to activation temperatures (E/k_B) of 0.280 K in the dark and 0.134 K at full illumination. This is clearly unphysical as the measurement is made at temperatures of the order of 20 to 4.2 K.

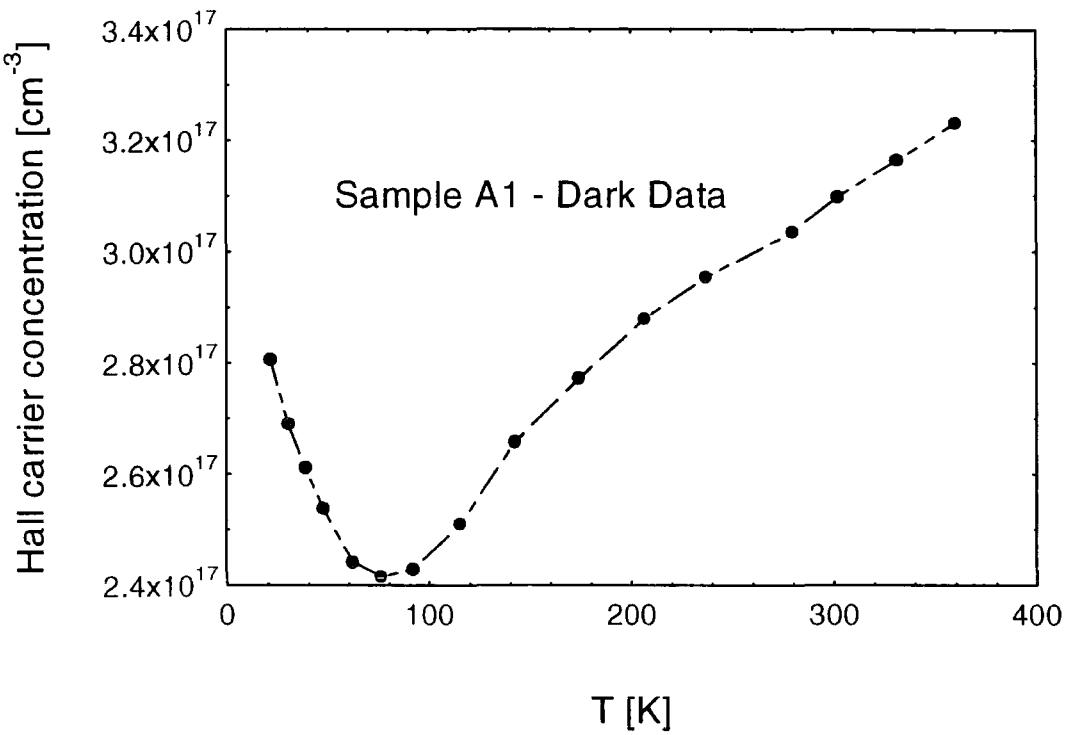

Figure 7.1.4. Temperature dependence of the Hall carrier density in sample A1.

The temperature dependence of the carrier concentration has already been discussed in some detail for samples A2 and A5 in chapter 5. They exhibit an interesting temperature dependence around 100 K, which was interpreted in terms of two band conduction effects when the conduction mechanism crosses over from activation from the deep level, to impurity band conduction. Hall carrier concentration data is shown in figure 7.1.4 for sample A1. As can be seen from this figure the room temperature value of the carrier density is as high as 3 x 10^{17} cm^{-3}, which explains why the sample is so metallic if one considers that the critical density is likely to be as low as ~ 1.5 x 10^{17} cm^{-3} for this composition. The interesting point about this figure is that the apparent carrier

concentration actually *increases* with decreasing temperature below about 80 K. At higher temperatures one observes the expected activated temperature dependence. Just as with the anomalous temperature dependence of the carrier density in sample A2 and A5, it is tempting to interpret this data in terms of some mechanism linked to the crossover in conduction mechanism from activation from the deep level, to metallic conduction in an impurity band at lower temperatures. Figure 7.1.5 shows the Hall data for sample A1, re-plotted with the equivalent data for sample A2. It seems clear that we could be observing the same effect in these two samples. It should be noted that the minimum in the dark carrier concentration occurs at a lower temperature for sample A1 (77K) than sample A2 (103 K). It is possible that this is due to the fact that the deep level activation energy is smaller for sample A1 than sample A2, meaning that the crossover in the conduction mechanism would be expected to occur at a lower temperature. In fact the temperature values differ by a factor of 1.3, which is consistent with the fact that the ratio of the deep level activation energies for these samples is 1.2. The agreement is not exact as other factors such as the density of states in the impurity band, mobilities etc, will play an important role in determining the temperature at which the crossover occurs. If this explanation is correct, then one would expect the carrier density to eventually level off at lower temperatures as for sample A2. Unfortunately the Hall coefficient becomes rather difficult to measure in this temperature region due to the fact that the magnetoresistance is becoming increasingly large, while the Hall coefficient is rather small.

The mobility of sample A1 is plotted as a function of temperature in figure 7.1.6. The remarkable thing about this plot is that the anomalous temperature dependence of the carrier concentration below 80 K is not reflected in the mobility. In fact the mobility shows a typical form over the whole temperature range, with values as large as 235 $cm^2V^{-1}s^{-1}$ being measured at low temperatures, due to the metallic nature of this crystal.

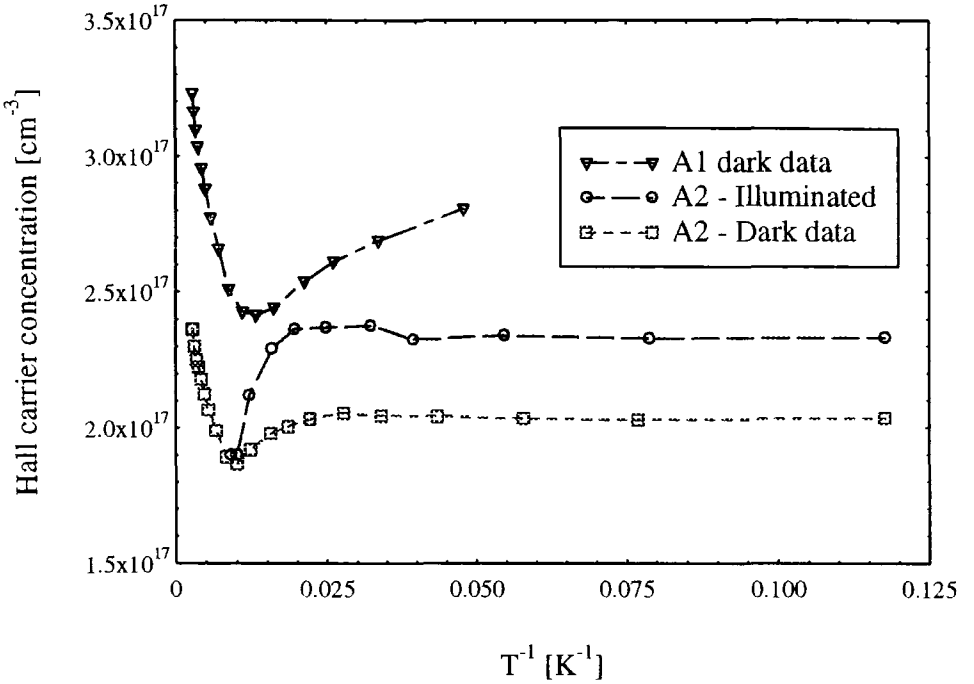

Figure 7.1.5. Temperature dependence of the Hall carrier density for samples A1 and A2.

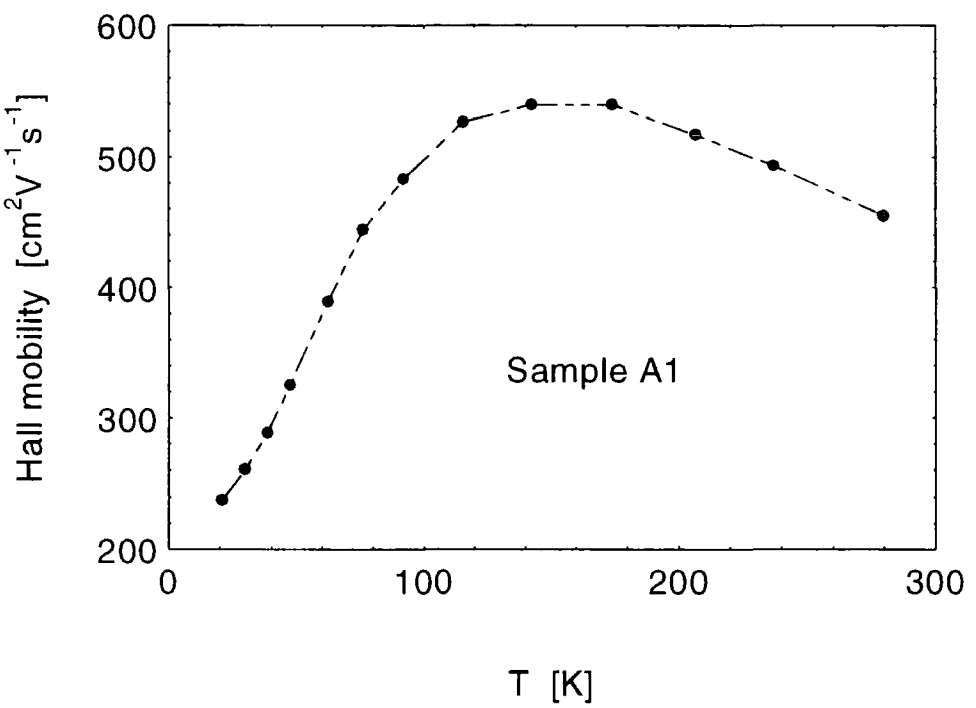

Figure 7.1.6. Temperature dependence of the Hall mobility in sample A1.

One final point to make before proceeding with a discussion of the MIT, is that it is clear that we still observe PPC even on the metallic side of the transition, just as in AlGaAs:Si [1]. This means that the localized DX^- states still exist in the metallic phase, despite the fact that the conduction must be proceeding via long range extended states. This is clearly consistent with our picture of a crossover from deep level activation to metallic conduction in an impurity band. *The localized deep levels provide the PPC, while the MIT occurs in an impurity band.* It is also consistent with our explanation of the large values of the room temperature resistivity ratio at the MIT in this system : large resistivity ratios occur due to the significant amount of carrier freeze out which occurs as the temperature is lowered, until eventually a crossover to impurity band conduction occurs.

7.2. The Zero Magnetic Field MIT in a Persistent Photoconductor.

This section presents the results of experiments on two samples of CdMnTe:In, which can be photodoped through the insulator-metal transition in zero magnetic field. These two samples are the aforementioned A5 and a sister sample C5. Sample C5 exhibits almost identical transport properties to its sister sample down to 4.2 K, and has almost identical composition.

7.2.1. Temperature Dependence of the Conductivity.

Figure 7.2.1 shows the temperature dependence of the conductivity from 4.2 K down to 335 mK for sample C5. It should be noted that the dark level is not shown here as the temperature dependence of the conductivity was only measured in the critical and metallic regimes. Each curve is labelled with a Hall carrier concentration determined using a calibration curve of $\rho(n)$ as mentioned earlier (section 6.1.1). It seems clear that we are observing a metal-insulator transition here : the lowest carrier density curve would appear to have zero conductivity at absolute zero, whereas the higher carrier concentration curves have a finite value of the extrapolated zero temperature conductivity. It will be seen in the

next section that the lowest carrier concentration curve (which appears to be insulating) actually displays a temperature dependence of the conductivity which is consistent with variable range hopping. The rest of these curves show no such hopping behaviour, which is consistent with their being metallic.

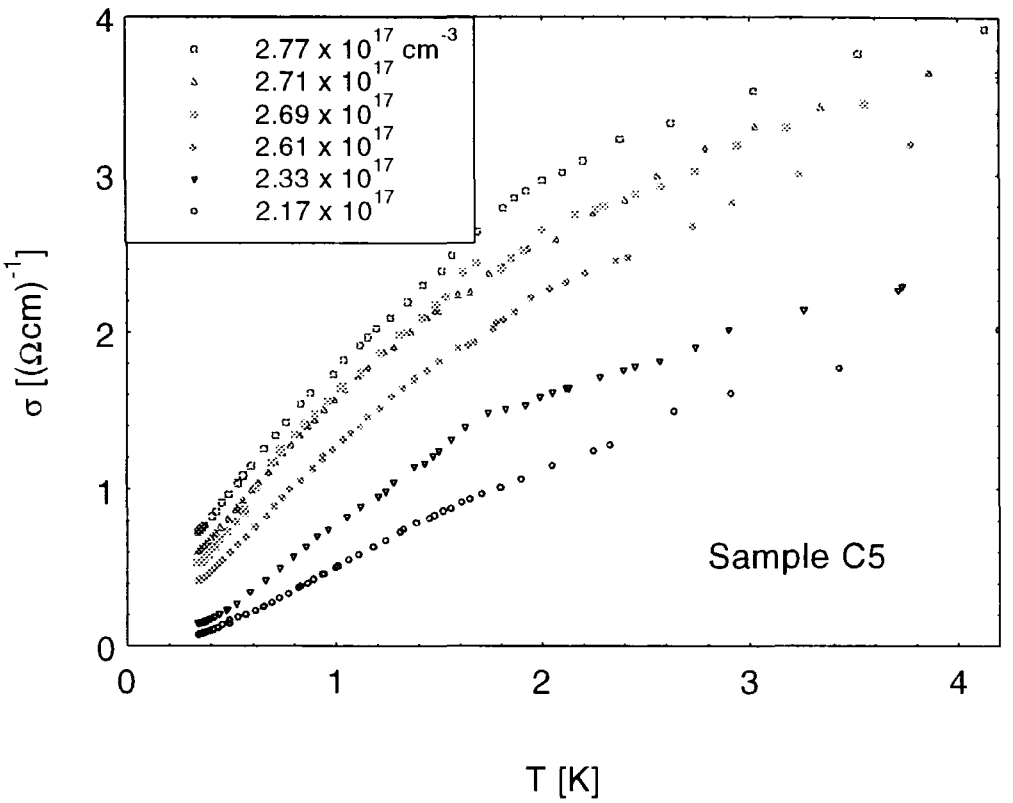

Figure 7.2.1. Temperature dependence of the conductivity of sample C5 down to 335 mK

Theory [2] and past experimental work on doped semiconductors [3,4], has suggested that the temperature dependence of the conductivity in the metallic region near the MIT can be quantitatively described by taking into account the effects of electron-electron interactions and weak localization on the zero temperature conductivity. This was discussed in detail in section 3.5 where it was shown that taking these effects into account results in the following form for the low temperature conductivity,

$$\sigma(n, T) = \sigma(T = 0) + m(n)T^{1/2} + B(n)T^{p/2} \qquad (7.2.1),$$

where the symbols were defined earlier. At T < 1 K, this form does indeed provide a rather good fit to our experimental points as seen in figure 7.2.2.

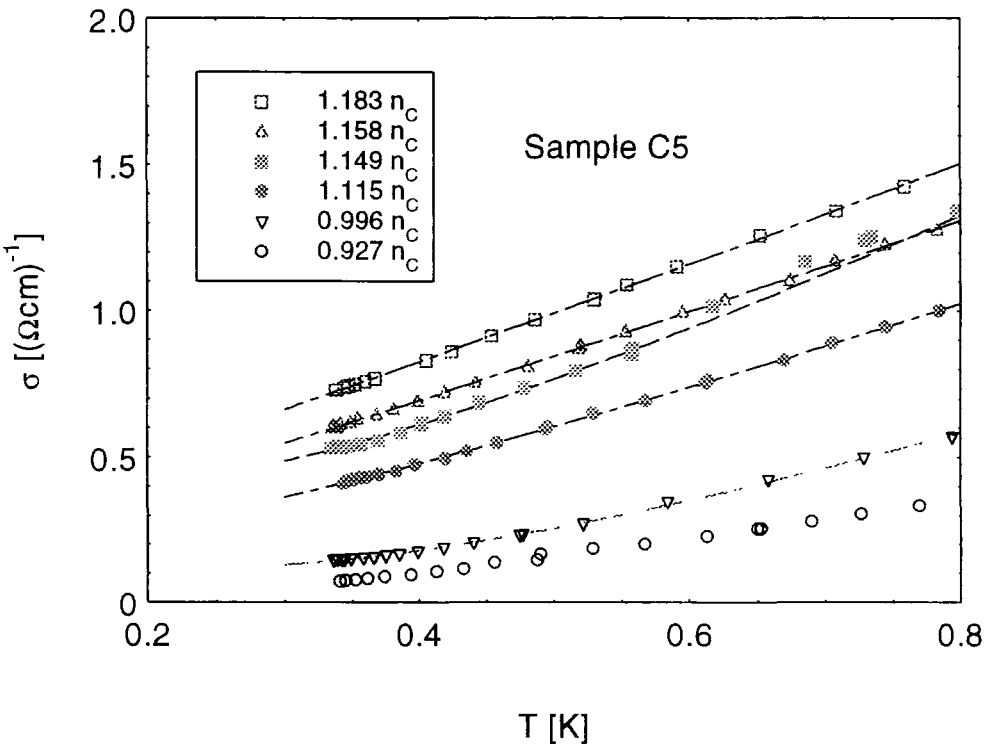

Figure 7.2.2. Fits to the temperature dependence of the conductivity of sample C5 below 1K.

There are a number of points to be made about the values of the parameters deduced from this fitting procedure. Firstly, a reasonable fit can only be achieved with values of p very close to 2.0. As mentioned in section 3.5 this is consistent with the theoretical prediction for a system where the dominant dephasing mechanism is due to electron-electron scattering in the clean limit [2]. Therefore, the rest of the fits were made with p set at 2.0 to reduce the number of fitting parameters to three. The determined values of m and B are dependent on the carrier density as shown in table 7.2.1.

Sample	n/n_c	m $(\Omega cmK^{1/2})^{-1}$	D cm^2s^{-1}	γF_σ	B_{exp} $(\Omega cmK)^{-1}$	B_{theory} $(\Omega cmK)^{-1}$
A5	1.309	-2.57	0.112	1.167	2.73	2.08
A5	1.233	-2.20	0.108	1.123	2.30	2.06
A5	1.177	-1.41	0.105	1.037	1.61	2.05
C5	1.183	-1.90	0.178	1.148	3.08	1.74
C5	1.158	-1.43	0.174	1.082	2.57	1.71
C5	1.149	-1.85	0.173	1.138	2.66	1.73
C5	1.115	-1.65	0.169	1.108	2.49	1.70

Table 7.2.1. The parameters relevant to the temperature dependence of the conductivity in the metallic regime.

This table also includes the results of fits to the equivalent data for sample A5, where similar values are obtained. For this sample the low temperature conductivity in the metallic phase (three curves) is shown in figure 7.2.3, where it can be seen that the fit is reasonable up to approximately 1.2 K. In the insulating phase, the conductivity again shows the temperature dependence expected for Efros-Shklovskii VRH. The form of the hopping conduction in this sample is more complicated than for sample C5 and is discussed more fully in section 7.2.2.

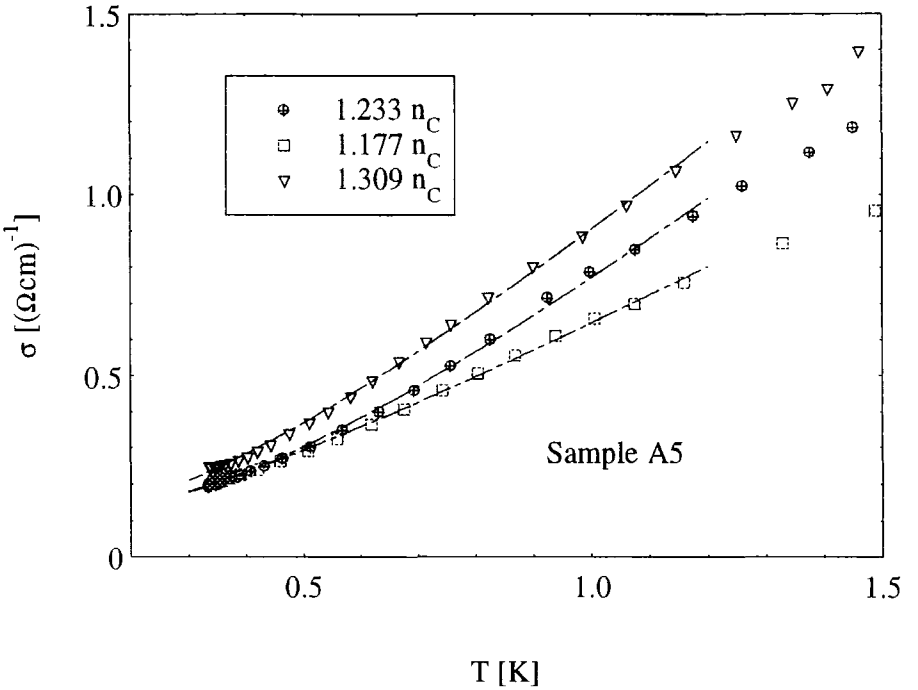

Figure 7.2.3. Temperature dependence of the conductivity of sample A5 down to 335 mK. Dashed lines are fits to the data as detailed in the text.

An interesting point is that despite the fact that $d\sigma/dT$ is positive in the metallic phase, all of the m values are negative. This suggests that $d\sigma/dT$ must change sign at temperatures below 300 mK, as is the case for Si and Ge [3,4]. One of the consequences of this is that any extrapolation of the conductivity to absolute zero is likely to be rather inaccurate, unless measurements are performed down to the millikelvin region. Minimising (7.1) with respect to temperature leads to a value for the temperature T^* at which $d\sigma/dT$ is expected to change sign,

$$T^* = \left(\frac{-m}{pB}\right)^{\left(2/p-1\right)} \qquad (7.2.2).$$

So for the most metallic curve in figure 7.2.1 this leads to $T^* = 95$ mK. Reference to table 7.2.1 shows that the magnitude of m decreases as the MIT is approached from the metallic

phase, suggesting that positive values could be obtained for n very close to n_c, as is the case for Si and Ge [3,4].

Theory outlined in section 3.5 allows determination of the Coulomb interaction parameter γF_σ from the values of m, by using Equations 3.5.2 and 3.5.3 :

$$m = \alpha\left[\frac{4}{3} - \left(\frac{3}{2}\gamma F_\sigma\right)\right] \tag{7.2.3}$$

$$\alpha = \frac{e^2}{\hbar}\left(\frac{1.3}{4\pi^2}\right)\left(\frac{k_B}{2\hbar D}\right)^{1/2} \tag{7.2.4}$$

where the symbols were defined earlier. The quantity α is calculated from the diffusion coefficient, D, which can in turn be calculated from the Einstein relation, $D = \mu k_B T/e$. Values for D, α, and γF_σ are listed in table 7.2.1 for the two samples. The quantity γF_σ shows a clear increase as n is increased, suggesting that, as expected intuitively, the Coulomb interaction parameter (and hence the Fermi liquid parameter) increases as the density of electrons increases. In contrast to the work on Si:B, the interaction parameter does not saturate just beyond the insulator-metal transition. It is worth noting that although the Fermi liquid parameter, F, is constrained to lie between 0 and 1, the values of γF_σ need not necessarily lie in this range. Work on Si:B suggested that γF_σ saturates at a value close to 2.0, indicating that $\gamma = 2$, although there is no real theoretical justification for this. In our case the fact that the values of γF_σ are so close to 1.0 suggests that γ is close to 1.0, or that the interaction parameter is far from saturation at ~1.3 n_c.

As discussed in section 3.5 there is also a theoretical prediction for the value of the parameter $B(n)$. From equations 3.5.5 and 3.5.6 we have that,

$$\tau_{\phi}^{-1} = cT^{p} \tag{7.2.5}$$

and,

$$B(n) = \frac{e^2}{\hbar\pi^2}\left[\frac{S_0\eta}{2}\left(\frac{c}{D}\right)^{1/2}\right] \tag{7.2.6),}$$

where the symbols were defined earlier. Thomas *et al* [4] showed that it is possible to define a parameter c' which is independent of n,

$$c' = 4\left(\frac{\pi}{4}\right)^3\left(\frac{1}{3\pi}\right)^{1/2}\left(\frac{\eta}{3\pi^2}\right)^{1/3}\frac{m^* k_B^2}{\hbar^3 a_B^{1/2}} = cn^{-5/6} \tag{7.2.7),}$$

where c' can be calculated to be 1.0 x 10^{10} $K^{-2}s^{-1}$ for CdTe. It should be noted that n is measured in units of 10^{18} cm^{-3} here. So, to calculate the theoretical prediction for the value of $B(n)$, we simply compute $c(n)$ from the measured value of n, determine D from the transport data and use equation 7.6. These calculated values of $B(n)$ are shown in table 7.2.1. Although the agreement is not perfect, the theoretical predictions are of the correct order of magnitude and show the experimentally observed trend of increasing B as n is increased. Calculated values are around 1.7 to 2.0 $(\Omega cmK)^{-1}$, whereas the experimentally determined values lie in the range 1.61 to 3.08 $(\Omega cmK)^{-1}$. All in all, the agreement is rather satisfactory.

The other studies on systems such as Si and Ge have suggested that $B(n)$ first increases with increasing n, reaches a maximum, and then decreases as n is increased further. Positive values are usually observed, although negative values have been reported for samples with a positive $d\sigma/dT$ [5,6]. In all cases, the observed and calculated values of $B(n)$ are of the same order of magnitude as found here. The interesting point about our data is that B always increases with increasing n rather than peaking and eventually

decreasing. For Si:B this peak occurs at ~ $1.17n_c$, whereas for Ge:Sb B peaks at approximately $1.4n_c$. In our experiment we are able to probe up to 1.3 n_c so this apparent discrepancy could simply be due to the fact that we need to measure samples with higher carrier densities in order to obtain a fuller understanding of the dependence of B on n. Certainly one would expect that eventually B must decrease with increasing carrier density, as the effects of weak localization are expected to die out as the carrier density is increased further into the metallic phase.

In conclusion, the temperature dependence of the conductivity in the metallic regime can be satisfactorily explained in terms of a model which takes into account the effects of e^--e^- interaction and weak localization. Both corrections to the conductivity are found to be of a similar size to those observed in other systems. Moreover, the sizes of the corrections are satisfactorily reproduced by theory. The metallic conductivity appears to be well understood with the exception that it is not totally clear whether $d\sigma/dT$ will change sign at lower temperatures. Obviously this could be determined by performing lower temperature measurements down to ~10 mK. The subject of the change in sign in $d\sigma/dT$ is a controversial one which is poorly understood. It seems that a large number of materials such as $Gd_{3-x}v_xS_4$ [7], CdMnSe [8] and AlGaAs [1] exhibit positive values of the parameter m (which varies weakly with n, or H) and no sign change in $d\sigma/dT$, whereas materials such as Si [3] and Ge [4] display a sign change in m and $d\sigma/dT$ near the MIT. The reason for this behaviour is an open issue at present.

7.2.2. Hopping Conduction.

As mentioned earlier the curve which definitely shows insulating behaviour in figure 7.2.1 actually displays a temperature dependence of the conductivity which is typical for variable range hopping conduction. This is shown in figure 7.2.4 where the logarithm of the resistivity is plotted as a function of $T^{1/2}$. This is the temperature dependence which is expected for Efros-Shklovskii VRH conduction, where the effects of

e^--e^- interaction are taken into account. The same data plotted as a function of $T^{-1/4}$ does not result in a straight line.

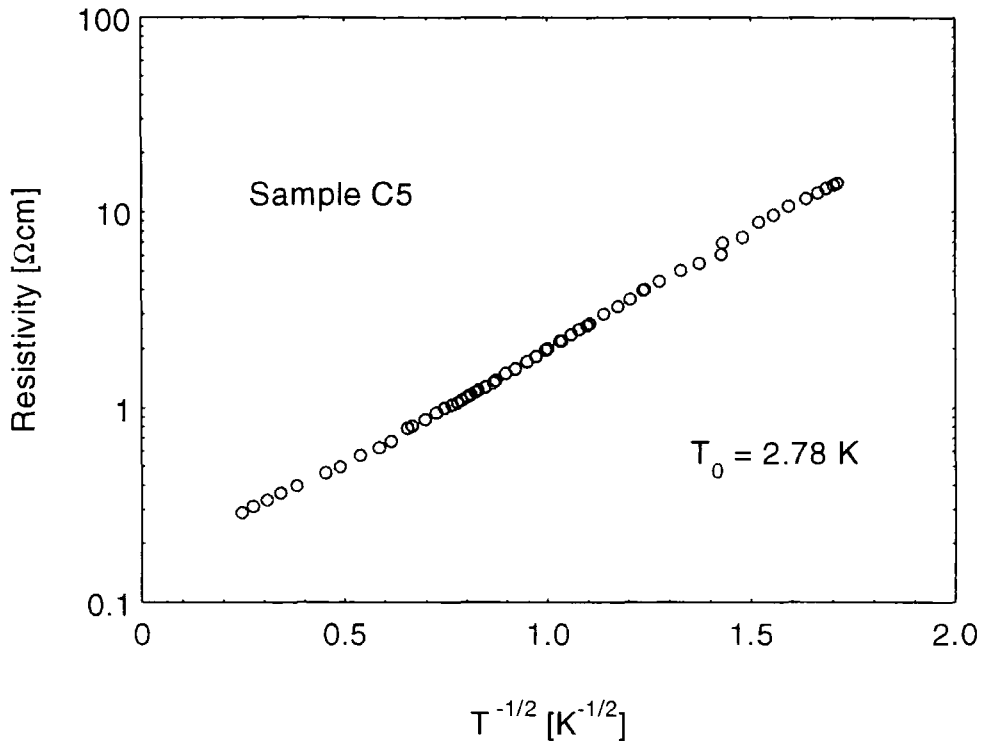

Figure 7.2.4. Temperature dependence of the resistivity of the lowest carrier density curve for sample C5. The data is plotted as logρ against $T^{-1/2}$.

This conclusion can be backed up by a quantitative analysis of the size of the exponent in the VRH form,

$$\sigma = \sigma_0 \exp\left[-\left(\frac{T_0}{T}\right)^s\right] \tag{7.2.8}$$

where s = 1/2 for Efros-Shklovskii hopping and s = 1/4 for Mott VRH. The exponent can be determined more accurately by performing an analysis devised by Finlayson *et al* [9], where the deviation of the experimental points from $\sigma_0\exp[-(T_0/T)^s]$ is determined for a

range of values of the exponent, s. Figure 7.2.5 shows the maximum deviation determined in this manner, as s is incremented from 0.05 to 1.0. Clearly, a minimum occurs at $s \approx 0.6$, which is close to the value of 0.5 expected from Efros-Shklovskii theory.

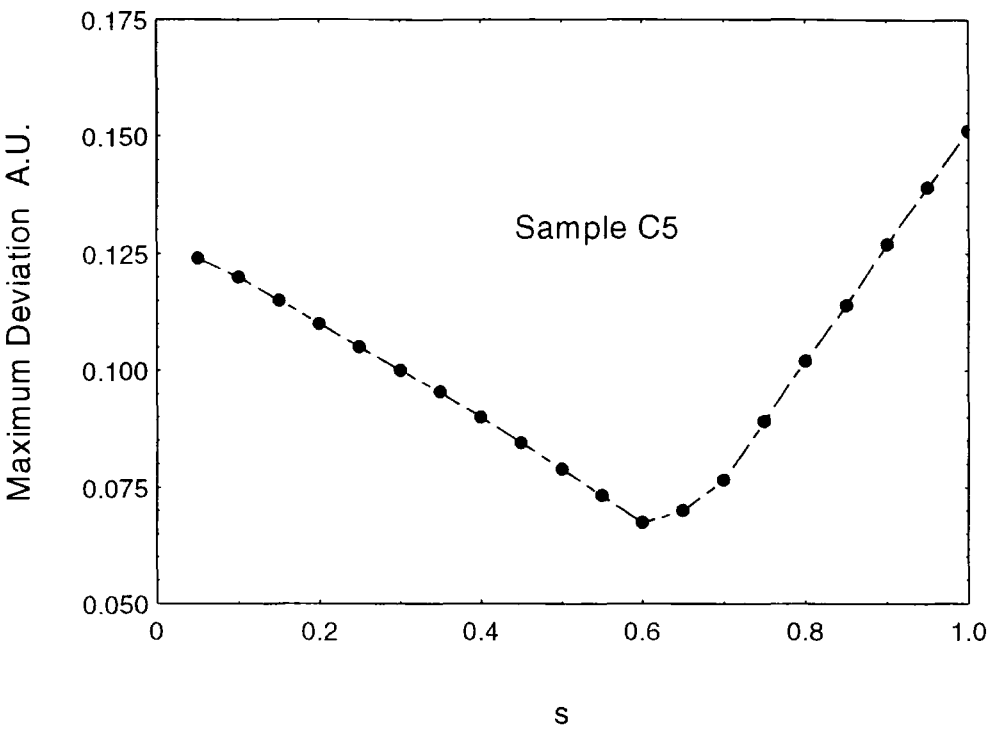

Figure 7.2.5. Maximum deviation from $\exp[-(T_0/T)^s]$ plotted against the exponent, s.

Another method of determining the exponent is to perform the differential analysis proposed by Mobius [10]. He noticed that if equation 7.2.8 is valid then,

$$\frac{d\ln\sigma}{d\ln T} = s\ln\sigma_0 - s\ln\sigma \qquad (7.2.9),$$

suggesting that if $d\ln\sigma / d\ln T$ is plotted against $\ln\sigma$, the negative gradient of the straight line obtained will be the exponent, s. Figure 7.2.6 shows just such a plot, where the gradient of the least square fit is found to be 0.440 ± 0.087. Again this low temperature

data is consistent with the value of 0.5 from the Efros-Shklovskii theory. Clearly our data is inconsistent with the Mott form for the VRH.

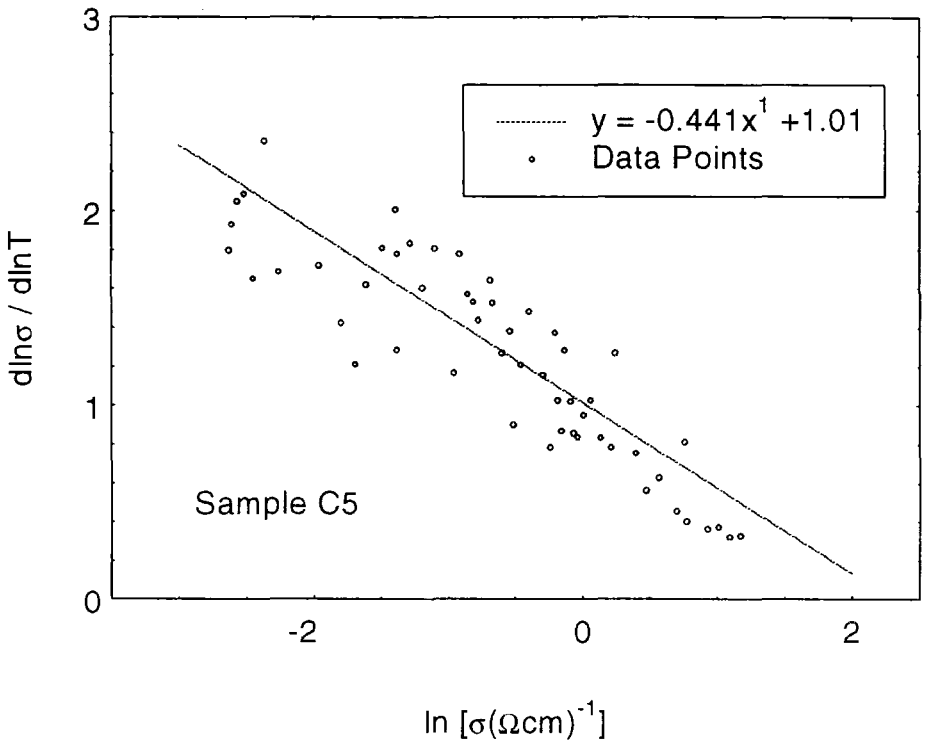

Figure 7.2.6. Differential analysis of the hopping data of sample C5. The solid line is a least squares fit to the data.

As shown in figure 7.2.4, the value of T_0 obtained from this data is 2.78 K, while ρ_0 = 0.121 Ωcm. These values are in qualitative agreement with the work of Terry *et al* [11] on the VRH conduction in $Cd_{0.91}Mn_{0.09}Te$:In. This point will be discussed in greater detail at the end of this section.

Sample A5 also shows a form of VRH conduction in the insulating phase. In this sample the temperature dependence of the conductivity was measured from $0.5n_c$ up to $1.3n_c$, allowing a study of the hopping conduction as the MIT is approached from the insulating phase. Figure 7.2.7 shows the temperature dependence of the conductivity

plotted as $\ln\rho$ against $T^{1/2}$, for six photogenerated carrier concentrations. Although the temperature dependence was measured for more carrier concentrations, only six are displayed in this figure for the purposes of clarity. The low carrier density curves show insulating behaviour, while the highest carrier density curves display a weak temperature dependence of the conductivity as expected in the metallic phase. As we have already seen, these curves appear to be metallic, and have a temperature dependence consistent with theory for metallic conduction.

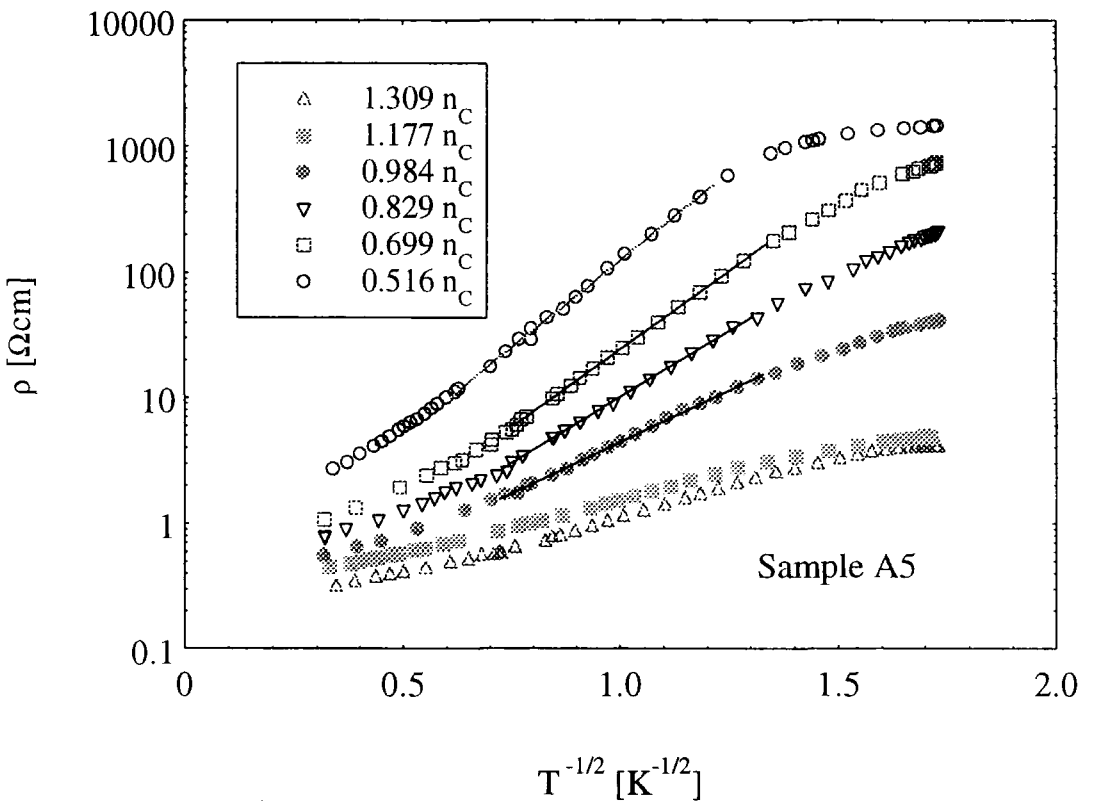

Figure 7.2.7. Temperature dependence of the resistivity for sample A5 for six photogenerated carrier densities. The data is plotted as $\log\rho$ against $T^{-1/2}$.

The insulating curves show a more complicated behaviour. Initially, as the temperature is lowered these curves show an entry to the hopping regime, followed by a region where the temperature dependence is consistent with Efros-Shklovskii VRH. In this region, a differential analysis of the hopping exponent yields values close to 0.5 in all

cases. At lower temperatures, below about 0.6 K the curves show a turnover to a more weakly temperature dependent form. This is shown with striking clarity in figure 7.2.8 where the differential analysis discussed earlier is shown. At higher temperatures (high values of $\ln\sigma$) an exponent of 0.501 is recovered, but at $\ln\sigma \approx -1.1$ (equivalent to 0.6 K) a sharp turnover is observed. It is difficult to analyse the form of the temperature dependence below the turnover temperature due to the small temperature interval involved, although appears to be impossible to fit the data with an expression of the form $\exp[-(T_0 / T)^s]$. It should also be noted that the temperature region over which the Efros-Shklovskii VRH form is obeyed reduces with increasing n as the MIT is approached. This is a consequence of the fact that as the carrier concentration is increased, the temperature at which the sample enters the hopping regime is lowered, while the temperature at which the turnover occurs is only weakly dependent on the carrier density. This is consistent with the fact that the value of T_0 decreases, meaning that the 'activation energy' associated with the hopping process is decreasing, as expected.

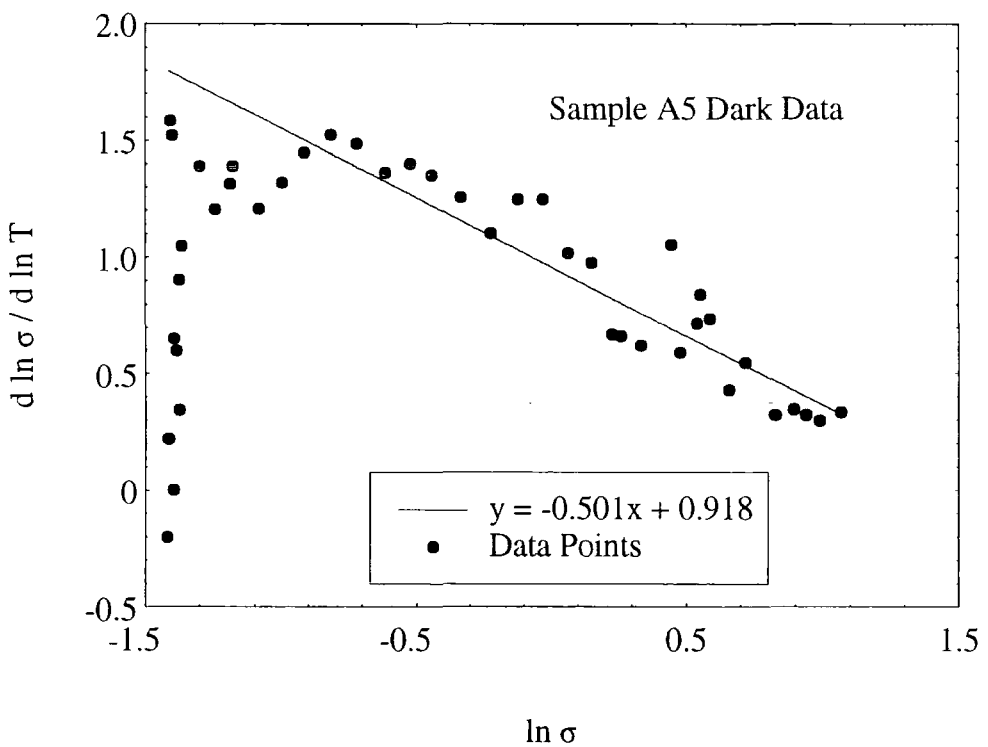

Figure 7.2.8. Differential analysis of the hopping data for sample A5 in the dark.

Table 7.2.2 shows the hopping parameters for this set of curves ; n, T_0, ρ_0, and T_{HR} (the temperature at which the sample enters the hopping regime) are included. All four parameters show a decrease on approaching the MIT, as expected. It is also interesting to compute the average range of a single hop, along with the average hopping energy associated with this process. These can be estimated from the following expressions [12],

$$\overline{R}_{hop}(T) = \frac{1}{4}\xi(n)\left(\frac{T_0}{T}\right)^{1/2} \qquad (7.2.10),$$

$$\overline{\Delta}_{hop}(T) = \frac{1}{2}k_B(TT_0)^{1/2} \qquad (7.2.11),$$

where the symbols were defined earlier. For the lowest carrier concentration curve in figure 7.2.7, we obtain an average hopping energy of 0.28 meV (3.25 K), at a temperature of 1.0 K. The work of Terry *et al* [11] suggested that at n = 1.7 x 10^{16} cm^{-3}, ξ = 16.6 nm, which increases to 157 nm at n ~ 1 x 10^{17} cm^{-3}. Using this value for the localization length, we obtain an average hop range of 260 nm at 1.0 K.

n [10^{17} cm^{-3}]	n / n_c	T_0 [K]	ρ_0 [Ωcm]	T_{HR} [K]
0.99	0.51	42.38	0.198	4.0 (= T_0/10.6)
1.34	0.69	33.76	0.085	3.0 (= T_0/11.3)
1.39	0.72	32.71	0.078	2.5 (= T_0/13.1)
1.58	0.82	24.11	0.081	2.0 (= T_0/12.1)
1.87	0.97	14.97	0.092	1.7 (= T_0/8.8)

Table 7.2.2. Hopping transport parameters for sample A5.

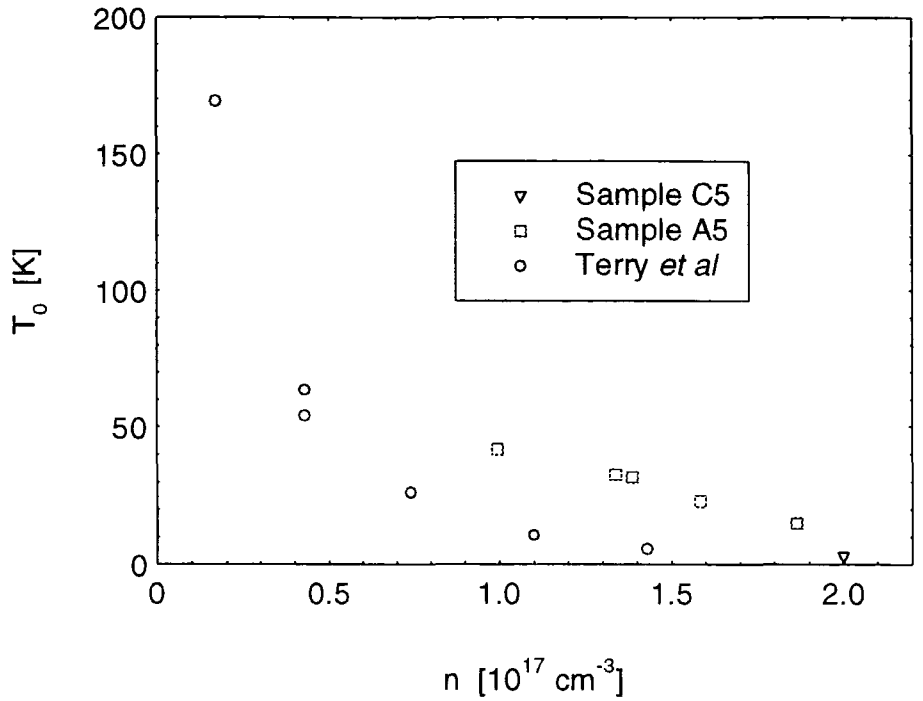

Figure 7.2.9. *n* dependence of the hopping parameter, T_0

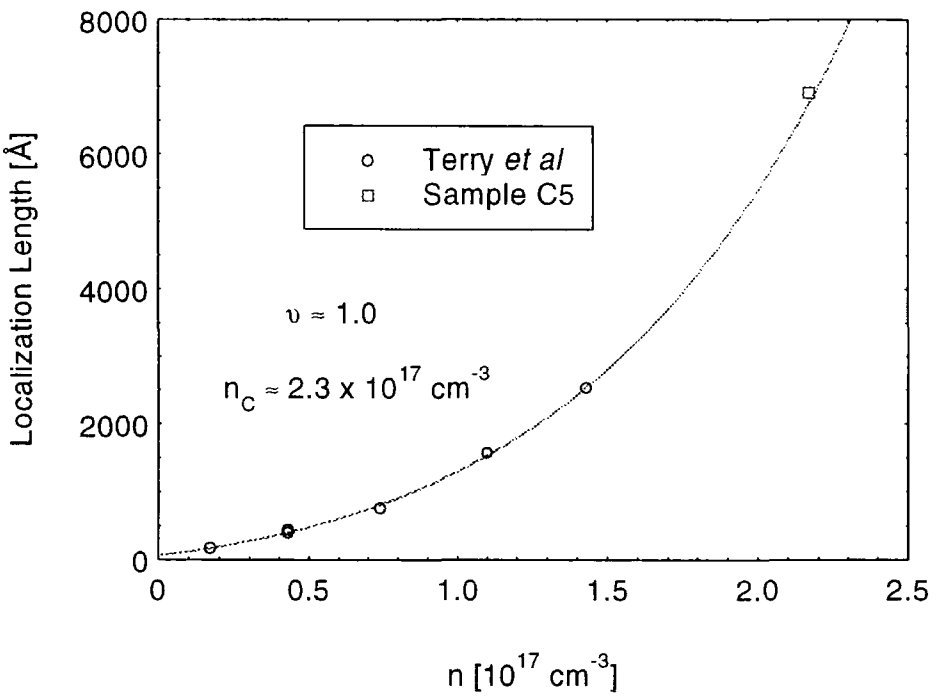

Figure 7.2.10. *n* dependence of the extracted localization length.

As mentioned in section 3.6, the n dependence of the parameter T_0 should show scaling behaviour as the insulator-metal transition is approached. This is due to the fact that T_0 is dependent on the localization length and dielectric constant as shown in equation 3.6.6. Both of these quantities have a scaling form in the vicinity of the MIT. Terry *et al* [11] measured the temperature dependence of the hopping conduction and the dielectric constant in the insulating phase in order to examine the critical behaviour of the dielectric constant and the localization length (computed from the measured values of $T_0(n)$ and $\kappa(n)$). They found that the dielectric constant and localization length appear to scale with the same exponent, i.e. $\nu = \nu' \approx 1$, contradicting Wegner's scaling law [13]. It is interesting to examine the n dependence of the parameter T_0 obtained from the data in this thesis with the data of Terry *et al,* as shown in figure 7.2.9. Data from ref [11] is plotted along with the data for sample A5, and the single point from sample C5. Although the range of carrier densities probed in the experiments on sample A5 is modest it is interesting to note that the measured values of T_0 and the dependence on n is in disagreement with the other data. In fact no scaling dependence is observed for the $T_0(n)$ data for this sample. The single point from sample C5 however, is in qualitative agreement with the other data. In fact, if the measured $\kappa(n)$ from ref [11] is used to calculate the value of the dielectric constant for sample C5 at $n = 2.16 \times 10^{17}$ cm^{-3}, this leads to a value of the localization length of 691 nm, which is in quantitative agreement with the data from ref [11], as shown in figure 7.2.10. This data leads us to tentatively suggest that the conclusions of Terry *et al* remain intact if their study is extended to higher carrier concentrations, closer to the MIT i.e. the dielectric constant and localization length have the same critical behaviour.

It is also revealing to examine the n dependence of the parameter ρ_0 extracted from the hopping data. These data are shown in figure 7.2.11, where the data from ref [11] are also included. As expected, ρ_0 decreases very rapidly as the MIT is approached, tending towards roughly constant value of ~ 0.1 Ωcm, which is equivalent to about twice the minimum metallic conductivity for CdTe. Again, the data for sample C5 appears to be in

excellent agreement with the data of Terry *et al,* while the data for sample A5 is slightly different, all the values being smaller.

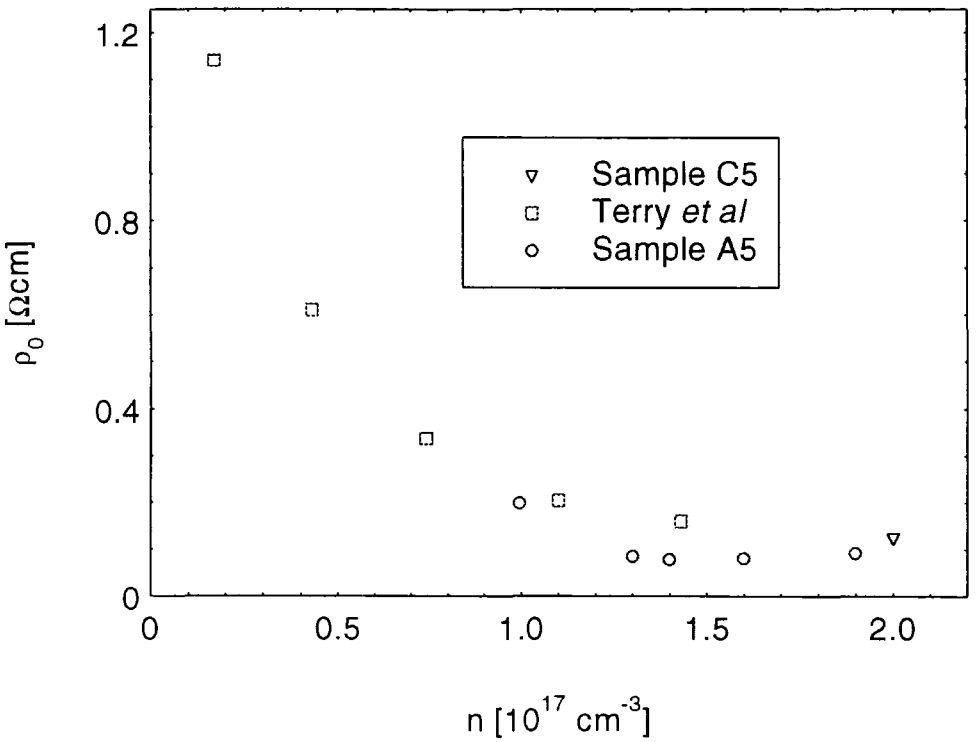

Figure 7.2.11. n dependence of the hopping prefactor ρ_0.

To summarise, we have seen that sample C5 shows hopping conduction of the expected form, with the parameters extracted from the data being consistent with previous work, whereas the behaviour in the sister sample, A5, is more difficult to understand. In particular, this sample shows a turnover in the resistivity below about 0.6 to 0.5 K, along with a carrier density dependence of the parameter T_0 which cannot be understood in terms of scaling theory or previous experiments. We can propose several possibilities for the origin of the turnover in the resistivity in this sample. It should first be noted though, that several possible experimental artefacts can be ruled out. Meticulous checks were made for sample self heating such as measurement of the V-I characteristics, ensuring that no time dependence of the conductivity is observed when the excitation current is switched on etc.

Also, care was taken to ensure that the sample is placed in excellent thermal contact with the ^{3}He pot and thermometer, while ample time was allowed for thermal equilibration of the sample. The size of the contact resistances were monitored to check for large values at low temperatures which are indicative of bad contacts (which are likely to be of a capacitive nature), which increase the likelihood of significant errors occurring due to sample self heating. Suffice to say that for the measurements made on this sample the excitation levels were kept below 10^{-11} W, and no effects of self heating were observed.

If we are to attempt to interpret the anomalous data on sample A5 it is instructive to note that such an unexplained weakening of the temperature dependence in the hopping regime has been observed before, albeit at lower temperatures [14,15]. It should also be pointed out at this stage, that it is not possible to crossover from Efros-Shklovskii VRH to Mott VRH as the temperature is lowered. This is due to the fact that the Coulomb gap energy is far smaller than the characteristic energy associated with Mott VRH. Therefore we cannot attempt to explain this data in terms of a crossover from $T^{1/2}$ hopping to the weaker $T^{1/4}$ temperature dependence, even if this form could be reliably fitted over the small temperature range available.

It is tempting to interpret the observed effect as being magnetic in origin, as the effects of the magnetic exchange interactions have certainly been evident in the past [11,16]. In fact it is interesting to note that the spin glass freezing temperature of $Cd_{0.92}Mn_{0.08}Te$:In is expected to be about 0.5 K. It is therefore possible that we are observing an anomaly in the temperature dependence of the conductivity due to the spin-glass formation. Further work will involve the measurement of the susceptibility as a function of temperature in this region, to determine whether the spin-glass freezing temperature occurs at the same point as the turnover in the resistivity. In conclusion though, the temperature dependence of the resistivity of sample A5 in the hopping regime is puzzling, especially when one considers that the sister sample C5 shows no such

behaviour. The behaviour of sample C5 can be explained rather satisfactorily in both the metallic and insulating phases.

Finally, it should be noted that none of the data obtained on these two samples shows any evidence for a magnetic hard gap in the density of states, as observed in ref [11]. This is an interesting point as one might expect a sample with carrier concentrations as high as these to display an $\exp(E_H / T)$ temperature dependence in the conductivity, if the same mechanisms are at work in these samples. This point will be discussed in some detail, along with data for several other samples in the WLR in sections 7.3 and 7.4.

7.2.3. The Transition : Comparison With the Scaling Theory of Electron Localization.

One of the major aims of the work presented in this thesis is to test the scaling theory of electron localization in a situation where it has never previously been possible to compare theory and experiment. This situation is the case of magnetic system in a zero magnetic field. As mentioned before, measurements have been made in the critical region of the MIT in magnetic [7] and dilute magnetic systems [8], but only in the presence of a magnetic field, which was used to induce a transition. In our case we are able to fine tune the transition using the PPC effect. One problem with this technique however is the difficulty in obtaining samples with a dark carrier concentration sufficiently close to n_c. A suitable sample must have n close to, but less than, n_c, as well as having a large enough increase in n on illumination to span the critical region. Figure 7.2.12 shows the n dependence of the change in resistivity on illumination, to illustrate the problem. As can be seen from the figure, $\Delta\rho/\rho_0$ shows a dramatic decrease as $n \rightarrow n_c$. This section is concerned with the two samples of CdMnTe:In which we have found to satisfy both of our requirements.

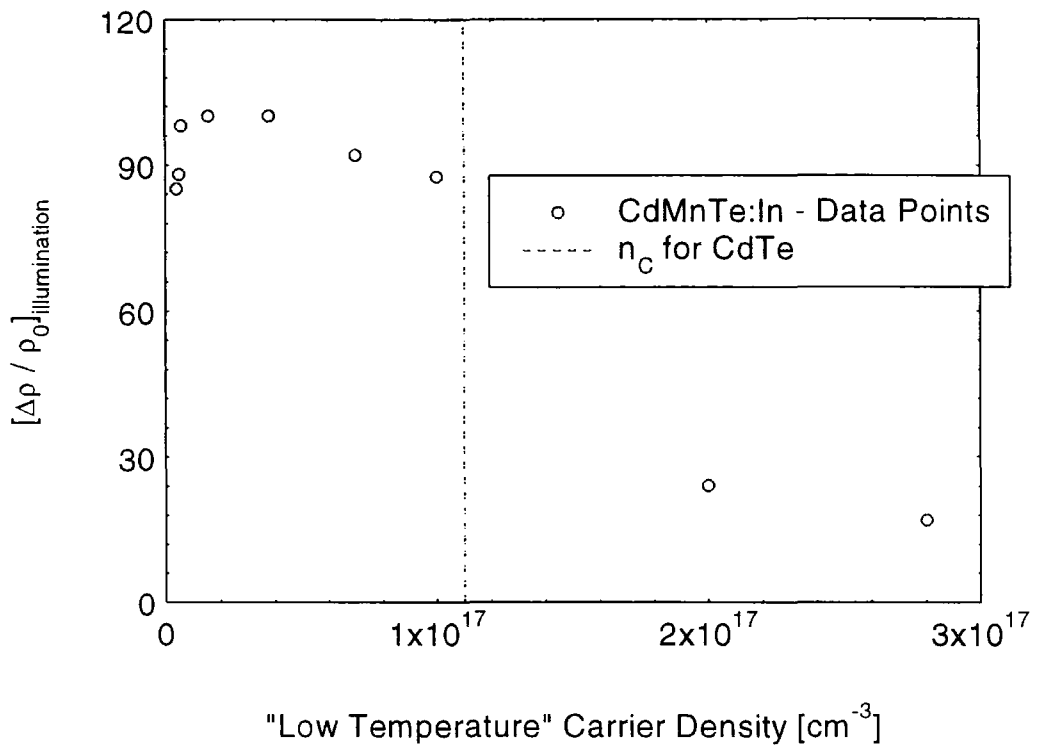

Figure 7.2.12. The percentage change in resistivity on illumination, against the Hall carrier concentration. The carrier concentration is measured at low temperatures where it is independent of temperature.

As was discussed in section 3.3 on the scaling theory of electron localization, the scaling theories can be tested by measuring the zero temperature extrapolated value of the conductivity as a function of the carrier concentration. This indicates whether the transition is actually continuous or discontinuous. If a continuous transition is observed then the scaling theory predicts a critical form for $\sigma(n)$ which can be compared to experiment. In our case we have a problem in that the lowest temperature available for these experiments is 300 mK, making the extrapolation to zero an ambiguous procedure. In fact, we have seen in this chapter that the temperature dependence of the conductivity in the metallic phase is such that a sensible extrapolation to absolute zero is extremely difficult. For these reasons we simply plot the 300 mK conductivity against the carrier concentration as a reasonable approximation to the true zero temperature value. This

procedure is one which has been carrier out successfully by several authors in the past, and can be shown to be well justified [17,18,19]. The work of von Molnar *et al* [17] showed rather conclusively that measurements at 300 mK provided a very close approximation to the true critical behaviour at ultra low temperatures. They found the measured critical exponent to be unchanged from the value determined by 300 mK measurements, down to temperatures as low as 6 mK. The only artefacts of this 300mK analysis is that there is likely to be a considerable amount of thermal rounding in the vicinity of the transition, and that the determined value of n_c is likely to be slightly low.

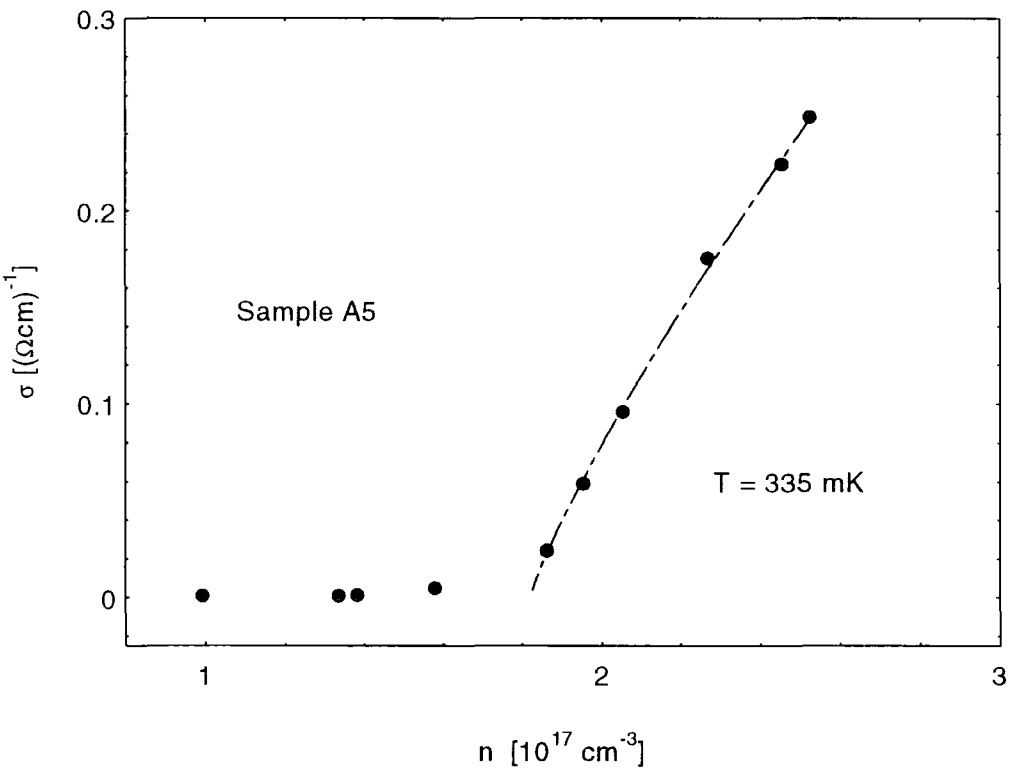

Figure 7.2.13. The *n* dependence of the 335 mK conductivity for sample A5. The dashed line is a scaling theory fit to the data.

Figure 7.2.13 shows the n dependence of the base temperature conductivity for sample A5. *Clearly we are observing a continuous metal-insulator transition.* The conductivity shows a dramatic increase with increasing n at a carrier concentration of

approximately 2 x 10^{17} cm^{-3}. As expected there is a considerable amount of thermal rounding near n_c. The dotted line shown in the figure is a fit to the scaling theory prediction for the conductivity. We find that the conductivity obeys,

$$\sigma(335\ \text{mK}, n) = \sigma_0 (n/n_c - 1)^{\nu} \qquad (7.2.12).$$

The values of the fitting parameters, along with their experimental error are shown in table 7.2.3 for this sample and sample C5. Similar results are obtained for sample C5 as shown in figure 7.2.14, the only major difference being that the conductivity prefactor and critical density are slightly higher. It should be noted that the rounding effect commented on earlier is particularly acute for the case of sample C5. For this reason, the scaling theory fit is restricted to the region above 2.4 x 10^{17} cm^{-3}. It seems clear in this case that measurements to lower temperatures would certainly result in a smaller value for the critical carrier concentration. The determination of the critical exponent however, is more accurate.

Sample	σ_0 $[(\Omega cm)^{-1}]$	n_c $[10^{17}\ cm^{-3}]$	ν
A5	0.55 ± 0.05	1.93 ± 0.15	$0.83 \pm^{0.20}_{0.14}$
C5	3.57 ± 0.35	2.34 ± 0.25	$0.98 \pm^{0.18}_{0.15}$

Table 7.2.3. The parameters deduced from a fit to the scaling theory form for σ(300 mK, n). The values are shown for both samples.

There are several important points to be made about the results of this fitting procedure. First of all it is clear that the MIT is continuous, and the scaling theory describes the data very well. The most important conclusion however, is that the critical exponent, being 0.83 and 0.98 in the two cases, is rather close to 1. This is in agreement with the previous experimental work on magnetic and diluted magnetic semiconductors in the presence of magnetic fields, suggesting that either the application of a magnetic field

has no influence on the critical behaviour, or that the magnetic field applied in previous measurements is not sufficiently strong to induce a change in universality class (there is also the possibility that $\nu = 1.0$ in both the low field and high field universality classes). It is worth noting that an exponent close to 1.0 is also in agreement with the experimentally determined fact that the vast majority of heavily compensated semiconductors show $\nu \approx 1.0$.

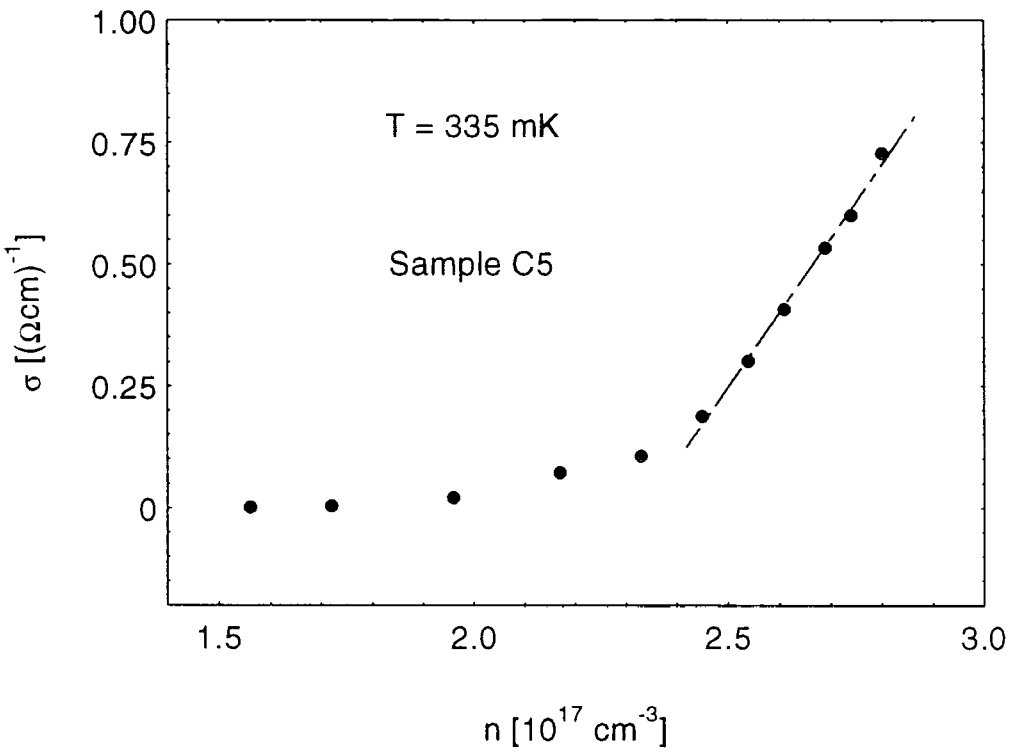

Figure 7.2.14. n dependence of the 335 mK conductivity of sample C5. The solid line is a scaling theory fit to the data.

The values of the critical carrier concentrations obtained is in good agreement with the experimental work of Shapira *et al* [20] who suggested that n_c lies between 1.7 and 2.1 x 10^{17} cm^{-3} for $x \approx 0.05$. It is also in reasonable agreement with the value of 2.3 x 10^{17} cm^{-3} which was suggested by Terry *et al* [11] for $x = 0.09$.

The value of the prefactor, σ_0, is also of interest. We obtain $\sigma_0 = 0.55 = 0.11\sigma_{min}$ for A5 and $\sigma_0 = 3.57 = 0.71\sigma_{min}$ for sample C5. The reason for this discrepancy is unknown although the value for A5 happens to be in agreement with the work of Dietl *et al* [8] on the DMS CdMnSe:In. They found $\nu = 0.86$ and $\sigma_0 = 0.1\sigma_{min}$, which shows remarkable agreement with our data on CdMnTe:In. It seems clear that in this system the minimum metallic conductivity value is of little significance. It should also be noted that other systems show a conductivity prefactor rather different to σ_{min}. In particular the work on Si [21,3] has shown that $\sigma_0 \sim 10\sigma_{min}$. At present, the issue of the value of the prefactor in comparison to the minimum metallic conductivity is an open one. Figure 7.2.15 shows a plot of σ_0/σ_{min} against σ_{min} for several systems. The interesting point here is that a pattern emerges in that materials with a large minimum metallic conductivity tend to have a larger scaling theory prefactor. No theoretical explanation for this observation is available at the moment.

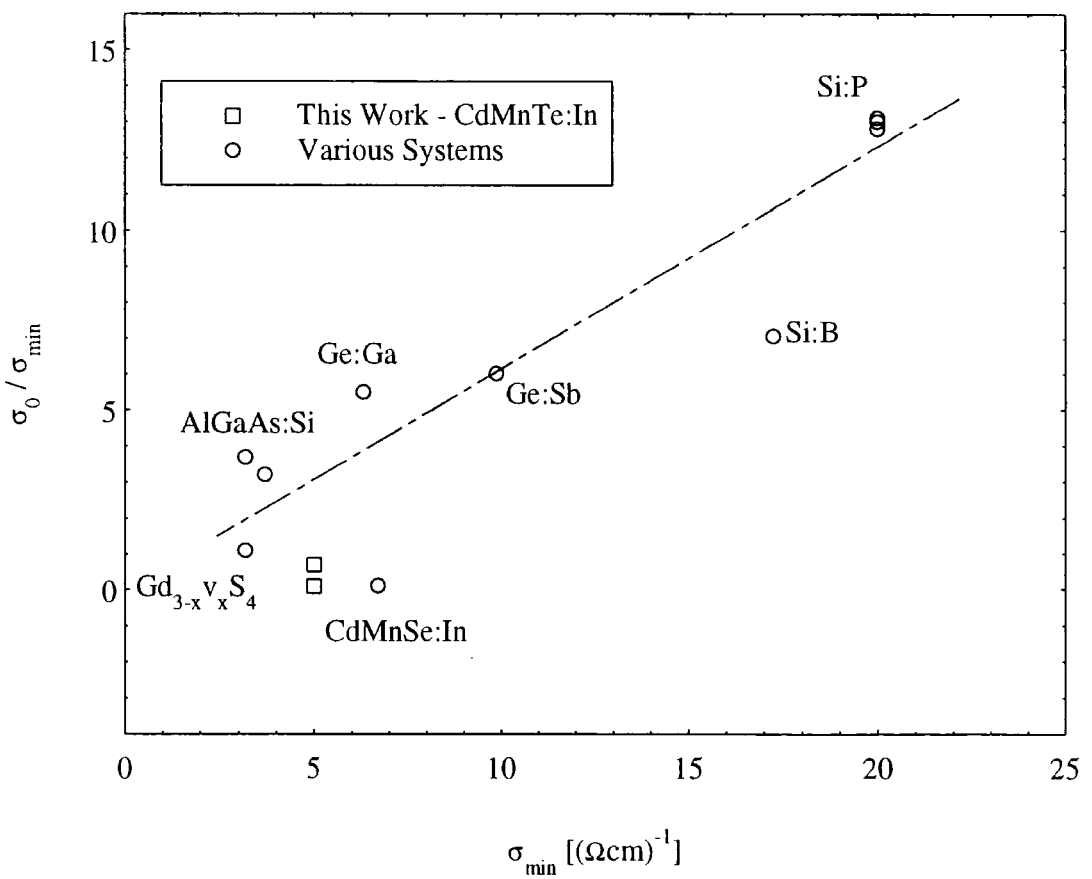

Figure 7.2.15. Plot of σ_0/σ_{min} against σ_{min} for a variety of materials.

One final point to make about figures 7.2.13 and 7.2.14 is that the scaling theory describes the data very well up to $(n/n_c - 1) \approx 1.31$. As was mentioned in chapter 3 the region over which the scaling theory is likely to apply is not well known. This data certainly suggests that the region of agreement between experiment and theory is quite large.

7.3. Conductivity of CdMnTe:In in the WLR.

The last section was concerned with measurements on two samples of CdMnTe:In which can be illuminated from insulating to metallic at low temperatures. This section is concerned with two samples, A1 and A2, which are metallic before illumination. Extensive electrical characterization data has been presented earlier for these samples (see sections 6.1 and 7.1). The transport data for these samples is summarised in table 6.1.2. The temperature dependence of the conductivity down to 4.2 K has already been presented for both of these samples (section 7.1), where it was seen that they appear to be metallic from these relatively high temperature measurements. We shall see that although the temperature dependence of the conductivity down to 300 mK is not of a simple form, both of these samples are, as expected, metallic in nature.

The temperature dependence of the conductivity of these samples has been measured down to 300 mK, to examine the value of the conductivity in the zero temperature limit. Figure 7.3.1 shows the data for sample A1, in the dark and at full illumination, while figure 7.3.2 shows data for the dark level, and two photogenerated carrier densities, in sample A2. At temperatures down to 1.5 K the conductivity is of a typical form with a weak temperature dependence roughly following $T^{1/2}$. Below this temperature a rapid and unexpected drop in conductivity occurs. Such behaviour is immediately reminiscent of the data of Dietl *et al* on CdMnSe:In [8, 16] as discussed in section 2.3.4 and displayed in figure 2.3.11. They made the reasonable hypothesis that the effect is magnetic in origin, as CdTe:In of similar carrier density showed no such effect.

The data was interpreted in terms of additional spin-disorder scattering at low temperatures due to the formation of bound magnetic polarons (BMPs).

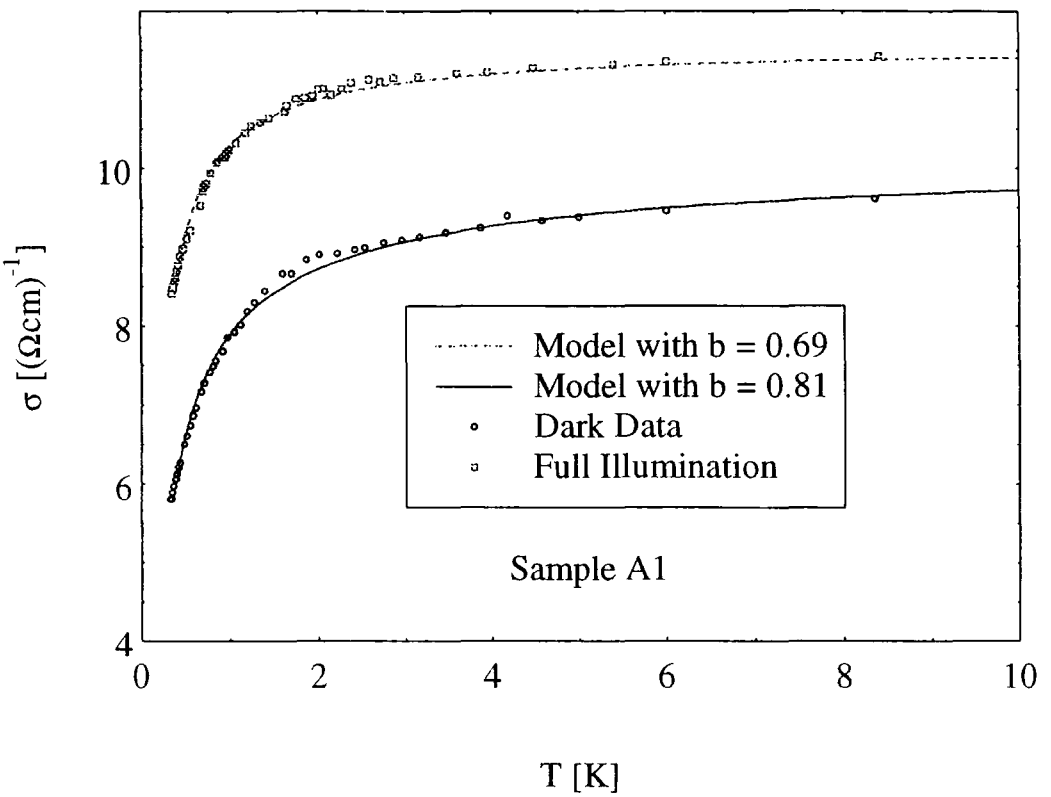

Figure 7.3.1. The temperature dependence of the conductivity of sample A1 down to 336mK, in the dark and at full illumination.

If we are to attempt to interpret our data in the same fashion it is first important to prove that this data cannot be a result of the effects of electron-electron interaction and weak localization as seen in the previous sections. Although the data can be fitted to equation 7.1, the fit is rather poor and, moreover, the deduced parameters are ludicrous in comparison to those observed previously in this material as well as other materials. For example, in figure 7.3.1 the fit is restricted to the region below 0.8 K, with values as high as 40 for B, and values of p around 0.2. Equation 7.1 certainly cannot explain the sudden drop in the conductivity observed in both samples. Again with figure 7.3.2 a poor fit can be obtained, but the parameters are unreasonable. In fact this sample produces a poorer fit

than A1, due to the slight weakening of the temperature dependence near 300 mK. Perhaps the most convincing point however, is that for both samples the fitting procedure always results in a zero value for the conductivity at absolute zero. This suggests that both of these samples would have to be insulating which is inconsistent with their carrier concentrations ($n > n_c$ in both cases) and the absolute value of the conductivity at relatively low temperatures (for sample A1 the conductivity at 4.2 K is actually in excess of the minimum metallic conductivity, and is greater than our determined value of the scaling theory conductivity prefactor by a factor of approximately 20 !). It should also be noted that for samples with carrier densities as high as these the temperature dependence of the conductivity would be expected to be far weaker than for samples close to the MIT such as A5. It seems clear therefore, that this model for the temperature dependence of the conductivity is not suitable to explain the observed data.

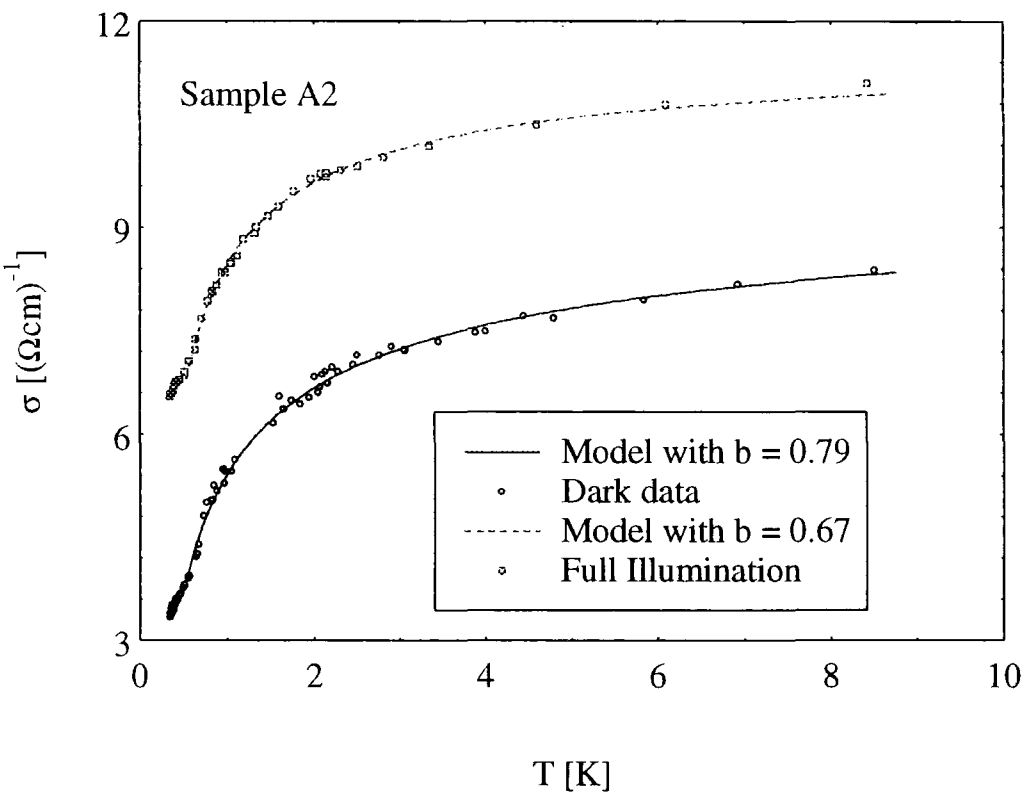

Figure 7.3.2. Temperature dependence of the conductivity of sample A2 down to 332 mK, in the dark and at full illumination.

It is possible to quantitatively account for the temperature dependence of the conductivity, if the model of Dietl *et al* is correct. In this model we assume that in the WLR, quasi-localized s spins still exist [23], and so BMPs can form around these localized states. This leads to efficient scattering of conduction electrons by a spin-disorder mechanism in small or zero magnetic field. The sharp drop in conductivity occurs when the temperature is low enough for the s-d exchange interaction to dominate and the polarons begin to form. Following Sawicki *et al* [16] it is possible to model this situation using the scaling theory equation, $\sigma = \sigma_0(n/n_c - 1)^{\nu}$ and the Mott criterion, $n_c = (0.26/a_B)^3$. We propose that the s-d exchange interaction influences the size of the Bohr radius, because as the sample is cooled, the binding energy of the polaron increases, meaning that the effective Bohr radius decreases. A temperature dependent Bohr radius implies a temperature dependent n_c, which, through the scaling equation, leads to $\sigma(T)$. This leads to the following form for the conductivity,

$$\sigma(T) = \sigma_0\left(\frac{a_B^3 n}{0.0176} - 1\right) \tag{7.3.1}$$

The temperature dependence of the effective Bohr radius of the polaron can be derived from the (zero field) expression for the free energy of the BMP [24],

$$F_p = \frac{\hbar^2}{2m^* a_B^2} - \frac{e^2}{\varepsilon_0 a_B} - \frac{1}{2}E_p(T,H) \tag{7.3.2}$$

where $E_p = \dfrac{\alpha^2 \chi(T,H)}{32\pi g^2 a_B^3 \mu_B^2}$, is the characteristic energy of the magnetic polaron. Minimising F_p with respect to the Bohr radius, allows us to calculate $a_B(T)$ as,

$$a_B(T) = \frac{a_H}{2} + \frac{\varepsilon}{2e^2}\left[\frac{\hbar^4}{m^{*2}} - \frac{4e^2}{\varepsilon_0}\left(\frac{3\alpha^2\chi(T,H)}{64\pi g^2\mu_B^2}\right)\right]^{1/2} \qquad (7.3.3)$$

where a_H is the Bohr radius of a hydrogenic donor. Physically, this equation satisfies all the necessary requirements for the form of $a_B(T)$: at high temperatures, where the macroscopic susceptibility $\chi(T)$ is small, the second term in square brackets tends to zero, and we obtain a_H as the radius of the polaron. However, at low temperatures, where $\chi(T)$ is rapidly increasing, this term dominates, drastically reducing the observed conductivity. As the susceptibility of our samples is unknown in this temperature region we model the temperature dependence as $\chi(T) = aT^{-b}$, as observed in CdMnSe:In in this temperature region. This form is actually typical for nonmagnetic materials in the WLR, where the susceptibility is weaker than the Curie law T^{-1} dependence. Values of $b \approx 0.7$ were found for $Cd_{0.95}Mn_{0.05}Se$:In, with $n/n_c \sim 2.7$.

Figure 7.3.1 shows the fit to the conductivity using this model. The susceptibility exponent, b, (which is used as a fitting parameter) is shown in the figure. This model fits the data rather well, with a value of b which is in agreement with the previously observed values of approximately 0.7 [8]. The calculated values for the radius of the polaron are shown in figure 7.3.3, where it can be seen that the values are actually quite large (10 nm). This is presumably due to the fact that the quasi-localized s-spins which exist in the metallic phase are far more extended in nature than the localized states in the insulating phase. Figure 7.3.2 shows the fits to the low temperature conductivity data for sample A2, again with reasonable values of the parameter b.

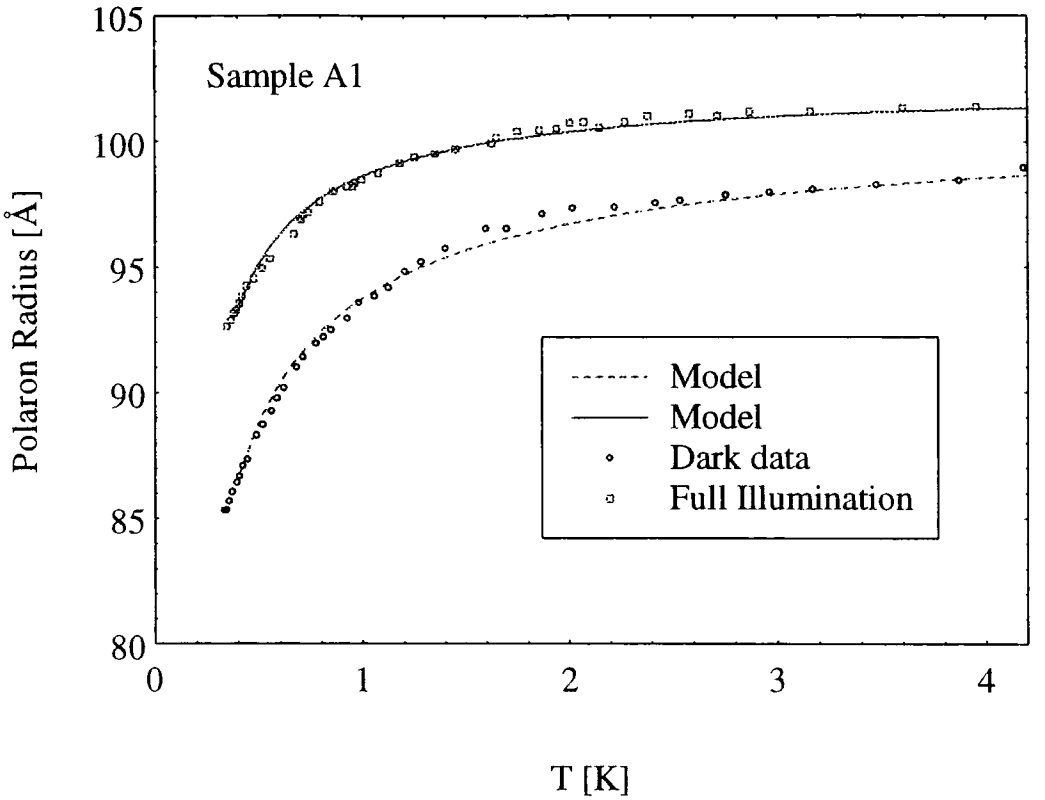

Figure 7.3.3. Temperature dependence of the polaron radius, as extracted from the conductivity data on sample A1.

It should be noted that the temperature at which the drop in conductivity occurs in our samples is actually larger than the temperature at which it occurs in CdMnSe. We suggest that this is due to the fact that the Fermi wavevector has a smaller value in our case due to the lower carrier densities, combined with the fact that the effective mass is lower. To explain more fully, consider the form of the regular spin-disorder scattering rate (due to Mn ions), τ_{si}^{-1}, in comparison to the polaron scattering rate τ_{pi}^{-1}, as given by the following expressions [8],

$$\tau_{si}^{-1} = \frac{k_B T \alpha^2 k_f m^* \mu \chi(T)}{4\pi\hbar^3 g^2 \mu_B^2} \tag{7.3.4}$$

$$\tau_{pi}^{-1} = f(T) N_p \mu \chi^2(T) \qquad (7.3.5),$$

where μ is an enhancement factor brought about by disorder and spin-fluctuations [8], $f(T)$ is a function calculated from the free energy, and N_p is the number of polarons. The drop in the conductivity due to polaron scattering will only occur when the polaron scattering rate dominates the conductivity. If the regular spin-disorder scattering rate is of a lower value due to the lower value of k_F and m^*, then this drop will occur at higher temperatures, despite the fact that the s-d exchange energy is slightly smaller for CdMnTe than CdMnSe. To quantify this, using the values of m^* and α and calculating k_f from the free electron formula we estimate that the regular spin-disorder scattering rate for CdMnTe is lower by a factor of 2.58 at $1.5n_c$. Dietl found that the polaron scattering begins to affect the conductivity at 0.5 K. Hence, if our calculation is correct then we would expect the polaron scattering to become apparent at ~1.3 K in CdMnTe. This is in reasonable agreement with the observed values of 1.5 - 2.0 K in our samples.

The most important open question about this observation of BMP scattering in CdMnTe is why is it not observed in other samples which have been studied in detail at low temperatures? Indeed, why has it not been observed in the insulating phase as for CdMnSe:In [25]? We believe that the central issue in the understanding of this problem is the paramagnetic to spin-glass magnetic phase transition. It has been recently suggested that the binding energy of the magnetic polaron is constant in the spin-glass phase [26], meaning that the rapid drop in the conductivity, due to the increasing binding energy of the polaron, will not occur. Now, the spin-glass freezing temperature (T_f) increases with Mn fraction, so that samples with low Mn fraction will have a very low T_f. These samples will show the effects of BMP scattering in the low temperature conductivity, while samples with higher Mn fraction can have $T_f > 300$ mK meaning that the binding energy of the BMP will be independent of temperature below T_f, and no drop in conductivity will be observed.

The x dependence of the freezing temperature has previously been measured for nominally undoped CdMnTe [27,28]. For sample A1, where $x = 0.047$, we expect $T_f \sim$ 150 mK, suggesting that we should observe a drop in the conductivity in measurements down to 300 mK, as the sample is in the paramagnetic phase and the binding energy of the polarons is temperature dependent. For sample A2, where $x = 0.061$, we expect $T_f \sim 300$ mK. This is interesting as the data of figure 7.3.2 shows a weakening of the temperature dependence at $T \approx 0.4$ K. We propose that this feature is associated with the slowing down of the spin dynamics near the spin-glass freezing temperature. Eventually at lower temperatures, the conductivity will flatten out and become a weak function of temperature, due to the fact that the polaron binding energy is constant when we are deep in the spin-glass phase. This weakening of the temperature dependence was also observed by Dietl *et al* [8] at a temperature of approximately 110 mK in a sample with a *measured* $T_f = 95$ mK, suggesting that their data is in agreement with our hypothesis. It should also be noted that the data of Terry *et al* [11], where an $\exp(E_H / T)$ dependence was observed due to a magnetic hard gap in the DOS, lends weight to our argument. This is because the resistivity curves are actually very linear in T^{-1} suggesting that E_H (a measure of the polaron binding energy) is independent of temperature in this region. This is exactly what we are hypothesising for the situation where the sample is in the spin-glass phase.

One test of this idea would be to measure the low temperature conductivity of a sample with a rather large Mn fraction, which is still in the WLR. At first sight this would appear impossible as samples with large x are invariably insulators. However, doping with both In and Al allows us to produce crystals with large Mn compositions that are still metallic. We will present data on just such a sample in the next section.

7.4. Metallic CdMnTe:In, Al and CdMnTe:Al.

This section presents the results of transport measurements on three samples of CdMnTe:In, Al and one sample of CdMnTe:Al. All of these samples are close to the MIT. The transport data is summarised in table 7.4.1, where the composition, 300 K carrier

concentration, resistivity and mobility, proximity to the MIT and deep level activation energy are shown (note that the deep level activation energies are only approximate as the temperature dependence of the resistivity was used in their determination).

Sample	x %	Proximity to MIT	σ(300K) $(\Omega cm)^{-1}$	n (300K) 10^{17} cm^{-3}	μ (300K) $cm^2V^{-1}s^{-1}$	E_D meV
AL1	19.0 ± 0.3	~Critical	9.1	3.42	166.3	10.2
INAL2	4.4 ± 0.3	Metallic	13.3	3.71	224.1	5.9
INAL3	13.5 ± 0.4	Metallic	14.0	5.01	174.6	7.4
LNAL4	18.1 ± 0.3	~Critical	4.1	3.98	85.2	8.4

Table 7.4.1. Summary of transport properties for In, Al doped samples.

The temperature dependence of the conductivity was measured down to 4.2 K for all four samples. All four samples show a qualitatively similar temperature dependence. Samples INAL2 and INAL4 are shown as examples in figures 7.4.1 and 7.4.2. Sample INAL2 shows a metallic temperature dependence, consistent with the fact that the carrier density is 3.7 x 10^{17} cm^{-3} while x is only 0.044. INAL4 is an interesting sample as it appears to very close to the MIT critical point. This fact enables us to make a prediction regarding the x dependence of the critical carrier density. For x = 18.12 ± 0.27 % we find that $n_c \approx 4.0 \times 10^{17}$ cm^{-3}. If we assume that $n_c(x)$ is of the form $n_c = a + bx$, then using $n_c \approx 1.1 \times 10^{17}$ cm^{-3} for CdTe, $n_c \approx 2.0 \times 10^{17}$ cm^{-3} for x = 0.081 and this new value, we obtain (from a least squares fitting procedure),

$$n_c(x) = 15.5x + 0.96 \qquad (7.4.1)$$

which should be reasonable approximation to the truth in the region $0 < x < 0.2$, which spans the region in which transport measurements are usually made. (Note that this

equation has n in units of 10^{17} cm^{-3}.) This equation is in agreement with the data of Terry *et al* [11] where n_c was suggested to be 2.3 x 10^{17} cm^{-3} for x = 0.091, compared to a predicted value of 2.4 x 10^{17} cm^{-3} from (7.4.1).

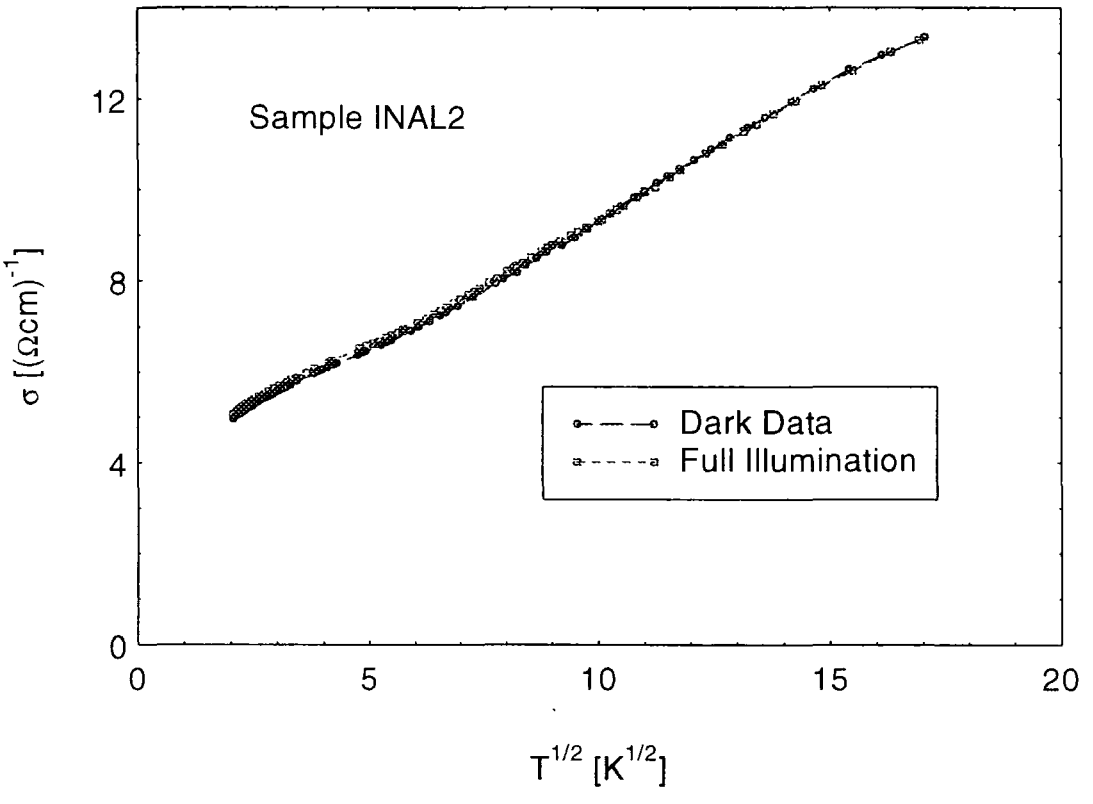

Figure 7.4.1. The temperature dependence of the conductivity of sample INAL2.

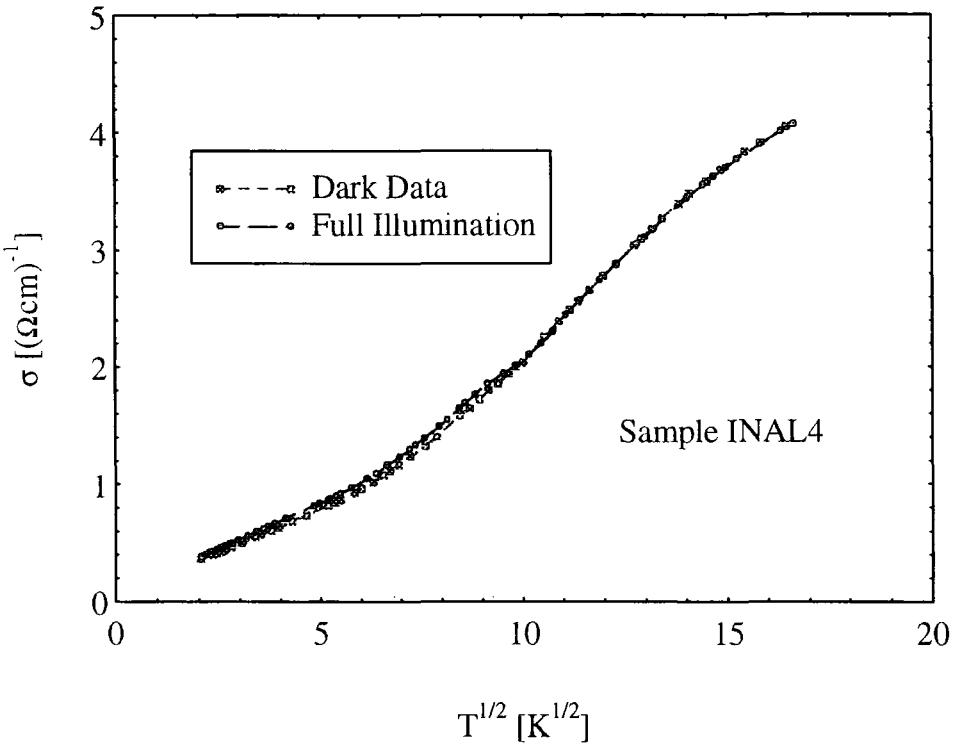

Figure 7.4.2. The temperature dependence of the conductivity of sample INAL4.

Samples INAL2, INAL3 and INAL4 all show a very small amount of PPC on illumination at 4.2 K. Changes in illumination of the order of 5 % are typical. Presumably this small change in resistivity is due to the fact that the carrier densities are so large, combined with the effect of the lower indium doping levels in this set of samples. The original motivation for growing samples such as these was to use these samples to fine tune the transition by illumination. It was envisaged that the Al doping would provide a large number of shallow donors while the In doping would provide sufficient PPC. Clearly these three samples are not suitable for this purpose as the change in resistivity on illumination is too small. Sample AL1 is doped with Al only and therefore shows no PPC at all.

There are several other comments to be made about the transport properties of these samples. Firstly, the values of the mobility in AL1, INAL3 and INAL4 are unusually

low for samples this conductive. This could be due to the added effect of alloy scattering due to the large Mn fractions present in these samples (13.46 to 19.04 %). The values of the deep level activation energies are also of interest. As expected, E_D exhibits an increase with increasing x in the region studied. However, all of the values measured are far smaller than that expected from our previous measurement of the x dependence of the deep level energy (figure 6.1.21). We propose that this observation is related to the high dopant levels present in this system. In particular it is plausible that the activation is not from the deep level to the conduction band edge, but that it is activation to a merged impurity band and conduction band. As we have already discussed, this situation is possible when the banding in the impurity states becomes so large that the top of the impurity band crosses the conduction band edge.

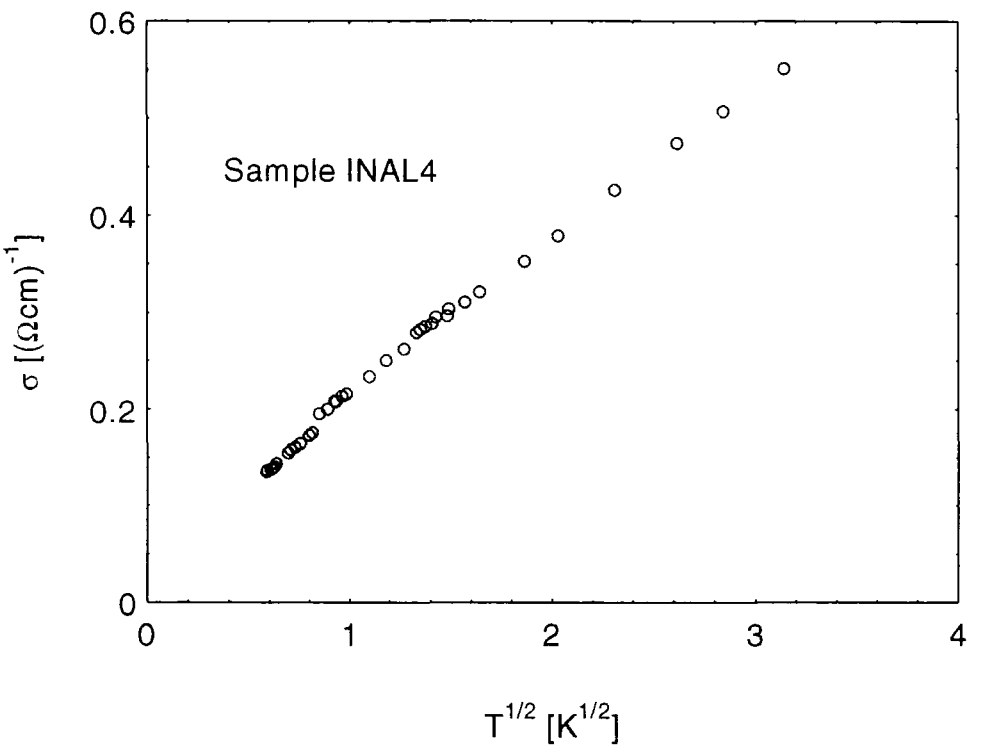

Figure 7.4.3. Temperature dependence of the conductivity of sample INAL4, measured down to 335 mK.

Finally, the temperature dependence of the conductivity of sample INAL4 was measured down to 332 mK. The purpose of this experiment was to ascertain whether this sample displays a sudden drop in the conductivity due to BMP spin-disorder scattering. Figure 7.4.3 shows that no such effect exists. It should be noted that in a sample with 18% Mn we would expect $T_f \sim 2$ K [27,28]. So, this would appear to confirm our hypothesis that the sudden drop in the conductivity at low temperature will only occur in samples which are in the paramagnetic phase at these temperatures. This sample is certainly in the spin-glass phase below 1 K, which explains why no polaron scattering is observed.

Chapter 7 - References.

1. S. Katsumoto. *Anderson Localization.* eds T. Ando and H. Fukuyama. (Springer-Verlag, 1987). p45.

2. See for example, P.A. Lee and T.V. Ramakrishnan. Rev. Mod. Phys. **57** 287 (1985).

3. P. Dai, Y. Zhang and M.P. Sarachik. Phys. Rev. B. **45** 3984 (1992).

4. G.A. Thomas, A. Kawabata, Y. Ootuka, S. Katsumoto, S. Kobayashi and W. Sasaki. Phys. Rev. B. **26** 2113 (1982).

5. W.N. Shafarman, D.W. Koon and T.G. Castner. Phys. Rev. B. **40** 1216 (1989).

6. N.J. Hirsch and D.F. Holcomb in *Disordered Semiconductors* eds M.A. Kastner, G.A. Thomas and S.R. Ovshinsky. (Plenum, New York, 1987). p45.

7. S. von Molnar, J. Flouquet, F. Holtzberg and G. Remenyi. Solid. State. Electron. **28** 127 (1985).

8. T. Dietl, M. Sawicki, T. Wojtowicz, J. Jaroszynski, W. Pleisewicz, L. Swierkowski and J. Kossut. *Anderson Localization.* eds T. Ando and H. Fukuyama. (Springer-Verlag, 1987). p58.

9. D.M. Finlayson, P.J. Mason and I.F. Mohammad. J. Phys. C. **20** L607 (1987).

10. A. Mobius. J. Phys. C. **21** 2789 (1988).

11. I. Terry, T. Penney, S. von Molnar and P. Becla. Phys. Rev. Lett. **69** 1800 (1992).

12. T.G. Castner. *Hopping Transport in Solids* eds M. Pollak and B. Shklovskii. (Elsevier, 1991) p.1.

13.See for exmple R.F. Milligan, T.F. Rosenbaum, R.N. Bhatt and G.A. Thomas. *Electron-Electron Interactions in Disordered Systems.* eds A.L. Efros and M. Pollak. (Elsevier, 1985) p. 270.

14. S. Washburn, R.A. Webb, S. von Molnar, F. Holtzberg, J. Flouquet and G. Remenyi. Phys. Rev. B. **30** 6224 (1984).

15. W.N. Shafarman, T.G. Castner, J.S. Brooks, K.P. Martin and M.J. Naughton. Solid. State. Electron. **28** 93 (1985).

16. M. Sawicki, T. Dietl, J. Kossut, J. Igalson, T. Wojtowicz and W. Pleisewicz. Phys. Rev. Lett. **56** 508 (1986).

17. S. von Molnar, A. Briggs, J. Flouquet and G. Remenyi. Phys. Rev. Lett. **51** 706 (1983).

18. R.M. Westervelt, M.J. Burns, P.F. Hopkins, A.J. Rimberg and G.A. Thomas. *Anderson Localization.* eds T. Ando and H. Fukuyama. (Springer-Verlag, 1987). p33.

19. J.F. DiTusa, K. Friemelt, E. Bucher, G. Aeppli and A.P. Ramirez. Phys. Rev. Lett. **78** 2831 (1997).

20. Y. Shapira, N.F. Oliveira Jr., P. Becla and T.Q. Vu. Phys. Rev. B. **41** 5931 (1990)

21. T.F. Rosenbaum, K. Andres, G.A. Thomas and R.N. Bhatt. Phys. Rev. Lett. **45** 1723 (1980).

22. D. Belitz and T.R. Kirkpatrick. Rev. Mod. Phys. **66** 261 (1994).

23. Zi-Zhao Gu and P.A. Lee. Phys. Rev. B. **33** 3595 (1986).

24. T. Dietl. *Diluted Magnetic Semiconductors* in *Handbook on Semiconductors* vol 3 ed. T.S. Moss (Elsevier, NY, 1994). p.1291.

25. T. Dietl, L. Swierkowski, J. Jaroszynski, M. Sawicki and T. Wojtowicz. Physica Scripta. **T14** 29 (1986).

26. A.L. Chudnovskiy, R. Oppermann, B. Rosenow, D.R. Yakovlev, U. Zehnder and W. Ossau. Phys. Rev. B. **55** 10519 (1997).

27. J. Kossut and W. Dobrowolski. *Diluted Magnetic Semiconductors* in *handbook of Magnetic Materials* ed. K.H.J. Buschow. (Elsevier, NY, 1993). p. 264.

28. S. Oseroff and P.H. Keesom in *Semiconductors and Semimetals* vol 25 eds. J.K. Furdyna and J. Kossut. (Academic Press,1988). p. 105.

8. Summary and Conclusions.

This chapter contains a summary of all the work presented in this thesis along with a set of conclusions which can be drawn from the work. Section 8.1 summarises the data of chapter 6 on the electrical characterization and PPC measurements, while section 8.2 summarises the data on the MIT in CdMnTe. Work on the conductivity in the WLR is included in this section. Finally, section 8.3 gives a list of suggestions for further work which could benefit the attempts to understand the physics discussed in the thesis.

8.1. Electronic Transport in CdMnTe:In - A Summary.

Detailed electrical transport measurements as a function of composition have led to a good understanding of the phototransport properties of this system. In particular, the compositional dependence of the DX^- deep level, hydrogenic shallow level and quenching temperature have been clarified. This work constitutes the first systematic study of the variation of these parameters with Mn fraction. Several new effects have been observed and attributed to the very heavy doping in the more conductive samples.

Some samples support PPC up to elevated temperatures close to 200 K. Several possible explanations for this effect have been discussed. We have been able to conclude that the high temperature PPC is due to the formation of multiple DX centres. Whether these multiple DX centres are of the type discussed by Park and Chadi [1] or whether they are due to the effects of the local atomic environment [2] is difficult to clarify. The elevated temperature PPC observed in these samples leads us to conclude that CdMnTe:In could be an interesting system in terms of realising the application potential of a room temperature persistent photoconductor.

Measurements of the low temperature magnetoresistance in the insulating phase suggest that the positive MR observed is not due to conventional hopping effects. In fact

the MR is intimately linked with the magnetization of the sample. This is consistent with previous work by Terry *et al* [3]. In the metallic phase the low field magnetoresistance is still positive down to 3.9 K. It is interesting to note that the MR shows little dependence on the carrier density in this region. An anomalous negative MR has been observed at high temperatures (about 100 K) when certain samples are continuously illuminated with infra-red. This effect peaks at a temperature very close to the quenching temperature of the material suggesting that it is linked with the PPC effect. We have interpreted this data in terms of the formation of small magnetic polarons on singly occupied deep levels. This polaron formation leads to a negative MR through the reduction in spin-disorder scattering on application of a magnetic field. Limited photomagnetization measurements appear to support this hypothesis.

Nearest neighbour phonon assisted hopping has been observed in the insulating phase in a 16 % Mn sample. This sample shows a crossover from activated conduction to hopping conduction at low temperatures. The activation energy associated with shallow indium donor level decreases monotonically with increasing carrier density, whereas the hopping energy (E_3) shows a peak with increasing carrier density. The infinite temperature extrapolations of the resistivity in the two regions also exhibit typical behaviour for a system which crosses over to nearest neighbour hopping as the temperature is lowered.

8.2. The MIT in $Cd_{1-x}Mn_xTe$:In - A Summary.

The PPC effect was used to fine tune the MIT in zero magnetic field. The critical behaviour is consistent with the scaling theory of electron localization. A critical exponent close to one is found for both samples which can be illuminated through the transition. The critical carrier concentration for 8.1 % Mn is approximately 2×10^{17} cm^{-3}. This is the first determination of the critical exponent in a magnetic semiconductor in zero magnetic field. Other experiments on the MIT in magnetic systems have used the application of magnetic fields to induce a transition [4, 5]. The measured exponent is in

agreement with scaling theory with electron-electron interactions taken into account, as well as previous work on magnetic semiconductors.

In the metallic phase the temperature dependence of the conductivity can be explained by a model where the effects of electron-electron interaction and weak localization are taken into account. These effects lead to a $mT^{1/2}$ term and a BT term in the expression for $\sigma(T)$ [6]. The size of the parameters m and B have been examined and compared to simple theoretical estimates. Reasonable agreement between experiment and theory is obtained.

In the insulating phase VRH conduction is observed with a temperature dependence which is consistent with the Efros-Shklovskii form [7]. This hopping conduction has been studied as a function of carrier density as the MIT is approached. At low temperatures (about 0.6 to 0.5 K) the temperature dependence of the resistivity shows an unexplained weakening in one sample. The reason for this behaviour is discussed, although no firm conclusions can be drawn. The values of the hopping parameters (such as T_0 and ρ_0) for the other sample, which shows no anomalous low temperature effects, are in excellent agreement with previous work [8].

An investigation of the temperature dependence of the conductivity in the WLR of CdMnTe:In and CdMnTe:In,Al has led to the observation of a rapid drop in the conductivity which we believe is associated with the formation of magnetic polarons. The BMPs lead to enhanced spin-disorder scattering at low temperature as in CdMnSe:In [9]. The observation that this drop in the conductivity is only observed in samples with low x has been explained by the hypothesis that this effect is only seen in the paramagnetic phase. Samples with a larger Mn fraction enter a spin-glass phase in which the polaron binding energy has been predicted to be constant [10]. Hence no sudden drop in the conductivity is observed. This explains the weakening of the temperature dependence near the spin glass freezing temperature in CdMnSe [9] as well as the lack of temperature dependence of the magnetic hard gap in CdMnTe [8].

8.3. Suggestions For Further Work.

Although the PPC effect in CdMnTe:In is quite well understood at this point there are several effects which merit further work.

First of all the negative MR effect observed in sample B5 under illumination is worthy of further experimentation. It would be useful to perform some wavelength dependent MR measurements to prove that the effect we observed is definitely linked to the PPC effect. If this is the case then the MR would only be present when the sample is illuminated with light at wavelengths which will excite the DX centre PPC. Also it would be useful to extend the photomagnetization measurements on this sample, to examine the temperature dependence of the photoinduced increase in magnetization on illumination in the vicinity of the quenching temperature. Examining other samples in order to ascertain whether they display negative MR under similar conditions would be highly desirable. As outlined in chapter 6 samples with a high mobility which is weakly temperature dependent are most likely to display the effect.

Sample A7 would also benefit form further measurements. Firstly it would be favourable to extend the temperature range of the measurements to lower temperatures. Although it becomes increasingly difficult to measure the resistances of this size it should be possible to continue the measurements down to ~ 1 K. This would determine whether the temperature dependence remains of the form $\exp(E_3/k_BT)$ or whether VRH conduction sets in. In addition to this it would be useful to measure the magnetoresistance in the hopping regime. It is unknown whether the magnetoresistance will be driven by the magnetization of the sample or conventional hopping MR effects.

With regard to the measurements on the metal-insulator transition, it seems clear that extending the temperature range down to the millikelvin regime would result in a more accurate determination of the values of ν and n_c, through an extrapolation to

absolute zero. These measurements would also elucidate the form of the temperature dependence of the conductivity in the metallic phase. It is unknown at present whether the sign of $d\sigma/dT$ will change at lower temperatures. In addition to these measurements it would be informative to measure the critical exponent in a strong magnetic field to determine whether a change in universality class might be taking place. This would involve measuring the temperature dependence of the conductivity in the critical regime in a relatively large magnetic field.

The experiments in the WLR would also benefit from measurements at lower temperatures. This would allow us to examine the temperature dependence of the conductivity as the temperature falls below the spin-glass freezing temperature. If our theory is correct the a weakening if the temperature dependence would be observed, as the polaron binding energy tends to a constant value. Most importantly it would be beneficial to measure the temperature dependence of the d.c. susceptibility at low temperatures. Thus would allow us to determine the spin-glass freezing temperature directly for each sample. A d.c. SQUID is currently being installed in the ^{3}He insert in Durham. This will allow the measurement of the susceptibility with high sensitivity down to 300 mK.

Chapter 8 - References.

1. C.H. Park and D.J. Chadi. Phys. Rev. B. **52** 11 884 (1995).

2. A. Gomez, E. Munoz, P.M. Mooney, T.N. Morgan and S.L. Wright. Appl. Phys. Lett. **56** 934 (1990).

3. I. Terry , T. Penney, S. von Molnar and P. Becla. J. Cryst. Growth. **159** 1070 (1996).

4. T. Dietl, M. Sawicki, T. Wojtowicz, J. Jaroszynski, W. Pleisewicz, L. swierkowski and J. Kossut. *Anderson Localization.* eds. T. Ando and H. Fukuyama. (Springer-Verlag, 1987). p.58.

5. S. von Molnar, A. Briggs, J. Flouquet and G. Remenyi. Phys. Rev. Lett. **51** 706 (1983).

6. P.A. Lee and T.V. Ramakrishnan. Rev. Mod. Phys. **57** 287 (1985).

7. B.I. Shklovskii and A.L. Efros. *Electronic Properties of Doped Semiconductors.* (Springer-Verlag, 1984).

8. I. Terry, T. Penney, S. von molnar and P. Becla. Phys. Rev. Lett. **69** 1800 (1992).

9. M. sawicki, T. Dietl, J. Kossut, J. Igalson, T. wojtowicz and W. Pleisewicz. Phys. Rev. Lett. **56** 508 (1986).

10. A.L. Chudnovskiy, R. Oppermann, B. Rosenow, D.R. Yakolev, U. Zehnder and W. Ossau. Phys. Rev. B. **55** 10 519 (1997).

Appendix A.

The probability of finding i Mn atoms in a DX centre configuration was estimated using simple statistical arguments. For example, if the percentage Mn fraction is x then one can write the probability of finding a configuration with zero Mn atoms as,

$$P(i=0)=\frac{100-x}{100}\left[\frac{100-(x+1)}{99}\right]\left[\frac{100-(x+2)}{98}\right]\left[\frac{100-(x+3)}{97}\right] \qquad \text{(A1).}$$

So for a 10 % crystal we have (90/100) x (89/100) x (88/100) x (87/100) for the probability of a configuration with zero of the four relevant sites being filed by Mn atoms. Correspondingly, the probability of finding one, two or three Mn atoms is given by the following expressions :

$$P(i=1)=\frac{4x}{100}\left[\frac{100-x}{99}\right]\left[\frac{100-(x+1)}{98}\right]\left[\frac{100-(x+2)}{97}\right] \qquad \text{(A2),}$$

$$P(i=2)=\frac{4x}{100}\left[\frac{x-1}{99}\right]\left[\frac{100-x}{98}\right]\left[\frac{100-(x+1)}{97}\right] \qquad \text{(A3),}$$

$$P(i=3)=\frac{4x}{100}\left[\frac{x-1}{99}\right]\left[\frac{x-2}{98}\right]\left[\frac{100-x}{97}\right] \qquad \text{(A4).}$$

The factor of four here is due to the fact that there are four ways of arranging the atoms.

It should be noted that this model is only valid for the case when the Mn atoms are distributed randomly in the lattice.